DATA AUGMENTATION AND ENHANCEMENT FOR CARDIOVASCULAR 4D FLOW MRI

by

Jiacheng Zhang

A Dissertation

Submitted to the Faculty of Purdue University

In Partial Fulfillment of the Requirements for the degree of

Doctor of Philosophy

School of Mechanical Engineering

West Lafayette, Indiana

May 2022

THE PURDUE UNIVERSITY GRADUATE SCHOOL
STATEMENT OF COMMITTEE APPROVAL

Dr. Pavlos Vlachos, Chair
School of Mechanical Engineering

Dr. Vitaliy Rayz
Weldon School of Biomedical Engineering

Dr. Ilias Bilionis
School of Mechanical Engineering

Dr. Michael Markl
Feinberg School of Medicine
Northwestern University

Approved by:
Dr. Nicole L. Key

Dedicated to my parents and my wife for motivating me throughout my journey

ACKNOWLEDGMENTS

The studies were supported by the National Institutes of Health under grants R21 NS106696 and R01 HL115267. The work in Chapter 2 was also supported by the National Institute of Biomedical Imaging And Bioengineering of the National Institutes of Health under Award Number T32EB025766. The work in Chapter 5 was also supported by National Science Foundation (Grant No. NSF 1706474). The work in Chapter 6 was also supported by the National Science Foundation's MRI program grant with award number 1725929.

This work would not be possible without the support of many people. I would like to thank my advisor, Professor Pavlos P. Vlachos, for guiding and supporting me throughout my PhD. His mentorship helped me to be a better researcher, and his expertise was invaluable in formulating the research questions and the methodology. Many thanks to my committee members, Professor Vitaliy Rayz, Professor Michael Markl, and Professor Ilias Bilionis for their insightful feedback and suggestions.

I would like to thank the past and present lab members in Vlachos Research Groups for the collaborations and helps at all stages of my PhD. I would like to thank Dr. Melissa Brindise for her contributions and suggestions on the 4D flow MRI and hemodynamic analysis works. I would like to thank Dr. Brett Meyers for his helps and insights on the cardiovascular flow mechanics. I would like to thank Dr. Sayantan Bhattacharya, Dr. Lalit Rajendran, and Dr. Adib Ahmadzadegan for their contributions and collaborations on the PIV/PTV based pressure reconstruction, BOS processing, and the diffusion measurement projects. I would like to thank my collaborators from Dr. Rayz's lab and Dr. Markl's lab for their helps and contributions on the 4D flow MRI development works. I would like to thank all my colleagues, fellow graduate students, and collaborators for your helps and encouragements during my PhD. I would also like to thank the School of Mechanical Engineering for the opportunity and support.

Finally, I would like to thank my parents and my wife for their selfless support and priceless encouragements throughout the journey. Special thanks to my wife Mandy for accompanying me and for helping me keeping my sanity during these years.

TABLE OF CONTENTS

LIST OF TABLES

LIST OF FIGURES

ABSTRACT

Cerebral aneurysms are presented in 3-5% of the population and account for approximately 10% of all strokes. The clinical decision on treating unruptured aneurysms should not be taken lightly because a majority of the asymptomatic cerebral aneurysm will not rupture, while both endovascular and microsurgical treatments carry the risk of morbidity and mortality. Thus, there is a need for objective risk assessment to reliably predict the high-risk aneurysms to intervene. Recent studies have found that the blood flow hemodynamic metrics such as pressure and wall shear stress (WSS) are related to the growth and rupture of the aneurysms. 4D flow magnetic resonance imaging (MRI) measures time-resolved three-dimensional velocity fields in the aneurysms *in vivo*, allowing for the evaluation of hemodynamic parameters. This work presents the developments of flow-physics constrained data enhancement and augmentation methods for 4D flow MRI to assist the risk stratification of cerebral aneurysms. First, a phase unwrapping and denoising method is introduced to enhance the dynamic range and accuracy of 4D flow MRI velocity measurement by incorporating the divergence-free constraint of incompressible flow. Moreover, methods are developed to improve the estimation of hemodynamic parameters from 4D flow data including pressure and WSS. The pressure reconstruction method is also applied to the flow data acquired using particle imaging velocimetry (PIV) and particle tracking velocimetry (PTV) and shows superior performance as compared to the existing methods by solving the pressure Poisson equation. We also proposed a framework to estimate the uncertainty of the PIV/PTV based pressure estimation by propagating the velocity uncertainty. In addition, a multi-modality approach is introduced to enhances the resolution and accuracy of 4D flow data with sparse representation, which improves the reliability of the hemodynamic evaluation. Finally, we present a method to measure the left ventricular flow propagation velocity from cardiac imaging to help in assessing the diastolic function.

1. INTRODUCTION

1.1 Motivation and background

Unruptured cerebral aneurysms are found in approximately 3.2% of the adult population worldwide (Vlak, Algra, Brandenburg, & Rinkel, 2011), and they are being discovered incidentally with an increasing frequency because of the widespread use of high-resolution magnetic resonance imaging (MRI) scanning (Thompson et al., 2015). A ruptured cerebral aneurysm can cause subarachnoid hemorrhage (SAH) with mortality rates ranging from 8% to 67% and a significant morbidity rate among survivors (Øie et al., 2020; Rivero Rodríguez et al., 2015). The large majority of the unruptured cerebral aneurysms will never rupture as the annual risk of rupture was reported to be 0.7% for aneurysms$<$10 mm and 4% for those$\geq$10 mm (Rinkel, Djibuti, Algra, & Van Gijn, 1998). The management options for unruptured aneurysms include conservative management, surgical clipping, and endovascular treatment (Ajiboye, Chalouhi, Starke, Zanaty, & Bell, 2015). Conservative management is usually recommended for patients over the age of 60 years and for small (<7 mm) asymptomatic aneurysms without strong family history of SAH. Microsurgical clipping requires access to the aneurysm via an open craniotomy. Findings from one meta-analysis reported a mortality rate of 1% and a major morbidity rate of 4% (Raaymakers, Rinkel, Limburg, & Algra, 1998). The different endovascular techniques include packing the aneurysm with coils, flow diverting stents, and liquid embolic agents. Data from meta-analysis suggests that the risk of unfavorable outcomes from endovascular management is approximately 4% to 5%, with a risk of mortality of 1% to 2% (Naggara, Lecler, Oppenheim, Meder, & Raymond, 2012). Optimal management should involve the comparison of the risk of an unruptured aneurysm without any intervene with the risks of surgical clipping or endovascular treatment.

1.1.1 Hemodynamic factors for risk stratification of unruptured cerebral aneurysm

Prediction of the risk of the aneurysm rupture has been focused on population (geographical location), hypertension, age, sex, tobacco smoking, size of aneurysm, earlier SAH from another aneurysm, and the location of the aneurysm (Ajiboye et al., 2015; Thompson et al., 2015). Several characteristics of the aneurysm morphology (bottleneck shape, the ratio of size of aneurysm to parent vessel) has been associated with rupture status (Lall, Eddleman, Bendok, &

Batjer, 2009; Sato & Yoshimoto, 2011; Wermer, Van Der Schaaf, Algra, & Rinkel, 2007; You et al., 2010). There is increasing interest in the relationship of hemodynamics (complex flow pattern, low wall shear stress, high oscillatory shear index) to aneurysm grow and rupture. CFD holds a prominent position in obtaining the hemodynamic parameters for the patient-specific evaluation of cerebral aneurysms. Based on the WSS distributions obtained from CFD simulations, Boussel et al. (Boussel et al., 2008) concluded that aneurysm growth is likely to occur in regions where the endothelial layer lining the vessel wall is exposed to abnormally low WSS. With the hemodynamic factors obtained by patient-specific CFD models, Sforza et al. (Sforza et al., 2016) found that growing aneurysm tend to have complex intrasaccular flow patterns that include non-uniform wall shear stress (WSS) distributions with areas of concentrated high WSS and large areas of low WSS. Regarding the conflicting findings on the relationship between WSS and aneurysm rupture, several studies have been conducted based on CFD models, and suggested that both high and low WSS can drive cerebral aneurysm growth and rupture, hypothesized through cell-mediated and inflammatory cell-mediated destructive remodeling pathways, respectively (Meng, Tutino, Xiang, & Siddiqui, 2014; J. Xiang, Tutino, Snyder, & Meng, 2014; G. Zhou, Zhu, Yin, Su, & Li, 2017). The vortex and complex flow structures were also studied and suggested to be relevant with the rupture of cerebral aneurysms (Amili et al., 2018; Gambaruto & João, 2012; Sunderland, Haferman, Chintalapani, & Jiang, 2016; Varble, Trylesinski, Xiang, Snyder, & Meng, 2017). The pressure distribution on the rupture of cerebral aneurysms were also investigated, and the correlation between high pressure with low WSS regions were found (Baek, Jayaraman, & Karniadakis, 2009). However, there was not strong evidence on the direct relevance between high pressure due to flow impinges with the aneurysm rupture (Shojima et al., 2005). Concerns have been risen regarding using CFD for the risk assessments of the cerebral aneurysm because of the conflicting findings reported in the literature and the growing number of hemodynamic parameters (Kallmes, 2012). In addition, the fidelity and reliability of CFD simulations are limited by the uncertainty in vessel geometries and assumptions for boundary conditions. Despite using the same image data and inflow conditions, clear differences have been observed between hemodynamic quantities obtained from independent CFD simulations or between the CFD simulations and PTV measurements (Brindise et al., 2019; Voß, Beuing, Janiga, & Berg, 2019). Moreover, conducting CFD simulations for the aneurysms of patient may not be feasible in clinical practices due to the overwhelming effort, time, and expertise. Recently, *in vitro* volumetric flow measurements have

been conducted using particle imaging velocimetry (PIV) or particle tracking velocimetry (PTV) to resolve the complex flow and determine the hemodynamic factors in patient-specific CAs (Brindise et al., 2019; Ford et al., 2008; Roloff, Stucht, Beuing, & Berg, 2019). However, similar fidelity issues also affected the *in vitro* methods (Brindise et al., 2019), and the experimental efforts and difficulties severely limit its clinical usage. Thus, it is preferable to acquire *in vivo* flow measurement to determine hemodynamic parameters for the risk evaluation of unruptured cerebral aneurysms.

1.1.2 4D flow MRI for *in vivo* measurements of hemodynamic factors of cerebral aneurysm

4D flow magnetic resonance imaging (MRI) allows for the *in vivo* acquisition of time-resolved three-dimensional (3D) blood flow (Dyverfeldt et al., 2015; M Markl et al., 2016; Michael Markl, Frydrychowicz, Kozerke, Hope, & Wieben, 2012; Nayak et al., 2015; Stankovic, Allen, Garcia, Jarvis, & Markl, 2014; Sträter et al., 2018), enabling quantitative evaluation of hemodynamic parameters to assist in the risk stratification of unruptured cerebral aneurysms (Boussel et al., 2009; Hope et al., 2010; Isoda et al., 2010; Kecskemeti et al., 2012; Meckel et al., 2008; Schnell et al., 2014; Wetzel et al., 2007). However, the accuracy of the flow-derived hemodynamic quantities is affected by the limited resolution and noise inherent to 4D flow MRI. The WSS magnitude derived from *in-vivo* 4D flow MRI measurement in CAs was about 60% lower than the results from computational fluid dynamics (CFD) due to PC-MRI's low spatial resolution (Van Ooij et al., 2013). The resolution of velocity data also influences the vortex identification and analysis in CAs (Sunderland et al., 2016). Moreover, the dynamic range of 4D flow MRI is affected by the predefined velocity encoding parameter (venc). If chosen too low, phase wraps may happen, making the imaged blood flow running on the opposite direction. Also, venc should not be set too high as it is inversely proportional to the velocity-to-noise ratio (VNR). The dual-venc techniques can be used to improve both the VNR and dynamic velocity range of 4D flow MRI (Ha et al., 2016; Schnell et al., 2017) but requires longer scan time in general. Thus, it is essential to enhance the resolution, accuracy, and dynamic range of 4D flow MRI data in order to reliably evaluate the flow-derived hemodynamic parameters.

1.2 Objective and tasks

Flow-physics constraints can be employed to enhance 4D flow MRI data. Blood is typically modelled as incompressible fluid, suggesting divergence-free velocity fields based on the conservation of mass. Therefore, a group of velocity filtering or reconstruction methods were developed to correct and smooth the flow field by eliminating the spurious divergence in the measured velocity field (Busch, Giese, Wissmann, & Kozerke, 2013; Michael Loecher, Kecskemeti, Turski, & Wieben, 2012; Ong et al., 2015; Santelli et al., 2016; X. Zhou, Papadopoulou, Leow, Vincent, & Tang, 2019). The objective of the dissertation is to develop and apply the flow-physics constrained data enhancement and augmentation methods for 4D flow MRI in cerebral aneurysms. The following tasks are completed to accomplish the objective.

Task 1: Develop a novel data-enhancement method for unwrapping and denoising the 4D flow MRI data. The gradients of the phase fields from 4D flow MRI are corrected based on the spatiotemporal continuity of the velocity fields, and the unwrapped phase fields are obtained by integrating the corrected phase gradients. The divergence-free constraint derived from COM is employed to regularize the resulting flow fields via least-squares formulations, thus improving the robustness of unwrapping and denoising the velocity fields. The developed method is tested with synthetic, in vitro, and *in vivo* datasets and compared to the current state-of-the-art algorithm to assess its performance.

Task 2: Develop and demonstrate novel data-augmentation methods for evaluating the hemodynamic quantities including pressure and WSS from 4D flow data. The calculations of instantaneous pressure and WSS are formulated as optimization problems incorporating both COM and COLM, which are solved using a robust least-squares approach. The methods are validated with synthetic and in vitro flow-data and demonstrated with *in vivo* 4D flow MRI data. Additionally, the proposed pressure reconstruction method is applied to the flow data measured with other techniques including particle imaging velocimetry (PIV) and particle tracking velocimetry (PTV).

Task 3: Improve the resolution and accuracy of 4D flow MRI data using a multi-modality approach with sparse representation. The high-resolution flow data from CFD and PIV is used to construct a high-resolution flow-library, and the flow field of 4D flow MRI is reconstructed as a sparse linear combination of the library components using the robust Lasso regression. The method is assessed with synthetic 4D flow MRI data and demonstrated with *in vivo* measurements.

Task 4: Develop a new method to measure the left ventricular (LV) diastolic flow propagation velocity (Vp) from multi-dimensional cardiac flow imaging to assist the evaluation of LV diastolic function. The flow propagation velocity is determined from the velocity fields acquired in the left ventricle by fitting the first order wave equation to the velocity gradients. The method is applied to *in vivo* cardiac flow-data measured with pc-MRI and 4D flow MRI to demonstrate the relationship between the Vp with the LV diastolic function.

1.3 Innovation and broader impact

The most important innovation of the work is in developing approaches to enhance the flow data and flow-derived parameters from 4D flow MRI by incorporating flow-physics constraints using robust mathematical formulations and advanced numerical methods. Previous developments have only demonstrated the use of divergence-free constraints to filter and reconstruct the velocity fields from phase-contrast MRI. In task 1, we incorporate the divergence-free constraints for phase unwrapping with a robust weighted least-squares method. In task 2, we use the constraints derived from COM and COLM to improve the calculation of pressure and WSS with least-squares methods. In task 3, the flow physics is incorporated implicitly by preparing the flow-library using CFD simulation and PIV measurement, and the robust LASSO regression is used for the reconstruction. In task 4, the propagation of the diastolic inflow in the left ventricle is extracted from velocity fields based on the first order wave equation via least-squares optimization.

Successful completion of the project provides valuable tools for the data enhancement and augmentation of 4D flow MRI, thus enables the framework of using *in vivo* 4D flow MRI to determine hemodynamic metrics for the risk stratification of unruptured cerebral aneurysms. Unlike a majority of the previous studies which focused on the flow-metrics obtained from CFD models, the novel data enhancement and augmentation methods allow for the reliable evaluation of hemodynamic factors during the clinically scheduled MRI session to benefit the clinical decisions.

The data enhancement and augmentation methods developed for this work are also applicable to the 4D flow MRI measurements in other part of the cardiovascular system besides the cerebral vessels, which potentially leads to improved hemodynamic analysis for a wider range of clinical applications. The flow-physics constrained phase unwrapping method proposed in task 1 has been applied to flow data in thoracic aorta. In task 4, the calculation of the flow propagation

velocity is applied to left ventricular flow to evaluate the diastole function of the subject. The proposed methods can also be applied to flow data acquired using other techniques. We have demonstrated the pressure-reconstruction method introduced in task 2 with the laminar and turbulent flows acquired using PIV and PTV.

1.4 Structure of dissertation

This dissertation consists of seven manuscripts which deliver on the tasks outlined in Section 1.1. Chapter 2 presents the proposed method to unwrap and denoise the 4D flow MRI data. In Chapter 3, a novel method for reconstructing the pressure field from 4D flow velocity data is introduced and applied. Chapter 4 introduces a WSS estimation method for 4D flow MRI using Navier Stokes equation correction. Chapter 5 presents the method that uses the velocity measurement uncertainty to improve the pressure reconstruction from PIV/PTV velocity data. Chapter 6 investigates the uncertainty propagation from velocity data to the reconstructed pressure field for PIV/PTV. Chapter 7 introduces a multi-modality framework to enhance the resolution and accuracy of the 4D flow data with sparse representation. Chapter 8 introduces and demonstrates the method to determine the left ventricular flow propagation velocity from multi-dimensional cardiac imaging. Finally, the conclusions and proposed future work are provided in Chapter 9.

2. DIVERGENCE-FREE CONSTRAINED PHASE UNWRAPPING AND DENOISING FOR 4D FLOW MRI USING WEIGHTED LEAST-SQUARES

This chapter is reproduced with permission from: Zhang, J., Rothenberger, S.M., Brindise, M.C., Scott, M.B., Berhane, H., Baraboo, J.J., Markl, M., Rayz, V.L., Vlachos, P.P., 2021. Divergence-Free Constrained Phase Unwrapping and Denoising for 4D Flow MRI Using Weighted Least-Squares. IEEE Trans. Med. Imaging 40, 3389–3399. https://doi.org/10.1109/TMI.2021.3086331

2.1 Background and literature review

4D flow magnetic resonance imaging (MRI) allows for *in vivo* acquisition of time-resolved three-dimensional (3D) blood flow, thus enabling quantitative analysis of volumetric, time varying hemodynamic quantities such as flow rates, wall shear stress (WSS), pressure difference, etc (Brindise et al., 2019; Donati, Figueroa, Smith, Lamata, & Nordsletten, 2015; Guzzardi et al., 2015; Ha et al., 2017; Michael Markl et al., 2012; Michael Markl, Wallis, & Harloff, 2011; Nayak et al., 2015; Potters, Ooij, & Nederveen, 2012; Stalder et al., 2008b; Stankovic et al., 2014; Zhang et al., 2019). 4D flow MRI has demonstrated its potential to improve the diagnostics of cardiovascular and cerebrovascular diseases (Dyverfeldt et al., 2015; Guzzardi et al., 2015; M Markl et al., 2016; Michael Markl et al., 2012; Nayak et al., 2015; Schnell et al., 2017; Stankovic et al., 2014; Sträter et al., 2018). 4D flow MRI is based on the phase contrast (PC) technique which encodes the blood velocity along all dimensions into the MRI signal phase data. A predefined velocity encoding sensitivity parameter (venc) determines the maximum and minimum velocity that can be recorded in the phase data as π and $-\pi$, respectively. Therefore, the velocity field can be obtained by multiplying the phase with venc/π. Whenever a velocity component is greater than venc or lower than -venc, the acquired phase is wrapped and leads to velocity aliasing. To avoid aliasing, the venc is suggested to be set approximately 10% higher than the maximum expected velocity (Dyverfeldt et al., 2015; Sträter et al., 2018). However, high venc leads to high noise level since the velocity-to-noise ratio (VNR) is inversely proportional to venc (Lee, Bruce Pike, & Pelc, 1995).

One strategy to capture the wide dynamic range associated with physiologic blood flow while maintaining the low noise level associated with low venc data is to perform acquisitions with a set of two or more vencs (Aristova et al., 2019; Carrillo, Osses, Uribe, & Bertoglio, 2019; Ha et al., 2016; Lee et al., 1995; Michael Loecher & Ennis, 2018; Nett et al., 2012; Schnell et al., 2017).

The acquired high-venc data can then be employed for unwrapping the low-venc data. However, despite the efforts to accelerate the multi-venc acquisition (Schnell et al., 2017), the total scan time with a 4-point low venc encoding is still unavoidably longer than a single scan, which is the major limitation of the approach. Using undersampled parallel encoding methods and Bayesian processing of phase data can further accelerate the 4D flow acquisition and enable flexible choice of velocity encoding ranges (Binter, Knobloch, Manka, Sigfridsson, & Kozerke, 2013; Rich et al., 2016, 2019). Another strategy is algorithmically unwrapping the wrapped phase data. Several algorithms have been proposed for 4D flow MRI (Bhalerao, Westin, & Kikinis, 1997; M. Loecher, Johnson, Landgraf, & Wieben, 2011; Michael Loecher, Schrauben, Johnson, & Wieben, 2016; M F Salfity, Huntley, Graves, Marklund, & Cusack, 2006; Q. Xiang, 1995). However, these algorithms are either untested or unreliable for low-venc acquisitions with large aliased areas or repeatedly wrapped regions. Phase noise also dramatically affects the performances of the unwrapping algorithms.

The purpose of this study was to introduce and evaluate a robust and reliable phase unwrapping method for 4D flow MRI. The proposed method, divergence-free constrained weighted least-squares (CWLS), incorporates the divergence-free constraint of incompressible flow with the estimated phase variations to formulate an optimization problem. The divergence-free constraint has been used in previous studies to reconstruct the velocity field from 3D phase contrast MRI and 4D flow MRI (Buonocore, 1994; Busch et al., 2013; Ong et al., 2015). The unwrapped phase is obtained using WLS with weights generated based on the phase variation uncertainty. CWLS also utilizes the temporal phase information to enhance the robustness by unwrapping from timepoints least-likely to be wrapped towards those likely to be wrapped. The CWLS method was tested using synthetic phase data of left ventricular (LV) flow and *in vitro* Poiseuille flow measured using 4D flow MRI. The method is then applied to *in vivo* aortic 4D flow MRI data from 30 subjects.

2.2 Theory

Phase wrapping in 4D flow MRI can be presented as:

$$\psi = \mathcal{W}(\phi) = \phi + 2n\pi \; with \; n = -round\left(\frac{\phi}{2\pi}\right) \in Z, \qquad (2\text{-}1)$$

where ψ is the wrapped phase, ϕ is the unwrapped phase, $\mathcal{W}()$ represents the wrapping operation which adds a multiple of 2π to ϕ such that ψ is within the range $(-\pi, \pi)$, $round()$ means rounding to the nearest integer, and Z is the set of integers. ϕ is related with the underlying velocity component v as $\phi = \frac{\pi}{venc} v$. If v is out of the dynamic range (-venc, venc), phase wrapping occurs as ψ differs from ϕ by a multiple of 2π. The objective of phase unwrapping is to find ϕ based on the acquired ψ so that the underlying velocity can be properly determined.

To unwrap the phase field, one common approach is to integrate the phase variation estimated as:

$$\widehat{\Delta\phi} = \mathcal{W}(\Delta\psi), \qquad (2\text{-}2)$$

where $\Delta\psi$ is the spatial or temporal variation of the acquired (wrapped) phase, $\widehat{\Delta\phi}$ is the estimated variation for the unwrapped phase by wrapping $\Delta\psi$ as in (2-1). Equation (2-2) assumes that the phase variation between neighboring voxels is within the range of $(-\pi, \pi)$, which is generally valid since the blood velocity varies continuously across the field. The phase variation integration can be treated as an optimization process and solved in a least-squares sense (Ghiglia & Romero, 1994; Pritt & Shipman, 1994; Song, Napel, Pelc, & Glover, 1995). This approach has been tested with 2D synthetic phase images, and the robustness can be improved by assigning proper weights to the objective function (Ghiglia & Romero, 1994). The weighted least-squares (WLS) method has been demonstrated to improve the pressure integration with the weights generated based on the accuracy of pressure variation (Zhang et al., 2019). A similar WLS approach can be developed and applied to the phase unwrapping of 4D flow MRI. Moreover, the divergence-free constraint can be incorporated into the WLS minimization to further improve the accuracy of the unwrapping and denoise the phase field.

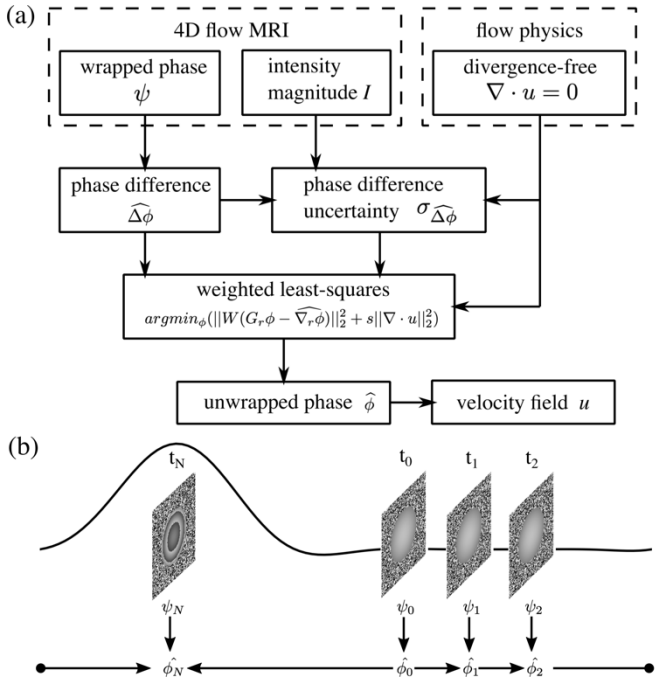

Figure 2.1 (a) Procedure of phase unwrapping with CWLS (b) The sequence of temporal phase unwrapping start from the time point with lowest average velocity at t_0 to the time point with highest average velocity at t_N along the forward and backward directions in a cyclic manner. The waveform demonstrates the flow rate in one cardiac cycle.

2.3 Methodology

2.3.1 Phase Unwrapping with CWLS

The procedure of phase unwrapping with CWLS is presented in Figure 2.1 (a). First, the phase variation $\Delta\psi$ was calculated from the wrapped phase field ψ. Specifically, the spatial phase variation was the difference between neighboring voxels, and the temporal phase variation was the difference between consecutive cardiac frames. Then $\widehat{\Delta\phi}$ was estimated using (2-1). The phase gradient was calculated as the phase variation divided by the corresponding spatial or temporal resolution, e.g.,

$$\widehat{\nabla_r\phi} = \widehat{\Delta_r\phi}/\Delta r, \qquad (2\text{-}3)$$

where $\widehat{\nabla_r \phi}$ is the spatial phase gradient, $\widehat{\Delta_r \phi}$ is the spatial phase variation, and Δr is the voxel size. The subscript r represents the spatial dimension. The unwrapped phase $\hat{\phi}$ is spatially related to the phase gradient $\widehat{\nabla_r \phi}$ as:

$$D_r \hat{\phi} = \widehat{\nabla_r \phi}, \tag{2-4}$$

where D_r is the discrete spatial gradient operator consisting of D_x, D_y, and D_z. In addition, the divergence-free constraint reveals the following relationship between the phases of u, v, and w velocity components (denoted as ϕ_u, ϕ_v, and ϕ_w) as:

$$\nabla \cdot \vec{u} \equiv D_x u + D_y v + D_z w = \frac{venc_u}{\pi} D_x \phi_u + \frac{venc_v}{\pi} D_y \phi_v + \frac{venc_w}{\pi} D_z \phi_w = 0, \tag{2-5}$$

where $\nabla \cdot$ represents the discrete divergence operator, $\vec{u}$ is the velocity vector containing three components as $\vec{u} = [u, v, w]^T$, $venc_u$, $venc_v$, and $venc_w$ are the vencs used for measuring the three velocity components u, v, and w, D_x, D_y, and D_z are the discrete gradient operators constructed as matrices, and ϕ_u, ϕ_v, and ϕ_w are the vectors of phases for the three velocity components. Equations (4) and (5) formulate a minimization problem which can be solved using weighted least-squares as:

$$\hat{\phi} = argmin_{\phi} \left(\left\| W\left(D_r \phi - \widehat{\nabla_r \phi}\right) \right\|_2^2 + s \left\| \frac{venc_u}{\pi} D_x \phi_u + \frac{venc_v}{\pi} D_y \phi_v + \frac{venc_w}{\pi} D_z \phi_w \right\|_2^2 \right), \tag{2-6}$$

$$with\, W = diag\left(\frac{1}{\sigma^2_{\widehat{\nabla_r \phi}}} \right), \tag{2-7}$$

where $\| \quad \|_2$ represents the L2 norm, D_r is the combined discrete gradient operator constructed by vertically stacking D_x, D_y, and D_z, ϕ is the vector consisting of ϕ_u, ϕ_v, and ϕ_w, $\widehat{\nabla_r \phi}$ is the vector of the spatial phase gradients determined using (2-3), W is the weight matrix generated based on the uncertainty of the phase gradient $\sigma_{\widehat{\nabla_r \phi}}$, $diag()$ generates the diagonal matrix with the given diagonal elements, and s is the constant controlling the level of regularization by the divergence-free constraint. The term $\left\| W\left(D_r \phi - \widehat{\nabla_r \phi}\right) \right\|_2$ is the weighted residual of phase variations, and the term $\left\| \frac{venc_u}{\pi} D_x \phi_u + \frac{venc_v}{\pi} D_y \phi_v + \frac{venc_w}{\pi} D_z \phi_w \right\|_2$ is the velocity divergence. The divergence-free constraint is considered to be more reliable than the phase gradients since the divergence-free

constraint is based on the flow-physics while the phase gradients were estimated from the measurement containing noise and errors. In order to minimize the velocity divergence, s was assigned to be significantly larger than the mean of the phase gradient weights ($\overline{W}$). The residual divergence in the resulting velocity fields can be completely eliminated by using an s value greater than $10^4\overline{W}$, thus s was set to $10^6\overline{W}$ unless specified otherwise in this work. LSQR, an iterative algorithm for sparse least-squares problems (Paige & Saunders, 1982b, 1982a), was employed to obtain the solution from (2-6). The discrete gradient and divergence operators were constructed using the second order central (SOC) difference scheme.

2.3.2 Field of View (FOV) Division

To properly apply the divergence-free constraint, the FOV was divided into three regions denoted as the region of blood flow ($\mathcal{D}_{ROI}$), the reference points ($\mathcal{D}_{ref}$), and the rest of the FOV. The divergence minimization in Equation 2-6 was only applied to the voxels within $\mathcal{D}_{ROI}$ since the divergence-free constraint might be invalid outside the flow. The $\mathcal{D}_{ref}$ is defined as a layer of voxels surrounding the $\mathcal{D}_{ROI}$, and was obtained by performing one iteration of morphological dilation of $\mathcal{D}_{ROI}$ then subtracting $\mathcal{D}_{ROI}$ from the dilated region. $\mathcal{D}_{ref}$ located in the tissue adjacent to the blood flow, which can be dynamic or static depending on the imaging location. The phase values in $\mathcal{D}_{ref}$ were set to zeros prior to the unwrapping for noise elimination, and used as the boundary condition for the CWLS phase unwrapping via gradient integration. The term $\left\|W\left(D_r\phi - \widehat{\nabla_r\phi}\right)\right\|_2$ in (2-6) was minimized in the combined region $\mathcal{D}_{ROI} \cap \mathcal{D}_{ref}$. The phase unwrapping via gradient integration was first performed with an arbitrary point set to zero. Then the median of $\hat{\phi}$ in $\mathcal{D}_{ref}$ was evaluated and subtracted from the $\hat{\phi}$ in the whole field in order to enforce a zero median of $\hat{\phi}$ in $\mathcal{D}_{ref}$ in order to be consistent with the boundary condition and ensure the robustness since the median is not affected by the extreme values obtained in $\mathcal{D}_{ref}$ due to noise. The rest of the FOV was excluded from the CWLS unwrapping to save computational effort.

2.3.3 Uncertainty Estimation of Phase Variation

The uncertainty $\sigma_{\widehat{\nabla_r\phi}}$ of each $\widehat{\nabla_r\phi}$ value needed for generating the weight matrix W in (2-7). $\sigma_{\widehat{\nabla_r\phi}}$ was estimated as the standard deviation of the distribution of the phase variation error $\epsilon_{\widehat{\nabla_r\phi}} \equiv \widehat{\nabla_r\phi} - \nabla_r\phi$, where $\nabla_r\phi$ is the true phase gradient. $\epsilon_{\widehat{\nabla_r\phi}}$ can be decomposed into two components:

$$\epsilon_{\widehat{\nabla_r\phi}} = \epsilon^N_{\widehat{\nabla_r\phi}} + \epsilon^W_{\widehat{\nabla_r\phi}}, \tag{2-8}$$

where $\epsilon^N_{\widehat{\nabla_r\phi}}$ is the error component due to the measurement noise in ψ, and $\epsilon^W_{\widehat{\nabla_r\phi}} \equiv \epsilon^W_{\widehat{\Delta_r\phi}}/\Delta r$ is caused by the incorrect phase variation estimation by (2-2). Since the two error components in (2-8) are uncorrelated, the uncertainty $\sigma_{\widehat{\nabla_r\phi}}$ can be determined as

$$\sigma_{\widehat{\nabla_r\phi}} = \sqrt{\left(\sigma^N_{\widehat{\nabla_r\phi}}\right)^2 + \left(\sigma^W_{\widehat{\nabla_r\phi}}\right)^2}, \tag{2-9}$$

where $\sigma^N_{\widehat{\nabla_r\phi}}$ and $\sigma^W_{\widehat{\nabla_r\phi}}$ are the uncertainties of $\epsilon^N_{\widehat{\nabla_r\phi}}$ and $\epsilon^W_{\widehat{\nabla_r\phi}}$, respectively.

The magnitude of $\epsilon^W_{\widehat{\Delta_r\phi}}$ can be inferred from the integration of $\widehat{\nabla_r\phi}$ along closed loops in space (Cusack & Papadakis, 2002). The smallest possible loops are 2×2 voxel rectangular loops denoted as loop elements. The integration ($\oint \widehat{\nabla_r\phi}$) of each loop element equals the sum of the four $\epsilon^W_{\widehat{\Delta_r\phi}}$ values on the loop element. Since each $\widehat{\Delta_r\phi}$ value can be on multiple loop elements, the phase variation uncertainty $\sigma^W_{\widehat{\Delta_r\phi}}$ was approximated as the sum of $\frac{1}{4}\left|\oint \widehat{\nabla_r\phi}\right|$ from all the loop elements. The $\oint \widehat{\nabla_r\phi}$ was calculated for all possible 2×2 voxel loop elements in the 3D field, and the value of $\sigma^W_{\widehat{\Delta_r\phi}}$ was additively updated. The phase gradient uncertainty $\sigma^W_{\widehat{\nabla_r\phi}}$ was then determined as $\sigma^W_{\widehat{\Delta_r\phi}}/\Delta r$.

The uncertainty $\sigma^N_{\widehat{\nabla_r\phi}}$ for the noise component was estimated based on the spurious divergence of the velocity field as well as the intensity magnitude field I. First, the velocity-divergence field $\nabla \cdot u$ was calculated from $\widehat{\nabla_r\phi}$ using (2-5). According to the divergence-free constraint, $\nabla \cdot u$ is related to the phase noise $\epsilon^N_{\widehat{\phi}}$ as:

$$\frac{venc_u}{\pi} D_x \epsilon^N_{\widehat{\phi_u}} + \frac{venc_v}{\pi} D_y \epsilon^N_{\widehat{\phi_v}} + \frac{venc_w}{\pi} D_z \epsilon^N_{\widehat{\phi_w}} = \nabla \cdot \vec{u}. \tag{2-10}$$

Similar to the velocity error estimation from velocity divergence (Zhang et al., 2019), $\epsilon_{\hat{\phi}}^{N}$ was obtained by solving (10) in a least-squares sense. The $\epsilon_{\hat{\phi}}^{N}$ was convolved with a 3D Gaussian kernel with a width of $2\Delta r$ corresponding to the three-point stencil-size of the SOC scheme to obtain the phase uncertainty field $\sigma_{\hat{\phi}}^{N,G}$. In addition, the root-mean-square (RMS) of $\epsilon_{\hat{\phi}}^{N}$ in $\mathcal{D}_{\mathrm{ROI}}$ was calculated to represent the global phase noise level as $\bar{\sigma}_{\hat{\phi}}^{N}$. Since the noise in the phase is inversely proportional to the intensity magnitude (Conturo & Smith, 1990; Lee et al., 1995), the ratio between the local and global phase noise uncertainty equals the reciprocal of the ratio between the local and global intensity. Thus, the phase noise uncertainty can be estimated based on the intensity field and the global phase noise uncertainty $\bar{\sigma}_{\hat{\phi}}^{N}$ as:

$$\sigma_{\hat{\phi}}^{N,I} = \bar{\sigma}_{\hat{\phi}}^{N}\bar{I}/I, \tag{2-11}$$

where $\bar{I}$ is the average of the intensity magnitudes in $\mathcal{D}_{\mathrm{ROI}}$. The quadratic mean of the two estimations of phase noise uncertainty was calculated as:

$$\sigma_{\hat{\phi}}^{N} = \sqrt{\frac{1}{2}\left[\left(\sigma_{\hat{\phi}}^{N,G}\right)^2 + \left(\sigma_{\hat{\phi}}^{N,I}\right)^2\right]}, \tag{2-12}$$

which was then propagated through the calculations of phase variation and phase gradient to acquire the phase gradient uncertainty $\sigma_{\overline{\nabla_r \hat{\phi}}}^{N}$.

2.3.4 Sequential Frame Unwrapping

Based on the temporal continuity of the velocity field, an unwrapped frame can be used to infer the temporally neighboring frames (Q. Xiang, 1995) as:

$$\hat{\phi}_{i\pm1}^{t} = \hat{\phi}_i + \mathcal{W}(\Delta_t\psi),\ with\ \Delta_t\psi = \psi_{i\pm1} - \psi_i, \tag{2-13}$$

where $\hat{\phi}_i$ is the unwrapped phase at i[th] cardiac frame, $\Delta_t\psi$ is the temporal phase variation, and $\hat{\phi}_{i\pm1}^{t}$ is the temporally unwrapped phase at the neighboring frames $i \pm 1$. The temporally unwrapped phase $\hat{\phi}^t$ was utilized in the CWLS unwrapping. First, the spatial variation of $\hat{\phi}^t$ was combined with the estimation from (2-2) to obtain the spatial phase variation as:

$$\widehat{\Delta_r\phi} = \frac{1}{2}\left(\Delta_r\hat{\phi}^t + \mathcal{W}(\Delta_r\psi)\right), \tag{2-14}$$

which was employed in the phase variation integration by (2-6). Second, the deviation between $\Delta_r\hat{\phi}^t$ and $\mathcal{W}(\Delta_r\psi)$ was used to update the phase gradient uncertainty as:

$$\sigma_{\widehat{\nabla_r\phi}} = \sqrt{\left(\sigma^N_{\widehat{\nabla_r\phi}}\right)^2 + \left(\sigma^{\mathcal{W}}_{\widehat{\nabla_r\phi}}\right)^2 + \left(\frac{\Delta_r\hat{\phi}^t - \mathcal{W}(\Delta_r\psi)}{\Delta r}\right)^2}, \tag{2-15}$$

which was employed to generate the weight matrix W in (2-7). In addition, $\hat{\phi}^t$ was used as the initial field for solving (6) with the iterative LSQR algorithm.

Since the reliability of $\hat{\phi}^t_{i\pm1}$ depends on the accuracy of $\hat{\phi}_i$, it is preferable to perform the temporal phase unwrapping from a less-wrapped frame towards a more-wrapped one. We adopted the frame sequences to start from the frame with lowest average velocity magnitude towards the frame with highest average velocity magnitude along both the forward and backward temporal directions as demonstrated in Figure 2.1(b). The frame with highest flow rate was unwrapped twice with the two temporal sequences as both neighboring timeframes had lower flow rates. Each of the two unwrapping operations on the frame with highest flow rate was performed independently and initialized with one of the neighboring frames, yielding two unwrapping results which were similar in general. The average of the two unwrapped fields were taken as the final result since taking the average can reduce the uncertainty compared to a single sample. The proposed temporal sequences can prevent the propagation of unwrapping errors from severely wrapped frames to the less-wrapped ones. The starting and the ending timepoints can be approximated as the peak diastole or peak systole depending on the locations in the cardiovascular system.

2.3.5 Synthetic Phase Data Generation

To evaluate the performance of the CWLS method, synthetic phase data was generated from computational fluid dynamics (CFD) simulated left ventricular (LV) flow velocity fields (Londono-hoyos et al., 2018). The CFD results were obtained on unstructured computational mesh with 180,000 tetrahedral cells and linearly interpolated to a fine Cartesian grid with spatial resolution of 0.2 mm. Complex-valued signal was generated at each grid node based on each velocity component as:

$$M_{fine} = Iexp\left(\frac{i\pi u}{venc}\right), \quad (2\text{-}16)$$

where M_{fine} denotes the complex signal at the fine grid node, I is the signal magnitude, and u is the velocity component at grid node. Another Cartesian grid with a resolution of 2.5 mm was employed as the MRI grid ($\mathcal{G}_{MRI}$) with each grid point corresponding to a voxel-center, in order to be consistent with the typical resolutions of heart scans (Sträter et al., 2018). The complex-valued signal at each voxel-center of the synthetic 4D flow MRI data was generated by convolving the signal on the fine Cartesian grid with a sinc-function kernel (K) as:

$$K(x, y, z) = sinc\left(\frac{x}{\Delta x}\right) \times sinc\left(\frac{y}{\Delta y}\right) \times sinc\left(\frac{z}{\Delta z}\right), \quad (2\text{-}17)$$

with $sinc(x) = \frac{sin(\pi x)}{\pi x}$, where Δx, Δy, and Δz represent the spatial resolution of the MRI grid. Previous studies have shown that the spatial blurring of Cartesian 4D flow MRI measurement due to limited coverage of the k-space equals to the convolution with the sinc-function kernel (Rispoli, Nielsen, Nayak, & Carvalho, 2015), and convolving with the sinc-function kernel has been used to simulate 4D flow MRI acquisitions (Jochimsen, Schäfer, Bammer, & Moseley, 2006; Latta, Gruwel, Jellúš, & Tomanek, 2010; Töger et al., 2020b). One reference (M_0) and 3 flow-sensitive datasets (M_u, M_v, and M_w) were simulated following a four-point reference method. Each flow-sensitive dataset was created based on the field of a velocity component, and the reference dataset was generated from a zero phase field such that the phase difference between the flow-sensitive and the reference datasets was consistent with the velocity field as in real applications. The signal noise ϵ in each component of the complex-valued data was assumed to be normally distributed with a standard deviation of $\sigma_I = \bar{I}/SNR_I$, where SNR_I is the intensity magnitude based SNR (Dietrich, Raya, Reeder, Reiser, & Schoenberg, 2007). The wrapped phase data ψ for each velocity component was generated from the complex-valued data, e.g.:

$$\psi_u = angle(M_u * M_0^*), \quad (2\text{-}18)$$

where ψ_u is the phase for u velocity component, M_0^* is the complex conjugate of M_0, and $angle(\quad)$ means calculating the angle from a complex signal as:

$$angle(a + bi) = arctan\left(\frac{b}{a}\right). \quad (2\text{-}19)$$

Since the reference dataset was shared among the three flow-sensitive datasets, the phase noise of different velocity components were correlated in a similar way as the real phase data (Friman et al., 2011).

The intensity magnitude field *I* was allowed to vary spatially as commonly seen from the FOV of 4D flow MRI. The spatial distribution of *I* was defined as:

$$I = 1.0 - 0.5\left(\frac{x}{L_{domain}}\right), \quad (2\text{-}20)$$

where L_{domain} is the total length of the FOV along the x direction. The *I* outside D_{ROI} was multiplied with 0.2 to mimic the low intensity outside the lumen. In addition to the predefined bulk variation, *I* would also vary locally due to the noise and the intravoxel dephasing effect caused by the spatiotemporal variation of velocity.

Since the SNR of MRI acquisitions can be greater than 100 for *in vitro* measurements and less than 10 for *in vivo* measurements (Difrancesco et al., 2008; Ha et al., 2016; Nett et al., 2012; Schnell et al., 2017; Yu, Agarwal, Stuber, & Schär, 2012), we employed the following 6 values to represent a wide range of SNRI as: 100, 50, 20, 10, 5, and 2. A wide range of vencs was also employed to test CWLS on different levels of phase wrapping. The venc ratio (VR) defined as the ratio between the venc and the maximum flow velocity was varied from 0.1 to 0.9 in increments of 0.1. In total, 54 test cases were created with different combinations of SNRI and VR.

To determine the effect of spatial resolution on CWLS unwrapping, several additional datasets were created using the same approach with MRI grid resolution varying from 2 to 6 mm in increments of 1 mm. For each spatial resolution, 10 datasets were created with an SNR of 10 and VR from 0.1 to 1.0 in increments of 0.1.

The mask of $\mathcal{D}_{ROI}$ was generated for each dataset and each time frame based on the geometry available from the CFD simulation. A voxel was considered to be in the blood flow domain if the voxel-center was within the geometry at the time instant.

2.3.6 In vitro 4D Poiseuille Flow Measurement

Steady, laminar Poiseuille flow in a circular pipe was measured using 4D flow MRI with different vencs. The working fluid was a blood mimicking water-glycerol (60:40 by volume) solution with a density of 1110 kg/m^3 and viscosity of 0.00372 Pa·s. A small amount (0.66 mg/mL) of Gadolinium contrast was added to enhance the SNR of the scan without altering the rheology of the fluid. A computer-controlled gear pump was used to drive the working fluid at a steady flow rate of 7.6 mL/s. The diameter of the pipe was 12.7 mm, and the length was sufficiently long prior to entering the FOV such that the velocity profile was fully developed. Three dual-venc (DV) acquisitions (Schnell et al., 2017) (denoted as A, B, and C) were performed on a Siemens 3T PRISMA scanner with a spatial resolution of $0.85 \times 0.85 \times 0.8\ mm^3$. The dual-venc acquisitions were split up, and the low and high venc acquisitions were analyzed separately, thus yielding 6 datasets with vencs ranging from 4 to 16 cm/s as presented in Table 1. The expected maximum velocity in the field was 12 cm/s. Each dataset contained 12 time frames with a temporal resolution of 120.4 ms. The echo time (TE) and repetition time (TR) are presented in Table 1. The bandwidth was 455 kHz and flip angle was 15°. The mask of $\mathcal{D}_{ROI}$ was generated based on the position and radius of the pipe. A voxel was considered to be within the flow if the distance from its center to the centerline of the pipe was less than the pipe radius. The SNR_I values were calculated for each acquisition as $SNR_I = \bar{I}/\sigma_I$, where σ_I is the standard deviation of I across the 12 frames, and $\bar{I}$ is the average of I within $\mathcal{D}_{ROI}$. The SNR_I values are given in Table 2.1.

2.3.7 In vivo Aortic 4D Flow MRI Measurement

In vivo aortic 4D flow MRI data was used to evaluate the performance of CWLS. Aortic flow was measured from 12 patients with bicuspid aortic valve (BAV), 12 patients with tricuspid aortic valve and aortic aneurysm (TAV-AA), and 6 healthy control subjects with tricuspid aortic valve. The scans were performed in a sagittal oblique volume on a 1.5 T scanner (MAGNETOM Avanto, Aera, Siemens, Erlangen, Germany) with prospective ECG gating and during free-breathing. All patients (BAV and TAV-AA) except the control subjects were imaged with gadolinium-based contrast (Magnevist, Ablavar, or Gadavist). The voxel sizes were 2-2.5 mm isotropic in-plane with a slice thickness of 2.4-3.2 mm. The temporal resolution was 37.6-39.2 ms with 10-25 cardiac time frames. TE/TR were 2.184-2.463 ms/4.6-4.9 ms, flip angle was 7° in

controls and 15° in patients, and the bandwidth was 446-460 kHz. A single venc was used for each scan. The venc was 150-350 cm/s for BAV patients, 150-200 cm/s for TAV-AA patients, and 150 cm/s for control subjects. All patient data for this HIPPA compliant and IRB approved study were retrospectively included with waiver of consent. The mask of $\mathcal{D}_{ROI}$ for each dataset was approximated by thresholding the time-averaged product of the intensity and the magnitude of the phase components $\left(I \cdot \sqrt{\psi_u^2 + \psi_v^2 + \psi_w^2}\right)$ (J. Bock, Kreher, Hennig, & Markl, 2007) and manually corrected by an expert observer using Mimics (Materialise NV, Belgium).

In vivo datasets were assessed for aliasing, with four TAV-AA and four BAV datasets containing velocity aliasing, while no velocity aliasing was observed in the remaining 22 datasets. Phase unwrapping was applied to the datasets with velocity aliasing, and the resulting velocity fields were analyzed to assess the performance. For datasets without aliasing, the phase data were artificially wrapped based on virtual vencs that were lower than the vencs from original scans as $\mathcal{W}\left(\frac{\pi V}{venc}\right)$, where V is the original velocity data and $venc$ is the virtual venc. This wrapping operation maintains the mathematical relationship between wrapped and unwrapped phase data without bringing additional noise or error to the phase field. Five VRs ranging from 0.1 to 0.5 were employed to set the virtual vencs based on the maximum velocity value within the blood flow. Outliers were excluded from the maximum velocity calculation using universal outlier detection (UOD) (Westerweel & Scarano, 2005) followed by median filtering on the unaliased velocity data. The originally unaliased datasets were used as the benchmark to assess unwrapping performance. Since the measurement noise in the benchmark datasets could affect the error analysis on the unwrapped phase fields, UOD was applied to the benchmark phase field to remove outliers.

2.3.8 Performance evaluation

The performance of CWLS on phase unwrapping and denoising was assessed by analyzing the unwrapped phase field as well as the resulting velocity field obtained by multiplying the unwrapped phase by venc/π. The current state-of-the-art 4D single-step Laplacian algorithm (Michael Loecher et al., 2016) (4D Lap) was also employed in this study and compare to CWLS. 4D Lap unwraps time-resolved phase data along temporal dimension and all three spatial dimensions by evaluating the phase Laplacian with Fourier transform. All of the preprocessing

was kept constant between CWLS and 4D Lap such that the input phase data were same between the unwrapping techniques.

To assess the overall performance on each test case for the synthetic phase data of LV flow, the unwrapped phase $\hat{\phi}$ was compared to the true phase ϕ generated from CFD results voxel by voxel at each cardiac frame. A voxel was considered as wrapped if the deviation $|\hat{\phi} - \phi|$ was greater than π. The success rate (SR) of phase unwrapping was calculated as:

$$SR = 1 - \frac{N_{\mathcal{W},\hat{\phi}}}{N_{\mathcal{W},\psi}}, \tag{2-21}$$

where $N_{\mathcal{W},\hat{\phi}}$ is the total number of wrapped voxels in the unwrapped data, and $N_{\mathcal{W},\psi}$ is the total number of wrapped voxels in the synthetic data. $N_{\mathcal{W},\hat{\phi}}$ and $N_{\mathcal{W},\psi}$ were counted within D_{ROI} for each of the 3 velocity components at each frame, which were then summed together as $N_{\mathcal{W},\hat{\phi}} = \sum_{i=1}^{N}\left(N^i_{\mathcal{W},\widehat{\phi_u}} + N^i_{\mathcal{W},\widehat{\phi_v}} + N^i_{\mathcal{W},\widehat{\phi_w}}\right)$, where the superscript i indicates the ith cardiac frame. SR=1 means that all voxels were correctly unwrapped. The SR can be less than 0 if the unwrapping created more wrapped voxels than the original data. The error in the resulting velocity (ϵ_V) was calculated as the deviation from the CFD results. To evaluate the accuracy of the resulting velocity fields, the velocity error level (V_{error}) was calculated as:

$$V_{error} = \frac{RMS(\epsilon_V)}{\overline{|V|}} \times 100\%, \tag{2-22}$$

where $\overline{|V|}$ is the average velocity magnitude in D_{ROI}, and $RMS(\epsilon_V)$ represents the RMS velocity error in D_{ROI}.

For the in vitro 4D Poiseuille flow, the unwrapped phase $\hat{\phi}$ data was compared with the true phase ϕ generated from the analytical velocity fields described by:

$$u_r = 0, u_\theta = 0, u_z(r) = \frac{2Q}{\pi R^4}(R^2 - r^2), \tag{2-23}$$

where u_r is the radial velocity component, u_θ is the circumferential velocity component, u_z is the axial (along z-axis) velocity component (m/s), r is the radial distance from the pipe centerline (m), R is the pipe radius (m), and Q is the volumetric flow rate (m^3/s). The number of wrapped voxels

$N_{\mathcal{W},\psi}$ and $N_{\mathcal{W},\widehat{\phi}}$ were calculated from the acquired phase fields and the unwrapped phase fields, respectively. To quantify the noise level, the VNRs were determined from the resulting velocity fields as:

$$VNR = \frac{\overline{|V|}}{RMS(\sigma_V)}, \tag{2-24}$$

where σ_V is the velocity standard deviation across 12 frames, and $RMS(\sigma_V)$ is the RMS of all the σ_V within D_{ROI}. The wrapped voxels were excluded from the VNR calculation such that the VNR only represented the noise level. From the unwrapped velocity fields using CWLS and 4D Lap, the WSS was calculated from the velocity gradients determined using thin-plate spline radial basis function interpolation (Brindise et al., 2019; Karri, Charonko, & Vlachos, 2009) with the non-slip (zero velocity) boundary condition applied on the wall. The WSS error (ϵ_{WSS}) was determined by comparing the magnitude of the WSS vector to the analytical value determined as:

$$|WSS| = \frac{4\mu Q}{\pi R^3}, \tag{2-25}$$

where μ is the dynamic viscosity of the fluid (Pa·s). For each dataset, the relative ϵ_{WSS} was calculated as the RMS of ϵ_{WSS} in D_{ROI} normalized by the analytical WSS magnitude.

To evaluate the performance with the in vivo aortic 4D flow data, the SRs defined by (2-21) on the artificially wrapped datasets were determined by comparing the unwrapped phase to the benchmark (the originally unaliased datasets). Because benchmark data is not available for the eight datasets with real aliasing, the error in the resulting velocity fields were estimated based on the velocity divergence using the least-squares algorithm (Zhang et al., 2019), which was then employed to calculate the V_{error}s using (2-22). To indicate the level of wrapping in the original phase data, the venc ratio was estimated based on the average of the maximum velocity values from the CWLS and 4D Lap unwrapped fields.

2.4 Results

2.4.1 Synthetic Phase Data of LV Flow

The u velocity field at peak diastole on the MRI grid is shown in Figure 2.2 (a). The generated phase and magnitude intensity fields for VR=0.2 and SNR_I=10 are shown in Figure 2.2 (b-c). The unwrapped u-component velocity fields at peak diastole are compared in Figure 2.2 (d) and (e) for the case of SNR_I=10 and VR=0.2. With 4D Lap, the large region of wrapped voxels in inflow jet remained, while all voxels were correctly unwrapped by CWLS. The SRs and V_{error}s of all the cases are compared in Figure 2.2 (a) between CWLS and 4D Lap. The CWLS completely unwrapped the phase data for most cases with VR≥0.2 and $SNR_I \geq 5$. Even with significant amount of noise ($SNR_I = 2$), the SRs were consistently greater than 0.8. Compared to 4D Lap, CWLS was more robust to noise and more reliable for low-venc acquisitions. The CWLS method effectively reduced the V_{error} in most cases compared to 4D Lap. The improvement was significant for the cases where 4D Lap failed to unwrap all the voxels and led to V_{error} reduction as much as 500%. It is also worth noting that CWLS reduced the V_{error}s by around 20% compared the 4D Lap results for the low-SNR_I cases where both methods completely unwrapped the phase.

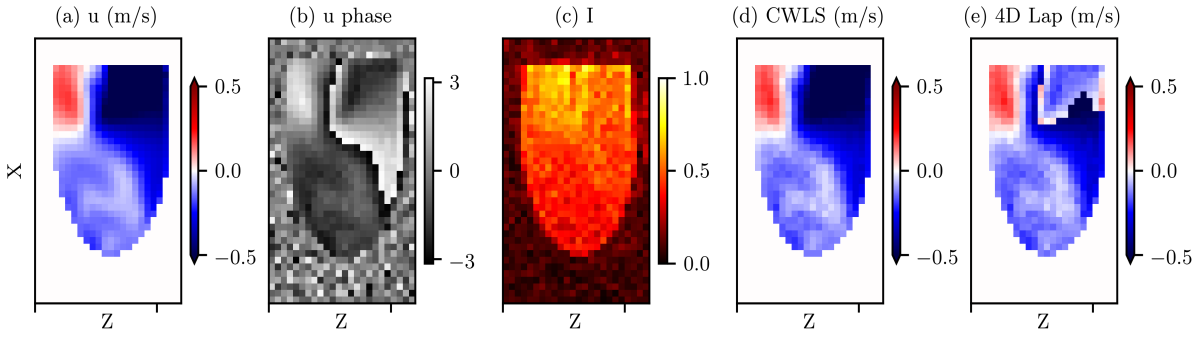

Figure 2.2 (a) The u velocity field at peak diastole on the center x-z plane. (b-c) The u phase and magnitude intensity fields at peak diastole for the case with VR=0.2 and SNR_I=10. (c-d) The resulting u velocity fields on the center x-z plane at peak diastole unwrapped with CWLS and 4D Lap, respectively, for the same case.

The effects of spatial resolution on the performances of CWLS and 4D Lap were presented in Figure 2.3 (b) in terms of the SRs and Verrors from the datasets with an SNR of 10, VR from 0.1 to 1.0, and grid size from 2 to 6 mm. The SR by CWLS remained around 1.0 for all the cases

with VR>0.1, whereas the SR by 4D Lap decreased with the increase of grid size for cases for VR from 0.2 to 0.4. Thus, greater improvement was achieved by CWLS compared to 4D Lap for cases with larger voxel size. The Verrors by CWLS were consistently lower than 4D Lap for all the cases with VR>0.1. At each VR, the Verror by CWLS slightly increased with the increase of grid size due to the voxel-averaging effect.

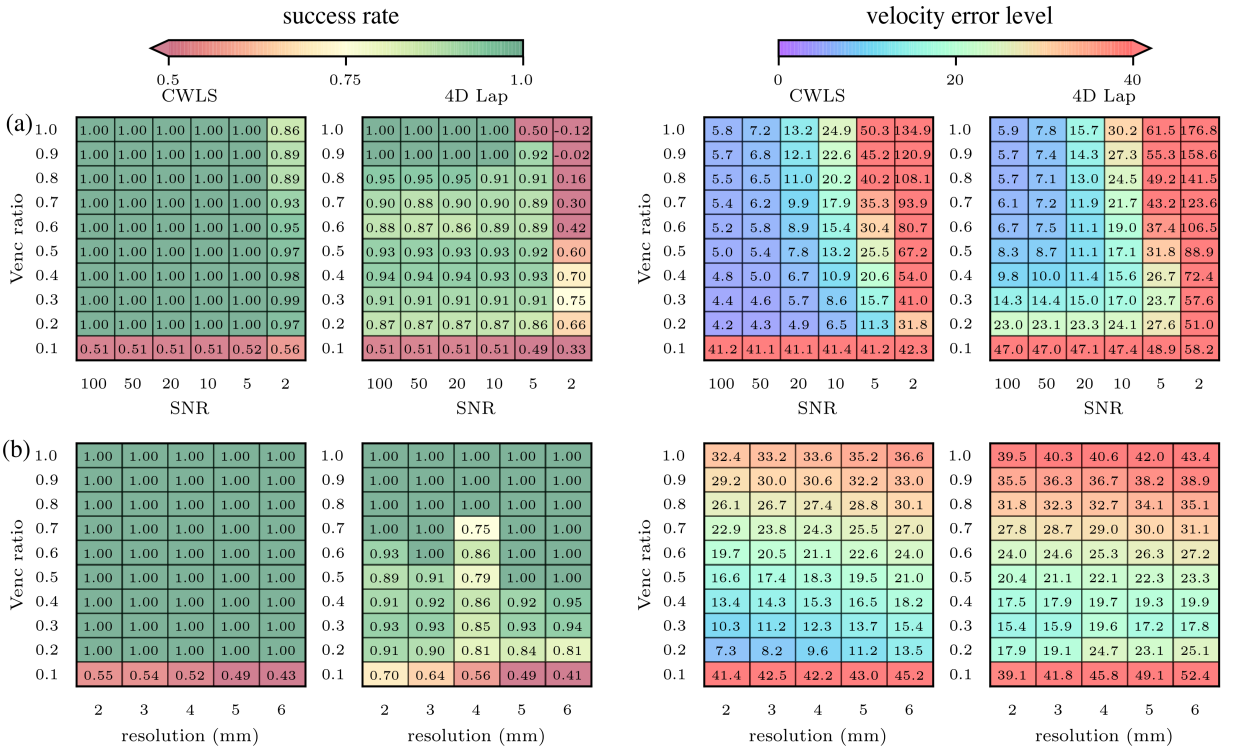

Figure 2.3 (a) The unwrapping SRs and V_{error}s (%) by CWLS and 4D Lap for the synthetic cases with different VRs and SNRs on 2.5 mm resolution grid. (b) The SRs and V_{error}s (%) on the synthetic datasets of LV flow generated with a SNR of 10, grid resolution from 2 to 6 mm, and VR from 0.1 to 1.0.

The effect of the uncertainty-based weighting and the divergence-free regularization was demonstrated by comparing CWLS with the unwrapping frameworks with unity weights or zero regularization constant *s*. With a SNR of 10 and VR from 0.2 to 1.0, the SRs and V_{error}s of the different unwrapping frameworks are presented in Fig. 4 as functions of VR. The method of "unity weights" means applying unity weights while "s=0" means setting *s* to zero, and "unity weights, s=0" employed both unity weights and zero regularization constant. As shown in Figure 2.4, CWLS yielded a SR around 1.0 for all the cases. Without either the uncertainty-based weighting

or the divergence-free regularization, the SRs were affected for cases with VR<0.4, indicating that both operations improved the unwrapping results at low VR. The “unity weights, s=0” yielded the lowest SRs for all cases with VR<0.8. For the cases with VR≥0.8, the phase data were unwrapped completely by all the methods as SR=1.0, and the V_{error}s of the two methods with divergence-free regularization were lower than the other two, indicating the denoising effect of the divergence-free regularization.

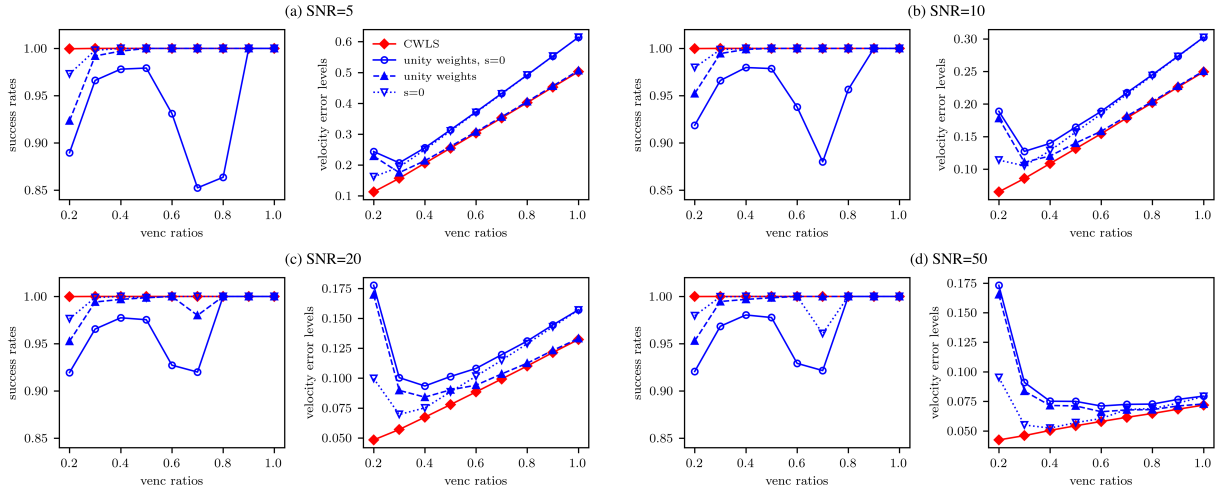

Figure 2.4 The SRs and Verrors (%) by the four different unwrapping methods with or without the uncertainty-based weighting and the divergence-free regularization for the synthetic cases with VRs from 0.2 to 1.0 and SNRs of 5, 10, 20, and 50.

2.4.2 In vitro 4D Poiseuille Flow

For the Poiseuille flow, the analytical solution had a maximum axial velocity (w_{max}) of 12 cm/s at centerline. The VRs of the 6 acquisitions were determined accordingly and given in Table 1. The intensity magnitude and phase fields from 3 datasets are presented in Figure 2.5. The intensity magnitude was higher near the center of the FOV, while it was lower near the pipe wall (partial volume effect(Miguel Ángel, Zisserman, & Brady, 2002)) and on the edges of the FOV. The voxels along the centerline of the phase field were wrapped twice at venc=4 cm/s and were wrapped once at venc=8 cm/s.

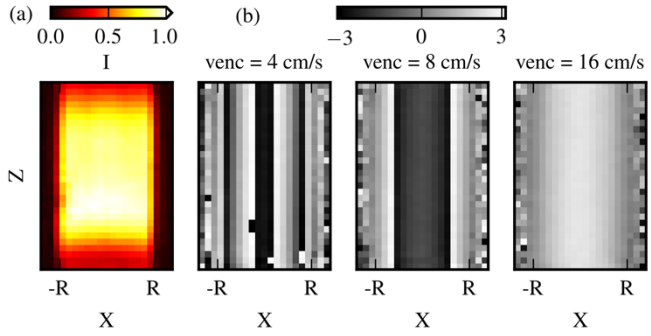

Figure 2.5 The intensity magnitude fields (a) and the streamwise velocity phase fields (b) from 3 acquisitions with vencs of 4, 8, and 16 cm/s. The fields are shown on the x-z plane along the centerline of the pipe.

The unwrapped phase $\hat{\phi}$ data was compared with the true phase ϕ generated from the analytical velocity fields. The number of wrapped voxels $N_{\mathcal{W},\psi}$ and $N_{\mathcal{W},\hat{\phi}}$ are presented in Table 1. As a reference, the total number of voxels within D_{ROI} (N_{ROI}) was 63720. One aliased voxel existed in the dataset with venc=16 cm/s, which was due to measurement noise. The 4D Lap unwrapped most of the voxels and failed to unwrap 2 to 104 wrapped voxels for each dataset, while CWLS completely unwrapped 5 datasets and failed to unwrap only 1 wrapped voxel for venc=4 cm/s. With venc=16 cm/s, the 4D Lap created 9 more wrapped voxels compared to the unprocessed data. The VNRs of the resulting velocity fields are presented in Table 2.1 together with the percentage increase of VNR by CWLS compared to 4D Lap. Compared to 4D Lap, the CWLS VNRs were 40-61% higher, demonstrating the denoising effect by CWLS unwrapping on velocity accuracy. With CWLS, the VNR was 131% higher using a venc of 4 cm/s than the VNR at a venc of 16 cm/s.

The mean WSS and relative ϵ_{WSS} from the velocity fields unwrapped with CWLS and 4D Lap are presented in Table 1 for the six datasets, together with the error reduction achieved by CWLS compared to 4D Lap. As a reference, the analytical WSS magnitude is 0.141 Pa. The WSS accuracy was consistently higher with CWLS for all datasets, with an error reduction of as much as 130% compared to 4D Lap. The relative ϵ_{WSS} was lowest for the CWLS-processed velocity fields at venc of 6 cm/s. Using a venc of 4 or 6 cm/s improved the relative ϵ_{WSS} by 31 and 43%, respectively, compared to using a venc of 16 cm/s.

Table 2.1 The venc, intensity based signal-to-noise ratio (SNR_I), number of wrapped voxels (N_w), velocity-to-noise ratio (VNR), mean WSS magnitude, and relative WSS magnitude error (ϵ_{WSS}) for the each *in vitro* Poiseuille flow dataset with CWLS and 4D Lap unwrapping

DV acquisitions		A	B	C	A	B	C
venc (cm/s)		4	6	8	8	12	16
TE (ms)		7.47	6.47	5.87	7.47	6.47	5.87
TR (ms)		10.2	9.2	8.6	10.2	9.2	8.6
SNR_I		60.9	54.1	47.9	60.9	54.1	47.9
N_w		41919	32819	24128	23434	3925	1
N_w	CWLS	1	0	0	0	0	0
	4D Lap	104	2	20	38	4	10
VNR	CWLS	33.2	38.4	28.1	16.0	18.5	14.4
	4D Lap	23.7	26.4	17.5	10.7	13.3	9.4
VNR improve (%)		40	46	61	50	39	53
mean WSS (Pa)	CWLS	0.17	0.16	0.17	0.20	0.18	0.20
	4D Lap	0.20	0.17	0.19	0.23	0.20	0.22
relative ϵ_{WSS}	CWLS	0.45	0.37	0.42	0.68	0.51	0.65
	4D Lap	0.70	0.56	0.78	1.38	1.02	1.50
ϵ_{WSS} reduction (%)		56	53	85	105	102	130

2.4.3 In vivo Aortic 4D Flow MRI

The SRs of 22 datasets for each VR are presented in Figure 2.6 (a) using boxplot (Frigge et al., 1989). The p-values from paired sample t-test between the SRs by CWLS and 4D Lap are also reported in Fig. 6(a), which indicated statistically significant difference (p-value<0.05) between the performances of the two methods at VRs of 0.1 to 0.4. The median SR is given in Table 2.2. Compared to 4D Lap, the improvement by CWLS was dramatic for VRs at 0.2 and 0.3. At a VR of 0.2, the median SR value was 81% higher by CWLS compared to 4D Lap. Examples of the unwrapped phase fields are given in Figure 2.6 (b) for a BAV dataset with a VR of 0.3 together with the benchmark ϕ and the wrapped phase ψ. Doubly-wrapped voxels can be observed in ψ near the aortic valve and in the descending aorta. CWLS completely unwrapped these voxels, while a large portion of wrapped voxels still remained from 4D Lap.

Table 2.2 The median success rates (SR) for each venc ratio (VR) of the artificially wrapped *in vivo* aortic datasets with CWLS and 4D Lap

VR		0.1	0.2	0.3	0.4	0.5
median of SRs	CWLS	0.43	0.87	0.98	0.99	1.0
	4D Lap	0.23	0.48	0.86	0.98	1.0

The VRs and Verrors for the in vivo datasets with real velocity aliasing are given in Table 2.3. The Verrors of the 4D Lap processed fields were minimally 10 times higher than the Verrors of the CWLS results. The unwrapped phase fields from one BAV case and one TAV-AA case with real aliasing are presented in Figure 2.6 (c) and (d). With 4D Lap unwrapping, phase jumps were observed near the aortic valve for the BAV case, as well as wrapped voxels in the descending aorta for the TAV-AA case. The CWLS completely unwrapped the voxels in the displayed field. The computational costs by CWLS on the aliased in vivo datasets were quantified with respect to the number of voxels (Nvoxels) within $D_{ROI} \cup D_{ref}$. As Nvoxels increased from 17640 to 35574, both the number of LSQR iterations and time-cost per iteration increased, resulting in a linear increase of the total time-cost per timeframe from 100 to 310 s. It should be noted that the computations were carried using a workstation with 16 cores (Intel Xeon CPU E5-2450 v2), and the time-cost may change with different computational capacity.

Table 2.3 The venc ratios (VR) of the acquisitions and the velocity error levels (V_{error}) of the resulting velocity fields for the 8 *in vivo* aortic datasets with real aliasing by CWLS and 4D Lap unwrapping

BAV	VR		0.51	0.70	0.63	0.72
	V_{error} (%)	CWLS	2.9	2.6	2.3	1.9
		4D Lap	55.9	34.0	41.9	30.8
TAV-AA	VR		0.54	0.64	0.95	0.71
	V_{error} (%)	CWLS	1.7	2.1	1.7	2.8
		4D Lap	36.7	30.1	30.5	35.3

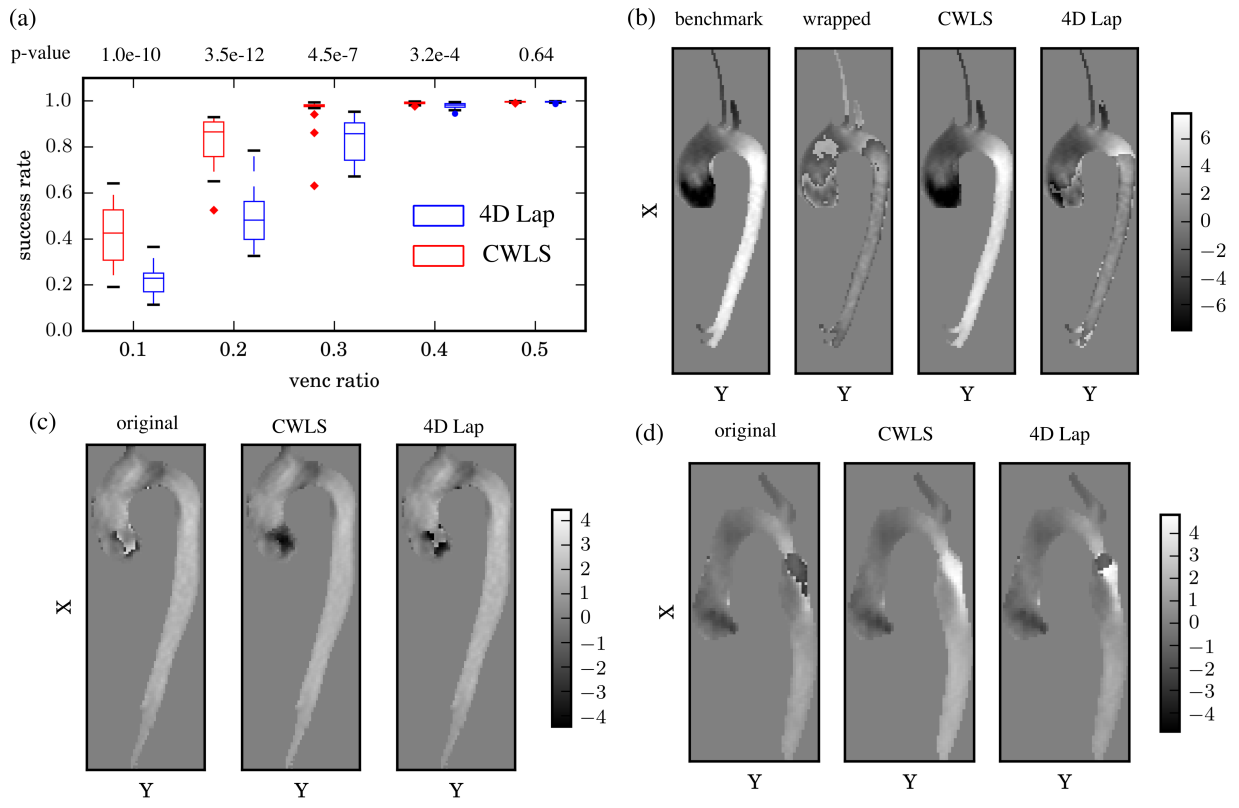

Figure 2.6 (a) Boxplots of the statistical distributions of SRs from the 22 artificially wrapped datasets for each VR. The centerline of each box indicates the median, while the edges are the 25th and 75th percentiles. (b) The u phase fields on the center x-y plane at peak systole of an artificially wrapped BAV dataset with VR=0.3. (c-d) With real-aliasing, the u phase fields at peak systole on the center x-y plane at peak systole for one BAV dataset (c) and one TAV-AA dataset (d) where the patient additionally had a repaired coarctation causing a high speed jet in the proximal descending aorta.

2.5 Discussion

The proposed CWLS method algorithmically unwraps the phase data without the need of additional high-venc acquisition. The performance of CWLS was evaluated and demonstrated with synthetic phase data, in vitro measurement of Poiseuille flow, and in vivo aortic 4D flow data. By incorporating the divergence-free constraint and using the robust WLS integration algorithm, CWLS reliably and robustly unwrapped the phase data with a venc as low as 20% of the maximum velocity and a SNR as low as 5, and also reduces the phase noise. As a consequence, CWLS improved the accuracy of the obtained velocity and hemodynamic quantities.

The CWLS method allows for the use of lower venc to obtain more accurate velocity and subsequent hemodynamic quantities in clinical applications of 4D flow MRI. Overall, a VNR increase of more than 100% can be achieved by using lower-venc acquisitions and the CWLS unwrapping according to the analysis on the in vitro Poiseuille flow. In addition, the CWLS method does not require any change in the 4D flow MRI acquisition in comparison with the multi-venc approaches which need additional high-venc acquisition with a 25-75% increase in scan time (Nett et al., 2012; Schnell et al., 2017). In applications where two 4D flow MRI scans are typically required for measuring venous and arterial flow with different vencs such as in the liver or brain, CWLS can reduce the scan time by omitting the high-venc acquisition and unwrapping the low-venc data.

Compared to 4D Lap, CWLS is more reliable for severely wrapped data, and more robust to noise and low spatial resolution. Unlike the 4D Lap method which unwraps along 4 dimensions in a single step (Michael Loecher et al., 2016), CWLS sequentially unwraps each time frame and employs WLS for spatial unwrapping. The time sequence proposed in section III-D prevents the error propagation from more-wrapped frames to less-wrapped frames, and the WLS integration mitigates the error propagation across the field. Moreover, CWLS incorporates the divergence-free constraint to regularize and denoise the phase field. Thus, CWLS better handles phase singularity and reduces noise during unwrapping. The advantage of 4D Lap over CWLS is its ease of use and low computational cost. Neither method needs aliasing-free reference timeframes as required by other temporal unwrapping algorithms (Q. Xiang, 1995). Compared to the unwrapping method which resolves phase singularity with branch cut surfaces (María F Salfity et al., 2006), the CWLS method does not rely on the estimation of phase singularity loops, making it more scalable for large and complex datasets. The advantage of CWLS over the 4D gradient based phase unwrapping (M. Loecher et al., 2011) is that CWLS can unwrap voxels wrapped multiple times and large wrapped regions.

There are several limitations of the CWLS method. First, the computational cost of CWLS was expensive compared to 4D Lap. Using a workstation with 16 cores (Intel Xeon CPU E5-2450 v2), the processing of each *in vivo* dataset took 1-2 hrs, whereas 4D Lap completed the unwrapping within seconds. Another limitation of CWLS was that the FOV needed to be segmented prior to unwrapping, which can be difficult for acquisitions with tissue movement despite the recent development on 3D segmentation algorithms (Berhane et al., 2020). The segmentation applied to

the *in vivo* aortic data based on the time-averaged quantity did not consider the motion of aorta and might affect the CWLS unwrapping. However, the CWLS still showed superior performance compared to 4D Lap on the *in vivo* aortic data with this segmentation. It is also worth noting that the CWLS unwrapping depends on the phase variation estimated using (2-2) with the assumption that the phase variation between neighboring voxels are within $(-\pi,\pi)$. Using an extremely low venc can violate the assumption and therefore affect the performance of CWLS as suggested by the low SRs from the cases with VR=0.1 in Fig. 3.

Furthermore, there are a number of limitations of this study. First, the benchmark phase data for the eight real-aliasing *in vivo* datasets was unavailable to evaluate the SR of unwrapping. Instead, we estimated the velocity errors from the velocity divergence and compared the V_{error}s between results from CWLS and 4D Lap. However, it should be noted that this divergence-based error metric could underestimate the error level from CWLS which penalized the velocity divergence during phase unwrapping. *In vivo* dual-venc datasets can be acquired in future studies and used as benchmark to evaluate the performance of phase unwrapping on low-venc acquisitions. Moreover, further investigation on CWLS unwrapping needs to be performed for severely wrapped *in vivo* datasets with VRs lower than 0.5. In addition, the intra-voxel phase dispersion due to the aortic valve pathologies was not considered in the synthetic data generation or the *in vitro* experiment, limiting the performance evaluation of CWLS on data with this artifact.

In conclusion, this study introduces a divergence-free constrained phase unwrapping method for 4D flow MRI and evaluates its performance with synthetic phase data, *in vitro* measurement of Poiseuille flow, as well as *in vivo* aortic 4D flow data. The proposed method is reliable with severely wrapped data and robust to noise. The method also denoises the phase field and thus enhances the VNR of the resulting velocity data. The method can benefit clinical applications of 4D flow MRI as it improves the accuracy of acquired velocity and hemodynamic quantities.

2.6 Authors' contributions

J.Z. developed and evaluated the method, performed the data analysis, and drafted the manuscript. M.C.B and S.M.R performed the in vitro measurement. M.B.S, H.B, and J.J.B. obtained and pre-processed the *in vivo* data. M.M., V.L.R. and P.P.V. designed and oversaw the study and all data analysis. All authors critically reviewed and edited the manuscript, and gave final approval for publication.

3. 4D FLOW MRI PRESSURE ESTIMATION USING VELOCITY MEASUREMENT-ERROR BASED WEIGHTED LEAST-SQUARES

This chapter is reproduced with permission from: Zhang, J., Brindise, M.C., Rothenberger, S., Schnell, S., Markl, M., Saloner, D., Rayz, V.L., Vlachos, P.P., 2020. 4D Flow MRI Pressure Estimation Using Velocity Measurement-Error-Based Weighted Least-Squares. IEEE Trans. Med. Imaging 39, 1668–1680. https://doi.org/10.1109/TMI.2019.2954697

3.1 Background and literature review

Pressure measured from the cardiovascular system is widely used to diagnose disease. Many pressure-based clinical biomarkers, such as pulmonary wedge pressure (Oliveira et al., 2014), are single point measurements typically acquired by placing a pressure catheter in the region of interest (Wood, Leusen, Warner, & Wright, 1954). However, this approach is invasive and still only provides a point measurement. Conversely, a spatial pressure distribution can provide a more complete view of the hemodynamics in the cardiovascular system. For example, the pressure distribution in the posterior communicating artery bifurcation has been explored and its correlation with the locations of the rupture of infundibulae or progression to aneurysms was established (Baek et al., 2009). Further, such pressure distributions can be obtained noninvasively. One such noninvasive approach includes estimating the pressure difference from Doppler echocardiography and is typically employed for evaluating intra-ventricular pressure difference (Nagueh et al., 2009; Vlachos, Niebel, Chakraborty, Pu, & Little, 2014). However, conventional Doppler Ultrasound only measures one component of the velocity which limits the accuracy of the estimated pressure difference. Pressure fields can also be obtained using computational fluid dynamics (CFD) simulations, but fidelity of the simulation depends on the accuracy of segmentation and flow boundary conditions prescribed to the solver. These assumptions, as well as solver parameters have been shown to have a significant effect on the resulting flow field (Berg et al., 2014; Brindise et al., 2019; Voß et al., 2019), the flow fields and flow-derived metrics were compared across cerebral aneurysm flow data obtained with *in vivo* 4D flow, *in vitro* PTV, and CFD. Minor flow field variations were found between modalities due to differences in the modeling assumptions and resolution limitations. High-resolution CFD simulations are also computationally expensive. Pressure reconstruction methods have become increasingly of interest with the development of flow measurement techniques such as 4D flow magnetic resonance imaging (MRI) which

measures time-resolved velocity fields. However, several error sources and limitations inherent to *in vivo* 4D flow MRI result in unreliable pressure fields. The setting of velocity encoding (venc) parameter for a 4D flow acquisition is determined by the maximum velocity expected in the region of interest. Velocity greater than the venc leads to velocity aliasing, while higher venc settings lead to increased noise which affects 4D flow measurements in low velocity regions (Ha et al., 2016). Artifacts such as concomitant gradient fields and eddy currents affect the accuracy of measured phase differences (Dyverfeldt et al., 2015). The partial volume effect and intravoxel dephasing are also common sources of systematic errors, especially for voxels near lumen boundaries (Nayak et al., 2015). For *in vivo* measurements, the limited scan time results in decreased spatiotemporal resolution and increased image artifacts (Dyverfeldt et al., 2015). Thus, a robust algorithm is needed to accurately reconstruct the pressure field from 4D flow MRI.

Several algorithms have been proposed to evaluate the pressure field from measured flow data. Most algorithms contain two major steps. The pressure gradient fields are first calculated from the velocity fields, which are then spatially integrated to obtain the instantaneous pressure fields.

For blood flow, the pressure gradient can be calculated using the incompressible Navier-Stokes momentum equation in the following form (Charonko, King, Smith, & Vlachos, 2010; R. De Kat & Van Oudheusden, 2012; Roeland de Kat, van Oudheusden, & Scarano, 2009; Tronchin, David, & Farcy, 2015; Violato, Moore, & Scarano, 2011):

$$\nabla \boldsymbol{p} = -\rho\left(\frac{\partial \boldsymbol{u}}{\partial t} + (\boldsymbol{u}\cdot\nabla)\boldsymbol{u}\right) + \mu\nabla^2\boldsymbol{u}, \qquad (3\text{-}1)$$

where $\boldsymbol{p}$ is pressure (Pa), ∇ is the spatial gradient operator such that $\nabla\boldsymbol{p}$ is the pressure gradient (Pa/m), ρ and μ are the density (kg/m^3) and dynamic viscosity (Pa·s) of the fluid, respectively, $\boldsymbol{u}$ is the velocity (m/s), and t is time (s). $\mu\nabla^2\boldsymbol{u}$ represents viscous diffusion. $\frac{D\boldsymbol{u}}{Dt}$ and $(\boldsymbol{u}\cdot\nabla)\boldsymbol{u}$ represent the local and convective accelerations (m/s^2), respectively. The body force term has been ignored in (3-1) and in the following equations but it could be included.

With pressure gradients calculated from velocity data using (3-1), the pressure field can be reconstructed by spatially integrating the pressure gradient field. One approach to this reconstruction calculates the pressure at each point in the flow field by integrating the pressure gradient along one path or multiple paths (Liu & Katz, 2006; Tronchin et al., 2015). Path

integration methods are rarely employed for 3D flow data due to the high computational cost. The most common approach for reconstructing pressure fields from 3D velocity data is by solving the pressure Poisson equation (PPE) in the following from (R. De Kat & Van Oudheusden, 2012; Roeland de Kat et al., 2009; N. J. Neeteson et al., 2016; Schneiders, Pröbsting, Dwight, van Oudheusden, & Scarano, 2016; Violato et al., 2011):

$$\nabla^2 \boldsymbol{p} = \nabla \cdot \boldsymbol{p}_{\boldsymbol{grad,u}} = -\rho \nabla \cdot (\boldsymbol{u} \cdot \nabla \boldsymbol{u}), \qquad (3\text{-}2)$$

where $\boldsymbol{p}_{\boldsymbol{grad,u}}$ is the pressure gradient field evaluated from the velocity field and $(\nabla \cdot)$ is the divergence operator which evaluates the divergences from a vector field. This approach has been successfully applied to both engineering applications (R. De Kat & Van Oudheusden, 2012; Roeland de Kat et al., 2009; N. J. Neeteson et al., 2016; Schneiders et al., 2016; Violato et al., 2011) and cardiovascular velocity measurements from phase-contrast MRI (Jelena Bock et al., 2011; Donati, Nordsletten, Smith, & Lamata, 2014; Ebbers & Farnebäck, 2009; Krittian et al., 2012; Lamata et al., 2014). For incompressible flow, equation (3-2) is valid for both steady and unsteady conditions. Boundary conditions are required for solving (3-2), which can be Dirichlet boundary conditions with prescribed pressure values, Neumann boundary conditions with prescribed pressure gradient values, or a mix of the two types. As discussed in (van Oudheusden, 2013), both the path integration method and the method of solving the pressure Poisson equation can be regarded as global optimization formulations of the pressure-gradient spatial integration. Another method that falls into this category is a least-squares reconstruction method referred to as ordinary least-squares (OLS) reconstruction in this study (Jeon, Gomit, Earl, Chatellier, & David, 2018). For OLS, the pressure integration is performed by solving the following linear system:

$$G\boldsymbol{p} = \boldsymbol{p}_{\boldsymbol{grad,u}}, \qquad (3\text{-}3)$$

where G is the discrete gradient matrix, and $\boldsymbol{p}$ is the unknown pressure field written as a column vector. Equation (3-3) is an over-determined linear system for 2D and 3D flow data. The OLS method solves the pressure field by minimizing the pressure gradient residuals in a least-squares sense as:

$$p_{OLS} \equiv \underset{p}{argmin}\left(\left\|\nabla \boldsymbol{p} - \boldsymbol{p}_{\boldsymbol{grad,u}}\right\|\right), \qquad (3\text{-}4)$$

where ‖ ‖ is the L2 norm. In matrix form, equation (4) becomes:

$$G^T G\boldsymbol{p} = G^T \boldsymbol{p}_{grad,u}. \qquad (3\text{-}5)$$

As stated in (C. Y. Wang, Gao, Wei, Li, & Wang, 2017), OLS reconstruction and Poisson share the same theoretical foundation, and solving the pressure Poisson equation with Neumann boundary conditions is mathematically equivalent to the solving the OLS formulation.

Due to the measurement inaccuracies in the *in vivo* 4D flow MRI, the calculated pressure gradient fields contain propagated errors. However, the above-mentioned pressure reconstruction methods do not have any way to account for or reduce the effect of such erroneous pressure gradient values. In order to improve the accuracy of reconstructed pressure fields, a weighted least-squares (WLS) reconstruction method for spatial integration of pressure gradients is introduced in this work. In this method, pressure fields are solved by minimizing the WLS of the pressure gradient residuals. The weights are determined based on estimated pressure gradient errors. To estimate such pressure gradient errors, velocity errors are calculated from the velocity divergence for incompressible flow and propagated through (3-1). Smaller weights are assigned to inaccurate pressure gradient values such that their effects are reduced during spatial integration. The performance of WLS was tested using synthetic velocity fields and *in vitro* Poiseuille flow measured using 4D flow MRI. The method was then applied to *in vivo* 4D flow MRI velocity data acquired for two aneurysms and *in vitro* PTV velocity data collected in patient-specific aneurysm models.

3.2 Methodology

3.2.1 Pressure reconstruction using weighted least-squares

Pressure gradient fields were calculated from velocity fields using (3-1). Velocity data employed in this study were on Cartesian grids with velocity values located on grid nodes. A second order central (SOC) difference scheme was employed to evaluate the temporal and spatial derivatives of the velocity fields. Pressure gradient values were calculated on grid nodes, then linearly interpolated to the face centers of each grid cell. The SOC scheme and grid arrangement are demonstrated in Figure 3.1. SOC computes the gradient at each point from its neighboring

points, e.g., $\frac{\partial p}{\partial x}(i,j) = \frac{p(i+1,j)-p(i-1,j)}{2\Delta x}$, where Δx is the grid size. The reconstructed pressure values are on grid nodes.

The pressure field is obtained by solving

$$G^T W G \boldsymbol{p} = G^T W \boldsymbol{p}_{\boldsymbol{grad,u}}, \tag{3-6}$$

which gives the pressure result that minimizes the least-squares of pressure gradient residuals as

$$\boldsymbol{p}_{\boldsymbol{WLS}} \equiv \underset{p}{argmin}\left(W\left\|\nabla \boldsymbol{p} - \boldsymbol{p}_{\boldsymbol{grad,u}}\right\|\right), \tag{3-7}$$

where W is the weight matrix. W is a diagonal matrix containing positive elements as weights for pressure gradient values $\boldsymbol{p}_{\boldsymbol{grad,u}}$. Greater weights are assigned to pressure gradient values anticipated to be more accurate. Unlike the Poisson equation, WLS reconstruction does not require boundary conditions to be explicitly assigned as the Poisson equation does. A minimum of one pressure reference point is needed. Pressure at the reference point can be obtained from direct measurement or a far-field pressure condition. If only the pressure differences between points in the flow field are of interest, the selection of reference point and reference pressure is arbitrary, e.g., zero pressure can be assigned at one point along the boundary.

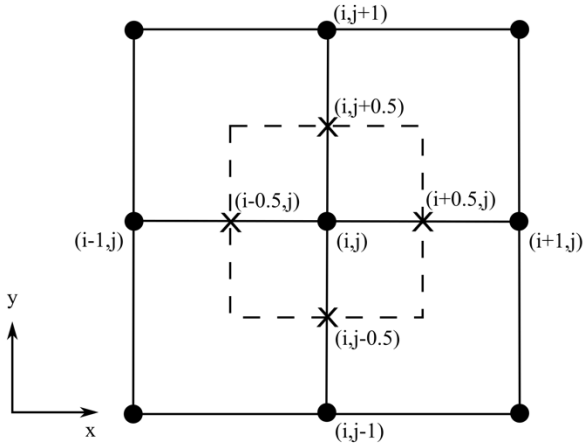

Figure 3.1 Grid arrangement and SOC scheme demonstrated using a 2D Cartesian grid. The grid nodes are labeled by dots. A grid cell is drawn using dashed lines. Cell face centers are labeled by "X" marks

3.2.2 Velocity error estimation from spurious divergence

For incompressible flow, the divergence of the true velocity field should be zero, expressed mathematically as:

$$\nabla \cdot \boldsymbol{u_T} = 0, \tag{3-8}$$

where $\boldsymbol{u_T}$ is the true velocity field. Because measured velocity data inevitably contain errors, the divergence of the measured velocity field is typically nonzero. The spurious divergence equals the divergence of the velocity error field as

$$\nabla \cdot \boldsymbol{u_M} = \nabla \cdot \boldsymbol{\epsilon_u}, \tag{3-9}$$

where $\boldsymbol{u_M}$ is the measured velocity field, $\boldsymbol{\epsilon_u}$ is the velocity error field, and $\boldsymbol{\epsilon_u} = \boldsymbol{u_M} - \boldsymbol{u_T}$. Equation (3-9) forms an underdetermined linear system as there are less rows than columns in the discretized divergence operator ($\nabla \cdot$). Thus, $\boldsymbol{\epsilon_u}$ cannot be uniquely determined from (3-9). We estimate $\boldsymbol{\epsilon_u}$ by finding the least-squares solution to (3-9) as

$$\widehat{\boldsymbol{\epsilon_u}} = (\nabla \cdot)^T (\nabla^2)^{-1} (\nabla \cdot \boldsymbol{u_M}) \equiv \underset{\epsilon_u}{argmin}(\|\nabla \cdot \boldsymbol{\epsilon_u} - \nabla \cdot \boldsymbol{u_M}\|), \tag{3-10}$$

where $\widehat{\boldsymbol{\epsilon_u}}$ is the estimated velocity error field. Previous studies have similarly employed the spurious velocity divergences to estimate the uncertainty of velocity data measured using tomographic particle image velocimetry (PIV) (Azijli & Dwight, 2015).

3.2.3 Generation of weight matrix

The pressure gradient error field is estimated by propagating $\widehat{\boldsymbol{\epsilon_u}}$ through (3-1) as

$$\widehat{\boldsymbol{\epsilon_{\nabla p}}} = f_{\nabla p}(\boldsymbol{u_M}) - f_{\nabla p}(\boldsymbol{u_M} - \widehat{\boldsymbol{\epsilon_u}}), \tag{3-11}$$

where $\widehat{\boldsymbol{\epsilon_{\nabla p}}}$ is the estimated pressure gradient error field and $f_{\nabla p}(\cdot)$ denotes evaluating (3-1) using the given velocity field.

Accuracy of the $\boldsymbol{p_{grad,u}}$ at each point from each time frame is determined from the weighted standard deviation (WSTD) of the estimated pressure gradient errors from neighboring points given as

$$\widehat{\boldsymbol{\sigma_{\nabla p}}} = \sqrt{\frac{\sum_{i=0}^{n} w_i \left(\widehat{\epsilon_{\nabla p}}\right)_i^{\,2}}{\sum_{i=0}^{n} w_i}}, \tag{3-12}$$

where $\widehat{\boldsymbol{\sigma_{\nabla p}}}$ is an estimation of the pressure gradient uncertainty and n is the number of points that are employed in the WSTD calculation. Weights w_i for WSTD calculations are determined using a bivariate Gaussian function:

$$w_i = exp\left(-\frac{1}{2}\left(\frac{r_t}{\delta_t}\right)^2 - \frac{1}{2}\left(\frac{r_s}{\delta_s}\right)^2\right), \tag{3-13}$$

where r_t and r_s are the spatial and temporal separations from the neighboring points to the point of interest, respectively. δ_t and δ_s are the correlation lengths along the temporal and spatial dimensions which are determined by the numerical difference scheme. Based on the SOC scheme employed for $p_{grad,u}$ calculation, neighboring $p_{grad,u}$ values should not be correlated farther than $2\Delta x$ spatially and Δt temporally. Thus, the correlation lengths were chosen to be $\delta_t = \Delta t$ and $\delta_s = 2\Delta x$. In addition, only points within the $r_t \leq \Delta t$ and $r_x \leq 2\Delta x$ neighborhood were employed in the WSTD calculation.

The weight matrix for WLS reconstruction is given by

$$W = diag\left(\frac{1}{\widehat{\sigma_{\nabla p}}^{\,2}}\right), \tag{3-14}$$

where $diag(\cdot)$ is the diagonal matrix generated from given diagonal elements. To avoid singularities due to zero weights, a lower bound of weights is given as 10^{-9} multiplied by the average of all weight elements.

3.2.4 Implementation of pressure reconstruction methods

The method of solving the PPE (denoted as 'Poisson' herein) was employed in this study to compare to the WLS method for evaluating its performance. The same formulation of PPE was

employed in the present study as in (Jelena Bock et al., 2011; Donati et al., 2014; Ebbers & Farnebäck, 2009; Krittian et al., 2012; Lamata et al., 2014) which considered both inertial and viscous effects of the blood flow. For the Poisson algorithm, pressure gradient fields were calculated from (3-1) by SOC and the grid arrangement described in section II-A. Divergence of the pressure gradients were calculated using SOC and employed as the source term for the pressure Poisson equation. At least one grid point along the boundary was prescribed with zero pressure as the Dirichlet boundary condition for both methods. Pressure gradients at all the other boundary points were employed as the Neumann boundary condition for solving the pressure Poisson equation. SuperLU, a general-purpose library for the direct solution of large, sparse, nonsymmetric systems of linear equations (Li, 2005), was employed to solve (3-2) and (3-6) for the reconstructed pressure fields.

3.2.5 Synthetic flow fields

Two flow fields were used for validating and analyzing the pressure reconstruction methods. The first is a 2D Lamb-Oseen vortex ring flow field which consists of two counter-rotating vortices. Velocity of each vortex can be described by

$$u_\theta = u_{\theta max}\left(1+\frac{1}{2\alpha}\right)\frac{r_{max}}{r}\left(1-e^{1-\alpha\left(\frac{r}{r_{max}}\right)^2}\right), \qquad (3\text{-}15)$$

where u_θ is the angular velocity, r is the distance from the center of the vortex, r_{max} is the distance where the maximum angular velocity $u_{\theta max} = 0.5\ m/s$ is reached, and $r_{max} = \sqrt{\alpha} \times r_c$ with $r_c = 0.01\ m$. The constant α was set to be 1.25643 according to (Devenport & Rife, 1996). The center points of vortices were separated by $2r_0$ with $r_0 = 0.01\ m$. A free stream velocity component u_{fs} was added to make the flow steady as

$$u_{fs} = u_{\theta max}\left(1+\frac{1}{2\alpha}\right)\frac{r_{max}}{2r_0}\left(1-e^{1-\alpha\left(\frac{r}{r_{max}}\right)^2}\right). \qquad (3\text{-}16)$$

The exact velocity fields were generated on a uniform Cartesian grid with 65^2 grid points. The size of the domain was $0.1\ m \times 0.1\ m$. The exact pressure field was obtained by numerically integrating the pressure gradients on a denser Cartesian grid with 129^2 points. Fluid density was

$1\ kg/m^3$ and the flow was inviscid. Figure 3.2 (a) and (b) present the exact velocity and pressure field, respectively.

The second is 2D pulsatile flow between two parallel infinite plates driven by the unsteady pressure gradient given as

$$\frac{dP}{dx} = \rho K + \gamma \rho K cos\omega t, \tag{3-17}$$

where the x direction is streamwise, γ is the ratio between the magnitude of the steady pressure gradient component and the amplitude of the oscillating pressure gradient component, K is the constant controlling the overall strength of the pressure gradient, and ω is the angular speed of the oscillating component. The velocity profile can be expressed as

$$u = u_{max}\left(1 - \frac{y^2}{h^2}\right) + \frac{\gamma K}{i\omega}\left(1 - \frac{cosh(y/h\sqrt{i}\lambda)}{cosh(\sqrt{i}\lambda)}\right) exp(i\omega t), \tag{3-18}$$

with $\lambda = h\sqrt{\frac{\rho}{\mu\omega}}$, where y is the spanwise direction, h is the channel half-width, and u_{max} is the centerline velocity of the steady flow component. In this paper the flow field contains a 20 mm long channel with a h of 4 mm. Blood-mimicking fluid properties were employed with ρ of 1110 kg/m^3 and μ of 0.0033 Pa·s. ω was set to be 2π rad^{-1} and the Womersley number of the flow was 5.75. u_{max} was set to be 1m/s, and the other parameters were given as $K = 0.38\ m/s^2$, $\gamma = 8.28$, and $\lambda = 5.75$. Figure 3.2 (c) shows the waveforms of pressure gradient and centerline streamwise velocity component within one cycle. Figure 3.2 (d) shows the streamwise velocity profile at 4 phases in a cycle. The flow fields were generated on a uniform Cartesian grid with a spatial resolution of 0.4×0.4 mm^2, yielding 21×51 grid points in the field. This type of flow was employed in (Charonko et al., 2010) to assess the performances of pressure reconstruction methods.

In order to test the robustness of the pressure reconstruction methods to errors in the velocity data, noise was added to the velocity fields in a manner similar to that done in (Azijli & Dwight, 2015; Charonko et al., 2010), which is designed to mimic experimental noise. Noise was added as a vector with a normally distributed magnitude and random direction at each point. The error magnitude can be expressed by

$$\boldsymbol{\epsilon_u^i} = \mathcal{N}\left(0, \lambda\left|u^i\right|\right), \tag{3-19}$$

where λ is the error percentage level. For the vortex ring flow, two types of velocity noise distributions were considered which are referred to as 'Uniform Noise Distribution (UND)' and 'Spatially Varying Noise Distribution (SVND)' in this study. For UND, the measurement quality was uniform across the field, and λ was set to be consistent across the field. 26 UND test cases were generated with λ varying linearly from 1 to 51%. For SVND, the flow field was divided into a "top half" and "bottom half" with different values of λ applied to each half. A total of 7 cases were generated with λ_{top} varying exponentially from 8% to 64%, and λ_{bottom} set to 8% for all cases. For each test case with UND or SVND, 100 time frames were created with a sampling frequency of 50 Hz ($\Delta t = 0.02\ s$). 0 Pa was assigned at the left end of the dashed horizontal line in Fig. 2(a) as the reference pressure. For the pulsatile flow, 26 UND test cases were generated with λ varying linearly from 1 to 51%. 1000 frames were created for a time span of 50 cycles, yielding 20 frames per cycle and a temporal resolution of 0.05 s. Dirichlet boundary condition with zero pressure was applied to the inlet of the 2D channel as the reference pressure.

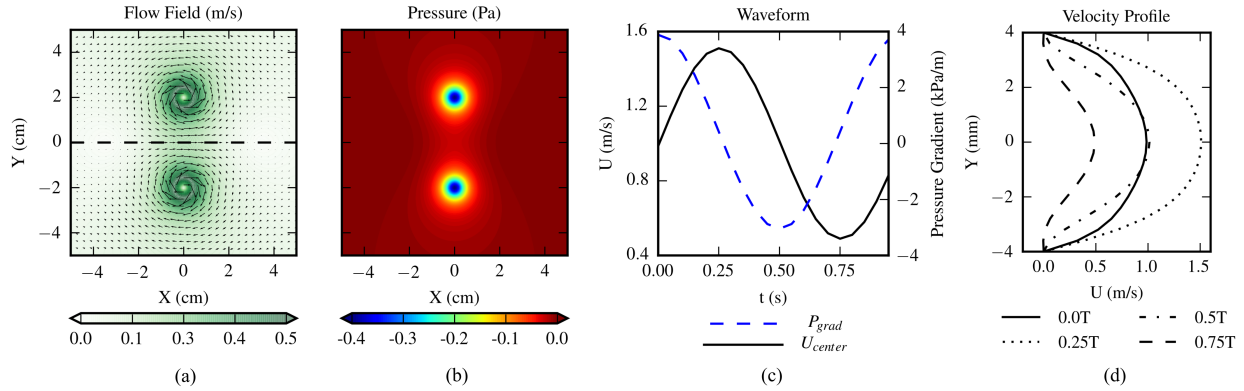

Figure 3.2 (a) Exact velocity field of the 2D Lamb-Oseen vortex ring. The vectors indicate the flow direction and color scale of the contours corresponds to velocity magnitude. The flow field is divided by the black dashed line into top and bottom halves. (b) Exact pressure field of the 2D vortex ring flow. (c) Waveforms of pressure gradient and centerline streamwise velocity within one cycle of the 2D pulsatile flow. (d) Streamwise velocity profiles at 4 time points in a cycle of the 2D pulsatile flow.

3.2.6 In vitro 4D Poiseuille flow

Experimental measurements of steady, laminar Poiseuille flow in a circular pipe were acquired using 4D-flow MRI. The Poiseuille flow allowed the usage of an analytical pressure field as the benchmark to assess the accuracy of the reconstructed pressure. A blood mimicking water-glycerol solution with a density and viscosity of 1110 kg/m^3 and 0.00372 Pa·s, respectively, was used as the working fluid. The volume ratio between water and glycerol was 60:40. A small amount (0.66 mg/mL) Gadolinium contrast was added to enhance the signal-to-noise ratio (SNR) of the 4D flow MRI scan without altering the rheology of the fluid. A computer-controlled gear pump drove the working fluid at a steady flow rate of 7.6 mL/s. The diameter of the pipe was 12.7 mm and the length was sufficiently long prior to entering the MRI field of view to ensure a fully developed velocity profile. The 4D flow MRI scan was performed on a Siemens 3T PRISMA scanner at a spatial resolution of $0.85 \times 0.85 \times 0.8$ mm^3. A total of 12 time frames were collected. The venc of this 4D flow MRI scan (prospectively triggered time-resolved 3D PC MRI with 3-directional velocity encoding) was set to 16 cm/s, which is sufficiently high to avoid velocity wrapping. The echo time (TE) and repetition time (TR) were 5.87 ms and 8.60 ms, respectively. The yielded temporal resolution was 120.4 ms. The bandwidth was 455 kHz and flip angle was 15º. The 4D-flow MRI images were pre-processed (phase offset correction, noise filtering) using a customized Matlab-based software package, Velomap-Tool, developed at University Medical Center Freiburg (J. Bock et al., 2007).

The analytical velocity field of the Poiseuille flow is given by:

$$W = -\frac{1}{4\mu}\frac{dP}{dz}(R^2 - r^2), \qquad (3\text{-}20)$$

where W is the axial (along z-axis) velocity component (m/s), r is the radial distance from the pipe centerline (m) which equals to $\sqrt{x^2 + y^2}$ and $\frac{dP}{dz}$ is the axial pressure gradient (Pa/m). The velocity components along other axes (U and V) are 0. The axial pressure gradient is defined by:

$$\frac{dP}{dz} = -\frac{8\mu Q}{\pi R^4}, \qquad (3\text{-}21)$$

where Q is the volumetric flow rate (m^3/s). This yields a linear analytical pressure drop along the pipe. The analytical velocity and pressure fields were considered as the ground truth for error analysis.

3.2.7 In vivo and in vitro flow in cerebral aneurysms

In vivo flow data in a basilar tip aneurysm were acquired at San Francisco VA Medical Center and an internal carotid artery (ICA) aneurysm was imaged at Northwestern Memorial Hospital (NMH). Both aneurysms were acquired with 4D flow MRI on a 3T MRI scanner (Skyra, Siemens Healthcare, Erlangen, Germany). An ECG-gated RF spoiled 4D-flow MRI sequence (Siemens WIP sequence) was used with gadolinium contrast for imaging the basilar tip aneurysm, while no contrast was used for the ICA aneurysm. Aliasing, phase offsets, and noise were corrected. Velocity data from the *in vivo* measurements were obtained on Cartesian grids. The spatial resolution was $1.25\times1.25\times1.33$ mm^3 for the basilar tip aneurysm and $1.09\times1.09\times1.30$ mm^3 for the ICA aneurysm. The temporal resolutions were 40.5 ms (20 frames per cycle) and 44.8 ms (13 frames per cycle) for the basilar tip aneurysm and the ICA aneurysm, respectively.

In vitro PTV velocity data was obtained using a 1:1 scale models of the patient-specific aneurysms. To reproduce the in vivo flow field, the inflow was driven by a computer-controlled gear pump with the inlet flow based on the in vivo data. DaVis 10.0 (LaVision Inc.) was used to process the particle images. Shake the Box (STB), a particle tracking method, was used to compute the velocity fields. The unstructured STB velocity fields were interpolated to Cartesian grids. For the basilar tip aneurysm, the grid size was 0.3 mm and the temporal resolution was 2.5 ms. For the ICA aneurysm, the grid size was 0.4 mm and the temporal resolution was 1.5 ms. Blood mimicking fluids composed of water-glycerol-urea were employed with the details provided in Table 3.1 (Brindise, Busse, & Vlachos, 2018). More details on the in vivo and in vitro measurements can be found in (Brindise et al., 2019). To mimic the in vivo 4D flow data, another dataset was created for each aneurysm by virtual spatial voxel averaging the in vitro PTV data, then temporally downsampling to the same frequency as the 4D flow measurement. Thus, the voxel-averaged and subsampled dataset (referred to as 'PTV-voxavg' herein) had the same spatial and temporal resolution as the corresponding in vivo 4D flow MRI dataset.

Table 3.1 Composition and properties of blood mimicking fluids used for *in vitro* measurements

Geometry	Composition (%wt)			Density (kg/m^3)	Kinematic Viscosity (m^2/s)
	Water	Glycerol	Urea		
Basilar tip	44.8	32.8	22.4	1103	3.04×10^{-6}
ICA	45.3	29.7	25.0	1132	3.50×10^{-6}

3.3 Results

3.3.1 Lamb-Oseen vortex ring

Velocity and pressure gradient error estimation

To validate the error estimation algorithm employed in this study, the estimated velocity and pressure gradient errors were compared with the exact errors from all the Lamb-Oseen vortex cases. As a demonstration, the distributions of estimated and exact errors from the case with λ_{bottom} and λ_{top} being 8 and 32%, respectively, are shown in Figure 3.3. Figure 3.3 (a) and (b) present the comparisons on velocity error magnitudes ($|\widehat{\epsilon_u}|$ versus $|\epsilon_u|$) and pressure gradient error magnitudes ($\left|\widehat{\epsilon_{\nabla p}}\right|$ versus $\left|\epsilon_{\nabla p}\right|$), respectively. Figure 3.3 (c) compares $\widehat{\sigma_{\nabla p}}$ with the pressure gradient uncertainty ($\sigma_{\nabla p}$) evaluated as the root-mean-square (RMS) of $\epsilon_{\nabla p}$ from all time frames. For both estimated and exact errors, the magnitudes were greater in the top half of the field than in the bottom half, and greater in the vortices than in the ambient regions, as suggested by the spatial distributions. The estimated magnitudes were lower than the corresponding exact magnitudes as suggested by the medians from the histograms in Figure 3.3. The median of $|\widehat{\epsilon_u}|$ was 5.5% while it was 6.0% for $|\epsilon_u|$. The medians of $\left|\widehat{\epsilon_{\nabla p}}\right|$ and $\left|\epsilon_{\nabla p}\right|$ were 4.5% and 6.3%, respectively. The median of $\widehat{\sigma_{\nabla p}}$ was 6.6% while it was 8.6% for $\sigma_{\nabla p}$. The error estimation algorithm performed consistently for all the cases.

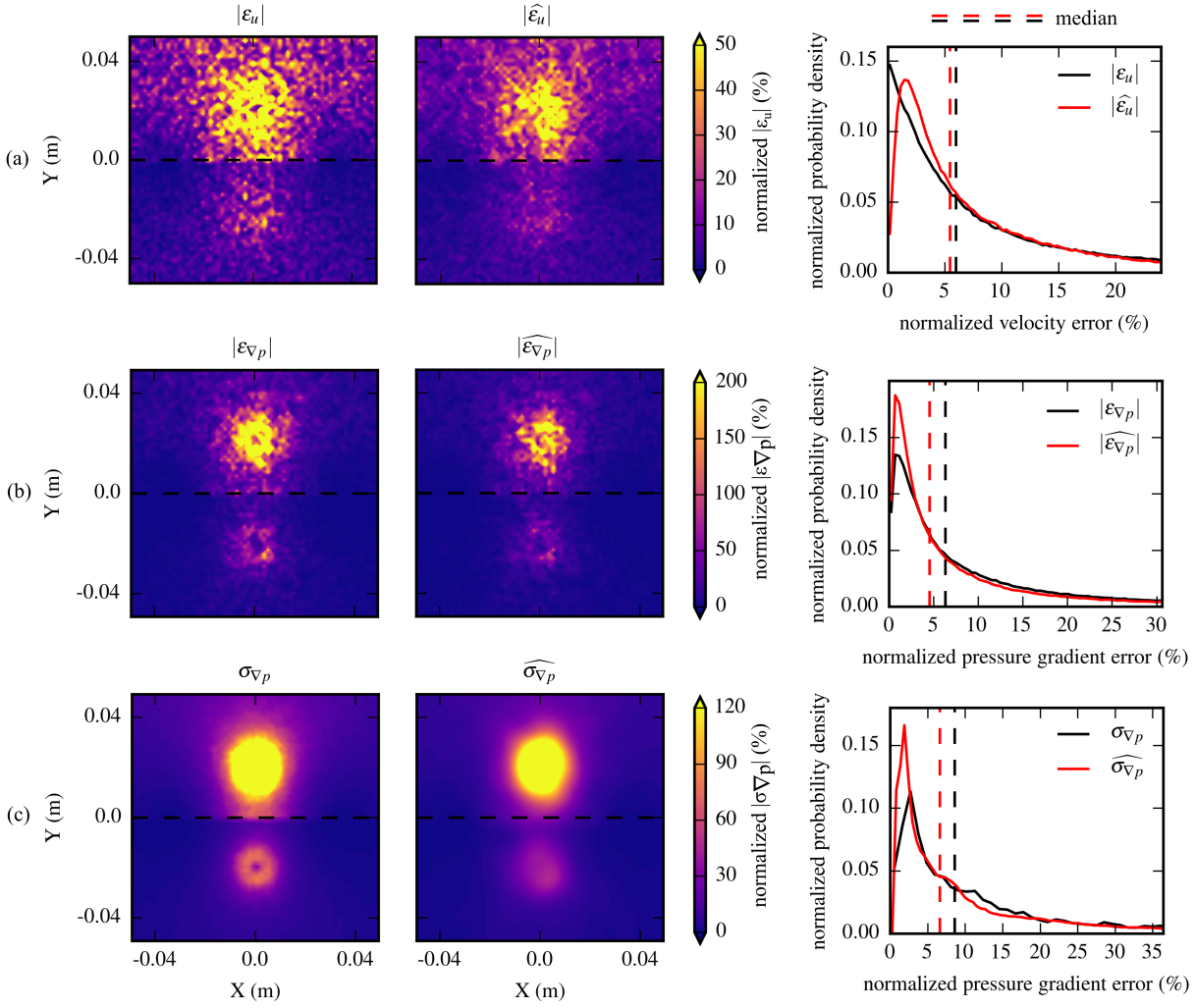

Figure 3.3 Examples of the estimated error distributions compared with the exact error distributions from the SVND case with λ_{top} being 32% and λ_{bottom} being 8% for the 2D vortex ring flow. The first two columns are the spatial distributions. The last column shows histograms of error magnitudes. The dashed vertical lines represent the medians of the distributions. (a) Comparison between exact velocity error magnitudes and estimated velocity error magnitudes. (b) Comparison between exact pressure gradient error magnitudes and estimated pressure gradient error magnitudes. (c) Comparison between the pressure gradient uncertainties and the WSTD of the estimated pressure gradient errors.

Pressure error analysis

The errors in the pressure fields reconstructed using Poisson and WLS were analyzed and compared. Pressure errors (ϵ_p) were quantified as the deviation between the reconstructed pressure and the exact pressure. ϵ_p and ϵ_u were normalized by the RMS of the exact pressure field and

velocity field, respectively. The distributions of velocity and pressure error magnitudes are shown in Figure 3.4 for three cases with λ_{bottom} being 8% while λ_{top} being 8%, 32%, and 64%. The spatial distributions in Figure 3.4 presents the RMS of normalized errors from all time frames. As suggested by both the spatial distributions and the histograms, the pressure error magnitudes for WLS ($|\epsilon_{p,WLS}|$) were lower than those for Poisson ($|\epsilon_{p,Poisson}|$). The medians of $|\epsilon_{p,WLS}|$ and $|\epsilon_{p,Poisson}|$ were 0.8% and 1.2%, respectively, with λ_{top} being 8%, 1.6% and 3.6% with λ_{top} being 32%, and 2.4% and 8.3% with λ_{top} being 64%.

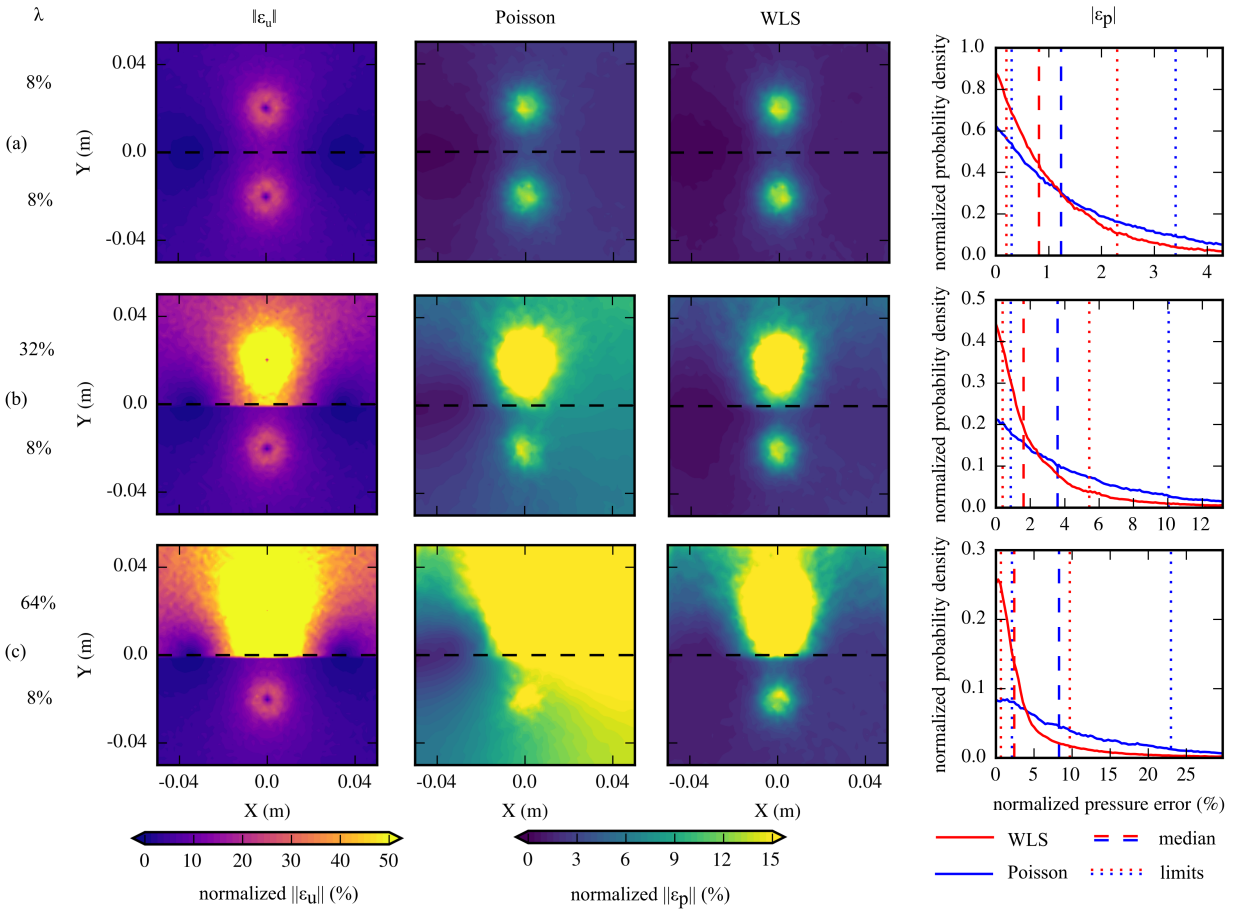

Figure 3.4 The spatial distributions of normalized velocity error magnitudes (1st column), normalized pressure error magnitudes (2nd and 3rd columns), and the histograms of normalized pressure error magnitudes (last column) for three test cases of the 2D vortex ring flow. The errors were normalized by the RMS of the exact fields. The vertical dashed lines in the histograms are medians of the distributions. The vertical dotted lines are the lower and upper limits of pressure error magnitudes. (a) $\lambda_{top} = 8\%$, $\lambda_{bottom} = 8\%$. (b) $\lambda_{top} = 32\%$, $\lambda_{bottom} = 8\%$. (c) $\lambda_{top} = 64\%$, $\lambda_{bottom} = 8\%$.

The performances of the pressure reconstruction methods are compared in Figure 3.5 (a) using results from all test cases with UND. The velocity error level for each case was determined as the median of the normalized velocity error magnitudes. As λ changed from 1 to 51%, the velocity error ranged from 0.39 to 19.9%. Similarly, the pressure error levels were determined as the median of the normalized pressure error magnitudes. For the noise level range used here, the pressure error for WLS increased from 0.10 to 6.0%, while it increased from 0.15 to 9.9% for Poisson. Thus, WLS maintained a 50% improvement on median pressure error over Poisson. Additionally, the lower and upper limits of the pressure errors were given as the 15.75th and 84.25th percentiles of the absolute error distribution, respectively. The upper limit for WLS increased from 0.28 to 17.3%, while it increased from 0.40 to 27.3% for Poisson. The lower limit for WLS increased from 0.025 to 1.44%, while it increased from 0.037 to 2.39% for Poisson.

Figure 3.5 (b) compares the error levels for the two methods from all cases with SVND. As λ_{top} changed from 8 to 64% and λ_{bottom} stayed at 8%, the overall velocity error level increased from 3.1 to 7.9%. The pressure error for WLS increased from 0.8 to 2.4%, while the it increased from 1.2 to 8.3% for Poisson. The lower error limit ranged from 0.2 to 0.6% for WLS and from 0.3 to 2.1% for Poisson. The upper limit ranged from 2.4 to 9.7% for WLS and from 3.4 to 23.0% for Poisson. In addition to the overall pressure error level, the pressure error level within each half of the field was quantified and presented in Figure 3.5 (c) and (d), respectively. The pressure error level in the top half ranged from 0.8 to 4.9% for WLS and from 1.2 to 11.4% for Poisson, while that in the bottom half ranged from 0.8 to 1.4% for WLS and from 1.2% to 6.4% for Poisson.

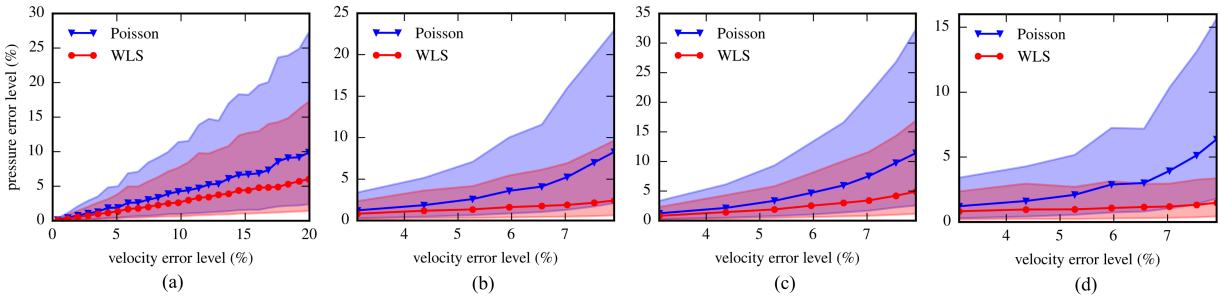

Figure 3.5 The pressure error level versus velocity error level from the test cases of the 2D vortex ring flow. The error levels were determined as the medians of error magnitudes. The shaded areas are bounded by the upper and lower limits of pressure error magnitudes. (a) Results from UND cases with λ changing from 1% to 51%. (b) Results from SVND cases with λ_{top} changing from 8% to 64% and λ_{bottom} being 8%. (c) Pressure error levels in the top half of the flow fields shown as a function of velocity error levels for SVND cases. (d) Pressure error levels in the bottom half of the flow fields for SVND cases.

3.3.2 2D Pulsatile flow

The pressure fields were calculated from velocity fields for all cases using Poisson and WLS. Velocity and pressure errors were quantified by comparing to the analytical solutions. Figure 3.6 (a) shows the pressure error levels as a function of the velocity error levels for results at 4 temporal phases. The velocity error level was evaluated as the median of the absolute velocity errors at all grid points normalized by u_{max}. The pressure error level was the median of the absolute pressure errors at all grid points, and the pressure error limits were 15.75th and 84.25th percentiles. The pressure scale employed for the normalization was given as $\frac{1}{2}\rho u_{max}^2$ which was the dynamic pressure based on u_{max}. As λ changed from 1 to 51%, the velocity error level increased from 0.3 to 15.3%. The ranges of pressure error levels were different at different phases. At peak systole (t/T=0.25), the pressure error level for Poisson increased from 0.6 to 40.6% and it increased from 0.7 to 20.1% for WLS. WLS reduced the pressure error level by around 100% for cases with velocity errors greater than 10%. At peak diastole, both methods accurately estimated the pressure fields as the pressure error levels were less than 3% for all cases.

Figure 3.6 (b) shows the pressure and velocity error distributions as a function of Y (spanwise direction) for the case of $\lambda = 33\%$ with a velocity error level of 9.9%. WLS improved

the pressure accuracy significantly in regions with lower velocity error level (near the walls). Figure 3.6 (c) compares the statistical distributions of the pressure error magnitudes by the two methods for the same case. The medians of $|\epsilon_{p,WLS}|$ and $|\epsilon_{p,Poisson}|$ were 4.2% and 6.8%, respectively.

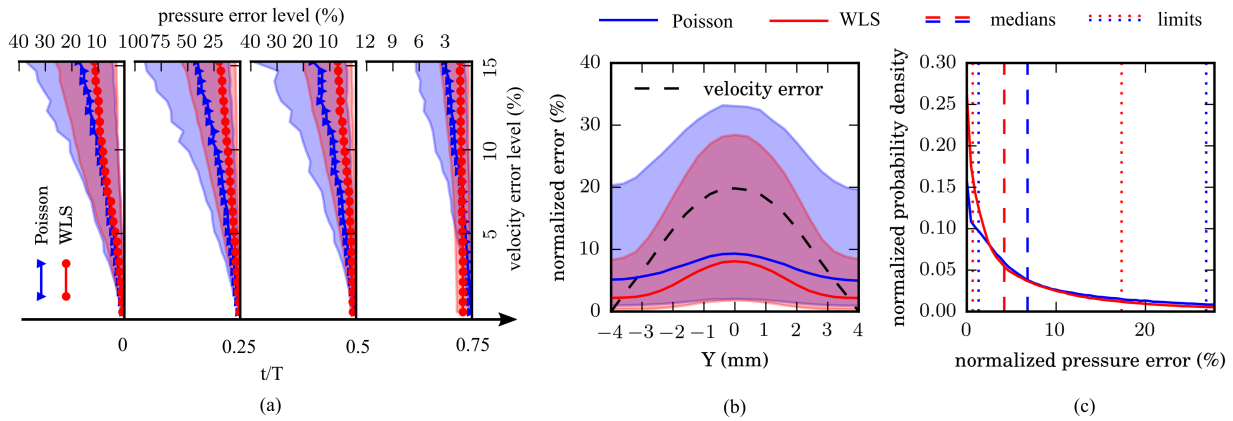

Figure 3.6 (a) The pressure error level versus velocity error level from the test cases of 2D pulsatile flow at four time phases. The error levels were determined as the medians of normalized error magnitudes. The shaded areas are bounded by the upper and lower limits of pressure error magnitudes. (b) The normalized error distributions of velocity and reconstructed pressure fields as a function of y (spanwise) for the case of λ=33% (velocity error level at 9.9%). (c) Histograms of the pressure error magnitudes for the two methods from the case of λ=33%. The vertical dashed lines represent the medians and the vertical dotted lines are the error limits.

3.3.3 In vivo 4D Poiseuille flow

The analytical velocity field is shown in Figure 3.7 (a) together with a time frame from the measured velocity data. Figure 3.7 (b) compares the velocity errors (ϵ_u) evaluated as the deviations between the analytical velocity and measured velocity with the velocity errors estimated based on velocity divergence ($\widehat{\epsilon_u}$). The error magnitudes were normalized by the centerline velocity of the analytical field. For both ϵ_u and $\widehat{\epsilon_u}$, the magnitudes were greater near the wall or close to the ends of the pipe.

Instantaneous pressure fields were reconstructed using Poisson and WLS from the measured velocity fields. The origin (r=0 mm, z=0 mm) was selected as the reference point with zero pressure. The pressure errors were evaluated as the deviation between analytical pressure and

reconstructed pressure, then normalized by the analytical pressure drop across the measurement region ($\Delta p_{analytical}$). Spatial distributions of the normalized pressure error magnitudes are presented as functions of r and z in Figure 3.7 (c). The pressure in the middle region of the pipe had significantly lower error when using WLS. To confirm this notion, the histograms of the relative pressure error magnitudes are shown in Figure 3.7 (d). The median of pressure error magnitude was 24.6 % for WLS and 35.6% for Poisson. The lower error limit was 7.8 % for WLS and 11.2% for Poisson. The upper error limit was 53.1% for WLS and 64.5% for Poisson.

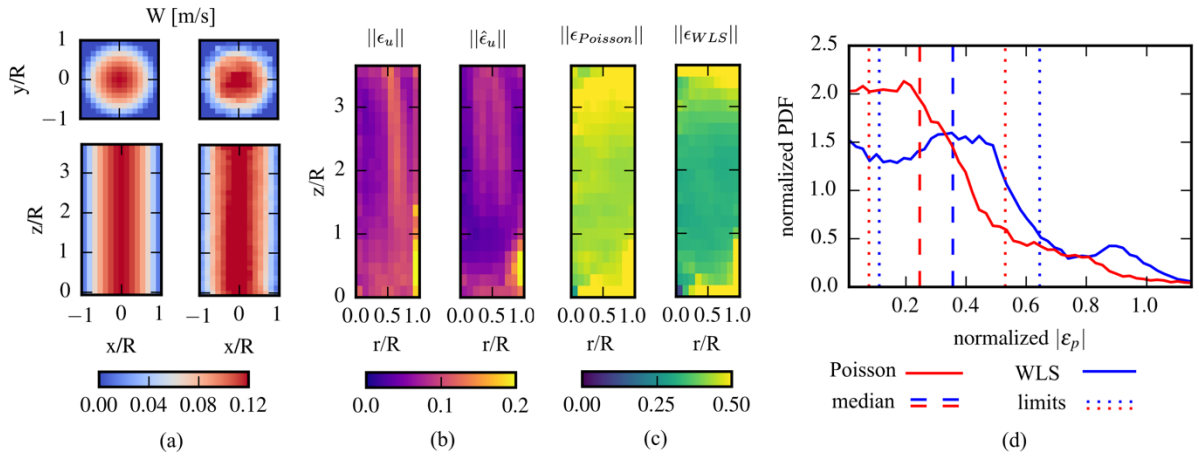

Figure 3.7 (a) The velocity profiles of laminar pipe flow from analytical solution (left) and measurement (right). The velocity profiles are shown on x-y plane at z=0 mm and on x-z plane at y=0 mm. (b) The spatial distributions of normalized velocity errors shown as functions of r and z. (c) The spatial distributions of normalized pressure errors for Poisson and WLS. (d) Histograms of the pressure error magnitudes from the pressure fields reconstructed using Poisson and WLS.

3.3.4 Patient specific aneurysmal flow

The velocity fields at peak systole are presented using 3D pathlines in Figure 3.8 (a) and 2D contours with arrows in Figure 3.8 (b) for the *in vivo* 4D flow and *in vitro* PTV data. The pressure fields reconstructed from the PTV data at peak systole using WLS are given in Figure 3.8 (c). Suggested by the 3D pathlines, the flow structures of the 4D flow and the PTV datasets are consistent for each aneurysm. For the basilar tip aneurysm, the inflow comes from the basilar artery and forms a vortical structure in the aneurysmal sac. For ICA aneurysm, the inflow comes from the curving ICA. Some of the flow enters the aneurysmal sac and forms the vortical flow

structure inside before exiting through the distal ICA. The comparisons for the inflow rate and waveform were made across all modalities of the two aneurysms (Brindise et al., 2019). The flow rate values, and general waveform trends showed reasonable agreement. However, the PTV data was obtained with higher spatiotemporal resolution and was contaminated with less noise for both aneurysms. For the basilar tip aneurysm, the average flow rate error (difference between inflow and outflow flow rates normalized by the maximum flow rate for each modality) was 24.0% for the 4D flow data, and 6.9% for the PTV data. For the ICA aneurysm, the average flow rate errors were 17.3 and 3.6% for 4D flow and PTV, respectively. The lower average flow rate errors suggest better accuracy for PTV. The limited spatial resolution of the 4D flow MRI acquisition resulted in under-resolved velocity profiles and a lack of pathlines in the basilar and ICA aneurysms (Fig. 8a). As demonstrated in (Hofinan et al., 1995), at least 5-6 voxels across vessel diameter are required for accurate flow quantification. There were less than 4 image voxels across the basilar artery (Fig. 8b), which reduced the accuracy of velocity measurements and the subsequently computed flow metrics. In addition, a low MR signal region was identified in the ICA upstream of the aneurysmal sac, which also contributed to the discontinuity of the pathlines in Figure 3.8 (a) and the low velocity region in Figure 3.8 (b). These factors would cause greater errors in velocity fields as well as reconstructed pressure fields in those regions of 4D flow data.

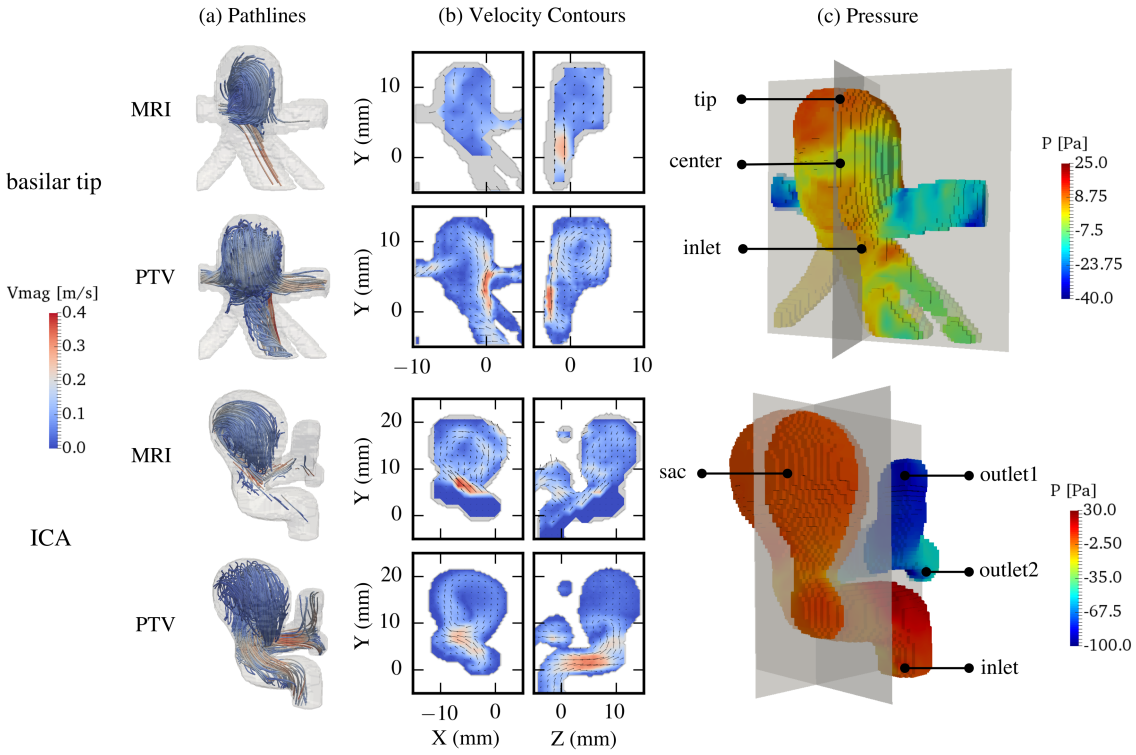

Figure 3.8 (a) Velocity fields at peak systole represented using 3D pathlines from *in vivo* 4D flow MRI and *in vitro* PTV measurements for the basilar tip aneurysm and the ICA aneurysm. Shaded regions represent the geometries of the aneurysms. (b) Velocity fields on orthogonal slices represented using 2D contours with arrows. One arrow was drawn for each voxel from 4D flow data, while each arrow represents the velocity of 9 voxels for PTV data. (c) The pressure fields reconstructed using WLS method from PTV data. The planes correspond to the locations of the slices in (b).

As the flow structures are consistent, similar pressure fields are anticipated for the *in vivo* data and *in vitro* data. Thus, even given the noisy and under-resolved *in vivo* 4D-flow data, a robust pressure reconstruction method should be capable of obtaining similar pressure fields to those reconstructed from the *in vitro* PTV data. Pressure fields were reconstructed from each dataset using WLS and Poisson for each aneurysm. Figure 3.9 compares the time series of pressure differences between several pairs of spatial points within the flow field. The locations of the points were labeled in Figure 3.8 (c). The discrepancies between the pressure differences of the three modalities were quantified for each pair of points and for each method. The RMS of the discrepancies was calculated and presented in Table 3.2. WLS reduced the RMS discrepancies for most locations, with some reductions being more than 100%. The lower RMS discrepancies suggested better consistency between the pressure results from different modalities for WLS. The

reduced signal in the 4D flow measurements of the ICA affected the calculated pressure difference between the inlet and sac shown in Figure 3.9 (b). Poisson overpredicted the pressure difference greatly, while WLS underestimated the pressure difference due to the low velocity caused by reduced signal in the ICA. WLS reduced the RMS discrepancy by 135% for this pair of locations. In general, WLS was more robust to velocity errors and the calculated pressure fields were more consistent with the measured flow field.

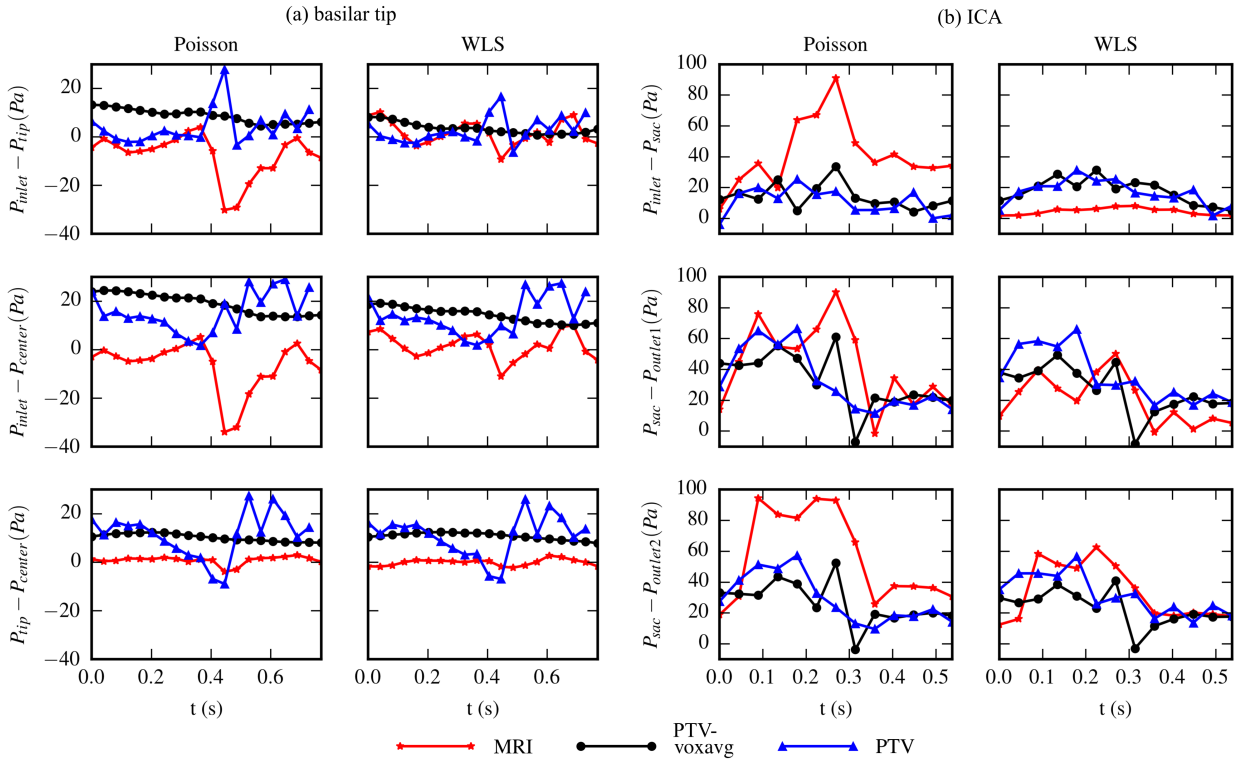

Figure 3.9 The time series of pressure differences between several points within the flow field. The pressure fields were reconstructed using the two methods from the datasets of basilar tip aneurysm (a) and ICA aneurysm (b). The locations of the points are given in Fig. 8(c).

Figure 3.10 compares the spatial distributions of pressure within the aneurysmal sacs from the in vivo 4D flow data and in vitro PTV and PTV-voxavg data. For 4D flow data, the pressure near the wall was not calculated due to the low signal intensity in near-wall voxels such that those measurements were less reliable. In addition, the pressure in the small branches were not calculated due to the insufficient number of voxels to perform the numerical differences. Thus, the pressure in these regions was not included in the following comparisons with pressure calculated from in

vitro data. The spatial distributions were shown on the 2D planes whose locations were given in Figure 3.8 (c). The pressure fields were normalized by the maximum pressure difference within the aneurysmal sac (Δp_{max}) from each modality. Additionally, the probability density function (PDF) histograms of the reconstructed pressure values in the aneurysmal sac from the entire cardiac cycle are shown in Figure 3.10. For the basilar tip aneurysm given in Figure 3.10 (a), WLS showed better agreement across all datasets than Poisson in both the spatial distributions as well as the histograms. The median pressure values by Poisson were –0.4 Pa for 4D flow, –8.9 Pa for voxavg, and –7.1 Pa from PTV. The median values obtained using WLS were –4.1 Pa for 4D flow, –4.7 Pa for PTV-voxavg, and –5.5 Pa for PTV. The standard deviation of the medians was 3.7 Pa for Poisson and 0.6 Pa for WLS. This indicates that WLS maintained a tighter spread of the pressure values and more similarity across modalities, suggesting it is more robust to low-resolutions and high-noise velocity fields. To quantify the amount of change made by WLS compared to Poisson on the reconstructed pressure fields from each modality, the deviations between the pressure fields reconstructed by WLS and the pressure fields reconstructed by Poisson were quantified and normalized by Δp_{max}. The total RMS of the normalized deviations was defined as the "effectiveness" of WLS on improving pressure reconstruction for each modality. The effectiveness was 28.7% for 4D flow, 17.9% for PTV-voxavg, and 8.7 % for PTV. For the ICA aneurysm given in Figure 3.10 (b), the median pressure value by Poisson was 0.06 Pa for 4D flow, 0.24 Pa for PTV-voxavg, and 0.52 Pa for PTV. The median by WLS was -0.07 Pa for 4D flow, 0.47 Pa for PTV-voxavg, and 0.25 Pa for PTV. The standard deviation of the medians was 0.19 Pa for Poisson and 0.22 Pa for WLS. The effectiveness of WLS was 34.2% for 4D flow, 6.8% for PTV-voxavg, and 11.9% for PTV.

Table 3.2 RMS discrepancies of pressure differences (Pa)

Basilar tip	Locations	Inlet - tip	Inlet - center	Tip - center
	Poisson	9.1	13.3	6.3
	WLS	3.8	7.6	6.5
ICA	Locations	Inlet - sac	Sac – outlet1	Sac – outlet2
	Poisson	16.7	13.2	18.3
	WLS	7.1	11.0	9.9

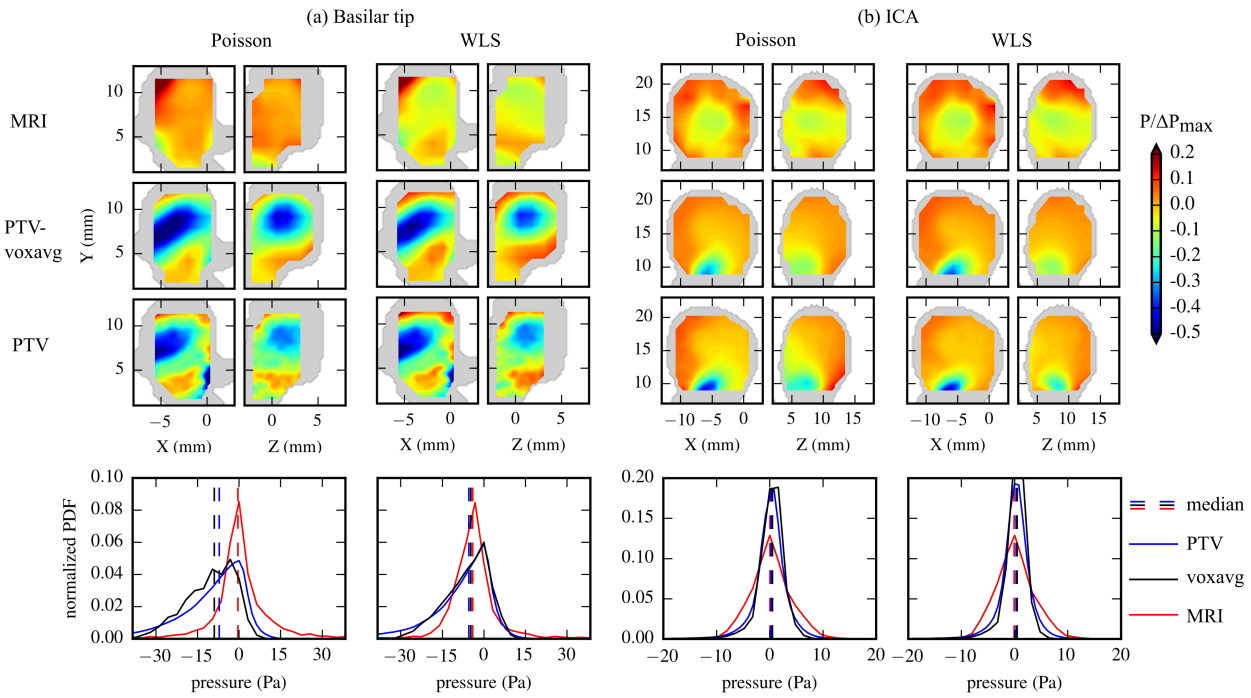

Figure 3.10 Spatial and probability density distributions of pressure fields within the aneurysm sacs reconstructed using Poisson and WLS from each modality of the basilar tip aneurysm (a) and the ICA aneurysm (b). The spatial distributions are presented by the normalized pressure values on a x-y plane and a y-z plane cutting through the aneurysm sac at peak systole. Locations of the planes are given in Fig. 8(c). Shaded regions correspond to the geometry of the aneurysm. The probability distributions are evaluated using the values on all grid points at all cardiac phases within the aneurysm sac.

3.4 Discussion

In this study we introduced a method which uses weighted least-squares for pressure integration. By assigning lower weights to less accurate velocity measurements and thus pressure gradient values, the WLS method reduces the effects of noisy measurements during the spatial integration, and improves the accuracy of the reconstructed pressure. Poisson and OLS can be seen as particular cases of WLS with uniform weights assigned to the pressure gradients. Compared to Poisson, the improvement made by WLS was a combination of the noise mitigation and the differences in the basic equations. However, the exact contribution of each aspect was not well understood, which is a limitation of this study. The accuracy of WLS relies on proper weight assignment. In this study, the weights were informed by the estimated velocity errors based on velocity divergence. Comparisons between exact velocity error and estimated velocity error

demonstrated that the velocity error estimation algorithm used here was capable of recognizing high-error regions such that lower weights were assigned to the less accurate pressure gradients in these regions. Although the velocity and pressure gradient error magnitudes were found to be slightly underestimated by this algorithm, this is not expected to affect the performance of WLS. This is because underestimating the error magnitudes would have a similar effect as normalizing the weights by a constant greater than 1. Further, the weight matrix W appears on both sides of (6), therefore the weights can be normalized by any arbitrary nonzero, real constant while the pressure results remain the same. Thus, the spatial distribution of the estimated error is primarily what effects the accuracy of WLS as opposed to the error values themselves. It should also be noted that the weights can be informed by the pressure gradient reliabilities estimated using other algorithms. For velocity fields measured using PIV, there are algorithms to estimate the spatial distributions of velocity uncertainties (Bhattacharya, Charonko, & Vlachos, 2018; Xue, Charonko, & Vlachos, 2015) and the pressure gradient uncertainties (Azijli, Sciacchitano, Ragni, Palha, & Dwight, 2016a). However, a corresponding algorithm for 4D-flow data has not been developed. The divergence-based algorithm employed in this study can be applied to velocity data measured from incompressible flows regardless of the measurement modality.

The WLS method reduces the spatial propagation of errors during pressure integration. From the spatial distributions of pressure errors for the synthetic Lamb-Oseen vortex flow in Figure 3.4, it can be observed that WLS reduced pressure errors in the ambient regions as the greater errors were more confined to the vortices. In addition, $|\epsilon_{p,WLS}|$ in the bottom half of SVND cases was significantly less affected by the increase of λ_{top} as compared with $|\epsilon_{p,Poisson}|$. As observed in Figure 3.5 (d), as λ_{top} increased from 8% to 64% and λ_{bottom} stayed at 8%, the increase of the pressure error in the bottom half was 433% for Poison while only 75% for WLS. From the spanwise distributions of pressure errors for the 2D pulsatile flow in Figure 3.6 (b), WLS reduced pressure errors in the near-wall regions significantly as the greater errors were more confined around the centerline. This is also suggested by the spatial distributions of pressure errors from *in vitro* Poiseuille flow in Figure 3.7 (b) and (c). WLS confined the pressure errors to the regions with greater velocity errors (near the ends of the pipe) compared with Poisson. In previous studies, the spatial error propagation was reduced by segmenting the flow field into subdomains based on local velocity reliability, then reconstructing the pressure field in each subdomain sequentially in a descending order of reliability (Jeon et al., 2018). However, such an algorithm requires that the

different levels of measurement reliability are spatially separable in the flow field such that the subdomains can be properly segmented. The WLS method proposed here does not require any segmentation, making it more usable across a larger variety of flow fields.

Improvement on pressure accuracy by WLS was more significant for velocity data with a greater range of errors. Results from synthetic Lamb-Oseen vortex flow fields demonstrated that the improvement by WLS was more significant for SVND cases with greater λ_{top}. Given in Figure 3.5(b), the pressure error level for Poisson was 240% larger than that for WLS with λ_{top} of 64%, and 50% when λ_{top} was 8%. This was also reflected by the results from the aneurysmal flows. Among the three datasets of the basilar tip aneurysm, the *in vivo* 4D flow data contained the widest range of velocity errors. The pressure fields reconstructed from 4D flow data using WLS were more consistent with the observed flow structure compared with Poisson as suggested by Figure 3.10 (a). Specifically, the center of the aneurysmal sac was expected to be a low-pressure region given the vortical flow in that region, and the high-pressure regions were expected to be near the inlet and the tip of the aneurysmal sac based on the flow deceleration. These anticipated distributions were observed using WLS, but not using Poisson. However, the pressure fields reconstructed from the *in vitro* datasets using the two methods were all consistent with the expected pressure distribution. The corresponding effectiveness of WLS was highest (28.7%) for 4D flow data compared with other datasets (17.9% for PTV-voxavg and 8.7% for PTV). For the ICA aneurysmal flow, the effectiveness of WLS was also higher (34.2%) for 4D flow data compared to other datasets (6.8% for PTV-voxavg and 11.9% for PTV). Overall, the analyses here suggest that WLS improved the pressure reconstruction from less accurate velocity data as compared to the Poisson method.

The improvement by WLS was more significant at time points with greater flow rates for pulsatile flows. Given in Figure 3.6 (a), WLS reduced the pressure error levels at peak systole by around 100% for 2D pulsatile flow cases with velocity errors greater than 10%, and the error reduction by WLS was not as significant at other phases. At peak diastole with the lowest flow rate, both methods were able to calculate the pressure accurately. This was also suggested by the results from the aneurysmal flows given in Figure 3.9. WLS improved the pressure differences of 4D flow effectively at time points around peak systole (0.45 s for basilar tip aneurysm, 0.25 s for ICA aneurysm) reflected by the reduction in the discrepancy between the results across modalities.

A limitation of this study is that no benchmark pressure was available for the comparison between the pressure fields reconstructed from the aneurysm flow data and, therefore, the errors in the reconstructed pressure fields could not be quantified. A comparison of the reconstructed pressure to a direct pressure measurement would improve the WLS pressure accuracy assessment and will be explored in future work. Instead, we could only compare the pressure fields calculated from *in vivo* data and *in vitro* data based on the notion that the pressure fields should be similar as the flow structures are consistent. Although the *in vivo* and *in vitro* flow data were found to be in good agreement (Brindise et al., 2019), they were not exactly the same and thus the pressure fields could maintain inherent differences. As given in Figure 3.10(b), the spatial distributions of pressure within the aneurysmal sac of the ICA aneurysm suggested a clear discrepancy between 4D flow and PTV.

There are also several limitations of the WLS pressure reconstruction method. The error estimation algorithm employed in this study can only be applied to incompressible flows as the divergence-free assumption is invalid for compressible flows. In addition, the algorithms for error estimation and pressure gradient calculation are only applicable to velocity data which fully resolves the gradients along all dimensions. For 3D flows, volumetric data with all 3 velocity components are required. 2D planar velocity data or 3 velocity components captured on a 2D plane measured from 3D flow would not be sufficient because the velocity gradient perpendicular to the measurement plane is not resolvable. However, this algorithm can be applied to 2D planar data if the flow is uniform along the perpendicular dimension, such as the 2D synthetic flows employed in this study. Another limitation of WLS is that the velocity data need to be temporally and spatially resolved to ensure accurate derivative evaluation. The pressure in small vessel branches (less than 3 voxels across the lumen diameter) cannot be estimated due to the insufficient number of voxels for numerical difference. However, this is a limitation for most pressure reconstruction methods.

3.5 Authors' contributions

J.Z. developed and evaluated the method, performed the data analysis, and drafted the manuscript. M.C.B and S.M.R performed the in vitro measurement and pre-processed the data. S.S., M.M., and D. S. obtained and pre-processed the *in vivo* data. V.L.R. and P.P.V. designed and oversaw the study and all data analysis. All authors critically reviewed and edited the manuscript, and gave final approval for publication.

4. WALL SHEAR STRESS ESTIMATION FOR 4D FLOW MRI USING NAVIER-STOKES EQUATION CORRECTION

4.1 Background and literature review

Vascular wall shear stress (WSS) is an important determinant of endothelial function and phenotype (Malek, Alper, & Izumo, 1999). WSS has emerged as an essential feature of atherogenesis (Cecchi et al., 2011; Cunningham & Gotlieb, 2005). The low WSS due to disturbed blood flow promotes atherogenesis (Cecchi et al., 2011; Chiu & Chien, 2011), while high WSS is associated with plaque rupture (Groen et al., 2007). Abnormal WSS is also related to the growth and rupture of intracranial aneurysms (Boussel et al., 2008; Castro, Putman, Sheridan, & Cebral, 2009; Jou, Lee, Morsi, & Mawad, 2008; Meng et al., 2014). Additionally, WSS and WSS-derived metrics such as oscillatory shear index (OSI) are correlated with aortopathy. The distribution of low WSS and high OSI resembles the regions of aortic atherosclerotic lesions (Frydrychowicz et al., 2009; Michael Markl et al., 2013), and the abnormal WSS in the Bicuspid Aortic Valve (BAV) patients was associated with the aortic dilation (Barker, Lanning, & Shandas, 2010; Barker et al., 2012; van Ooij et al., 2015). Therefore, the information on the magnitude, distribution, and variation of WSS can provide valuable insights for predicting and assessing vascular diseases.

WSS can be estimated from the velocity gradient at the vascular wall. 4D flow magnetic resonance imaging (MRI) resolves blood flow in space and time *in vivo*, enabling the estimation of WSS (Michael Markl et al., 2012; Stankovic et al., 2014). Stalder *et al.* (Stalder et al., 2008a) introduced a method to evaluate the aortic WSS from the B-spline interpolation of the 4D flow velocity on manually positioned 2D planes. However, this method only resolves the WSS on the 2D slices, and the plane selection can be laborious. Several methods were introduced later to resolve the 3D WSS distribution on the vessel wall from the velocity profile along the wall-normal direction at each wall point (Bieging et al., 2011; Boussel et al., 2009; Potters, Van Ooij, Marquering, VanBavel, & Nederveen, 2015). The method proposed by Potters *et al.* (Potters et al., 2015) uses smooth spline fitting of the velocity along the wall-normal direction and assumes no-slip boundary condition to evaluate the velocity gradients and WSS. The method has been applied to 4D flow data acquired in the aorta (Potters et al., 2015; van Ooij et al., 2015), carotid arteries (Cibis et al., 2016; Potters et al., 2015), and intracranial aneurysms (Van Ooij et al., 2013).

The accuracy of the WSS estimated from 4D flow data is affected by the spatial resolution and segmentation (Cibis et al., 2016; Perinajová, Juffermans, Mercado, et al., 2021; Potters et al., 2015). A significant inverse relationship was found between the estimated WSS and the spatial resolution of 4D flow data (Cibis et al., 2016). The WSS estimated from *in vivo* 4D flow MRI was inconsistent with the results from high-resolution modalities, including computational fluid dynamics (CFD) and *in vitro* particle imaging velocimetry (PIV), potentially due to the limited resolution of MRI. The aortic WSS estimated from *in vivo* 4D flow data was 0-2 Pa (Barker et al., 2012; Stalder et al., 2008a; van Ooij et al., 2015), while patient-specific CFD models yielded a range of 0-30 Pa (Leuprecht, Kozerke, Boesiger, & Perktold, 2003; Perinajová, Juffermans, Westenberg, et al., 2021; Rinaudo & Pasta, 2014). The WSS estimated from 4D flow MRI was also lower than the CFD results in intracranial aneurysms and carotid bifurcations, and the differences were more significant in regions of higher WSS (Szajer & Ho-Shon, 2018). Several multi-modality studies showed that the mean WSS evaluated from *in vivo* 4D flow MRI in the intracranial aneurysms was less than half of the results from patient-specific CFD simulations and *in vitro* PIV measurements (Brindise et al., 2019; Van Ooij et al., 2013). Because of the discrepancy in WSS magnitudes, the normalized parameters such as the normalized WSS and OSI are usually preferred for clinical and physiological investigations as they possess qualitatively similar distributions between MRI and other modalities (Brindise et al., 2019; Perinajová, Juffermans, Mercado, et al., 2021; Szajer & Ho-Shon, 2018).

This study aims to introduce a method to enhance the WSS estimation with 4D flow MRI. The proposed method, termed pressure-gradient induced velocity-gradient correction (PG-VGC), corrects the velocity gradient based on the reconstructed pressure field gradient to improve the estimated WSS's accuracy. The conservation laws of mass and linear momentum are incorporated to formulate a linear system. This linear system is used to estimate the velocity-gradient errors with a least-squares approach. The error is then subtracted from the velocity gradient to improve the assessment of WSS. The method was first tested with synthetic 4D flow data of Womersley flow and flow in two cerebral aneurysms. The method was then applied to *in vivo* 4D flow data acquired in the cerebral aneurysms and aortas.

4.2 Materials and Methods

4.2.1 Wall shear stress estimation with Navier-Stokes equation correction

The WSS vector $\vec{\tau}$ can be calculated as:

$$\vec{\tau} = 2\mu\bar{\bar{\varepsilon}} \cdot \vec{n}, \qquad (4\text{-}1)$$

where μ is the dynamic viscosity of the blood, $\vec{n}$ is the inward wall-normal vector with a magnitude of 1, and $\bar{\bar{\varepsilon}}$ is the deformation or strain rate tensor. The WSS value represents the magnitude of $\vec{\tau}$ in this study, and the time-averaged WSS (TAWSS) denotes the WSS averaged arithmetically over a cardiac cycle. The deformation tensor can be expressed as:

$$\bar{\bar{\varepsilon}} = \frac{1}{2}\left(\overline{\overline{\nabla u}} + \left(\overline{\overline{\nabla u}}\right)^T\right), \qquad (4\text{-}2)$$

where $\overline{\overline{\nabla u}}$ is the velocity gradient tensor which can be determined from the velocity field of the blood flow using numerical differentiation or interpolation (Bieging et al., 2011; Boussel et al., 2009; Potters et al., 2015).

Figure 4.1 (a) presents the proposed WSS estimation procedure with PG-VGC. The velocity gradient and the pressure field are first calculated from the 4D flow data. The spatial gradient of the pressure field is employed to correct the velocity gradient based on the conservation of mass (COM) and conservation of linear momentum (COLM). The WSS is then determined from the corrected velocity-gradient. Figure 4.1 (b) demonstrates that PG-VGC uses the data in the whole region with blood flow (ROI) for estimating WSS. The details of the algorithm are provided as follows:

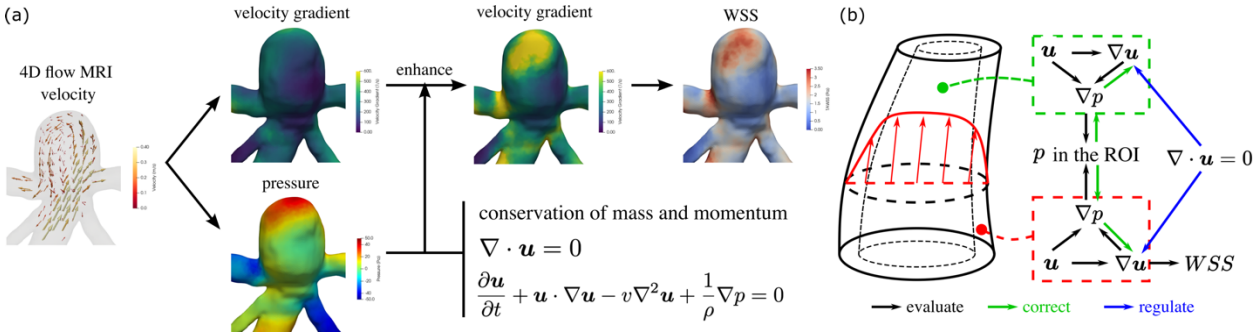

Figure 4.1 (a) The flow chart of the WSS estimation procedure with PG-VGC method. (b) The schematic demonstrates that the flow data in the whole region of interest (ROI) is used for enhancing the WSS estimation. The green box and red box indicate the data in the core-flow and near-wall regions, respectively.

Pressure reconstruction with wall-distance-based weighted least-squares

The wall points where the WSS is of interest and the center points of the 4D flow voxels within the blood flow are combined to a list of N spatial points. The instantaneous pressure gradients at these spatial points were estimated from the velocity field based on the COLM (Zhang, Brindise, et al., 2020) as:

$$\boldsymbol{\nabla_i p} = -\rho\left(\frac{\partial \boldsymbol{u_i}}{\partial t} + \boldsymbol{u} \circ G_x \boldsymbol{u_i} + \boldsymbol{v} \circ G_y \boldsymbol{u_i} + \boldsymbol{w} \circ G_z \boldsymbol{u_i}\right) + \mu\nabla^2 \boldsymbol{u_i}, \qquad (4\text{-}3)$$

where the subscript $i \in \{x, y, z\}$ indicates the spatial dimension. $\boldsymbol{\nabla_i p}$ is the column vector ($\in \mathbb{R}^{\boldsymbol{N}}$) of the pressure-gradient along each dimension at the spatial points. $\boldsymbol{u_x} \equiv \boldsymbol{u}$, $\boldsymbol{u_y} \equiv \boldsymbol{v}$, and $\boldsymbol{u_z} \equiv \boldsymbol{w}$ represent the column vectors ($\in \mathbb{R}^{\boldsymbol{N}}$) of the velocity component along each encoded direction. $\circ$ represents the Hadamard (elementwise) product, and ρ is the fluid density. The temporal derivatives of velocity were calculated using the second order central (SOC) difference scheme. G_x, G_y, and G_z are the discrete gradient operators (matrices) with a size of $N \times N$. The coefficients in the operators were determined using the RBF-generated finite difference method (RBF-FD) (G. B. Wright & Fornberg, 2006), which is a meshless computational method based on the localized RBF-interpolant in a compact finite-difference mode. The discrete Laplacian operator was generated from the gradient operators as:

$$\nabla^2 = G_x G_x + G_y G_y + G_z G_z. \quad (4\text{-}4)$$

The pressure field in the whole ROI was reconstructed by spatially integrating the pressure gradients with weighted least-squares (WLS) (Zhang, Brindise, et al., 2020) as:

$$\boldsymbol{p_{WLS}} = \underset{\boldsymbol{p}}{argmin}(\|\mathcal{W}(G\boldsymbol{p} - \boldsymbol{\nabla p})\|), \quad (4\text{-}5)$$

with $G = \begin{bmatrix} G_x \\ G_y \\ G_z \end{bmatrix}$ and $\boldsymbol{\nabla p} = \begin{bmatrix} \boldsymbol{\nabla_x p} \\ \boldsymbol{\nabla_y p} \\ \boldsymbol{\nabla_z p} \end{bmatrix}$,

where $\boldsymbol{p_{WLS}} \in \mathbb{R}^{\boldsymbol{N}}$ is the column vector containing the reconstructed pressure at the spatial points, $\|\cdot\|$ represents the L2 norm, and the weight matrix $\mathcal{W}$ is a diagonal matrix with a size of $3N \times 3N$. Each diagonal element of $\mathcal{W}$ corresponds to a spatial point and controls the influence of the pressure gradients at the point on the resulting pressure field. The weight was specified as:

$$w_{diag} = (w_{max} - w_{min})\frac{s}{s_{max}} + w_{min}, \quad (4\text{-}6)$$

with $w_{min} = 1$ and $w_{max} = 10$,

where $w_{diag} > 0$ is the diagonal element, s is the distance from the corresponding point to its closest wall point, s_{max} is the maximum s in the ROI and corresponds to the radius of the largest artery in the ROI, and w_{min} and w_{max} are the minimum and maximum weights, respectively. Equation (4-6) specifies the weights to increase linearly with the increase of the distance from the wall, therefore amplifying the effect of the core-flow pressure-gradient on the reconstructed pressure. It should be noted that the exact values of w_{min} and w_{max} do not affect the pressure result if the ratio w_{max}/w_{min} remains constant.

Pressure-gradient-induced velocity-gradient correction

The velocity gradient ($\overline{\overline{\nabla u}}$) evaluated from 4D flow data can be decomposed into a true component ($\overline{\overline{\nabla u}}_{true}$) and an error component ($\overline{\overline{\nabla u}}_{err}$) as:

$$\overline{\overline{\nabla u}} = \overline{\overline{\nabla u}}_{true} + \overline{\overline{\nabla u}}_{err}. \quad (4\text{-}7)$$

$\overline{\overline{\nabla u}}_{err}$ arises from the velocity measurement errors and gradient calculation. The COLM and COM can be expressed with the velocity gradient tensor as:

$$\frac{\partial \vec{u}}{\partial t} + \vec{u} \cdot \overline{\overline{\nabla u}} - \nu \nabla \cdot \overline{\overline{\nabla u}} + \frac{1}{\rho} \nabla p = 0, \quad (4\text{-}8)$$

$$\nabla \cdot \vec{u} \equiv \frac{\partial u}{\partial x} + \frac{\partial v}{\partial y} + \frac{\partial w}{\partial z} = \bar{\bar{I}} : \overline{\overline{\nabla u}} = 0, \quad (4\text{-}9)$$

where $\vec{u} = [u \quad v \quad w]^{\boldsymbol{T}}$ is the flow velocity vector, p is the pressure, ∇ represents the gradient operator, "$\nabla \cdot$" represents the divergence operator, and $\nu = \frac{\mu}{\rho}$ is the kinematic viscosity. $\bar{\bar{\mathrm{I}}}_{ij} = \delta_{ij}$ is the identity tensor, and ":" is the double dot product such that $\bar{\bar{\mathrm{I}}} : \overline{\overline{\nabla u}} = \delta_{ij}\overline{\overline{\nabla u}}_{ij}$. The left-hand-side of (4-8) and (4-9) can be nonzero because of $\overline{\overline{\nabla u}}_{err}$ and the errors in $\vec{u}$ and ∇p. Assuming that $\overline{\overline{\nabla u}}_{err}$ is the major source of error, the equalities of (4-8) and (4-9) can be achieved by replacing $\overline{\overline{\nabla u}}$ with $\overline{\overline{\nabla u}}_{true}$, and the following equations can be subsequently derived from (4-8) and (4-9) by substituting $\overline{\overline{\nabla u}}_{true}$ for $\overline{\overline{\nabla u}} - \overline{\overline{\nabla u}}_{err}$ according to (4-7) as:

$$(\vec{u} - \nu \nabla) \cdot \overline{\overline{\nabla u}}_{err} = \frac{\partial \vec{u}}{\partial t} + \vec{u} \cdot \overline{\overline{\nabla u}} - \nu \nabla \cdot \overline{\overline{\nabla u}} + \frac{1}{\rho} \nabla p, \quad (4\text{-}10)$$

$$\bar{\bar{I}} : \overline{\overline{\nabla u}}_{err} = \bar{\bar{I}} : \overline{\overline{\nabla u}}. \quad (4\text{-}11)$$

Equations (4-10) and (4-11) relate $\overline{\overline{\nabla u}}_{err}$ to the residuals of (4-8) and (4-9), respectively, and can be used to estimate $\overline{\overline{\nabla u}}_{err}$.

With the reconstructed pressure $\boldsymbol{p_{WLS}}$, the following linear system can be constructed based on (4-10):

$$[\boldsymbol{u} - \nu G_x \quad \boldsymbol{v} - \nu G_y \quad \boldsymbol{w} - \nu G_z] \begin{bmatrix} \boldsymbol{\nabla_x u_{i,err}} \\ \boldsymbol{\nabla_y u_{i,err}} \\ \boldsymbol{\nabla_z u_{i,err}} \end{bmatrix}$$

$$= \frac{\partial \boldsymbol{u_i}}{\partial t} + \boldsymbol{u} \circ G_x \boldsymbol{u_i} + \boldsymbol{v} \circ G_y \boldsymbol{u_i} + \boldsymbol{w} \circ G_z \boldsymbol{u_i} - \nu \nabla^2 \boldsymbol{u_i} + \frac{1}{\rho} G_i \boldsymbol{p_{WLS}}, \quad (4\text{-}12)$$

where the subscript $i \in \{x, y, z\}$ indicates the spatial dimension. $\boldsymbol{\nabla_x u_{i,err}} \in \mathbb{R}^{\boldsymbol{N}}$ is the column vector containing the errors in $\frac{\partial u_i}{\partial x}$, and this convention also applies to other velocity-gradient error terms. $G_i \boldsymbol{p_{WLS}}$ is the spatial gradient of the reconstructed pressure. Three linear systems can be constructed from (4-12) for the COLM along x, y, and z dimensions. A linear system for the COM can be formulated based on (4-11) as:

$$[I \quad I \quad I] \begin{bmatrix} \boldsymbol{\nabla_x u_{err}} \\ \boldsymbol{\nabla_y v_{err}} \\ \boldsymbol{\nabla_z w_{err}} \end{bmatrix} = G_x \boldsymbol{u} + G_y \boldsymbol{v} + G_z \boldsymbol{w}, \tag{4-13}$$

where I represents the identity matrix with a size of $N \times N$. The linear systems of (4-12) and (4-13) were combined to form a linear system with 4N equations and 9N unknown velocity-gradient errors. The combined linear system was solved with least-squares using the LSQR algorithm implemented in Python (Paige & Saunders, 1982b). The velocity gradients initially evaluated using the discrete gradient operators were corrected by subtracting the estimated velocity gradient errors, *e.g.*,

$$\boldsymbol{\nabla_x u_{corr}} = G_x \boldsymbol{u} - \boldsymbol{\nabla_x u_{err}}, \tag{4-14}$$

And the WSS was determined from the corrected velocity-gradient according to (4-1) and (4-2).

4.2.2 Aneurysmal flow acquisition and simulation

To test the proposed PG-VGC method with physiological flows, in vivo 4D flow MRI data were acquired in a basilar tip (BT) aneurysm at San Francisco VA Medical Center and an internal carotid artery (ICA) aneurysm at Northwestern Memorial Hospital with a 3T MRI scanner (Skyra, Siemens Healthcare, Erlangen, Germany). The 4D flow data were on Cartesian grids with the spatial resolution of $1.25 \times 1.25 \times 1.33\ mm^3$ for the BT aneurysm and $1.09 \times 1.09 \times 1.30\ mm^3$ for the ICA aneurysm. The temporal resolution was 40.5 ms (20 frames per cycle) and 44.8 ms (13 frames per cycle) for the BT and ICA aneurysms, respectively. The contrast-enhanced magnetic resonance angiography (CE-MRA) data was also acquired for the BT aneurysm with the spatial resolution of $0.7 \times 0.7 \times 0.7\ mm^3$. For the ICA aneurysm, non-contrast time of flight (TOF)

angiography was acquired with a spatial resolution of $0.4 \times 0.4 \times 0.6\ mm^3$. The CE-MRA and TOF images were segmented to create surfaces (STL) of the vessel wall. The wall points and wall-normal extracted from the STL surfaces were used for evaluating and analyzing the WSS. Approval of all ethical procedures and protocols was granted by the institutional review boards (IRB) at Purdue University, Northwestern Memorial Hospital, and San Francisco VA Medical Center.

Additionally, CFD simulations were performed using FLUENT 18.1 (ANSYS) with the created surfaces and the flow waveforms obtained from 4D flow data as the inflow and outflow boundary conditions. The flow was assumed to be laminar, incompressible, and Newtonian. The walls of the vessel were assumed to be rigid. The density and dynamic viscosity used for the simulations were $1060\ kg/m^3$ and $0.0035\ Pa \cdot s$. More details on the in vivo imaging and CFD simulations can be found in (Brindise et al., 2019).

4.2.3 In vivo aortic 4D flow MRI acquisition

In vivo 4D flow data were acquired in the aortas from three subjects to evaluate the performance of PG-VGC, including a patient with bicuspid aortic valve (BAV), a patient with tricuspid aortic valve and an aortic aneurysm (TAV-AA), and a health control subject with tricuspid aortic valve. The scans were performed in a sagittal oblique volume on a 1.5T scanner (MAGNETOM Avanto, Aera, Siemens, Erlangen, Germany) at Northwestern Memorial Hospital with prospective ECG gating and during free breathing. Gadolinium-based contrast (Magnevist, Ablavar, or Gadavist) were used for imaging the two patients, while no contrast was used on the control subject. The resolutions and scan parameters were presented in Table 4.1. The venc was 150 cm/s for the TAV-AA and control scans and 175 cm/s for the BAV scan. No velocity aliasing was observed. The patient data for this IRB approved study were retrospectively included with waiver of consent. The healthy control subject underwent a research cardiac MRI after written informed consent was obtained from the study participant. A static mask of the blood vessel was created for each dataset based on the magnitude image and the time-averaged velocity magnitude, which was manually corrected by an expert observer using Mimics (Materialise NV, Belgium). A smooth surface (STL) was then generated from the mask to represent the vessel walls. The wall points and wall-normal from the surfaces were used for estimating the WSS.

Table 4.1 The spatial and temporal resolutions, the number of cardiac timeframes (N_{time}), the flip angle, echo time (TE), and repetition time (TR) for the *in vivo* aortic scans

Subject	Voxel size (mm^3)	Δt (ms)	N_{time}	Flip angle (°)	TE/TR (ms)
TAV-AA	2.375×2.375×3	37.6	21	15	2.3/4.7
BAV	2.125×2.125×2.5	38.4	24	15	2.4/4.8
Control	2.375×2.375×2.4	38.4	21	7	2.5/4.8

4.2.4 Performance evaluation and WSS error analysis method

The proposed method's performance was first evaluated on synthetic 4D flow datasets of the analytical Womersley flow with varying Womersley number and spatial resolution as given in Appendix A, and the WSS from the analytical solution was employed as the "ground truth". Additionally, the method was tested on synthetic 4D flow datasets created based on the velocity fields from the CFD simulations of the cerebral aneurysms with the same spatial and temporal resolutions as the in vivo acquisition and a velocity-to-noise ratio (VNR) of 10%, and the WSS from the CFD was considered as the "ground truth".

The WSS error level of each test case was represented by the root-mean-square error (RMSE) evaluated as:

$$RMSE = \sqrt{\frac{\sum_{i=1}^{N_t}\sum_{j=1}^{N_{wall}}\left(WSS_{i,j}-WSS_{true,i,j}\right)^2}{N_t \times N_{wall}}}, \qquad (4\text{-}15)$$

where N_t and N_{wall} represent the number of timeframes and the number of wall points, respectively. The relative RMSE was determined as the RMSE normalized by the root-mean-square of the ground truth WSS.

To demonstrate the improvement by PG-VGC, the state-of-the-art method introduced by Potters et al. was employed in this study and referred to as “Spline” since it evaluates the WSS with the smooth-spline fitting of the velocity profile. WSS was also estimated using (4-1) and (4-2) from the uncorrected velocity gradients and was referred to as “Vgrads”. The accuracy of Spline and Vgrads was also assessed and compared to the PG-VGC method.

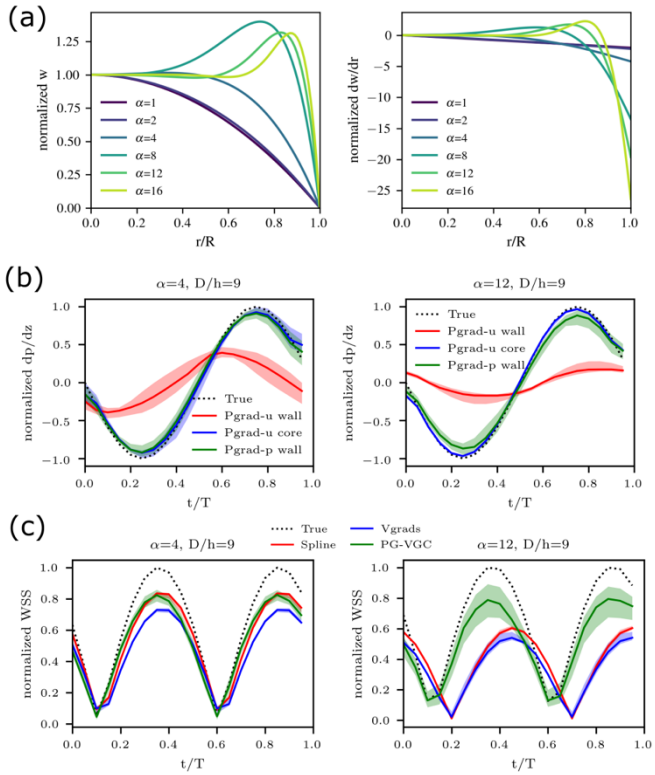

Figure 4.2 (a) The streamwise velocity and velocity gradient profiles for Womersley flow with different Womersley numbers (α). The velocity is normalized by the centerline velocity (w_{center}), and the velocity gradient is normalized by w_{center}/R. (b) The time-dependent median and interquartile range (IQR) of the streamwise pressure-gradient estimated at the wall points and in the core-flow region. Pgrad-u denotes the pressure gradient evaluated from the local velocity data, and Pgrad-p indicates the gradient of the reconstructed pressure field. The pressure gradients were normalized by the amplitude of the streamwise pressure-gradient from the analytical solution. (c) The time-dependent median and IQR of the WSS estimated from different methods in one flow cycle.

4.3 Results

4.3.1 Error analysis with synthetic 4D flow data

Figure 4.2 (a) presents the normalized streamwise velocity profile and the velocity gradient with respect to radius (dw/dr) at the peak flow rate from the analytical solutions of the Womersley flow with different Womersley number (α). With an increase of α, the shear layer became thinner leading to a steeper velocity gradient near the wall. Figure 4.2 (b) shows the time-dependent median of the streamwise pressure gradient (dp/dz) estimated from the flow data with α of 4 and 12 and a spatial resolution of D/9. The pressure gradient directly evaluated from velocity field with (4-3) is denoted as "Pgrad-u", while "Pgrad-p" represents the gradient of the reconstructed pressure field. The legends "wall" and "core" indicate the pressure gradient at the wall points and in the core-flow region with $r < 0.5R$, respectively. For both datasets, the Pgrad-u in the core-flow matched the true dp/dz with errors less than 0.1 for most timeframes, while the Pgrad-u at the wall deviated from the true solution by as much as 0.5 for $\alpha = 4$ and up to 0.8 for $\alpha = 12$. The Pgrad-p at the wall achieved similar accuracy as the Pgrad-u in the core-flow and was more reliable than the Pgrad-u at the wall. Figure 4.2 (c) compares the WSS estimated using different methods with the "ground truth" from the analytical solution, and the WSS was normalized by the amplitude of the true WSS. The Spline and PG-VGC methods estimated similar WSS results at $\alpha = 4$ and were more accurate than the estimation by Vgrads. With α=12, Spline and Vgrads underestimated the WSS amplitude by 40% with a phase shift of approximately 0.1 s, while PG-VGC underestimated the WSS amplitude by 20%.

Figure 4.3 presents the relative RMSE of the estimated WSS from the synthetic Womersley flow datasets with different α, grid resolution, and noise level. The cases with a grid resolution less than 0.5 mm or greater than 3.5 mm were uncommon in practical applications and were excluded from the analysis. The wedge area corresponds to the relative RMSE of each method, and the color on the wedge indicates the RMSE by Spline or Vgrads as compared to PG-VGC. A red wedge suggests higher RMSE by Spline or Vgrads than PG-VGC, while a blue wedge indicates that the WSS estimated by Spline or Vgrads were more accurate than PG-VGC. The proposed PG-VGC method yielded more accurate WSS for most datasets than Spline and Vgrads. Greater improvement was achieved by PG-VGC for higher α with more than 100% improvement at α of 12 and 16. The estimated WSS's accuracy was affected by the resolution and α. The 10% noise

led to slightly increased RMSE for several cases with relatively fine resolution as compared to the results without noise.

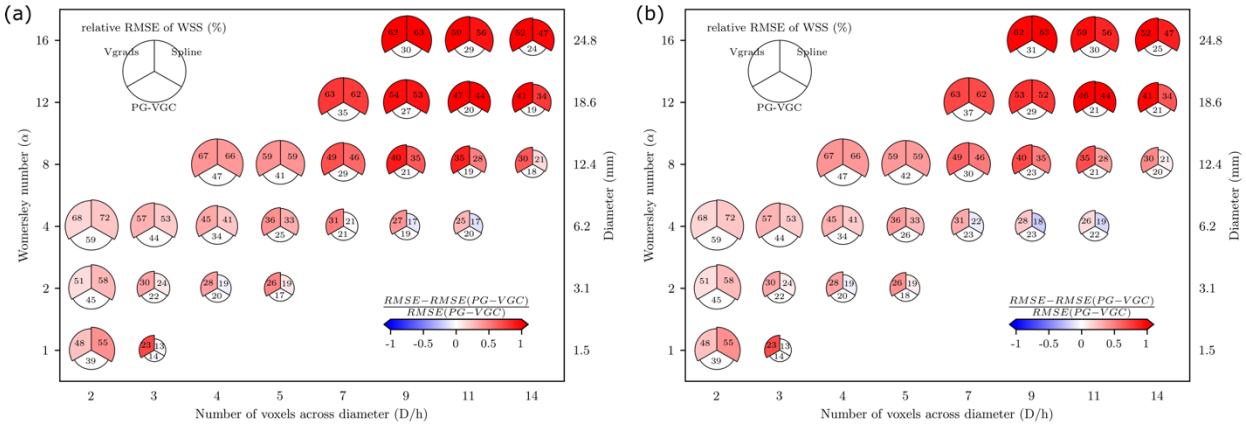

Figure 4.3 The relative RMSE of WSS estimated from synthetic Womersley 4D flow datasets with 0% noise (a) and 10% noise (b). The area of each wedge corresponds to the relative RMSE by each method, and the color scale indicates the comparison between the RMSE from Spline or Vgrads with PG-VGC as expressed by the formula over the colorbar.

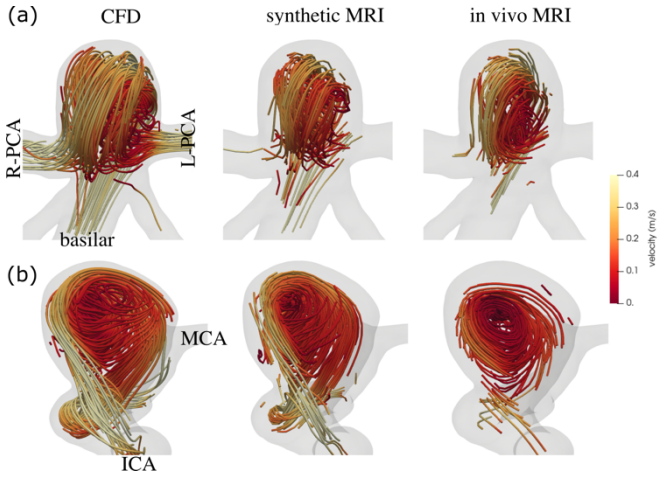

Figure 4.4 The velocity fields at peak systole of the BT (a) and ICA (b) aneurysms from CFD, synthetic MRI, and in vivo MRI.

4.3.2 Synthetic and in vivo aneurysmal 4D flow

The velocity fields at peak systole from the CFD simulations, the synthetic 4D flow data, and the *in vivo* 4D flow data were shown in Figure 4.4 for the BT and ICA aneurysms. For the BT

aneurysm, the flow entered from the basilar artery, circulated in the aneurysmal sac, and then exited primarily through the posterior cerebral arteries (PCAs). For the ICA aneurysm, the flow entered from the ICA, circulated in the aneurysmal sac, and exited through the distal ICA and the middle cerebral artery (MCA).

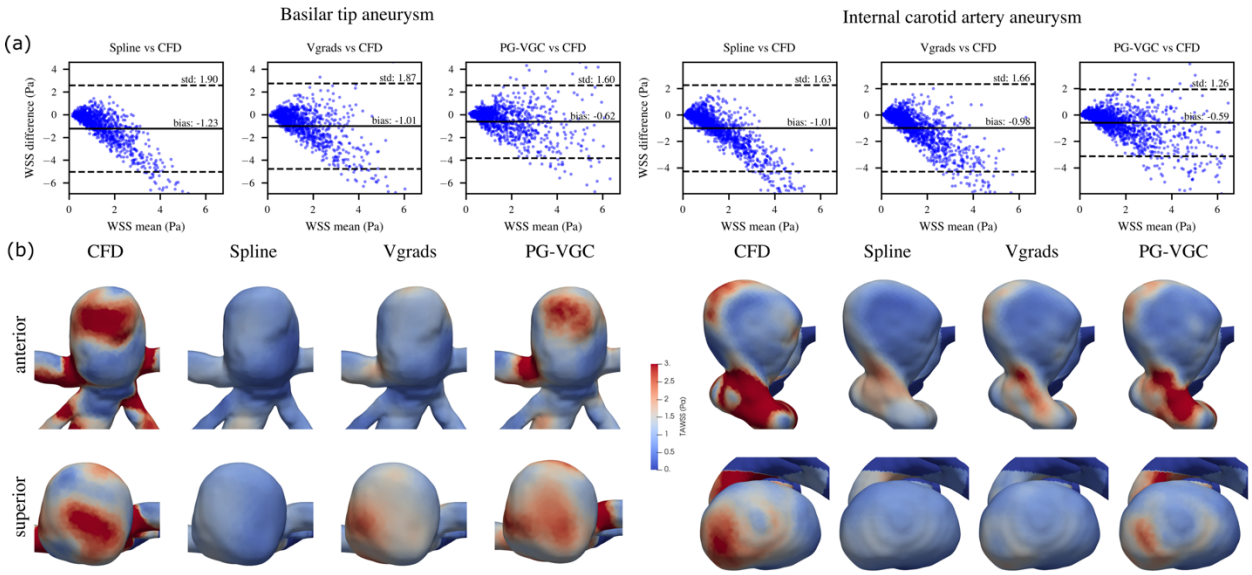

Figure 4.5 (a) The Bland-Altman plots comparing the WSS estimated from synthetic 4D flow data with the WSS from CFD, with the mean and standard deviation (std) of the WSS differences presented in the plots. (b) The spatial distributions of the TAWSS estimated from the synthetic 4D flow data and from CFD.

The Bland-Altman plots in Figure 4.5 (a) compare the CFD WSS with the WSS estimated by Spline, Vgrads, and PG-VGC from the synthetic aneurysmal data. The mean WSS from CFD was 2.1 Pa and 1.9 Pa for the BT aneurysm and ICA aneurysm, respectively, while the mean WSS was underpredicted by 0.59 to 1.23 Pa by the three methods as presented in Figure 4.5 (a). The PG-VGC method reduced the WSS underestimation by 39% to 50% and improved the robustness compared to the other methods, as suggested by the lower bias values and standard deviations. Figure 4.5 (b) compares the spatial distributions of the TAWSS from CFD and synthetic MRI. High WSS regions were observed in the anterior view and superior view of the BT aneurysmal sac in CFD results, which PG-VGC also predicted, but absent in the results obtained by Spline and Vgrads. For the ICA aneurysm, the PG-VGC method predicted the high WSS region at the tip of the aneurysmal sac from the superior view, which was missing from Spline and Vgrads results.

Moreover, PG-VGC yielded higher WSS in the ICA than Spline and Vgrads, which was more consistent with CFD.

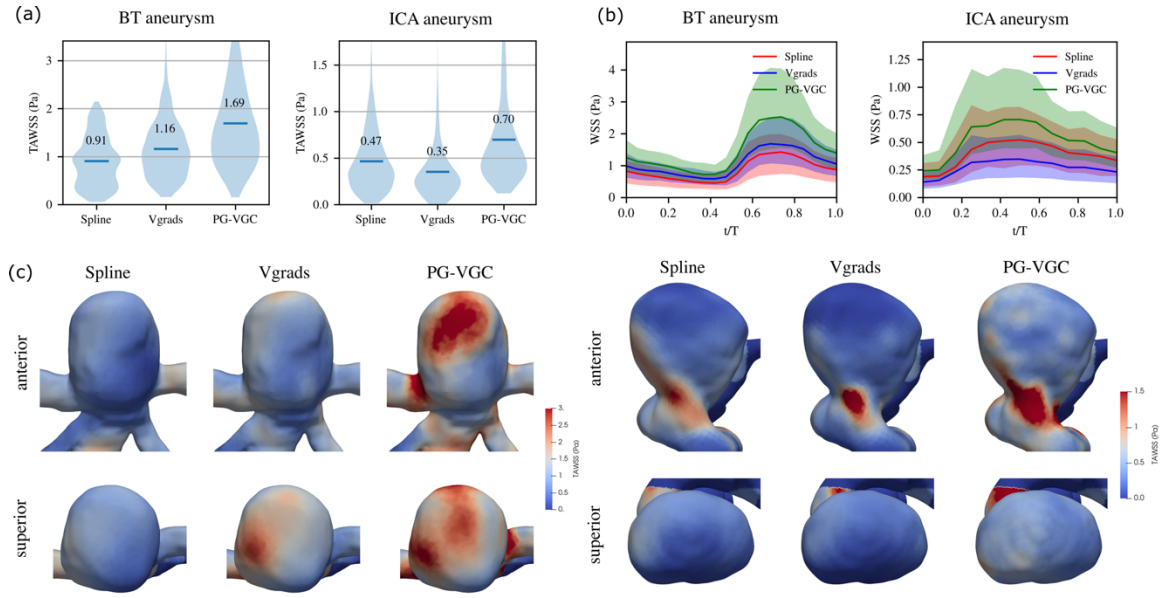

Figure 4.6 (a) The statistical distributions and mean values of the TAWSS estimated from *in vivo* 4D flow data of the BT aneurysm and the ICA aneurysm. (b) The time-dependent median and IQR of the WSS estimated from the *in vivo* 4D flow data in a cardiac cycle. (c) The spatial distributions of the TAWSS estimated from the *in vivo* 4D flow data.

Figure 4.6 (a) compares the statistical distributions of the TAWSS estimated from the *in vivo* aneurysmal data. The mean TAWSS estimated by Spline was 46% and 33% lower than that estimated by PG-VGC for the BT and ICA aneurysm, respectively, while the mean TAWSS obtained by Vgrads was 31% and 50% lower than that from PG-VGC for the BT and ICA aneurysm respectively. Figure 4.6 (b) presents the time-dependent median and IQR of the estimated WSS for the two aneurysms. The different methods obtained similar WSS waveforms; however, PG-VGC predicted higher WSS than the other methods at all timeframes. Figure 4.6 (c) shows the spatial distributions of the estimated TAWSS. PG-VGC predicted additional high WSS regions in the BT aneurysmal sac as shown on the anterior and superior views. The three methods yielded qualitatively similar TAWSS distributions for the ICA aneurysm, with higher WSS predicted by PG-VGC than the other two methods around the “neck” of the aneurysmal sac.

4.3.3 In vivo aortic 4D flow MRI

Figure 4.7 (a) compares the statistical distributions of the TAWSS estimated from the in vivo aortic data of the three subjects. The mean TAWSS by PG-VGC was 5.6 to 6.6 times the mean TAWSS assessed by Spline and 3.7 to 4.7 times the mean TAWSS assessed by Vgrads. Similar profiles of the time-dependent median of WSS were obtained from all methods as shown in Figure 4.7 (b), while PG-VGC predicted higher WSS and larger IQR for all the timeframes. The median WSS estimated at peak systole was 5 to 7 Pa by PG-VGC and 1 to 2 Pa by Spline and Vgrads.

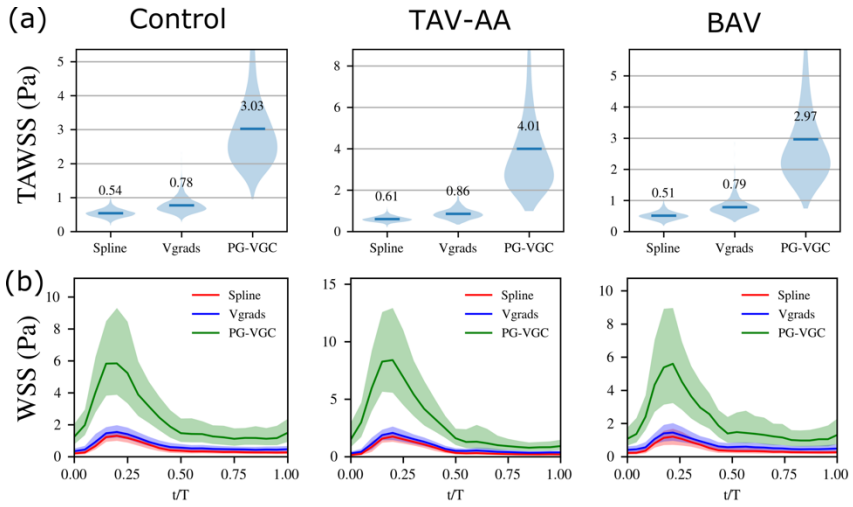

Figure 4.7 (a) The statistical distributions and mean values of the TAWSS estimated from the in vivo aortic data. (b) The time-dependent median and IQR of the estimated WSS in the cardiac cycle.

Figure 4.8 presents the velocity field, the vortical structure (VS), the pressure distribution on the wall, and the relative WSS. The relative WSS is defined as the WSS normalized by its global average at peak systole for the three subjects. The velocity fields are represented using 3D pathlines whose color corresponds to the velocity magnitude. The VSs are included because it has shown to be correlated with high WSS in the aorta (Biasetti, Hussain, & Gasser, 2011). The VSs were detected using the Q-criterion (Hunt, Wray, & Moin, 1998) and are represented by the iso-surfaces in Figure 4.8 (a). Both the right-anterior (R-A) and the posterior-left (P-L) views were presented. The green circles in the PG-VGC WSS distributions indicate the high WSS regions predicted by PG-VGC but are absent from the Spline or Vgrads estimations. For all subjects, VSs were observed in the ascending aorta near the aortic root and in the descending aorta near the aortic

arch, with a corresponding location of the local minimum pressure. For the control subject, high WSS regions around the VSs were calculated by all three methods, as shown on the R-A view. However, only PG-VGC predicted the marked high WSS regions on the P-L view. For the TAV-AA subject, PG-VGC predicted the high WSS region in the aneurysm at the aortic arch, which was missing from the results obtained with Spline and Vgrads. PG-VGC also yielded the high WSS region next to the VS in the ascending aorta near the P-L wall. For the BAV subject, PG-VGC predicted multiple regions with high WSS in the ascending aorta corresponding to the VSs near the R-A and P-L wall, which were not seen in the Spline or Vgrads results.

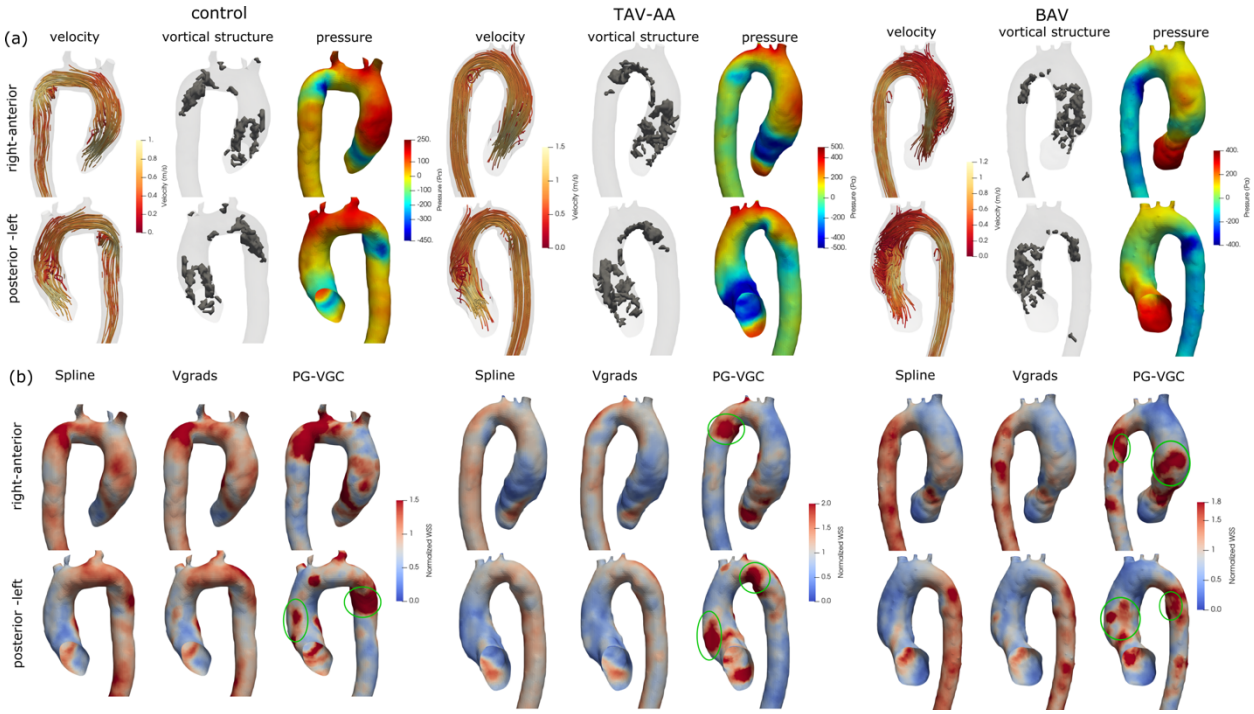

Figure 4.8 (a) The velocity fields represented using 3D pathlines, the vortical structure indicated by iso-surfaces, the pressure distribution on the wall, and (b) the relative WSS estimated by the three methods at peak systole from the *in vivo* 4D flow data of the three subjects. The green circles in the PG-VGC WSS distributions indicate the high WSS regions predicted by PG-VGC but are absent from the Spline or Vgrads estimations.

4.4 Discussion

This study introduced, evaluated, and applied a method for WSS estimation from 4D flow MRI. The proposed method, PG-VGC, improves the WSS estimation by enhancing the near-wall

velocity gradients. The near-wall velocity-gradient calculation from 4D flow data is commonly unreliable because of the systematic velocity errors caused by the partial-volume effects and intravoxel phase dispersion (Rothenberger et al., 2022; Wolf, Ehman, Riederer, & Rossman, 1993). Moreover, the velocity gradient near the wall is typically higher than the core-flow region, therefore increasing the bias error in the gradient calculation in cases with limited spatial resolution. The uncertainty in the wall location also affects the velocity-gradient's accuracy if the wall points are incorporated in the gradient evaluation. The velocity-gradient correction by PG-VGC was based on the flow physics constraints of COLM and COM. At the stationary wall, the COLM is reduced to the balance between the pressure force and the viscous diffusion and directly relates the velocity gradient to the pressure gradient. The near-wall pressure gradient evaluated using (4-3) based on the near-wall velocity gradient can be unreliable, while the pressure gradient estimated in the core-flow is more accurate as shown in Figure 4.2(b). We reconstructed the pressure field in the ROI by spatially integrating the pressure-gradients using WLS. This WLS approach is a global optimization process, dominated by the pressure-gradients in the core-flow regions due to their greater weights. The spatial gradient of the reconstructed pressure in the near-wall region is more reliable than the uncorrected pressure-gradient as shown by comparing Pgrad-u and Pgrad-p in Figure 4.2(b). Therefore, the more reliable Pgrad-p was used and proved to be effective for correcting the near-wall velocity-gradient.

The PG-VGC method improves the mean and the range of WSS estimated from 4D flow data. A previous study has shown that the WSS estimated in intracranial aneurysms depend on the spatial resolution of the phase-contrast MRI data with 50 to 60% underestimation of the mean WSS at a resolution of 1 mm (Van Ooij et al., 2013). Therefore, the 31 to 50% increase on the mean WSS prediction by PG-VGC as compared to Spline and Vgrads improved the accuracy of the WSS estimation in the cerebral aneurysms. For the *in vivo* aortic data, Spline and Vgrads yielded a median WSS of 1 to 2 Pa at peak systole, which was consistent with the results in previous studies using similar methods (Barker et al., 2012; Stalder et al., 2008a; van Ooij et al., 2015). However, the common range of mean aortic WSS at peak systole was 5 to 20 Pa according to CFD studies (Leuprecht et al., 2003; Perinajová, Juffermans, Mercado, et al., 2021; Perinajová, Juffermans, Westenberg, et al., 2021; Rinaudo & Pasta, 2014). The underestimation of WSS in the aorta with 4D flow MRI was due to the low spatial resolution of the imaging data. Perinajová *et al.* (Perinajová, Juffermans, Mercado, et al., 2021) estimated the WSS from spatially downsampled

CFD data in a flow phantom of aortic coarctation, and the mean WSS was underestimated by 34% at a resolution of 0.2 mm and by 63% at a resolution of 0.7 mm. In the present study, the spatial resolution of *in vivo* aortic MRI data was 2-3 mm, which was expected to cause greater WSS underestimation compared to higher resolutions. PG-VGC predicted 4 to 6 times higher mean WSS than Spline and Vgrads resulting in better agreement with the results from previous CFD studies (Leuprecht et al., 2003; Perinajová, Juffermans, Mercado, et al., 2021; Perinajová, Juffermans, Westenberg, et al., 2021; Rinaudo & Pasta, 2014). The overall increase of the WSS magnitude computed by PG-VGC can potentially resolve the inconsistency between the WSS obtained from different modalities as observed in previous studies (Brindise et al., 2019; Szajer & Ho-Shon, 2018; Van Ooij et al., 2013). The improvements achieved by PG-VGC method promote the use of WSS in addition to the normalized parameters such as relative WSS and OSI for the investigation of WSS-related cardiovascular diseases with 4D flow MRI.

The PG-VGC method also improves the prediction of the relative WSS distribution. From the synthetic aneurysmal flow data, PG-VGC recovered the high WSS regions absent in the Spline and Vgrads results, as shown in Fig. 5(b). PG-VGC also predicted additional high WSS regions for the *in vivo* BT aneurysm data that were absent in results computed with the other methods as shown in Figure 4.6(c), thus obtaining WSS distribution more consistent with the CFD results shown Figure 4.5(b). Based on *in vivo* aortic 4D flow data, PG-VGC predicted high WSS in regions corresponding to near the VSs, which is consistent with the previous finding that high WSS correlates with VSs in the aorta (Biasetti et al., 2011). The Spline and Vgrads methods failed to predict several of these high WSS regions, as highlighted in Figure 4.8. The improved prediction of relative WSS distribution by PG-VGC is valuable for detecting regions with abnormal WSS, as these are related to cardiovascular disease progression such as growth and rupture of intracranial and aortic aneurysms.

There are several limitations of the PG-VGC method. First, time-resolved flow data is needed to determine the temporal derivative of velocity for pressure-gradient estimation. The *in vivo* 4D flow data employed in this study had 13-24 timeframes per cycle, which is standard in clinical acquisitions and was shown to be adequate for PG-VGC to enhance the WSS estimation. Moreover, the uncertainty on the wall locations can affect the WSS's accuracy. However, this is a limitation for most WSS estimation methods, and PG-VGC is expected to be more robust than the

other methods since it should also reduce the velocity-gradient errors caused by the inaccurate wall location.

There are several additional limitations in this study. First, the "ground truth" WSS was unavailable for assessing the WSS errors for the *in vivo* 4D flow data. Moreover, Newtonian flow was assumed for the WSS calculations and the CFD simulations, which may not be ideal in low WSS regions. Additionally, rigid walls were assumed for the cerebral aneurysms and the aorta. Although the rigid wall assumption is reasonable for modeling the flow in cerebral arteries as cine MR images showed no appreciable movements of these vessels over the cardiac cycle in a previous investigation (Boussel et al., 2008), it may not be appropriate for the aortic wall. However, this limitation should not affect the comparison between different WSS estimation methods.

In conclusion, this study introduced a novel WSS estimation method for 4D flow MRI. The method uses the pressure gradient estimated from the flow data in the whole ROI and flow physics constraints to correct the velocity gradient, therefore enhancing the WSS estimation. The method's performance was evaluated using synthetic and *in vivo* 4D flow data in cerebral aneurysms and thoracic aortas. The proposed method showed reliable estimation of the mean and the relative distribution of WSS with as much as 100% improvement in WSS accuracy. The method can benefit clinical applications of 4D flow MRI as it improves the accuracy of the WSS estimation.

5. USING UNCERTAINTY TO IMPROVE PRESSURE FIELD RECONSTRUCTION FROM PIV/PTV FLOW MEASUREMENTS

This chapter is reproduced with permission from: Zhang, J., Bhattacharya, S., Vlachos, P.P., 2020. Using uncertainty to improve pressure field reconstruction from PIV/PTV flow measurements. Exp. Fluids 61, 131. https://doi.org/10.1007/s00348-020-02974-y

5.1 Nomenclature

x, y, z	spatial coordinates	p_{ref}	reference pressure
Δx, Δy	grid sizes	$\epsilon_{p_{ref}}$	error in the reference pressure
Δt	time interval between consecutive frames	$\boldsymbol{p_{grad,u}}$	pressure gradient calculated from the measured velocity
u, v, w	velocity components	$\boldsymbol{p_{grad,t}}$	true pressure gradient
$\boldsymbol{u}$	velocity vector	$\boldsymbol{\epsilon_{\nabla p}}$	error in the calculated pressure gradient
$\boldsymbol{u_m}$	measured velocity	$\boldsymbol{\sigma_{\nabla p}}$	standard deviation of pressure gradient errors
$\boldsymbol{u_t}$	true velocity	$\Sigma_{\nabla p}$	covariance matrix of pressure gradient errors
$\boldsymbol{\epsilon_u}$	error in measured velocity	ϵ_{pgradx}	streamwise pressure gradient errors
Σ_u	covariance matrix of velocity errors	σ_{pgradx}	standard deviation of streamwise pressure gradient errors
$\boldsymbol{\sigma_u}$	standard deviation of velocity errors	ρ_{pgradx}	auto-correlation coefficients between streamwise pressure gradient errors
$\rho_{u1,u2}$	auto-correlation coefficient between velocity errors	ρ	fluid density
$Cov_{u1,u2}$	covariance between velocity errors	μ	fluid dynamic viscosity
p	pressure	STD	standard deviation
ϵ_p	error in the reconstructed pressure	RMS	root mean square

5.2 Background and literature review

Measurement of pressure in a fluid flow is important in engineering applications as well as in investigations of flow physics. Pressure measurement devices such as wall pressure ports, static

tubes, pressure-sensitive painting (PSP) etc, are either invasive, provide point measurements or a surface distribution (McKeon and Engler, 2007). Further, most pressure measurement techniques have limitations in dynamic range and resolvable frequency bandwidth. With the development of flow measurement techniques such as particle image velocimetry (PIV) and particle tracking velocimetry (PTV), the velocity fields can be obtained and utilized for instantaneous pressure evaluation (Charonko et al., 2010; Fujisawa, Tanahashi, & Srinivas, 2005; Huhn, Schanz, Gesemann, & Schröder, 2016; Liu & Katz, 2006; Nathan J. Neeteson & Rival, 2015). Most pressure reconstruction methods require two major steps to calculate the pressure fields from velocity measurements. The pressure gradient fields are first evaluated from the velocity fields using the Navier-Stokes momentum equation, which are then spatially integrated to reconstruct the pressure fields. For incompressible flows, the momentum equation can be expressed in the following form:

$$\nabla p = -\rho \frac{D\boldsymbol{u}}{Dt} + \mu \nabla^2 \boldsymbol{u}, \qquad (5\text{-}1)$$

where p is the pressure, $\boldsymbol{u}$ is the velocity, ρ and μ are the density and dynamic viscosity of the fluid, respectively. ∇ represents the divergence operator and ∇^2 is the Laplacian operator. $\frac{D\boldsymbol{u}}{Dt}$ is the material acceleration which can be evaluated using the Eulerian approach from gridded velocity data (Charonko et al., 2010; Roeland de Kat et al., 2009; Fujisawa et al., 2005; Tronchin et al., 2015). $\frac{Du}{Dt}$ can also be evaluated from particle tracks obtained using PTV (Gesemann, Huhn, Schanz, & Schröder, 2016; Huhn et al., 2016; Nathan J. Neeteson & Rival, 2015) or time-resolved PIV with pseudo-tracking approach (R. de Kat & Van Oudheusden, 2012; Ghaemi, Ragni, & Scarano, 2012; Liu & Katz, 2006; P. L. Van Gent, Schrijer, & Van Oudheusden, 2018a, 2018b; Violato et al., 2011). For pressure integration, one common approach is path-integration (also referred to as spatial-marching) which integrates the pressure gradient along paths across the flow domain (Dabiri, Bose, Gemmell, Colin, & Costello, 2014; Liu & Katz, 2006; Tronchin et al., 2015). Most path-integration schemes employ redundant number of paths to reduce the influence of erroneous pressure gradient values. The path-integration approach is rarely employed for 3D flow-data due to its high computational cost. The most widely used pressure integration approach is solving the pressure Poisson equation (PPE) (R. de Kat & Van Oudheusden, 2012; Fujisawa et al.,

2005; Nathan J. Neeteson & Rival, 2015; Schneiders & Scarano, 2016; Violato et al., 2011). The performances of PIV-based pressure calculation methods have been explored by Charonko et al. (2010), and a comparative assessment of pressure field reconstructions from PIV and PTV have been performed by van Gent et al. (2017) based on a simulated experiment.

However, the pressure reconstruction from flow measurements have inherent limitations. First, spatio-temporally resolved velocity measurements are normally required to accurately reconstruct the instantaneous pressure fields. Schneiders et al. (2014) proposed a vortex-in-cell based algorithm for time-supersampling of 3D PIV measurements. Schneiders and Scarano (2016) developed a dense velocity reconstruction method for tomographic PTV. Gesemann et al. (2016) employed a B-splines based global minimization method to obtain high-resolution pressure fields from particle tracks by STB method. Moreover, the accuracy of the reconstructed pressure fields is significantly affected by the measurement error in the velocity fields (Azijli, Sciacchitano, Ragni, Palha, & Dwight, 2016b; Charonko et al., 2010; Pan, Whitehead, Thomson, & Truscott, 2016). The velocity errors propagate through the pressure gradient calculation and pressure integration to the reconstructed pressure fields with an error amplification of as much as 100 times depending on the type of flow, the governing equation, and the prescribed boundary conditions (Charonko et al., 2010). Smoothing and filtering can be employed to mitigate errors during pressure gradient evaluation (Charonko et al., 2010; Schiavazzi, Nemes, Schmitter, & Coletti, 2017; Z. Wang, Gao, Wang, Wei, & Wang, 2016). In order to reduce error propagation during pressure integration, Tronchin et al. (2015) and Jeon et al. (2018) employed approaches which divided the flow field into subdomains with respect to local velocity reliabilities, then performed pressure integration in the subdomains in descending order of the reliabilities. The reliability of each subdomain could be defined by the Frobenius norm of the velocity gradient tensor (Tronchin et al., 2015) or the Frobenius norm of the pressure gradient tensor (Jeon et al., 2018). Consequently, the evaluated pressure in a more reliable subdomain was not affected by the erroneous velocity measurements in a less reliable subdomain. This type of approaches is particularly effective for flow fields that can be segmented into regions with different levels of measurement accuracy. One example is the flow field around an airfoil which can be divided into outer-region, wake-region, near-body region, and near-edge region with descending accuracy (Jeon et al., 2018).

Since the pressure reconstruction process is significantly affected by the errors in the estimated velocity field, the uncertainty bounds on each velocity measurement can also be used as

a measure of reliability to subsequently optimize the error propagation in pressure field estimation. The standard uncertainty is estimated as the standard deviation of the error distribution and provides a bound on the error distribution with certain confidence. For flow measurements using PIV, recent developments have enabled the uncertainty estimation for each velocity vector in the flow field (Bhattacharya, Charonko, & Vlachos, 2017; Bhattacharya et al., 2018; Charonko et al., 2010; Schneiders & Sciacchitano, 2017; Xue, Charonko, & Vlachos, 2014; Xue et al., 2015). The local and instantaneous velocity uncertainty has been used to denoise the velocity fields using a spatial averaging scheme (B Wieneke, 2017) and can be propagated to estimate the uncertainty in the calculated pressure gradient fields as well as the reconstructed pressure fields (Azijli et al., 2016b). However, to the best of the authors' knowledge, the uncertainty information has not been utilized to improve the pressure integration.

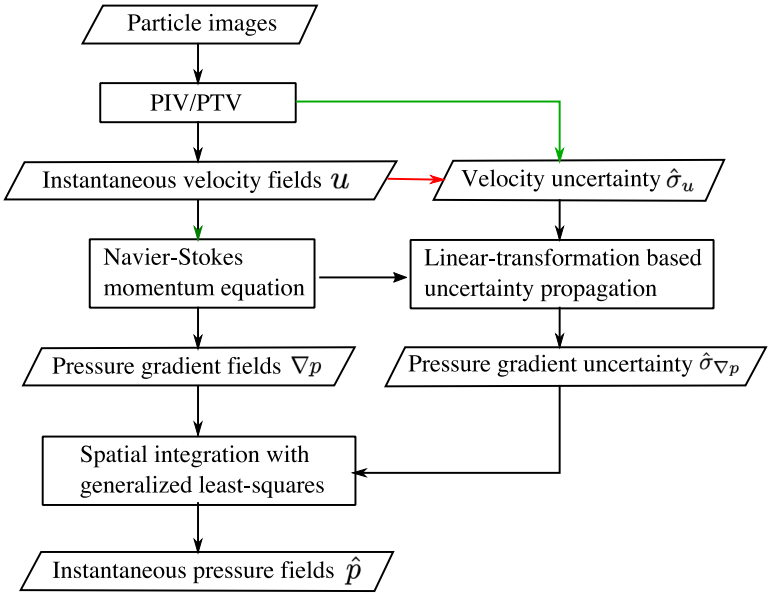

Figure 5.1 Procedure of the GLS pressure reconstruction. The velocity uncertainty can be obtained from the flow measurements (green arrow) or estimated from the velocity fields (red arrow) using the divergence-based algorithm.

In the present study, a robust pressure reconstruction method is proposed which employs the velocity uncertainty to improve the accuracy of reconstructed pressure fields. A linear-transformation based uncertainty propagation algorithm is developed to acquire the pressure gradient uncertainty as variances and covariances. The pressure integration on a discretized domain is formulated as an overdetermined linear system involving pressure gradients and

pressure boundary conditions. The generalized least-squares (GLS) is employed to reconstruct the pressure fields with the estimated pressure gradient uncertainty. The performance of the GLS pressure reconstruction method is tested with synthetic velocity fields and applied to volumetric flow-data measured using PTV.

5.3 Methodology

5.3.1 Uncertainty-based pressure reconstruction with generalized least-squares

The procedure of the pressure reconstruction using uncertainty information with GLS is presented in Figure 5.1. The pressure gradient calculation is described in Sect. 5.4.1.1 The linear-transformation based uncertainty propagation algorithm is introduced in Sect. 5.4.1.2. The pressure integration methods and numerical schemes are introduced in Sects. 5.4.1.3 and 5.4.1.4, respectively. In Sect. 5.4.1.5, a velocity-divergence based uncertainty estimation algorithm is introduced as a substitute to provide velocity uncertainty for GLS reconstruction.

Pressure gradient calculation

The pressure gradient field is estimated by substituting the velocity field in the Navier-Stokes equations. As the velocity fields employed in the present study were on Cartesian grids, the pressure gradient fields were calculated using the Eulerian approach as:

$$\boldsymbol{p}_{\boldsymbol{grad,u}} = -\rho\left(\frac{\partial \boldsymbol{u}_{\boldsymbol{m}}}{\partial t} + \boldsymbol{u}_{\boldsymbol{m}} \cdot \nabla \boldsymbol{u}_{\boldsymbol{m}}\right) + \mu\nabla^2 \boldsymbol{u}_{\boldsymbol{m}}, \qquad (5\text{-}2)$$

where $\boldsymbol{p}_{\boldsymbol{grad,u}}$ is the pressure gradient evaluated from the measured velocity $\boldsymbol{u}_{\boldsymbol{m}}$, $\frac{\partial \boldsymbol{u}_{\boldsymbol{m}}}{\partial t}$ is the local acceleration, and $\boldsymbol{u}_{\boldsymbol{m}} \cdot \nabla \boldsymbol{u}_{\boldsymbol{m}}$ is the convective acceleration. The spatial and temporal derivatives were calculated using the second-order central difference scheme for grid points in the domain. The first-order one-sided scheme was used at the boundaries for spatial derivatives and at the first and last frames for the temporal derivatives. The evaluated pressure gradient values were on the same grid points as the velocity. The pressure gradient calculation is carried out using matrix/vector operations. At each frame, the velocity field and the calculated pressure gradient field were organized as column vectors containing all the components from all the grid points, i.e.,

$\boldsymbol{u_m} = [u\ v\ w]^T$ and $\boldsymbol{p_{grad,u}} = \left[\frac{dp}{dx}\ \frac{dp}{dy}\ \frac{dp}{dz}\right]^T$ for volumetric flow-data. The discretized gradient and Laplacian operators were 2D matrices with respect to the selected difference schemes.

Pressure gradient uncertainty estimation using linear transformations

The proposed pressure reconstruction methods requires both pressure gradients and the pressure gradient uncertainty for pressure integration. To estimate the uncertainty in $\boldsymbol{p_{grad,u}}$, we implemented a linear-transformation based uncertainty propagation algorithm.

Considering the measurement errors, $\boldsymbol{u_m}$ and $\boldsymbol{p_{grad,u}}$ can be decomposed into true components and error components as,

$$\boldsymbol{u_m} = \boldsymbol{u_t} + \boldsymbol{\epsilon_u}, \tag{5-3}$$

$$\boldsymbol{p_{grad,u}} = \boldsymbol{p_{grad,t}} + \boldsymbol{\epsilon_{\nabla p}}, \tag{5-4}$$

where the subscript t suggests the true component, $\boldsymbol{\epsilon_u}$ and $\boldsymbol{\epsilon_{\nabla p}}$ are error components of velocity and pressure gradient, respectively. With the assumption that the velocity fields are acquired with sufficient spatiotemporal resolutions such that the numerical truncation errors are negligible, the true pressure gradient can be evaluated as,

$$\boldsymbol{p_{grad,t}} = -\rho\left(\frac{\partial \boldsymbol{u_t}}{\partial t} + \boldsymbol{u_t}\cdot\nabla\boldsymbol{u_t}\right) + \mu\nabla^2\boldsymbol{u_t}. \tag{5-5}$$

Combining Eqns. 5-2, 5-4 and 5-6, the pressure gradient error can be obtained in terms of the measured velocity $\boldsymbol{u_m}$ and the velocity error $\boldsymbol{\epsilon_u}$ as follows:

$$\boldsymbol{\epsilon_{\nabla p}} = -\rho\left(\frac{\partial \boldsymbol{\epsilon_u}}{\partial t} + \boldsymbol{u_m}\cdot\nabla\boldsymbol{\epsilon_u} + \boldsymbol{\epsilon_u}\cdot\nabla\boldsymbol{u_m} - \boldsymbol{\epsilon_u}\cdot\nabla\boldsymbol{\epsilon_u}\right) + \mu\nabla^2\boldsymbol{\epsilon_u}, \tag{5-6}$$

Assuming that $\boldsymbol{\epsilon_u}$ is sufficiently less than the velocity $\boldsymbol{u_m}$, the term $\boldsymbol{\epsilon_u}\cdot\nabla\boldsymbol{\epsilon_u}$ can be neglected (Pan et al., 2016). Therefore, equation 5-7 can be simplified and expressed using matrix/vector operations as:

$$\boldsymbol{\epsilon_{\nabla p}} = M_+\boldsymbol{\epsilon_u^{i+1}} + M_-\boldsymbol{\epsilon_u^{i-1}} + M\boldsymbol{\epsilon_u^{i}},$$

$$with\, M_+ = -\frac{\rho}{\Delta t} I, M_- = \frac{\rho}{\Delta t} I, and\, M = -\rho\left(diag(\boldsymbol{u_m^i}) \cdot \nabla + diag(\nabla \boldsymbol{u_m^i})\right) + \mu\nabla^2, \quad (5\text{-}7)$$

where $\boldsymbol{\epsilon_u^i}$ is the column vector containing velocity errors from the ith frame, I is the identity matrix whose dimension is same with the length of $\boldsymbol{\epsilon_u^i}$, and the function $diag()$ constructs a diagonal matrix with the diagonal elements from the given column vector. Equation 8 estimates the pressure gradient errors at the ith frame as the linear transformations of velocity errors at frames i, i-1, and i+1. The transformation coefficients in M_+, M_-, and M are decided by the measured velocity field and the selected discretization schemes. By stacking the transformation matrices and concatenating the velocity error vectors, Eqn. 5-7 can be written as:

$$\boldsymbol{\epsilon_{\nabla p}} = [M_+ \quad M_- \quad M] \begin{bmatrix} \boldsymbol{\epsilon_u^{i+1}} \\ \boldsymbol{\epsilon_u^{i+1}} \\ \boldsymbol{\epsilon_u^{i}} \end{bmatrix} \equiv M_c \boldsymbol{\epsilon_u^c}, \quad (5\text{-}8)$$

where M_c, and $\boldsymbol{\epsilon_u^c}$ are the combined transformation matrix and error vector, respectively. The uncertainty of pressure gradient can be determined as $\Sigma_{\nabla p}^i = M_c \Sigma_u^c M_c^T$, where Σ_u^c is the covariance matrix of $\boldsymbol{\epsilon_u^c}$ containing the spatiotemporal correlations between velocity errors. Due to the lack of an established tool to estimate the temporal correlation of velocity errors for PIV/PTV, the velocity errors at different frames are assumed to be independent in the present study. The uncertainty of pressure gradient can be determined as:

$$\Sigma_{\nabla p}^i = M_+ \Sigma_u^{i+1} M_+^T + M_- \Sigma_u^{i-1} M_-^T + M \Sigma_u^i M^T, \quad (5\text{-}9)$$

where Σ_u^i and $\Sigma_{\nabla p}^i$ are the covariance matrices of velocity errors and pressure gradient errors at the ith frame, respectively. The velocity uncertainty σ_u forms the diagonal elements of Σ_u, while the covariances of the spatially-correlated velocity errors are stored as the off-diagonal elements of Σ_u.

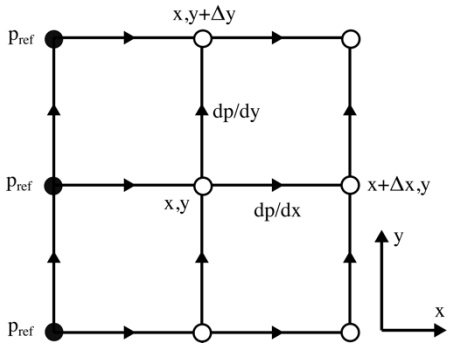

Figure 5.2 Demonstration of the grid arrangement for the pressure integration with generalized least-squares. dp/dx and dp/dy represent the pressure gradients along x and y directions, respectively. $\boldsymbol{\Delta x}$ and $\boldsymbol{\Delta y}$ are the grid sizes. $\boldsymbol{p_{ref}}$ represents the reference pressure values.

Pressure integration

The pressure field is inherently related to the pressure gradient field as,

$$G\boldsymbol{p} = M_L \boldsymbol{p}_{\boldsymbol{grad,u}}, \qquad (5\text{-}10)$$

where $\boldsymbol{p}$ is a column vector of the estimated pressure field, G is the discretized gradient operator constructed with a staggered grid arrangement similar as employed by Jeon et al. (2018), and M_L is the transformation matrix that linearly interpolates $\boldsymbol{p}_{\boldsymbol{grad,u}}$ from grid points to staggered nodes. As demonstrated in Figure 5.2, the grid points are represented with circles, the arrow heads indicate the staggered nodes for the interpolated pressure gradients, and the arrow directions indicate the component of pressure gradients. As an example, the staggered grid interpolations in x and y directions at points $x + \Delta x/2, y$ and $x, y + \Delta y/2$ can be written as, $\left.\frac{dp}{dx}\right|_{x+\Delta x/2,y} = \frac{1}{2}\left(\left.\frac{dp}{dx}\right|_{x,y} + \left.\frac{dp}{dx}\right|_{x+\Delta x,y}\right)$ and $\left.\frac{dp}{dy}\right|_{x,y+\Delta y/2} = \frac{1}{2}\left(\left.\frac{dp}{dy}\right|_{x,y} + \left.\frac{dp}{dy}\right|_{x,y+\Delta y}\right)$, respectively. The filled circles (mentioned

as reference points in the present study) are the grid points with prescribed pressure values. The following equation relates the reference points with the reconstructed pressure field as

$$L\boldsymbol{p} = \boldsymbol{p_{ref}}, \tag{5-11}$$

where L is a labeling matrix consisting of zeros and ones, and $\boldsymbol{p_{ref}}$ is the column vector containing the reference pressure values which can be obtained by direct measurement. With the errors in the pressure gradient fields and the pressure reference values, a linear system can be constructed by combining Eqs. 5-10 and 5-11 as

$$\begin{bmatrix} M_L \boldsymbol{p_{grad,u}} \\ \boldsymbol{p_{ref}} \end{bmatrix} = \begin{bmatrix} G & 0 \\ 0 & L \end{bmatrix} \boldsymbol{p} + \begin{bmatrix} M_L \boldsymbol{\epsilon_{\nabla p}} \\ \boldsymbol{\epsilon_{p_{ref}}} \end{bmatrix}, \tag{5-12}$$

where $\boldsymbol{\epsilon_{p_{ref}}}$ is the column vector of possible errors in the reference pressure values. For the sake of simplicity, we denote $[M_L \boldsymbol{p_{grad,u}} \quad \boldsymbol{p_{ref}}]^T$ by $\mathbf{b}$, $\begin{bmatrix} G & 0 \\ 0 & L \end{bmatrix}$ by A, and $\begin{bmatrix} M_L \boldsymbol{\epsilon_{\nabla p}} & \boldsymbol{\epsilon_{p_{ref}}} \end{bmatrix}^T$ by $\boldsymbol{\epsilon_b}$. Since $\boldsymbol{\epsilon_{\nabla p}}$ are uncorrelated with $\boldsymbol{\epsilon_{p_{ref}}}$, the covariance matrix Σ_b of the error term $\boldsymbol{\epsilon_b}$ can be obtained as

$$\Sigma_b = \begin{bmatrix} M_L \Sigma_{\nabla p} M_L^T & 0 \\ 0 & \Sigma_{p_{ref}} \end{bmatrix}, \tag{5-13}$$

where $\Sigma_{p_{ref}}$ is the covariance matrix of $\boldsymbol{\epsilon_{p_{ref}}}$. The pressure field can be estimated ($\widehat{\boldsymbol{p}}$) from Eqn. 5-12 using GLS which minimizes the following equation as

$$\widehat{\boldsymbol{p}} = \underset{p}{argmin} (\boldsymbol{b} - A\boldsymbol{p})^T \Sigma_b^{-1} (\boldsymbol{b} - A\boldsymbol{p}). \tag{5-14}$$

$\widehat{\boldsymbol{p}}$ can be obtained as the solution of the following equation

$$(A^T \Sigma_b^{-1} A)\, \widehat{\boldsymbol{p}} = A^T \Sigma_b^{-1} \boldsymbol{b}. \tag{5-15}$$

To avoid singularity, at least one pressure reference point is required. In addition, the variance terms in the diagonal elements in Σ_b must be greater than 0 for the inverse Σ_b^{-1} to be taken. For $\boldsymbol{p_{ref}}$ with negligible uncertainty, the standard deviation of $\boldsymbol{\epsilon_{p_{ref}}}$ can be set at a small fraction of the pressure scale, e.g. $10^{-3}p_0$, where p_0 is the characteristic pressure of the flow.

Two other variants of the least-squares reconstruction were also implemented, namely ordinary least-squares (OLS) and weighted least-squares (WLS). Both OLS and WLS calculate pressure fields using Eqn. 5-15 with extra assumptions compared to GLS. OLS assumes independent and homoscedastic errors in $\boldsymbol{\epsilon_b}$ such that Σ_b can be ignored or treated as an identity matrix, while WLS assumes independent errors in $\boldsymbol{\epsilon_b}$, thus the off-diagonal elements (covariances) are zeros in Σ_b. The least-squares method proposed by Jeon et al. (2018) can be considered as an OLS approach.

The pressure reconstruction by solving the PPE was employed as the baseline method. The following form of PPE was selected which generates the source term as the divergence of pressure gradients as

$$\nabla^2 \boldsymbol{p} = \nabla \cdot \boldsymbol{p_{grad,u}}. \qquad (5\text{-}16)$$

where the Laplacian operator ∇^2 was discretized using the second-order central difference scheme with a five-point stencil for planar data and a seven-point stencil for volumetric data. The boundary conditions for solving the PPE were assigned with reference pressure values (Dirichlet BC) or pressure gradients (Neumann BC). For Neumann BC, the pressure gradients were given as the $\boldsymbol{p_{grad,u}}$ calculated at the boundary points.

Numerical schemes for solving linear systems

For pressure integration using GLS, solving the linear system of Eq. 5-15 is prohibited as it requires matrix operations involving Σ_b^{-1}. Although the covariance matrix Σ_b is sparse due to the fact that the pressure gradient errors are only correlated within a small neighborhood, the inverse matrix Σ_b^{-1} is normally dense with a dimension of approximately $2N_{pts}\times 2N_{pts}$ for planar data or $3N_{pts}\times 3N_{pts}$ for volumetric data, where N_{pts} is the total number of grid points in the flow field. By introducing the vector $\boldsymbol{\lambda} = \Sigma_b^{-1}(\boldsymbol{b} - A\boldsymbol{p})$, the following equation can be solved for $\boldsymbol{p}$ (Rao 1973)

$$\begin{bmatrix} \Sigma_b & A \\ A^T & 0 \end{bmatrix} \begin{bmatrix} \boldsymbol{\lambda} \\ \boldsymbol{p} \end{bmatrix} = \begin{bmatrix} \boldsymbol{b} \\ 0 \end{bmatrix}. \quad (5\text{-}17)$$

which avoids the operations involving the large dense matrix Σ_b^{-1}. Therefore, more efficient algorithms can be employed to solve the sparse linear system. For OLS and WLS, the pressure fields can be solved from Eq. 5-15 since Σ_b is ignored or treated as a diagonal matrix such that Σ_b^{-1} is also a diagonal matrix.

To solve the linear systems of Eqs. 15-17, different numerical schemes were selected depending on the size of the flow-data. For planar data and small volumetric data, SuperLU, a general-purpose library for the direct solution of large, sparse, nonsymmetric systems of linear equations (Li, 2005), was employed. For large volumetric flow-data, the linear systems were solved using Conjugate Gradient iteration (Björck, 1996).

Divergence-based velocity uncertainty estimation

For some flow measurement techniques such as volumetric PIV and PTV, the estimation of local and instantaneous velocity uncertainty is still unestablished or limited. To inform the GLS pressure reconstruction, a divergence-based approach can be employed to estimate the velocity uncertainty directly from the velocity fields. For incompressible flow, the velocity errors cause nonzero velocity divergence as:

$$\nabla \cdot \boldsymbol{\epsilon_u} = \nabla \cdot \boldsymbol{u_m}, \quad (5\text{-}18)$$

which can be solved in a least-squares sense to estimate the velocity errors $\hat{\boldsymbol{\epsilon}}_{\boldsymbol{u}}$ as:

$$\hat{\boldsymbol{\epsilon}}_{\boldsymbol{u}} = (\nabla \cdot)^T (\nabla^2)^{-1} (\nabla \cdot \boldsymbol{u_m}) \quad (5\text{-}19)$$

This approach was employed by (Zhang et al., 2019) to estimate velocity errors which were then propagated for $\boldsymbol{\epsilon_{pgrad}}$ to inform the weighted least-squares pressure reconstruction. In the present study, the velocity uncertainty at each grid point of each frame can be estimated as the weighted standard deviation (WSTD) of $\hat{\boldsymbol{\epsilon}}_{\boldsymbol{u}}$ from the spatiotemporally neighboring points as:

$$\widehat{\boldsymbol{\sigma}}_{\boldsymbol{u}} = \sqrt{\frac{\sum w(\widehat{\epsilon_u})^2}{\sum w}} \; with$$

$$w = exp\left(-\frac{1}{2}\left(\frac{\Delta s_r}{\Delta x}\right)^2 - \frac{1}{2}\left(\frac{\Delta s_t}{\Delta t}\right)^2\right), \qquad (5\text{-}20)$$

where Δs_r and Δs_t are the spatial and temporal separations from the neighboring points to the point of interest, respectively. Only the points within the $\Delta s_r \leq \Delta x$ and $\Delta s_t \leq \Delta t$ neighborhood are employed for the $\widehat{\boldsymbol{\sigma}}_{\boldsymbol{u}}$ calculation to ensure the local and instantaneous dependency of $\widehat{\boldsymbol{\sigma}}_{\boldsymbol{u}}$.

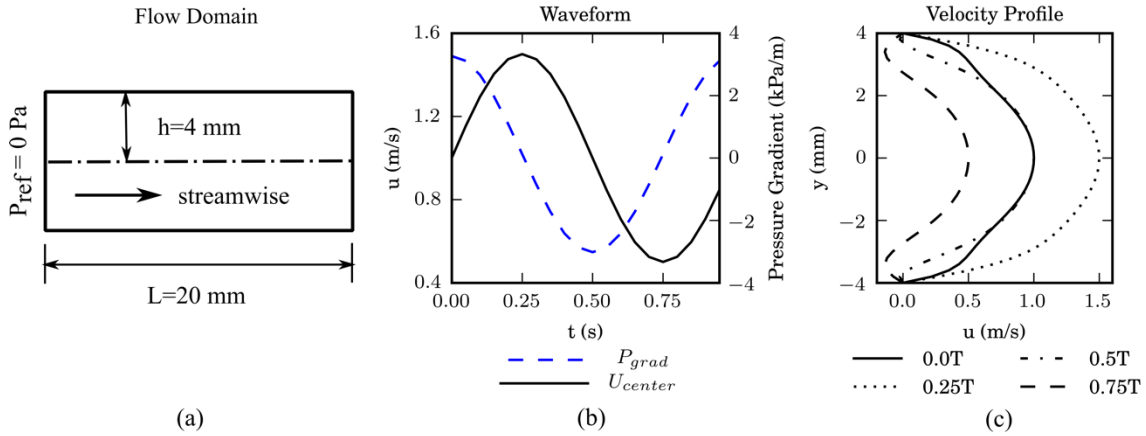

Figure 5.3(a) The domain arrangement of the 2D pulsatile flow. (b) The streamwise centerline velocity and pressure gradient waveforms within a cycle. (c) The streamwise velocity profile at 4 temporal phases.

5.3.2 Synthetic flow fields

Following Charonko et al. (2010), the synthetic velocity fields of a 2D pulsatile flow between two infinite parallel plates were employed to test the uncertainty estimation algorithm and assess the performances of the pressure reconstruction methods. The pulsatile flow is driven by the oscillating streamwise pressure gradient as

$$\frac{dp}{dx} = \rho K + \gamma \rho K cos\omega t, \qquad (5\text{-}21)$$

and the streamwise velocity profile can be expressed as

$$u = u_{max}\left(1 - \frac{y^2}{h^2}\right) + \frac{\gamma K}{i\omega}\left(1 - \frac{cosh(y/h\sqrt{i}\lambda)}{cosh(\sqrt{i}\lambda)}\right) exp(i\omega t) \qquad (5\text{-}22)$$

with $\lambda = h\sqrt{\frac{\rho}{\mu\omega}}$, where γ is the ratio between the magnitude of the steady pressure gradient component and the amplitude of the oscillating pressure gradient component, K is the constant controlling the overall strength of the pressure gradient, ω is the angular speed of the oscillating component, h is the channel half-width, and u_{max} is the centerline velocity of the steady flow component. The parameters were selected as $\omega = 2\pi$ rad/s (period T = 1 s), $u_{max} = 1\ m/s$, and $\gamma = 25.13$. A flow domain with h=4 mm and a length of 20 mm was employed as shown in Figure 5.3(a). The pressure along the inflow boundary was set to be 0 Pa, which was employed as Dirichlet BC for solving the PPE and as the reference points for the least-squares based methods. The fluid properties were given as $\rho = 1000\ kg/m^3$ and $\mu = 1 \times 10^{-3}$ Pa·s. The velocity fields were generated on a uniform Cartesian grid with a grid size of 0.1 mm, yielding 101×41 grid points. For each test case, 1000 velocity fields were generated with a span of 50 cycles at a sampling rate of 20 Hz. The waveforms of streamwise centerline velocity and pressure gradient are shown in Figure 5.3(b) for one cycle. The streamwise velocity profiles at 4 phases are shown in Figure 5.3(c). The characteristic velocity and pressure are defined as $u_0 = u_{max}$ and $p_0 = \frac{1}{2}\rho u_0^2$, respectively.

To test the robustness of pressure reconstruction methods, Gaussian noise with different levels of spatial auto-correlation was added to the true velocity fields. Spatially correlated errors have been reported by Sciacchitano and Wieneke (2016) for PIV fields and are anticipated in gridded velocity fields interpolated from PTV measurements since the error of each single particle track can affect the velocity values on multiple grid points. Three levels of spatial correlation were considered, namely uncorrelated (UC), weakly correlated (WC), and strongly correlated (SC). The spatial auto-correlation coefficient was specified as

$$\rho_{u1,u2} = exp\left(-s\left(\frac{r_{1,2}}{\Delta x}\right)^2\right), \quad (5\text{-}23)$$

where $\rho_{u1,u2}$ is the auto-correlation coefficient between velocity errors at two points denoted as 1 and 2, $r_{1,2}$ is the spatial distance between the two points, Δx is the grid size, and s is a positive constant controlling the strength of the correlation. s is zero for UC errors, and was set at 0.22 and 0.88 for WC and SC errors, respectively. The SC $\rho_{u1,u2}$ was similar to the results of PIV measurements with 32 × 32 pixels interrogation window and 75% overlap (Sciacchitano & Wieneke, 2016). The covariance was then calculated based on the auto-correlation coefficient as

$$Cov_{u1,u2} = \rho_{u1,u2}\sigma_1\sigma_2, \quad (5\text{-}24)$$

where $Cov_{u1,u2}$ is the covariance between velocity errors at points 1 and 2 whose standard deviations are σ_1 and σ_2. The velocity error standard deviation was defined as a fraction of the true velocity magnitude at each point as

$$\sigma = \alpha|\boldsymbol{u_t}|, \quad (5\text{-}25)$$

where α controls the level of imposed errors. To mimic the noise of double-pulse PIV measurements, the errors at different time frames were assumed to be uncorrelated. In addition, the velocity noise was assumed to be uncorrelated between different velocity components due to the lack of an established model for the cross-component correlation within the existing literature. The covariance matrix Σ_u was constructed based on the specified variances and covariances, then the spatially correlated velocity errors were generated by multiplying the Cholesky decomposition of Σ_u to a vector containing uncorrelated, unbiased, and Gaussian distributed random noise with unity standard deviation (Azijli & Dwight, 2015). To test the pressure reconstruction methods for a wide range of error levels, 11 test cases were created for each correlation level with α varying from 1% to 50%, resulting 33 test cases in total.

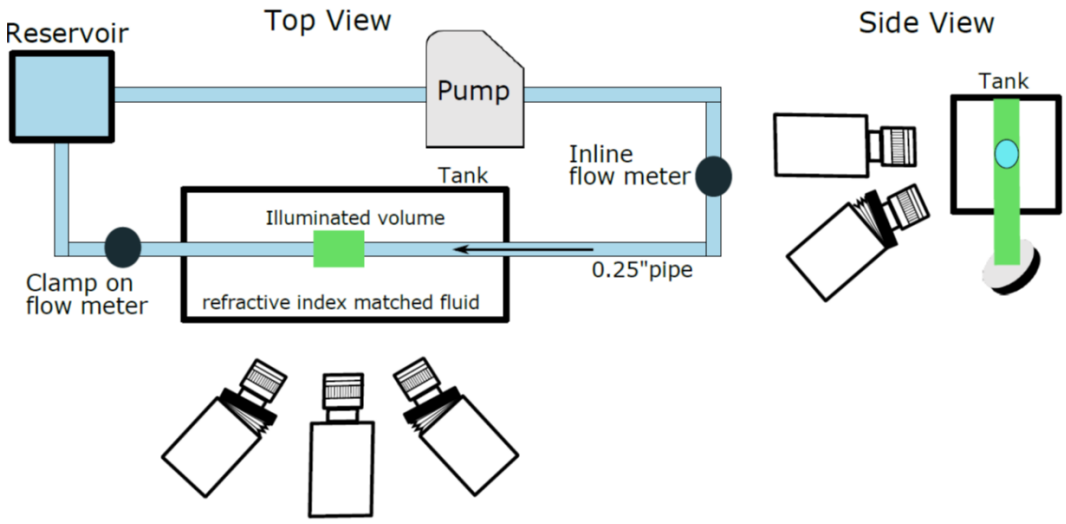

Figure 5.4 Schematic of laminar pipe flow set up showing the flow loop and camera arrangement.

5.3.3 Pipe flow measurements

The laminar flow and transitional flow in in a circular pipe were measured using a volumetric PTV experiment and were employed to validate and demonstrate the GLS pressure reconstruction method. The schematic illustration of the experimental setup is shown in Figure 5.4. More details about the experiment can be found in the work by Bhattacharya and Vlachos (2019). The flow was driven using a gear pump with a steady flow rate Q of 0.17 L/min for the laminar case and with 0.93 L/min for the transitional case. The flow rate upstream and downstream of the pipe was measured using an ultrasonic flowmeter and the average flow rate was used to determine the true velocity profile. A clear FEP tube of diameter (R_{pipe}) 0.25 inch was used for the experiment. The working fluid inside the pipe was distilled water-urea (90:10) solution with a density of 1015 kg/m^3 and dynamic viscosity of 0.915 mPas. The Reynolds number was 630 and 3447 for the laminar case and transitional case, respectively. The pipe was also immersed within the water-glycerol solution such that it is refractive index matched. The measurement volume was 9×6.5×6.5 mm^3 and was illuminated by a continuum Terra-PIV laser with appropriate optical setup. The time-resolved measurements were taken at 6 kHz with 4 cameras, and the image size was 640×624 pixels. The effective angle estimated from the self-calibrated mapping function was about 15° for the left and right cameras and about 18° for the bottom camera, where each angle was measured

normal to the illuminated laser volume. 24-micron fluorescent particles were used with a particle Stokes number of 0.0005. For the laminar case, the particle images were processed using in-house camera calibration, particle reconstruction and tracking code. A polynomial mapping function (Soloff, Adrian, & Liu, 1997) was used to establish a relation between image coordinates and physical coordinates. Three iterations of volumetric self-calibration (B. Wieneke, 2008) were done to eliminate any disparity between the measurement volume and calibration target location or alignment. The 3D triangulation (Maas, Gruen, & Papantoniou, 1993) was used to reconstruct the particle positions in physical coordinate system and subsequently the 3D particle locations were tracked using a "nearest-neighbor" pairwise tracking algorithm. A total of 499 velocity frames were obtained from 500 snapshots of particle images, and the number of tracked particles was around 850 in each frame. For the transitional case, the particle images were processed using STB in Lavision software Davis 10.0.5 with self-calibration and 4 iterations of inner and outer loop for IPR (Schanz, Gesemann, & Schröder, 2016; Bernhard Wieneke, 2013). A total of 200 velocity frames were obtained with around 1500 tracked particles in each frame. For both cases, the velocity values at particle locations were interpolated to a uniform Cartesian grid using "FlowFit" (Gesemann et al., 2016). The grid resolution was 0.385 mm for the laminar case and 0.268 mm for the transitional case. Some measurements at the pipe wall and the edges of the measurement volume were trimmed to avoid the significant errors due to lack of tracked particles in those regions.

To reconstruct the pressure fields of the laminar pipe flow, the proposed GLS method was applied to the gridded velocity fields. A zero reference pressure was assigned at the center point of inflow plane, while Neumann BC was given at the rest of the boundaries with the pressure gradients calculated from the velocity data. The velocity standard deviation (STD) between all the 499 frames were calculated at each spatial point, which was then utilized to generate the covariance matrix $\Sigma_{u,STD}$ for GLS reconstruction. In addition, another set of covariance matrix $\Sigma_{u,UNC}$ was generated from $\widehat{\boldsymbol{\sigma}}_{\boldsymbol{u}}$ estimated using the velocity-divergence based algorithm introduced in Sect. 5.2.1.5. The covariances were assumed to be zero in both $\Sigma_{u,STD}$ and $\Sigma_{u,UNC}$. The GLS reconstructions with $\Sigma_{u,STD}$ and $\Sigma_{u,UNC}$ are denoted as GLS STD and GLS UNC, respectively. In addition, the PPE method and the sequential least-squares method (OLS SEQ) introduced by Jeon et al. (2018) were applied to the pipe flow for the validation of the GLS method. Following Jeon et al. (2018), the Frobenius norm of the pressure gradient was calculated to determine the reliability of the velocity measurements. The flow field was divided into the less reliable near-wall region

($r > 0.5R$) and the more reliable core-region ($r \leq 0.5R$). The pressure field was sequentially reconstructed in the core-region followed by the near-wall region with OLS. The zero pressure reference point at the center of inflow plane was the Dirichlet boundary condition for the core-region reconstruction, and the resulting pressure at the edge of the core region was served as the Dirichlet boundary condition for the pressure reconstruction in the near-wall region. For PPE, the same boundary conditions were given as the GLS reconstruction. To provide a reference of the expected pressure field, the analytical solution of the laminar pipe flow was obtained as:

$$U = -\frac{1}{4\mu}\frac{dP}{dx}\left(R_{pipe}^2 - R^2\right), \textit{ with}$$
$$\frac{dP}{dx} = \frac{8\mu Q}{\pi R_{pipe}^4}, \qquad \textit{(5-26)}$$

where x is the streamwise direction, R is the radial distance, and U is the streamwise velocity. The centerline velocity magnitude $U_{centerline}$ was employed as the characteristic velocity, and the characteristic pressure p_0 was $\frac{1}{2}\rho U_{centerline}^2$.

For the pressure reconstruction of the transitional flow, both GLS and PPE were employed with the same BC arrangement as the laminar case. The velocity covariance matrix $\Sigma_{u,UNC}$ required by GLS was generated from the $\widehat{\boldsymbol{\sigma}}_{\boldsymbol{u}}$ estimated using the velocity-divergence based algorithm introduced in Sect. 5.2.1.5. The reference value of the pressure drop (Δp) along the pipe was estimated using the empirical Darcy-Weisbach pressure loss equation as:

$$\Delta p = f\frac{L}{D}\frac{\rho\bar{U}^2}{2}, \qquad \textit{(5-27)}$$

where f is the friction factor, L is the axial length, D is the diameter of the pipe. and $\overline{U}$ is the average streamwise velocity. Since the flow was in transitional regime, the possible value of f was between 0.03 and 0.045 (Moody, 1944) for the smooth FEP pipe.

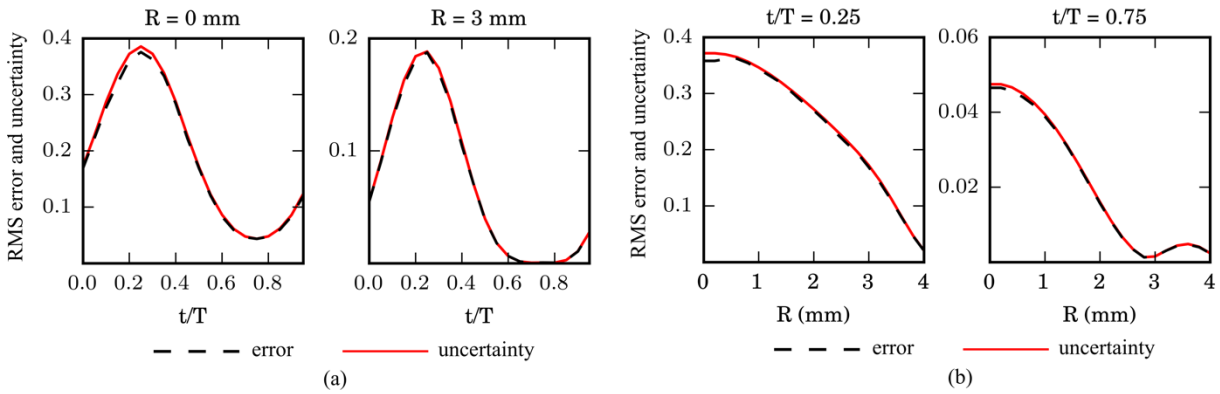

Figure 5.5 For the case with 9.6% SC velocity errors, (a) The RMS of streamwise relative pressure gradient errors ϵ_{pgradx} and uncertainties σ_{pgradx} at all temporal phases for the grid points along centerline (R=0 mm) and at R=3 mm. (b) The spanwise distributions of RMS errors and uncertainties at t/T=0.25 and at t/T=0.75.

5.4 Results

5.4.1 Synthetic flow fields

Pressure gradient uncertainty estimation

For the 2D pulsatile flow fields, the relative velocity error magnitudes ($|\epsilon_{\boldsymbol{u}}|$) were calculated as $\sqrt{\epsilon_u^2 + \epsilon_v^2}/u_0$. The overall velocity error level for each test case was represented as the median $|\epsilon_{\boldsymbol{u}}|$ from all the points in space and time. The pressure gradient fields were calculated as introduced in Sect. 5.2.1.1, and the relative pressure gradient errors $\boldsymbol{\epsilon_{\nabla p}}$ were evaluated as the deviations from the analytical solutions, then normalized by $p_0/\Delta x$. To validate the linear-transformation based uncertainty propagation algorithm for both instantaneous and local prediction, the root mean square (RMS) value of the estimated uncertainty distributions were compared with the RMS of the true error distributions in time and space since the RMS error should match the RMS uncertainty for a successful prediction (Sciacchitano et al., 2015). In Figure

5.5(a), the temporal variations of the RMS values of the estimated relative streamwise pressure gradient uncertainty ($\hat{\sigma}_{pgradx}$) and the relative streamwise pressure gradient errors ($|\epsilon_{pgradx}|$) were compared for the test case with 9.6% SC velocity errors (α=15%) at two spatial locations (along the centerline and at R=3mm), and the RMS values of $\hat{\sigma}_{pgradx}$ were consistent with those of $|\epsilon_{pgradx}|$ for both spatial locations at all time points. In Figure 5.5(b), the spanwise distributions of the RMS values of $|\epsilon_{pgradx}|$ and $\hat{\sigma}_{pgradx}$ were compared at two phases (t/T=0.25 and 0.75). Greater $|\epsilon_{pgradx}|$ and $\hat{\sigma}_{pgradx}$ were found near the centerline of the flow field for both phases, and the RMS values of $\hat{\sigma}_{pgradx}$ were consistent with those of $|\epsilon_{pgradx}|$. Overall, the comparisons suggested that the proposed algorithm was capable of predicting the instantaneous and local uncertainty of the calculated pressure gradients.

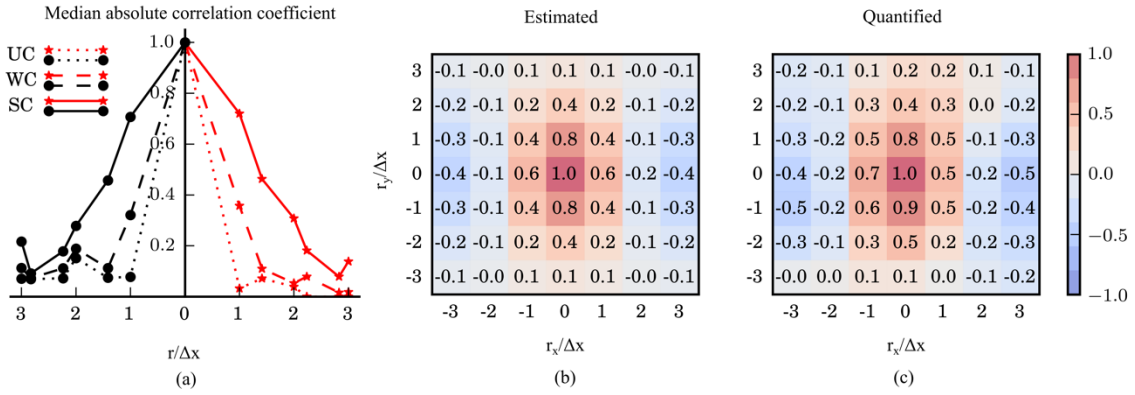

Figure 5.6 (a) The median absolute auto-correlation coefficients of $\boldsymbol{\rho_{pgradx}}$ as a function of normalized spatial separation $\boldsymbol{r/\Delta x}$. The statistically quantified $\boldsymbol{\rho_{pgradx}}$ from $\boldsymbol{\epsilon_{pgradx}}$ (left quadrant) is compared with the estimated $\boldsymbol{\hat{\rho}_{pgradx}}$ using proposed linear-transformation based algorithm (right quadrant). The distributions of $\boldsymbol{\hat{\rho}_{pgradx}}$ (b) and $\boldsymbol{\rho_{pgradx}}$ (c) around the center point at t/T=0.25.

The estimated auto-correlation coefficients $\hat{\rho}_{pgradx}$ were validated by comparing to the statistically quantified coefficients ρ_{pgradx} based on the true errors. For each test case and each time phase, the ρ_{pgradx} between all pairs of spatial points were quantified using the errors across all the frames as

$$\rho_{pgradx} = \frac{Cov(\epsilon_{pgradx,1}, \epsilon_{pgradx,2})}{\sigma_{pgradx,1}\sigma_{pgradx,2}} \quad (5\text{-}28)$$

where $Cov(\epsilon_{pgradx,1}, \epsilon_{pgradx,2})$ is the covariance between pressure gradient errors at points 1 and 2, while $\sigma_{pgradx,1}$ and $\sigma_{pgradx,2}$ are the STDs of pressure gradient errors at the two points, respectively. The median absolute ρ_{pgradx} was determined to illustrate the auto-correlation strength for each spatial separation r. As a demonstration, the median absolute ρ_{pgradx} as a function of $r/\Delta x$ is shown in Figure 5.6(a), for the test cases with 9.6% velocity errors. The estimated coefficients on the right quadrant were consistent with the quantified coefficients on the left quadrant. In general, the auto-correlation of ϵ_{pgradx} was stronger for smaller r as well as for the test case with stronger correlated $\boldsymbol{\epsilon_u}$. At $r = \Delta x$, the median absolute ρ_{pgradx} was 0.07 for UC case, while the values were 0.32 and 0.71 for WC and SC cases, respectively. The corresponding $\hat{\rho}_{pgradx}$ values were 0.03 for UC, 0.36 for WC, and 0.72 for SC. To validate the local and instantaneous prediction of auto-correlation coefficients, the ρ_{pgradx} and $\hat{\rho}_{pgradx}$ values between the center point (x=10 mm and y=0 mm) and its neighboring points are presented in Figure 5.6(b) and (c), respectively, for the test case with 9.6% SC velocity errors at phase t/T=0.25. The estimated values were also in good agreement with quantified results. The ρ_{pgradx} decreased monotonically from the center point along both spanwise and streamwise directions, and the decreasing rate was greater along streamwise direction than the spanwise direction with negative coefficients near the edges. The ρ_{pgradx} distributions were also investigated for other regions as well as other phases of the flow and were found to be dependent on the local and instantaneous flow conditions. The proposed uncertainty estimation algorithm was able to estimate the ρ_{pgradx} accurately for all the investigated locations and phases.

Pressure reconstruction

The instantaneous pressure fields were reconstructed using the methods introduced in Section 5.2.1. From each test case, the pressure errors were calculated as the deviations from analytical solution at all the points in space and time, then normalized by p_0. Three pressure error metrics were employed to evaluate the performances of the methods. The median absolute pressure error was used to represent the overall pressure error level, while the 15.75th and 84.25th percentiles

of the probability distribution of absolute pressure error were defined as the lower-bound (LB) and upper-bound (UB), respectively. The pressure error metrics as functions of the velocity error levels are compared in Figure 5.7(a) between PPE and GLS, and in Figure 5.7 (b) between least-squares based methods. In addition, the pressure error level was also determined based on the bias error and the random error separately. The bias error at temporal phase ϕ and spatial location $\boldsymbol{r}$ was quantified as $\epsilon_{bias}^{\phi,\boldsymbol{r}} = \frac{1}{N_{cycle}} \sum_{k=1}^{N_{cycle}} \epsilon_p^{k,\phi,\boldsymbol{r}}$, where $N_{cycle} = 50$ is the total number of cycles, and $\epsilon_p^{k,\phi,\boldsymbol{r}}$ is the pressure error at cycle k, temporal phase ϕ, and spatial location $\boldsymbol{r}$. The random error was then evaluated by subtracting the bias error from the total error as $\epsilon_{random}^{k,\phi,r} = \epsilon_p^{k,\phi,\boldsymbol{r}} - \epsilon_{bias}^{\phi,\boldsymbol{r}}$. As shown in Figure 5.7, with α in Eqn. 25 varied from 1 % to 50 %, the velocity error level increased from 0.64% to 32.1%. The GLS method was more robust to velocity errors compared with the other methods. For the case with 32.1% UC velocity errors, the total pressure error was 20.3% by PPE and only 5.8% by GLS as suggested in Figure 5.7 (a). For the same case, WLS and OLS yielded 6.9% and 20.4% pressure errors, respectively, as suggested in Figure 5.7 (b). The error bounds of GLS were also lower than those by PPE, OLS, and WLS. The improvement by GLS was more significant for cases with greater velocity errors. Compared to PPE, the GLS method reduced the total pressure error level by 50% (2.4% vs 3.6%) with 9.6% UC velocity errors, and by 250% (5.8% vs 20.3%) with 32.1% UC velocity errors.

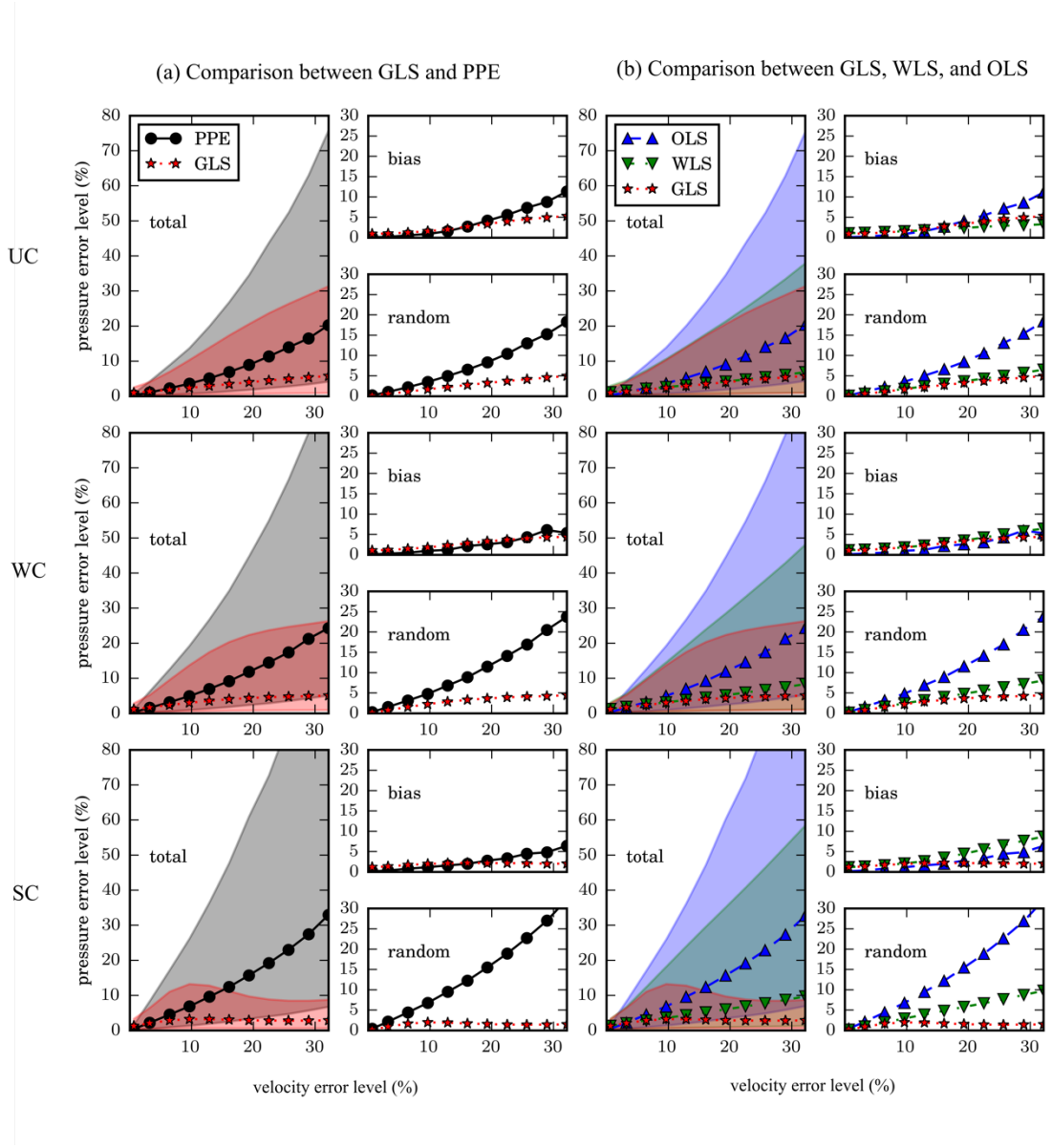

Figure 5.7 Comparisons of the pressure reconstruction methods for a wide range of velocity error levels and three correlation levels. (a) Comparison between GLS and PPE. (b) Comparison between GLS, WLS, and OLS. From top to bottom, the correlation levels are uncorrelated (UC), weakly correlated (WC), and strongly correlated (SC).

The spatial correlation of velocity errors amplified the pressure errors by PPE, OLS, and WLS, as suggested in Fig. 7. With 32.1% velocity errors, the pressure error levels by PPE as 20.3% for UC, 24.3% for WC, and 32.9% for SC. In contrast, GLS yielded lower pressure errors for cases with stronger correlated velocity errors. With 32.1% velocity errors, the pressure error levels were 5.8% for UC, 5.1% for WC, and only 2.9% for SC. At around 10% SC velocity level, the pressure

error level by GLS plateaued, and the increase of velocity error level no longer amplified the resulted pressure error level. As a consequence, the improvement by GLS was more significant for cases with spatial correlated velocity errors. The WLS had similar performances as GLS for cases with UC velocity errors, but not for WC or SC cases as shown in Figure 5.7 (b).

However, the GLS method yielded greater pressure errors for cases with minimal velocity errors compared to PPE and OLS. As suggested in Figure 5.7, the total pressure error level by GLS was 0.96% with 0.64% UC velocity errors, while it was 0.24% and 0.27% by PPE and OLS, respectively. GLS created more bias errors for cases with low velocity errors compared to OLS and PPE. With 0.64% UC velocity errors, the bias error level was 0.93% by GLS, while it was 0.10% and 0.12% by PPE and OLS, respectively. With 9.6% UC velocity errors, the bias error levels were 1.58% by GLS, 0.89% by PPE, and 0.89% by OLS. The bias error in the reconstructed pressure was also amplified by the spatial correlation of velocity errors. With 9.6% SC velocity errors, the bias error levels were 1.96% by GLS, 1.15% by PPE, and 1.14% by OLS. The random errors were consistently reduced by GLS across all the cases compared to the other methods. Since the random errors were more significant than bias errors in most cases, the GLS reduced the overall pressure error levels. For the cases with higher velocity error levels (greater than 20%), GLS reduced both bias and random errors, therefore improved the pressure accuracy significantly.

The effect of temporal resolution on the performances of different pressure reconstruction methods were studied by using different number of timeframes (from 2 to 20) to reconstruct the pressure fields for each cycle of the Womersley flow. The total error, bias error, and random error levels of the reconstructed pressure fields as a function of Δt normalized by the cycle period is reported in Figure 5.8. As the normalized Δt increased from 0.05 to 0.5, the bias error levels by PPE and OLS increased from 1% to 6% due to the increase in the truncation error for evaluating the temporal derivatives, while the bias error by GLS or WLS remained at around 2%. The GLS and WLS created greater bias errors than PPE or OLS for the majority of tested Δt but better suppressed the increase of bias error for severely under-resolved data. The random error levels were not significantly affected by the change of Δt by all the methods, and GLS consistently yielded the least amount of random error.

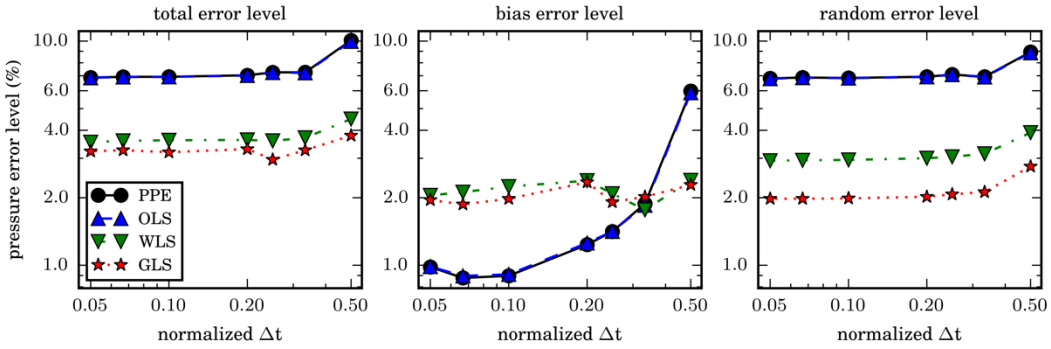

Figure 5.8 Comparison between PPE, OLS, WLS, and GLS for the pressure reconstruction with different temporal resolutions with 9.6% SC velocity errors

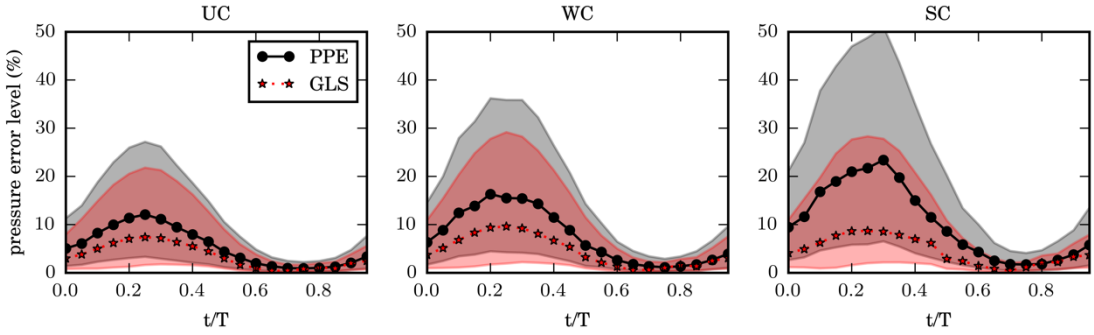

Figure 5.9 Comparison between GLS and PPE at all time phases for the cases with 9.6% velocity error level.

The performance of GLS was investigated at different time phases of the pulsatile flow. Figure 5.9 compares the pressure error levels and error bounds between GLS and PPE at each phase for the test cases with 9.6% velocity errors. The pressure errors were greater for the phases with stronger flow. With SC velocity errors, the pressure error level by GLS was 3.2% for the whole cycle, while it was 8.7% at t/T=0.25 (maximum flow rate) and 1.2% at t/T=0.75 (minimum flow rate). For phases with low flow rates (t/T between 0.6 to 0.8), both GLS and PPE yielded accurate pressure fields with error levels less than 5%. However, GLS improved the pressure accuracy significantly for the phases with greater flow rates. At t/T=0.25 with SC velocity errors, the pressure error level by PPE was 21.7% , while it was 8.7% by GLS.

The spatial distributions of relative RMS pressure errors are compared in Figure 5.10 between GLS and PPE at phase t/T=0.25 for the cases with 9.6% velocity errors. The RMS pressure errors were greater near the centerline of the flow field due to the greater pressure gradient errors as suggested in Figure 5.5(b). Compared to PPE, the GLS constrained the high pressure errors within the centerline region and dramatically reduced the pressure errors in near-wall regions. In addition, the improvement by GLS was more significant for test cases with spatial correlated velocity errors. With SC errors, the GLS reduced the pressure errors significantly for both centerline region and the near-wall regions.

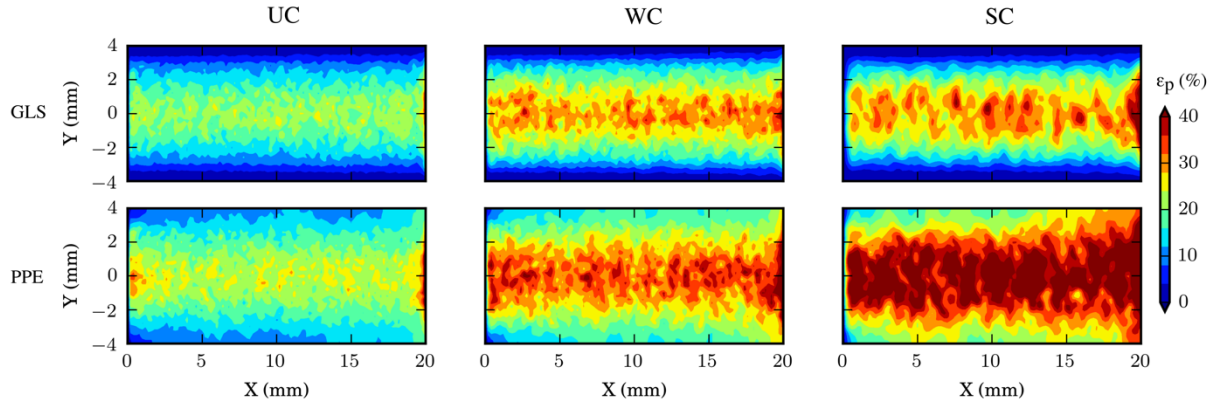

Figure 5.10 The spatial distributions of pressure RMS errors by GLS (top row) and PPE (bottom row) for the test cases with 9.6% velocity error level.

The GLS pressure reconstruction was also performed for WC and SC cases with the assumption of zero velocity error covariances (GLS 0Cov). Compared to GLS, the GLS 0Cov underestimated the covariances of $\epsilon_{\nabla p}$ due to the ignorance of the auto-correlation of velocity errors, and the captured $\epsilon_{\nabla p}$ covariances were caused by the numerical differentiations during pressure gradient calculation. The pressure error levels as functions of velocity error levels were compared between PPE, GLS, and the GLS 0Cov in Figure 5.11. As the velocity error level increased from 0.64% to 32.1%, the pressure error level by GLS 0Cov changed from 1.0 to 7.1 % for WC cases and from 1.0 to 8.8 % for SC cases. By neglecting the velocity error covariances, the GLS 0Cov had a slightly worse performance than GLS for WC cases, while the performance deficit became more dramatic for SC cases due to the significance of velocity error auto-correlations. With 16.1% velocity errors, the pressure error level by GLS 0Cov was 8% larger than GLS for the WC case and 70% larger for the SC case. Compared to the baseline method PPE, GLS

0Cov still reduced the pressure errors dramatically for most cases. With 16.1% velocity errors, the pressure error reduction by GLS 0Cov was 110% for the WC case and 138% for the SC case.

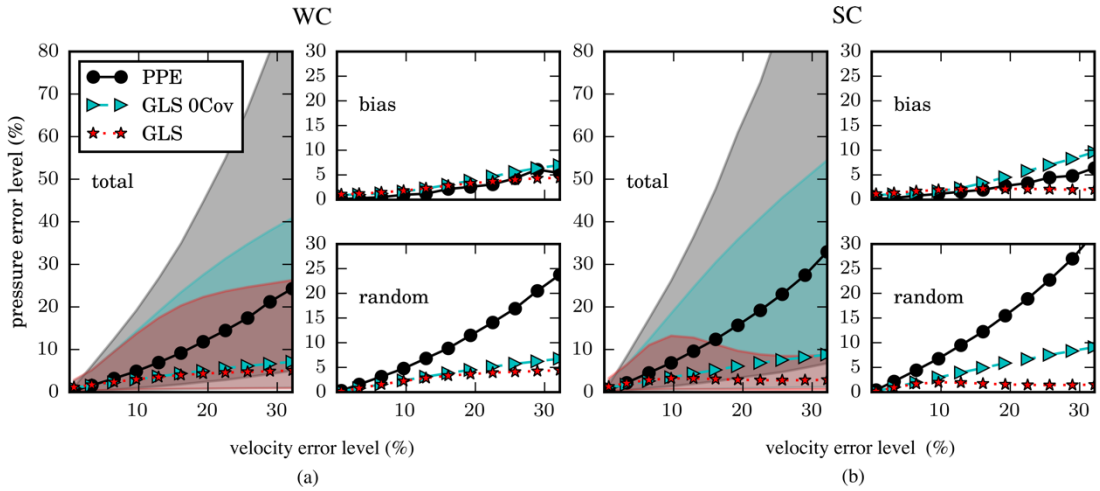

Figure 5.11 Comparisons between pressure reconstruction using PPE, GLS with full velocity error covariances, and GLS with zero velocity error covariances for the test cases with WC velocity errors (a) and SC velocity errors (b).

5.4.2 Laminar pipe flow

For the experimental validation case of laminar pipe flow, the parabolic streamwise (along X direction) velocity profile is shown in Figure 5.12(a) as a function of Y and Z using the averaged values across all the frames and Y-Z slices. The velocity errors were calculated as the deviations between the gridded velocity data and the analytical solution given by Eqn. 26 then normalized by the characteristic velocity $U_{centerline}$. To assess the accuracy of the measurement, the histograms of the relative velocity error magnitudes ($|\boldsymbol{\epsilon_u}|$), velocity STD magnitudes ($|\boldsymbol{\sigma_u}|$), and velocity uncertainty magnitudes ($|\hat{\boldsymbol{\sigma}}_{\boldsymbol{u}}|$) estimated using the divergence-based algorithm introduced in 2.1.5 are shown in Figure 5.12 (b). The RMS values was 12.0% for $|\boldsymbol{\epsilon_u}|$, 10.9% for $|\boldsymbol{\sigma_u}|$, and 5.9% for $|\hat{\boldsymbol{\sigma}}_{\boldsymbol{u}}|$, as suggested by the vertical lines. The spatial distributions of $|\boldsymbol{\sigma_u}|$ and $|\hat{\boldsymbol{\sigma}}_{\boldsymbol{u}}|$ as functions of radial location $R = \sqrt{Y^2 + Z^2}$ and streamwise location X were shown in Figure 5.12 (c), and greater $|\boldsymbol{\sigma_u}|$ was found near the wall of the pipe. In general, the $|\hat{\boldsymbol{\sigma}}_{\boldsymbol{u}}|$ had a 50% underprediction and less spatial variation. The relative errors of the calculated pressure gradients $\boldsymbol{\epsilon_{\nabla p}}$ were determined as the deviations from the analytical solution then normalized by $p_0/\Delta x$. Two sets of pressure gradient uncertainties were estimated using the proposed linear-transformation based

algorithm from $\boldsymbol{\sigma_u}$ and $\widehat{\boldsymbol{\sigma}}_{\boldsymbol{u}}$, and are denoted as $\widehat{\boldsymbol{\sigma}}_{\boldsymbol{\nabla p}}(\boldsymbol{\sigma_u})$ and $\widehat{\boldsymbol{\sigma}}_{\boldsymbol{\nabla p}}(\widehat{\boldsymbol{\sigma}}_{\boldsymbol{u}})$, respectively. The histograms of the relative errors and uncertainties are shown in Figure 5.12 (d). The RMS values were 198% for $|\boldsymbol{\epsilon}_{\boldsymbol{\nabla p}}|$, 200% for $|\widehat{\boldsymbol{\sigma}}_{\boldsymbol{\nabla p}}(\boldsymbol{\sigma_u})|$, and 109% for $|\widehat{\boldsymbol{\sigma}}_{\boldsymbol{\nabla p}}(\widehat{\boldsymbol{\sigma}}_{\boldsymbol{u}})|$ as suggested by the vertical lines. The spatial distributions of the STD of pressure gradients ($\boldsymbol{\sigma}_{\boldsymbol{\nabla p}}$) and the uncertainties are shown in Figure 5.12 (e) as functions of R and X. The $\widehat{\boldsymbol{\sigma}}_{\boldsymbol{\nabla p}}(\boldsymbol{\sigma_u})$ was consistent with the $\boldsymbol{\sigma}_{\boldsymbol{\nabla p}}$ in terms of the histograms and the spatial distributions**,** while $\widehat{\boldsymbol{\sigma}}_{\boldsymbol{\nabla p}}(\widehat{\boldsymbol{\sigma}}_{\boldsymbol{u}})$ yielded an underprediction and less spatial variation since it was based on $\widehat{\boldsymbol{\sigma}}_{\boldsymbol{u}}$. In addition to the uncertainty of the pressure gradient, the Frobenius norm of the pressure gradient tensor ($\|\nabla p\|_F$) was calculated to indicate the local reliability of the flow measurement for setting up the OLS SEQ subdomains as introduced by Jeon et al. 2018. The $\|\nabla p\|_F$ normalized by its global L2 norm was presented in Figure 5.12 (f) as a function of R and X. The distribution of $\|\nabla p\|_F$ also suggested that the measurement near the wall was less reliable than the region near the centerline.

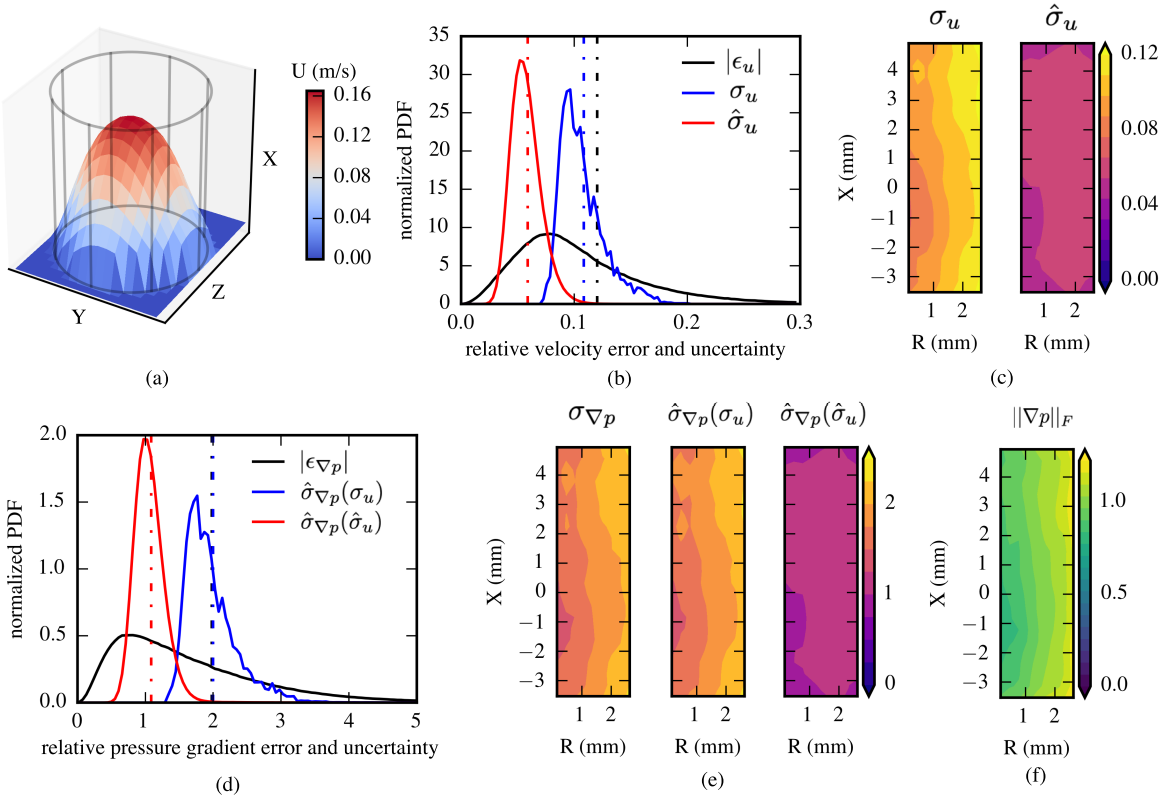

Figure 5.12 (a) The average streamwise velocity profile as a function of Y and Z. (b) The histograms of the magnitudes of velocity errors ($|\epsilon_u|$), standard deviations (σ_u) and estimated uncertainties ($\hat{\sigma}_u$). The vertical lines represent the RMS values of the distributions. (c) The spatial distributions of σ_u and $\hat{\sigma}_u$. (d) The histograms of the magnitudes of pressure gradient errors ($|\epsilon_{\nabla p}|$), the uncertainties estimated from σ_u ($\hat{\sigma}_{\nabla p}(\sigma_u)$), and the uncertainties estimated from $\hat{\sigma}_u$ ($\hat{\sigma}_{\nabla p}(\hat{\sigma}_u)$). The vertical lines represent the RMS values of the distributions. (e) The spatial distributions of the magnitudes of pressure gradient STD ($\sigma_{\nabla p}$) and the estimated uncertainties $\hat{\sigma}_{\nabla p}(\sigma_u)$ and $\hat{\sigma}_{\nabla p}(\hat{\sigma}_u)$. (e) The spatial distribution of $\|\nabla p\|_F$ normalized by its global L2 norm.

The errors of the reconstructed pressure fields were quantified as the deviations from the analytical solution then normalized by the characteristic pressure p_0. The pressure STDs over the 499 velocity frames were also calculated to assess the precision of the pressure results. The histograms of the absolute pressure errors ($|\epsilon_p|$) and pressure STDs (σ_p) were compared in Figure 5.13 (a) and (b), respectively. The median of $|\epsilon_p|$ was 219% for PPE, 164% for OLS SEQ, 112% for GLS STD, and 135% for GLS UNC, as suggested by the vertical dashed lines in Figure 5.13 (a). Compared to PPE, the error reduction was 96% by GLS STD and 62% by GLS UNC in terms of median $|\epsilon_p|$. The median of σ_p was 308% for PPE, 244% for OLS SEQ, 165% for GLS STD,

and 200% for GLS UNC, which suggested a precision improvement of 87% by GLS STD and 54% by GLS UNC compared to PPE. The spatial distributions (as functions of R and X) of the RMS ϵ_p were compared in Figure 5.13 (c) between PPE, OLS SEQ, and GLS reconstructions. The pressure errors were lower near the center of inflow plane where the reference pressure was assigned, and increased towards the outflow plane and pipe walls. The GLS method mitigated the error propagation across the field and therefore effectively improved the pressure accuracy. The OLS SEQ method improved the accuracy of the reconstructed pressure compared to PPE as it prevented the error propagation from the unreliable wall region to the reliable core region. A hybrid method which performed the GLS reconstruction sequentially in subdomains (GLS SEQ) were also tested on the laminar pipe flow with velocity STD employed as the velocity uncertainty. GLS SEQ provided more accurate pressure than OLS SEQ. However, the global GLS reconstructions still had better performances than GLS SEQ.

To study the effect of time-resolution on the pressure reconstruction methods, the 499 time frames of velocity data were downsampled by skipping frames to create four additional datasets with Δt of 2 times, 4 times, 8 times, and 16 times of the original $\Delta t_0 = \frac{1}{6000}$ s. The pressure fields were reconstructed from each dataset using PPE, OLS SEQ, GLS STD, and GLS UNC with the same settings as the original full time-resolution dataset. The relative median absolute pressure errors were presented in Figure 5.13 (d) as a function of the normalized time-resolution $\Delta t/\Delta t_0$. The pressure error levels were effectively reduced by the increase of Δt with a first order relationship for the laminar pipe flow. The analysis also suggested that the improvement by GLS was not affected by Δt as GLS consistently provided the best performances among the tested methods on the datasets different Δt.

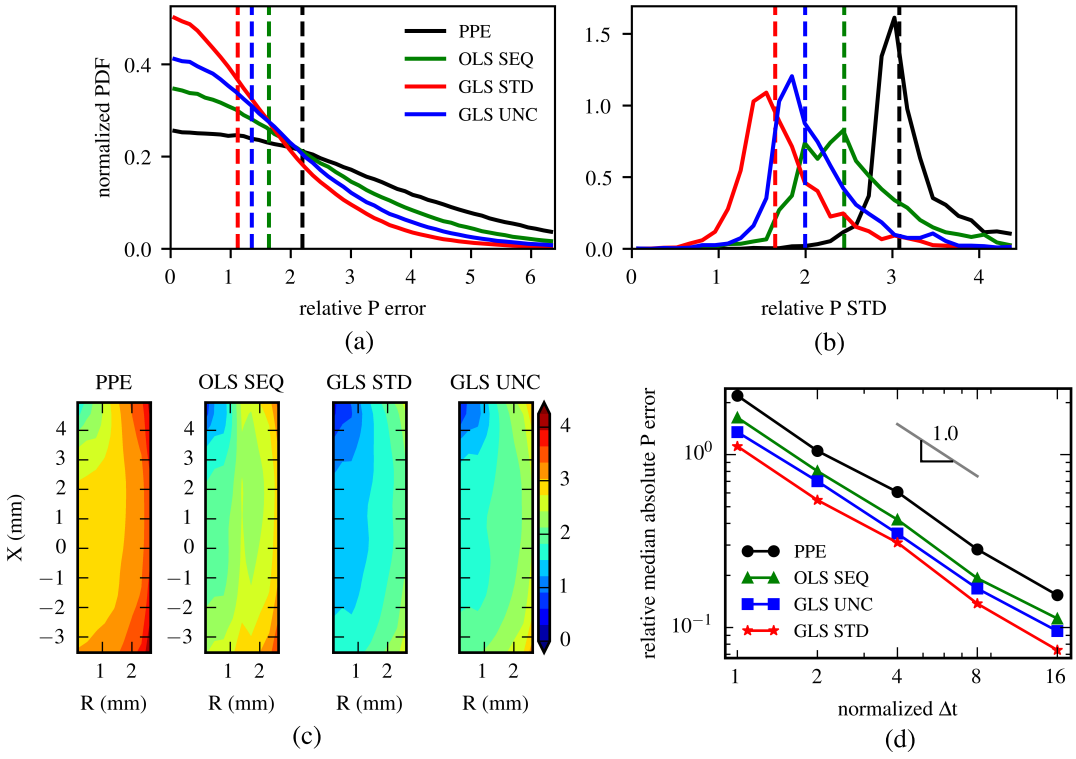

Figure 5.13 Histograms of the absolute pressure errors $|\boldsymbol{\epsilon_p}|$ (a) and pressure STDs $\boldsymbol{\sigma_p}$ (b) by PPE, OLS SEQ and the GLS reconstructions with different velocity uncertainty sources (GLS STD with $\boldsymbol{\sigma_u}$ and GLS UNC with $\widehat{\boldsymbol{\sigma}}_{\boldsymbol{u}}$). The vertical dashed lines represent the medians. (c) The spatial distributions of pressure RMS errors as functions of R and X. (d) The relative median absolute pressure errors by PPE, OLS SEQ, and GLS reconstructions as a function of time-resolution.

5.4.3 Transitional pipe flow

The pressure drop related to inflow plane was evaluated along 431 axial lines from 200 frames of the reconstructed pressure fields by GLS and PPE. The mean pressure drop as a function of X location by GLS and PPE were presented in Figure 5.14 together with the estimation using the empirical equation. The shaded region for the reconstructed pressure corresponds to the uncertainty of the mean calculated as $\sigma_{\Delta p}/\sqrt{n}$ with $\sigma_{\Delta p}$ being the STD of the Δp and n being the number of samples (431×200). The shaded regions of the empirical estimation indicated the uncertainty in the friction coefficient as $0.03 \leq f \leq 0.045$. The mean of the total Δp along the reconstructed 8.3 mm pipe length was 6.44 Pa by GLS and 8.87 Pa by PPE. The empirical

estimation of the total Δp ranged from 4.77 to 7.15 Pa. The Δp by GLS was more consistent with the empirical estimation, and the total pressure drop was within the range of the empirical estimation.

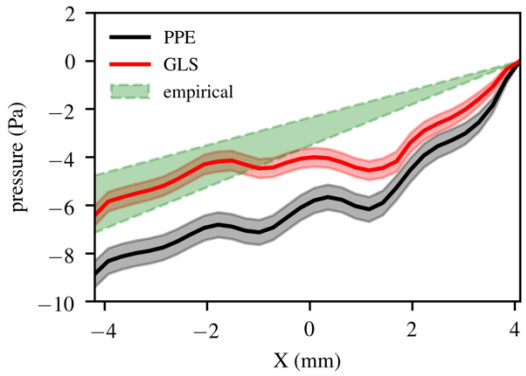

Figure 5.14 The mean pressure drop related to the inflow plane as a function of X location evaluated from reconstructed pressure fields by GLS and PPE, and the empirical estimation of pressure drop using Eqn. 27. The shaded red/black area corresponds to the uncertainty in the mean of the reconstructed pressure drop, and the shaded green area represents the range of empirical estimation.

The spatial distributions of vorticity and reconstructed pressure fields are presented in Figure 5.15 on the X-Y plane at center Z location for one time frame. The out-of-plane vorticity ω_z was shown in Figure 5.15 (a) with the velocity vectors representing the in-plane flow direction. The vortices were detected using the Q criteria, and the contours in Figure 5.15 corresponded to Q=1e+4 $1/s^2$ (thin line) and Q=5e+4 $1/s^2$ (thick line). The reconstructed pressure fields normalized by the characteristic pressure $P_0 = \rho \bar{U}$ were presented in Figure 5.15 (b) and (c) for GLS and PPE, respectively. Both GLS and PPE captured the regions of local minimum pressure around the vortex cores as observed in Figure 5.15 (b-c).

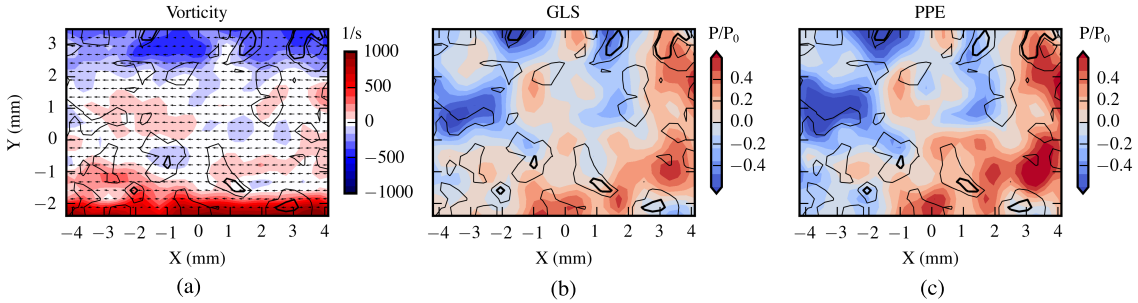

Figure 5.15 (a) The in-plane velocity (vectors) and out-of-plane vorticity (color scale) on the X-Y plane at center Z location for a time frame. (b) The normalized pressure distribution on the center X-Y plane reconstructed by GLS. (c) The normalized pressure distribution on the center X-Y plane reconstructed by PPE. Vortices were identified using Q criteria and the contours correspond to Q=1e+4 $1/s^2$ (thin line) and Q=5e+4 $1/s^2$ (thick line).

5.5 Discussion

In this study we introduced a novel pressure reconstruction method using uncertainty-based generalized least-squares. By propagating the velocity uncertainty with the proposed linear-transformation based algorithm, the pressure gradient uncertainty are estimated in the form of covariance matrices of the heteroscedastic and correlated pressure gradient errors. The pressure integration was formulated as solving an overdetermined linear system involving pressure gradient fields and boundary conditions. The error mitigation by GLS was the result of incorporating the pressure gradient uncertainty into the pressure integration. The OLS method, which solves the same linear system (Eqn. 5-15) as GLS without utilizing the uncertainty, yielded a similar performance as PPE for all the synthetic flow cases. This suggested that the change of formulation alone (the overdetermined linear system compared to the PPE) does not affect the robustness of pressure reconstruction, which was consistent with the statement by Wang et al. (2017) that PPE and OLS are mathematically identical given the same stencil and boundary conditions. The comparisons between OLS, WLS, and GLS in Figure 5.7(b) indicated that both the variance and covariance of the pressure gradient errors contributed to the improvement of pressure accuracy. The WLS method, which only employs the variances, had a better performance than OLS. By considering both variances and covariances, the GLS method further improved the pressure accuracy compared to WLS. With stronger correlated velocity errors, the covariances of pressure

gradient errors became more significant as suggested by Figure 5.6(a), thus the GLS was more effective as it utilized the covariances for pressure reconstruction as suggested in Figure 5.7.

The proposed linear-transformation based algorithm was capable of predicting the variances and covariances of the pressure gradient errors locally and instantaneously, as suggested in Figure 5.5 and Figure 5.6. Compared with the approaches introduced by Azijli et al. (2016) which performed exact uncertainty propagation assuming Gaussian-distributed velocity errors or carried out Monte Carlo simulations, the proposed algorithm does not assume any particular form of the velocity error distribution and is more computationally efficient due to the linearization of the error propagation. The formulation of Eqn. 5-7 and the analyses in Sect. 5.3.1.1 also suggested that the pressure gradient uncertainty is dependent on many factors including the velocity uncertainty, the discretization scheme, the spatiotemporal resolution, the local velocity profile, etc. As a consequence, the variances and covariances of the pressure gradient errors usually differ from those of velocity errors. One example is the auto-correlation coefficients ρ_{pgradx} around the center point in Figure 5.6(b-c). Although the $\rho_{u1,u2}$ (as defined by Eqn. 5-23) varied isotropically with nonnegative values, the variation of ρ_{pgradx} was anisotropic with both positive and negative correlations. In addition, the error magnitudes of the calculated pressure gradient can be significantly different from those of the measured velocity. For the laminar pipe flow, the RMS error amplification from velocity to pressure gradient was 16.5 as suggested in Figure 5.12(b) and (d). This dramatic error amplification was due to the small time separation Δt (1/6000 s) of the flow measurement. As discussed by van Oudheusden (2013), decreasing Δt reduces the truncation error of finite difference, but increases the effect of velocity error on pressure gradient calculation with Eulerian approach. For steady flows, using a large Δt would effectively reduce the error amplification as suggested in Figure 5.13 (d). For the unsteady Womersley flow, the effect of Δt was less significant as suggested in Figure 5.8. The GLS method created more bias error than PPE or OLS but better suppressed the increase of bias error for severely under-resolved data.

The performance of GLS pressure reconstruction was affected by the reliability of the provided velocity uncertainty. Since the a-posterior method to estimate velocity uncertainty from volumetric PTV has not been established, the uncertainty of the laminar pipe flow data was obtained from the velocity fields with two approaches in this study. The first approach took the STD over all the velocity frames ($\boldsymbol{\sigma_u}$) and was a reliable estimation for the steady flow. The second approach estimated $\hat{\boldsymbol{\epsilon}}_{\boldsymbol{u}}$ from the spurious velocity-divergence of the incompressible flow then

estimated the $\widehat{\boldsymbol{\sigma}}_{\boldsymbol{u}}$ as the WSTD of $\hat{\boldsymbol{\epsilon}}_{\boldsymbol{u}}$. As the $\hat{\boldsymbol{\epsilon}}_{\boldsymbol{u}}$ was calculated from Eqn. 5-19 in a least-squares sense, an underestimation of $\widehat{\boldsymbol{\sigma}}_{\boldsymbol{u}}$ was caused as suggested in Figure 5.12(b). With the less reliable $\widehat{\boldsymbol{\sigma}}_{\boldsymbol{u}}$, the GLS UNC had a slightly worse performance than GLS STD, while both GLS UNC and GLS STD still effectively improved the pressure accuracy compared to PPE.

The performance of GLS was also affected by the completeness of the provided velocity uncertainty. To ensure an accurate prediction of the pressure gradient uncertainty, both the variances and covariances of the velocity errors are required. However, there has not been any established method to estimate the covariances of velocity errors for PIV/PTV. A more practical condition was considered in this study by performing the GLS with zero velocity covariances (GLS 0Cov) on the synthetic flow fields with correlated velocity errors (nonzero covariances). As suggested in Figure 5.11, the GLS 0Cov had slightly worse performances than GLS, while still effectively improved the pressure accuracy compared to PPE. For the experimental laminar pipe flow, the velocity error covariances were also unavailable and assumed to be zero, and the GLS pressure reconstructions yielded more accurate pressure estimations than PPE as suggested in Figure 5.13. These analyses indicated the practical benefits of using GLS for pressure reconstruction even without the velocity error covariances.

There are several limitations of the GLS pressure reconstruction method. First, the GLS method requires the velocity uncertainty to be estimated instantaneously and locally. For planar/stereo PIV measurements, there are several methods to estimate the velocity uncertainty (Bhattacharya et al., 2017, 2018; Charonko & Vlachos, 2013; Timmins, Wilson, Smith, & Vlachos, 2012; Xue et al., 2015). However, these methods remain untested for volumetric PIV, and only one recent development has covered the a-posterior uncertainty quantification for volumetric PTV (Bhattacharya & Vlachos, 2019). The velocity-divergence based algorithm introduced in Section 5.2.1.5 can provide velocity uncertainty regardless of the measurement technique. However, the algorithm underestimates the velocity uncertainty as it is based on the least-squares estimation of velocity error from velocity-divergence using Eqn 5-19. Moreover, none of these methods can provide the covariances of velocity errors. The performance of GLS with the velocity uncertainty estimated using the existing uncertainty quantification methods can be explored in future work. In addition, the GLS method created greater pressure bias error compared to PPE and OLS for cases with low velocity noise level (less than 10%) as suggested in Figure 5.7. Furthermore, the GLS method has greater computational cost than the other methods employed in the present study. As

described in Section 5.2.1.4, the GLS reconstruction needs to solve the augmented linear system to avoid operations with the dense matrix Σ_b^{-1}. The augmented systems are approximately 3 times and 4 times as large as the linear systems of PPE for planar data and volumetric data, respectively. Thus, more computational effort is required for GLS reconstruction compared to PPE, OLS, or WLS. For the laminar pipe flow data with 3772 grid points within the flow field, the average elapsed time per frame using a workstation with 16 cores (Intel Xeon CPU E5-2450 v2) was 1.45 s for PPE, 1.18 s for OLS, 2.37 s for WLS, and 28.0 s for GLS. For larger volumetric flow fields, the WLS method is preferred which requires much less computational cost than GLS as suggested by the elapsed time. The WLS reconstruction was demonstrated with synthetic flow fields and showed significant improvement compared to PPE as suggested in Figure 5.7(b). The WLS has also been employed to estimate the instantaneous pressure fields from velocity fields measured using PTV in patient-specific aneurysm models (Zhang et al., 2019). In addition, the proposed GLS pressure reconstruction can only be applied to incompressible flow fields since the formulations of pressure gradient calculation and uncertainty propagation are only valid for incompressible flows. Also, the current framework of GLS pressure reconstruction and the pressure gradient uncertainty estimation algorithm are only applicable to gridded velocity data with the Eulerian approach for pressure gradient calculation. For Lagrangian approach with material acceleration acquired from particle tracks, additional error sources such as interpolation errors and propagation position errors need to be considered (Van Gent et al. 2018a, b). To ensure the accuracy of numerical differentiations, the GLS method requires spatiotemporal resolved velocity measurements.

This study presented an instantaneous pressure reconstruction method using uncertainty information with generalized least-squares. The pressure gradient fields were calculated from the velocity fields measured by PIV/PTV, and a linear-transformation based algorithm was introduced to estimate the local and instantaneous pressure gradient uncertainty-based on the velocity uncertainty. The pressure fields are reconstructed by GLS which utilizes the pressure gradient and its uncertainty. The performance of GLS was tested for synthetic flow fields with a wide range of velocity error levels and both correlated and uncorrelated velocity errors. The GLS method effectively reduced the random errors in the pressure fields compared to the baseline method of solving the PPE. The error mitigation by GLS is due to the utilization of both variances and covariances of the pressure gradient errors. The improvement by GLS was more significant for

cases with greater velocity errors. Compared to PPE, the pressure error reduction by GLS was 50% and 250% with 9.6% and 32.1% velocity errors, respectively. With spatially correlated velocity errors, the GLS was more effective as it utilized the stronger correlation of pressure gradient errors during reconstruction. For velocity data with high accuracy, the PPE or OLS should be used as they create less bias error in the reconstructed pressure field compared to GLS. The laminar pipe flow measured by volumetric PTV was employed to demonstrate the GLS pressure reconstruction, and a 96% error reduction was achieved compared to PPE. The GLS also predicted reasonable estimations on the pressure drop as well as the spatial pressure distribution for the transitional pipe flow. Overall, the present study successfully demonstrates the framework of employing uncertainty information to improve the pressure reconstruction from 2D or 3D velocity fields. Further development could include the usage of estimated velocity uncertainty from flow measurements for the GLS pressure reconstruction.

5.6 Authors' contributions

J.Z. developed and evaluated the method, performed the data analysis, and drafted the manuscript. S.B. performed the experimental measurement and pre-processed the data. P.P.V. designed and oversaw the study and all data analysis. All authors critically reviewed and edited the manuscript, and gave final approval for publication.

6. UNCERTAINTY OF PIV/PTV BASED EULERIAN PRESSURE ESTIMATION USING VELOCITY UNCERTAINTY

This chapter is reproduced with permission from: Zhang, J., Bhattacharya, S., Vlachos, P.P., 2022. Uncertainty of PIV/PTV based Eulerian pressure estimation using velocity uncertainty. Meas. Sci. Technol. 33, 065303. https://doi.org/10.1088/1361-6501/ac56bf

6.1 Background and literature review

Pressure reconstruction from velocity measurements using particle image velocimetry (PIV) and particle tracking velocimetry (PTV) provides instantaneous pressure fields without invasively altering the flow (Charonko et al., 2010; Fujisawa et al., 2005; Huhn et al., 2016; Liu & Katz, 2006; Nathan J. Neeteson & Rival, 2015). The PIV/PTV-based pressure reconstruction starts with calculating the pressure-gradients from velocity fields using the Navier-Stokes equation, which is then spatially integrated to obtain the pressure fields. The pressure gradients can be calculated using Eulerian approaches from gridded data (Charonko et al., 2010; Roeland de Kat et al., 2009; Fujisawa et al., 2005; Tronchin et al., 2015) or Lagrangian approaches from particle tracks (R. De Kat & Van Oudheusden, 2012; Gesemann et al., 2016; Ghaemi et al., 2012; Huhn et al., 2016; Liu & Katz, 2006; N. J. Neeteson et al., 2016; P. L. Van Gent et al., 2018a, 2018b) with different formulations for evaluating the material acceleration. The pressure-gradients are usually integrated using the path-integration algorithms (Dabiri et al., 2014; Liu & Katz, 2006; Tronchin et al., 2015), by solving the pressure Poisson equation (PPE) (R. De Kat & Van Oudheusden, 2012; Fujisawa et al., 2005; Nathan J. Neeteson & Rival, 2015; Schneiders et al., 2016; Violato et al., 2011), or using least-squares methods (Jeon et al., 2018; P. L. Van Gent et al., 2018a; Zhang, Bhattacharya, & Vlachos, 2020; Zhang et al., 2019).

Previous studies have assessed the accuracy of the pressure fields reconstructed from PIV/PTV measurements with different methods (Charonko et al., 2010; McClure & Yarusevych, 2017b; P. L. Van Gent et al., 2018a, 2018b; P. van Gent et al., 2017; van Oudheusden, 2013; Zhang, Bhattacharya, et al., 2020). The error analysis results suggested that several factors can affect the accuracy of the pressure-gradients and subsequently the pressure fields, including the spatial and temporal resolutions, the velocity measurement error levels and error profiles, the level of out-of-plane motion for planar measurement, and the approaches for calculating the material acceleration

(Charonko et al., 2010; R. De Kat & Van Oudheusden, 2012; Faiella, Grant Jeon Macmillan, Whitehead, & Pan, 2021; van Oudheusden, 2013). Moreover, the accuracy of the obtained pressure fields also depends on the algorithms for pressure-gradient integration, the type and reliability of the pressure boundary conditions, and the size, shape, and dimension of the domain (Charonko et al., 2010; Faiella et al., 2021; Pan et al., 2016; Zhang, Bhattacharya, et al., 2020; Zhang et al., 2019).

In addition to the many factors that affect the reconstructed pressure's accuracy, it is also essential to understand the error propagation characteristics for estimating the pressure uncertainty. De Kat and Van Oudheusden (R. De Kat & Van Oudheusden, 2012) used a simplified linear propagation for modeling the noise propagation from velocity to pressure gradient and compared the sensitivity of the Eulerian and Lagrangian approaches. Following this, Laskari *et al.* (Laskari, de Kat, & Ganapathisubramani, 2016) proposed the uncertainty propagation formulations for the pressure-gradient calculation with the Eulerian, pseudo-Lagrangian, and Talyor's hypothesis approaches. However, these two approaches did not consider the spatial variation of velocity uncertainty or the propagation through the pressure-gradient integration. Several methods have also been proposed to use the physical and mathematical constraints to estimate the pressure uncertainty. Azijli *et al.* (Azijli et al., 2016b) introduced a Bayesian framework that estimates the velocity uncertainty from velocity divergence and propagates the posterior covariance matrix of velocity field to the pressure field, assuming normal-distributed errors. McClure and Yarusevych (McClure & Yarusevych, 2017a, 2017b) estimated the instantaneous pressure-gradient error based on the divergence and curl of the pressure-gradient field and used a line-integration approximation to model the uncertainty propagation from pressure-gradient to pressure field. Focusing on the the pressure integration, Pan et al. (Pan et al., 2016) investigated the dynamics of error propagation through PPE and quantified the error bounds of the pressure field related to the uncertainty in the pressure gradient and the boundary condition. Faiella et al. (Faiella et al., 2021) also quantified the effect of the location and profile of the error in the data field on the resultant error in the reconstructed pressure field, which was achieved by analyzing the Green's function of the PPE and the eigenvalue of a Poisson operator. Liu and Moreto (Liu & Moreto, 2020) analyzed the error propagation characteristics of the pressure-gradient integration carried with the omni-directional method.

Besides modeling the error propagation dynamics, the error level and error profile in the measured velocity fields are needed to estimate the uncertainty of the reconstructed pressure fields. The existing uncertainty quantification algorithms can provide the local and instantaneous uncertainty of the velocity measurement with PIV (Bhattacharya et al., 2018; Charonko & Vlachos, 2013; Sciacchitano, 2019; Sciacchitano, Wieneke, & Scarano, 2013; Timmins et al., 2012; Bernhard Wieneke, 2015; Xue et al., 2014, 2015) and PTV (Bhattacharya & Vlachos, 2020), which can be used to infer the pressure uncertainty. The velocity uncertainty is typically defined as the standard deviation of the velocity error distribution (standard uncertainty) or the confidence interval for a predefined probability (expanded uncertainty) (Sciacchitano, 2019). This study introduces a method to propagate the standard velocity uncertainty to the reconstructed pressure field. The uncertainty propagations through the calculation and integration of the pressure-gradient were modeled as linear transformations, which were able to reproduce the effects of the spatiotemporal resolutions, numerical schemes, the integration algorithms, and the pressure boundary conditions on the pressure accuracy. The method was first validated with synthetic velocity fields contaminated with artificial velocity errors correlated in space, time, and between components. The method was then applied to experimental flow fields measured using PIV and PTV.

6.2 Methods

The procedures of PIV/PTV-based pressure reconstruction and pressure uncertainty estimation are demonstrated in Figure 6.1. The pressure-gradient field is calculated from the measured velocity fields using the Navier-Stokes momentum equation, and the pressure field is reconstructed by spatially integrating the pressure gradients. The pressure-gradient uncertainty was estimated by propagating the velocity covariance matrix consisting of the velocity uncertainty and the covariances between velocity errors. The covariances were determined by modeling the correlation coefficients for PIV measurements or estimated based on the spatial interpolation of particle tracks to gridded velocity data for PTV measurements. The pressure uncertainty is then determined by propagating the pressure-gradient uncertainty through the integration process. The details on the methodology are presented in sections 6.2.1 and 6.2.2.

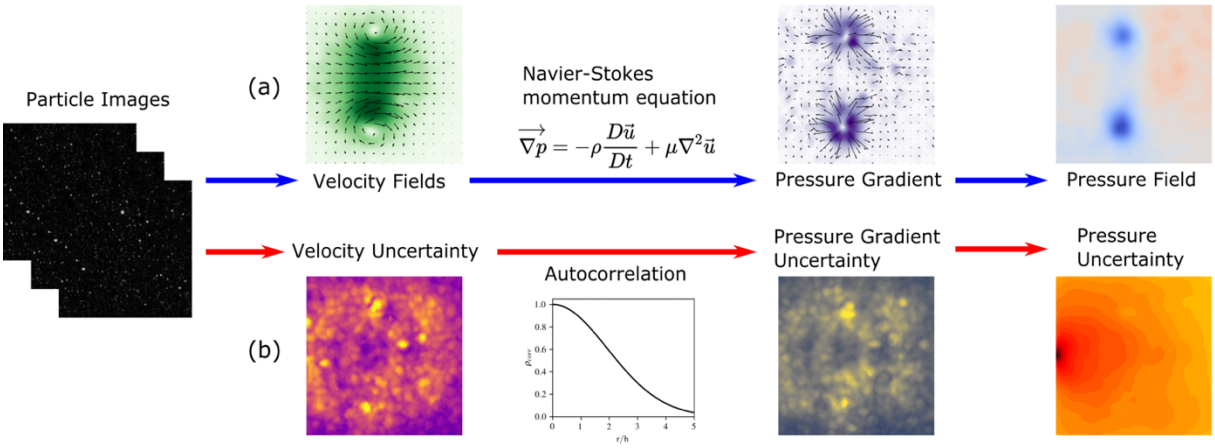

Figure 6.1 The schematic demonstrating the procedure of PIV/PTV based pressure reconstruction (a, blue arrows) and the estimation of pressure uncertainty (b, red arrows).

6.2.1 Pressure-gradient calculation and uncertainty propagation

The pressure-gradient can be calculated from the velocity field using the Navier-Stokes momentum equation as:

$$\boldsymbol{\nabla p} = -\rho\frac{D\boldsymbol{u}}{Dt} + \mu\nabla^2\boldsymbol{u}, \tag{6-1}$$

where p is the pressure, $\boldsymbol{u}$ is the velocity, ρ is density, μ is dynamic viscosity, $\frac{D\boldsymbol{u}}{Dt}$ is the material acceleration, and $\mu\nabla^2\boldsymbol{u}$ is the viscous diffusion. For gridded velocity data, the pressure-gradient can be calculated using the Eulerian approach, which determines the material acceleration as the combination of the local acceleration ($\frac{\partial\boldsymbol{u}}{\partial t}$) and the convective acceleration ($\boldsymbol{u}\cdot\nabla\boldsymbol{u}$) as:

$$\boldsymbol{\nabla p} = -\rho\left(\frac{\partial\boldsymbol{u_m}}{\partial t} + \boldsymbol{u_m}\cdot\nabla\boldsymbol{u_m}\right) + \mu\nabla^2\boldsymbol{u_m}, \tag{6-2}$$

The temporal derivative $\frac{\partial\boldsymbol{u_m}}{\partial t}$ was evaluated as the differences between the velocity fields at neighboring time points normalized by the time separation. The velocity fields were organized into column vectors with $3N$ elements by concatenating all the velocity components (u, v, and w) from

all the N grid points in the field, and the spatial differentiation was conducted with the discrete linear operators (2D matrices). Therefore, equation **Error! Reference source not found.** was evaluated using matrix/vector operations, and $\boldsymbol{\nabla p}$ was obtained as a column vector with 3N elements including all the pressure-gradient components ($\frac{dp}{dx}$, $\frac{dp}{dy}$, and $\frac{dp}{dz}$) from all the grid points. The present study employed the second-order central (SOC) difference scheme to calculate the spatial and temporal derivatives except for the boundary points where the first-order one-sided scheme was used.

With the assumptions that the truncation error is negligible compared to the random error, and the velocity error ($\boldsymbol{\epsilon_u}$) is significantly less than $\boldsymbol{u_m}$, the pressure-gradient error ($\boldsymbol{\epsilon_{\nabla p}}$) can be derived from equation (6-3) as:

$$\boldsymbol{\epsilon_{\nabla p}} = -\rho\left(\frac{\partial \boldsymbol{\epsilon_u}}{\partial t} + \boldsymbol{u_m}\cdot\nabla\boldsymbol{\epsilon_u} + \boldsymbol{\epsilon_u}\cdot\nabla\boldsymbol{u_m}\right) + \mu\nabla^2\boldsymbol{\epsilon_u}. \qquad (6\text{-}3)$$

Like equation (6-2), equation (6-3) was evaluated using matrix/vector operations as:

$$\boldsymbol{\epsilon_{\nabla p}} = [M_- \quad M \quad M_+]\begin{bmatrix}\boldsymbol{\epsilon_u^{i-1}}\\ \boldsymbol{\epsilon_u^{i}}\\ \boldsymbol{\epsilon_u^{i+1}}\end{bmatrix} \equiv M_c\boldsymbol{\epsilon_u^c}, \qquad (6\text{-}4)$$

with $M_+ = -\frac{\rho}{\Delta t}I$, $M_- = \frac{\rho}{\Delta t}I$,

and $M = -\rho\left(diag(\boldsymbol{u_m^i})\cdot\nabla + diag(\nabla\boldsymbol{u_m^i})\right) + \mu\nabla^2$,

where the superscript i corresponds to the i-th timeframe, I is the identity matrix, and $diag()$ represents the diagonal matrix with the diagonal elements from the given vector. The matrices M, M_-, and M_+ transform the velocity errors from the previous, current, and following timeframes denoted as $\boldsymbol{\epsilon_u^{i-1}}$, $\boldsymbol{\epsilon_u^{i}}$, and $\boldsymbol{\epsilon_u^{i+1}}$ to the components of the pressure-gradient error $\boldsymbol{\epsilon_{\nabla p}}$. The matrix $M_c \equiv [M_- \quad M \quad M_+]$ represents the combined transformation corresponding to the combined velocity errors $\boldsymbol{\epsilon_u^c} \equiv [\boldsymbol{\epsilon_u^{i-1}} \quad \boldsymbol{\epsilon_u^{i}} \quad \boldsymbol{\epsilon_u^{i+1}}]^T$.

The standard uncertainty of the velocity measurement with PIV and PTV was used to construct the covariance matrix of $\boldsymbol{\epsilon_u}$. For volumetric measurement with three velocity-components, the covariance matrix Σ_u with a shape of $3N \times 3N$ can be expressed as:

$$\Sigma_{\boldsymbol{u}} = \begin{bmatrix} \Sigma_{uu} & \Sigma_{uv} & \Sigma_{uw} \\ \Sigma_{uv} & \Sigma_{vv} & \Sigma_{vw} \\ \Sigma_{uw} & \Sigma_{vw} & \Sigma_{ww} \end{bmatrix}. \tag{6-5}$$

Each diagonal block (Σ_{uu}, Σ_{vv}, and Σ_{ww}) of $\Sigma_{\boldsymbol{u}}$ has a shape of $N \times N$ and represents the covariance matrix of each velocity component. The diagonal elements in the diagonal blocks are the variances of the velocity errors, while the off-diagonal elements correspond to the autocorrelation between different grid points. The off-diagonal blocks of $\Sigma_{\boldsymbol{u}}$ consist of the covariances between the errors from different velocity components indicated by the subscripts and are null-matrices if different velocity components are uncorrelated. The dimension of $\Sigma_{\boldsymbol{u}}$ becomes smaller for planar two-component data by removing the blocks associated with the w-component. The covariance matrix for the combined error vector ϵ_u^c containing multiple timeframes can be constructed accordingly as:

$$\Sigma_u^c = \begin{bmatrix} \Sigma_u^{i-1,i-1} & \Sigma_u^{i,i-1} & \Sigma_u^{i-1,i+1} \\ \Sigma_u^{i,i-1} & \Sigma_u^{i,i} & \Sigma_u^{i,i+1} \\ \Sigma_u^{i-1,i+1} & \Sigma_u^{i,i+1} & \Sigma_u^{i+1,i+1} \end{bmatrix}, \tag{6-6}$$

where the diagonal blocks are the covariance matrices for the velocity errors at frame $i-1$, i, and $i+1$ as indicated by the superscript. The off-diagonal blocks contain the covariances between the velocity errors from different timeframes, which are zeros for temporally uncorrelated errors. The pressure-gradient uncertainty can be determined by propagating Σ_u^c through equation (6-4) as:

$$\Sigma_{\nabla p} = M_c \Sigma_u^c M_c^T \tag{6-7}$$

where $\Sigma_{\nabla p}$ is the covariance matrix of $\epsilon_{\nabla p}$ whose diagonal elements are the variances of the pressure-gradient errors at each grid point, and the off-diagonal elements correspond to the correlation in space or between different pressure-gradient components. This linear-transformation-based uncertainty propagation has been applied to synthetic flow fields with spatially correlated velocity errors and could predict both variances and covariances of the pressure-gradient errors (Zhang, Bhattacharya, et al., 2020).

6.2.2 Pressure field calculation and uncertainty propagation

The present study considered the uncertainty propagation through the pressure-gradient integration with the PPE method and the least-squares methods, estimated as linear transformations.

Pressure Poisson equation

The PPE can be formulated as:

$$\nabla^2 \boldsymbol{p} = \nabla \cdot \boldsymbol{\nabla p} \equiv \boldsymbol{s}, \tag{6-8}$$

where $\boldsymbol{p}$ is a column vector containing the pressure to be solved, and the source term $\boldsymbol{s}$ is evaluated as the divergence of the pressure-gradient calculated from equation (6-2). The Laplacian (∇^2) and divergence ($\nabla \cdot$) calculations were performed using discrete linear operators constructed with the SOC scheme. At the boundary points with known pressure values, Dirichlet boundary condition can be imposed by:

$$L\boldsymbol{p} = \boldsymbol{p_{BC}}, \tag{6-9}$$

where L is the labeling matrix consisting of ones and zeros, and $\boldsymbol{p_{BC}}$ is the column vector of the known pressure values at the boundary points. The linear system of PPE with Dirichlet boundary condition is denoted as:

$$A_{PPE}\boldsymbol{p} = \boldsymbol{b_{PPE}}, \tag{6-10}$$

with $A_{PPE} \equiv \begin{bmatrix} \nabla^2 \\ L \end{bmatrix}$ and $\boldsymbol{b_{PPE}} \equiv \begin{bmatrix} \mathbf{s} \\ \boldsymbol{p_{BC}} \end{bmatrix}$. The covariance matrix of the source term $\boldsymbol{s}$ can be determined by propagating the uncertainty of the pressure-gradients $\Sigma_{\nabla p}$ through equation (6-8) as:

$$\Sigma_{\boldsymbol{s}} = (\nabla \cdot)\Sigma_{\nabla p}(\nabla \cdot)^T \tag{6-11}$$

The covariance matrix of the combined source term $\boldsymbol{b_{PPE}}$ can be obtained as:

$$\Sigma_{b,PPE} = \begin{bmatrix} \Sigma_{\boldsymbol{s}} & \\ & \Sigma_{p,BC} \end{bmatrix}, \tag{6-12}$$

where $\Sigma_{p,BC}$ is the covariance matrix for the Dirichlet boundary condition, which is a null-matrix if there is no uncertainty in the Dirichlet values. Thus, the pressure and the pressure uncertainty can be obtained by solving equation (10) and propagating Σ_b (Azijli et al., 2016b), respectively:

$$\boldsymbol{p} = A_{PPE}^{-1}\boldsymbol{b_{PPE}}, \tag{6-13}$$

$$\Sigma_p = A_{PPE}^{-1}\Sigma_{b,PPE}A_{PPE}^{-T}. \tag{6-14}$$

where Σ_p is the covariance matrix of the reconstructed pressure field.

Least-squares methods

Least-squares methods reconstruct the pressure field based on the following relationship:

$$G\boldsymbol{p} = M_L\boldsymbol{p_{grad,u}}, \tag{6-15}$$

where G is the discrete gradient operator, and M_L is a linear operator that interpolates the $\boldsymbol{p_{grad,u}}$ on the grid nodes to the staggered points located in the middle between neighboring grid nodes (Jeon et al., 2018; Zhang, Bhattacharya, et al., 2020). The Dirichlet boundary condition can be applied by incorporating equation (6-9) as:

$$\begin{bmatrix} G \\ L \end{bmatrix}\boldsymbol{p} = \begin{bmatrix} M_L\boldsymbol{p_{grad,u}} \\ \boldsymbol{p_{BC}} \end{bmatrix}, \tag{6-16}$$

The least-squares solution of equation (6-16) can be directly solved from:

$$(A_{LS}^T A_{LS})\boldsymbol{p} = A_{LS}^T\boldsymbol{b_{LS}}, \tag{6-17}$$

with $A_{LS} = \begin{bmatrix} G \\ L \end{bmatrix}$ and $b_{LS} = \begin{bmatrix} M_L\boldsymbol{p_{grad,u}} \\ \boldsymbol{p_{BC}} \end{bmatrix}$.

This pressure reconstruction approach is referred to as the ordinary least-squares (OLS) in this study, and the reconstructed pressure field is obtained as:

$$\boldsymbol{p} = (A_{LS}^T A_{LS})^{-1} A_{LS}^T \boldsymbol{b_{LS}}. \tag{6-18}$$

The uncertainty of the right-hand side of equation (6-18) can be estimated as:

$$\Sigma_{b,LS} = \begin{bmatrix} M_L \Sigma_{\nabla p} M_L^T & \\ & \Sigma_{p,BC} \end{bmatrix}, \tag{6-19}$$

which can be propagated through equation (6-17) to the reconstructed pressure field as:

$$\Sigma_p = ((A_{LS}^T A_{LS})^{-1} A_{LS}^T) \Sigma_{b,LS} ((A_{LS}^T A_{LS})^{-1} A_{LS}^T)^T. \tag{6-20}$$

The pressure-gradient uncertainty can be used to improve the pressure reconstruction with the weighted least-squares (WLS) or the generalized least-squares (GLS) methods (Zhang, Bhattacharya, et al., 2020; Zhang et al., 2019) by incorporating a weight matrix (W) to equation (6-17) as:

$$(A_{LS}^T W A_{LS}) \boldsymbol{p} = A_{LS}^T W \boldsymbol{b_{LS}}. \tag{6-21}$$

For WLS reconstruction, W is constructed as a diagonal matrix containing the reciprocals of the variances from Σ_{rhs}. For GLS, $W = \Sigma_{rhs}^{-1}$ and can be a dense matrix. The pressure uncertainty from WLS and GLS reconstructions can be estimated by propagating Σ_{rhs} as:

$$\Sigma_p = ((A_{LS}^T W A_{LS})^{-1} A_{LS}^T W) \Sigma_{b,LS} ((A_{LS}^T W A_{LS})^{-1} A_{LS}^T W)^T. \tag{6-22}$$

To improve the numerical stability, the following augmented linear system was formulated by introducing the vector $\boldsymbol{\lambda} = {\Sigma_{b,LS}}^{-1} (\boldsymbol{b_{LS}} - A_{LS} \boldsymbol{p})$ and solved for the GLS reconstruction (Zhang, Bhattacharya, et al., 2020) in the present study:

$$\begin{bmatrix} \Sigma_{b,LS} & A_{LS} \\ A_{LS}^T & 0 \end{bmatrix} \begin{bmatrix} \boldsymbol{\lambda} \\ \boldsymbol{p} \end{bmatrix} = \begin{bmatrix} \boldsymbol{b_{LS}} \\ 0 \end{bmatrix}, \tag{6-23}$$

and therefore, the uncertainty of the pressure field was determined as:

$$\begin{bmatrix} \Sigma_{\lambda} & \Sigma_{\lambda,p} \\ \Sigma_{\lambda,p} & \Sigma_p \end{bmatrix} = \begin{bmatrix} \Sigma_{b,LS} & A_{LS} \\ A_{LS}^T & 0 \end{bmatrix}^{-1} \begin{bmatrix} \Sigma_{b,LS} & 0 \\ 0 & 0 \end{bmatrix} \begin{bmatrix} \Sigma_{b,LS} & A_{LS} \\ A_{LS}^T & 0 \end{bmatrix}^{-T}. \tag{6-24}$$

6.2.3 Validation using synthetic velocity fields and experimental datasets

Synthetic velocity fields

The uncertainty propagation algorithm was first tested with the synthetic velocity fields of a 2D pulsatile flow between two infinite parallel plates (Charonko et al., 2010; Zhang, Bhattacharya, et al., 2020). The streamwise oscillating pressure gradient and velocity profile can be expressed as:

$$\frac{dp}{dx} = \rho K + \gamma \rho K cos\omega t, \tag{6-25}$$

$$u = u_{max}\left(1 - \frac{y^2}{h^2}\right) + \frac{\gamma K}{i\omega}\left(1 - \frac{cosh(y/h\sqrt{i}\lambda)}{cosh(\sqrt{i}\lambda)}\right) exp(i\omega t), \tag{6-26}$$

with $\lambda = h\sqrt{\frac{\rho}{\mu\omega}}$. h is the channel half-width, γ represents the ratio between the steady and oscillating pressure-gradients, and ρK is the pressure-gradient caused by a steady flow with a centerline velocity of u_{max}. The same parameters were used here as in (Zhang, Bhattacharya, et al., 2020), with $\omega = 2\pi$ rad/s, $u_{max} = 1$ m/s, and $\gamma = 25.13$. The fluid properties were $\rho = 1000$ kg/m^3 and $\mu = 1 \times 10^{-3}$ Pa s. The characteristic velocity and pressure were $u_0 = u_{max}$ and $p_0 = \frac{1}{2}\rho u_0^2$, respectively. The distance between the two plates (the channel width) was 8 mm. Only the bottom half of the channel (y from -4 to 0 mm) was used to save computational effort. The streamwise length of the domain was 20 mm. The velocity fields were generated on a Cartesian grid with a grid size of 0.1×0.1 mm^2 and 101×21 grid points in the domain. One thousand

timeframes were generated with a sampling rate of 20 Hz across 50 cycles. The uncertainty of the velocity fields was introduced by adding Gaussian noise to each component of the velocity field with the standard deviation proportional to the local velocity magnitude as:

$$\sigma = \alpha|\boldsymbol{u_t}|, \tag{6-27}$$

where σ is the standard deviation of the noise, $\boldsymbol{u_t}$ is the actual velocity, and α represents the noise level. To investigate the effect of velocity noise level on the pressure uncertainty, eight datasets were created with α ranging from 1% to 30%. Additional datasets were created to mimic the noise from PIV and PTV measurements with the artificial noise correlated in space, time, or between different velocity components (Sciacchitano & Wieneke, 2016). The spatial and temporal autocorrelations were prescribed using a Gaussian function of the spatial or temporal separation as:

$$\rho_{corr} = exp(-s \times r^2), \tag{6-28}$$

where ρ_{corr} is the autocorrelation coefficient between two measurements separated spatially or temporally, r represents the spatial separation normalized by the grid resolution h_{grid} Alternatively, the temporal separation normalized by the time resolution Δt, and s is the coefficient that controls the strength of the autocorrelation. Two levels of autocorrelation were considered with s being 0.22 and 0.88, leading to $\rho_{corr}(r = 1)$ of 0.8 and 0.4, respectively. Four levels of component-wise correlation coefficients ($\rho_{u,v}$) were considered, including 0.25, 0.5, 0.75, and 0.9. The correlated noise still follows equation (6-23) with a noise level of 10%. Only one type of correlation (spatial, temporal, or component-wise) was considered for each dataset to separate and investigate the effects of different correlations. The pressure fields were reconstructed with each dataset's PPE, OLS, WLS, and GLS methods. The information on the imposed velocity uncertainty and the correlations were used for estimating the pressure uncertainty.

Planar PIV measurement of a laminar vortex ring

The uncertainty estimation algorithm was tested with the planar PIV measurements of the vortex ring flow obtained from the central camera images of case E in the fourth PIV challenge (Kähler et al., 2016). The PIV processing was carried using Prana and DaVis 8.2, with standard cross-correlation (SCC) and iterative window deformation (Scarano, 2002). Four passes were performed with a window overlap of 75% for the first pass and 87.5% for the following three passes. The window size was 64×64 pixels for all the passes, and the windows were masked by a 50% Gaussian filter (Eckstein & Vlachos, 2009), such that the effective window resolutions (WR) were 32. The obtained velocity fields contain 81×81 grid points in the domain with $\Delta x = \Delta y = 0.67$ mm. A total of 50 timeframes were collected with a sampling rate of 1000 Hz. The moment of correlation (MC) (Bhattacharya et al., 2018) and image matching (IM) (Sciacchitano et al., 2013) methods were used to estimate the velocity uncertainty from the prana processing, while the velocity uncertainty from DaVis processing was obtained with the correlation statistics (CS) (Bernhard Wieneke, 2015) method. The pressure fields were reconstructed from the velocity fields using PPE, OLS, WLS, and GLS methods, and the pressure uncertainty from each reconstruction was estimated based on velocity uncertainty from MC, IM, or CS. The center point on the left boundary of the domain was assigned with 0 Pa as the Dirichlet boundary condition. To simulate the effect of the interrogation window overlap on the spatial autocorrelation of velocity errors (Sciacchitano & Wieneke, 2016), the autocorrelation coefficient ρ_{corr} was approximated as a Gaussian function of the spatial separation:

$$\rho_{corr} = exp\left(ln\left(w_{op}\right) \times r^2\right), \qquad (6\text{-}29)$$

where w_{op} is the window overlap, and r is the spatial separation normalized by the grid resolution. Thus, $\rho_{corr} = w_{op}$ between neighboring velocity measurements. The modeling of ρ_{corr} with equation (6-29) was validated with the PIV fields processed using different window overlaps. For calculating the temporal derivatives, a more prolonged time separation is preferred to reduce noise amplification. A time separation of $10\Delta t$ was selected for this dataset as:

$$\frac{du^i}{dt} = \frac{u^{i+5} - u^{i-5}}{10\Delta t}, \qquad (6\text{-}30)$$

where the superscript indicates the frame number. The obtained temporal derivatives were compared to the results with shorter time separations, and the comparison suggested that using $10\Delta t$ was sufficient to resolve the temporal variations of this flow data. The temporal autocorrelation between the frames (i-5) and (i+5) were assumed to be zero. To assess the accuracy of the velocity and pressure fields, the reference velocity fields were obtained from the three-dimensional tomographic PIV measurement using the images from all five cameras (Kähler et al., 2016). The velocity data were temporally smoothed using a 3rd order polynomial fitting to reduce the measurement noise and improve the reliability of the temporal derivative evaluation for estimating the "ground truth" pressure. The "ground truth" velocity fields were on a 121×121 grid with an isotropic resolution of 0.45 mm. The pressure fields reconstructed from the "ground truth" velocity fields using PPE and OLS methods were employed as the "ground truth" pressure for the PPE and least-squares reconstructions, respectively. The characteristic velocity (u_0) of the vortex ring flow was determined as the root-mean-square (RMS) of the velocity magnitudes from the "ground truth", and the characteristic pressure was defined as $p_0 = \frac{1}{2}\rho u_0^2$.

Volumetric PTV measurement of a laminar pipe flow

The uncertainty estimation was applied to the laminar flow in a circular pipe measured with volumetric PTV (Bhattacharya & Vlachos, 2020). A gear pump drove the flow at a steady flow-rate Q of 0.17 L/min in a FEP tube of diameter ($2R_{pipe}$) of 0.25 inches. The working fluid inside the pipe was distilled water urea (90:10) solution with a density of 1015 kg/m3 and dynamic viscosity of 0.915 mPas, and the Reynolds number was 630. The images were acquired at 6 kHz with a size of 640 × 624 pixels. The velocity fields were obtained using the triangulation (Maas et al., 1993) and Iterative Particle Reconstruction (IPR) (Bernhard Wieneke, 2013) based reconstruction and nearest-neighbor tracking, and the uncertainties from both methods were quantified using the algorithms introduced in (Bhattacharya & Vlachos, 2020). The velocity and velocity-uncertainty were determined as:

$$u_i = \frac{(x_{i+1} - x_i)}{\Delta t}, \qquad (6\text{-}31)$$

$$\sigma_{u_i}^2 = \sigma_{x_b}^2 + \sigma_{x_i}^2 + \sigma_{x_{i+1}}^2 - 2\rho_{x_i x_{i+1}}\sigma_{x_i}\sigma_{x_{i+1}}, \qquad (6\text{-}32)$$

where the subscript i indicate the timeframe number, $\sigma_{x_b}^2$ is the bias uncertainty of the particle positions, and $\rho_{x_i x_{i+1}}$ represents the correlation coefficient between the particle positions from the two neighboring frames. The velocity obtained at particle positions was interpolated using inverse distance weighting (IDW) to a Cartesian grid with an isotropic resolution of 0.42 mm, yielding around 15 grid points across the diameter of the pipe. The IDW interpolation was carried as a linear transformation:

$$u_g = M_g u_p, \tag{6-33}$$

where u_g and u_p are the velocity values on the grid nodes and the particle positions, respectively. M_g represents the coefficient matrix for the IDW interpolation. Therefore, the uncertainty of the gridded velocity data was determined as:

$$\Sigma_{u_g} = M_g \Sigma_{u_p} M_g^T, \tag{6-34}$$

where Σ_{u_g} and Σ_{u_p} are the covariance matrices for the gridded and particle velocity, respectively. The covariances of u_p were assumed to be zeros, while the covariances in the obtained Σ_{u_g} were due to the IDW interpolation. The pressure fields were reconstructed from the gridded velocity fields using PPE, OLS, WLS, and GLS methods. Same as equation (6-30), the temporal derivatives were evaluated with a time separation of $10\Delta t$ to reduce noise amplification. The center node of the inflow plane at X=0 and R=0 was assigned with 0 Pa as the Dirichlet boundary condition, while Neumann boundary was applied to the rest of the boundary points based on the local pressure gradients. The analytical solution of the laminar flow based on the flow rate was used as the "ground truth" for velocity and pressure:

$$u = -\frac{1}{4\mu}\frac{dP}{dx}\left(R_{pipe}^2 - R^2\right),$$
$$with\ \frac{dP}{dx} = -\frac{8\mu Q}{\pi R_{pipe}^4}, \tag{6-35}$$

where x is the streamwise direction, u is the streamwise velocity, and R is the radial distance from the centerline. The streamwise velocity along the pipe centerline from the analytical solution was employed as the characteristic velocity (u_0) of the flow, and the characteristic pressure was $p_0 = \frac{1}{2}\rho u_0^2$.

6.3 Results

6.3.1 Synthetic flow fields

The errors in the reconstructed pressure fields were determined as the deviation from the analytical solution, and the pressure uncertainties were estimated by propagating the imposed velocity uncertainty using the proposed method. The pressure errors and uncertainties were normalized by the flow's characteristic pressure (p_0). For the case with 10% uncorrelated velocity noise, the normalized error and uncertainty histograms were compared in Figure 6.2. An agreement was found between the RMS error and RMS uncertainty of each reconstruction as suggested by the vertical lines, which were 0.04 for PPE and OLS, and 0.026 for WLS and GLS. The spatial distributions of the pressure error and uncertainty were shown in Figure 6.4 using the RMS values evaluated at each spatial point. The pressure errors were lower near the wall ($y = -4$ mm) than the channel's centreline ($y = 0$ mm). This is because the velocity errors were lower near the wall since the standard deviation of the imposed velocity errors was proportional to the local velocity magnitude as expressed in equation (6-27). Compared to the results from PPE and OLS, better pressure accuracy was achieved in both the near-wall region and the core-flow region by WLS and GLS, leading to improved accuracy near the wall. The estimated uncertainty was consistent with the pressure error in terms of the distributions and the magnitudes for the reconstruction with each method. The pressure errors and uncertainties temporal variations were presented in Figure 6.3 using the RMS from all the spatial points at each temporal phase. The pressure uncertainty reproduced the temporal waveform of the pressure error, and the RMS uncertainty was within 10% of the corresponding RMS error at all the temporal phases for each reconstruction method.

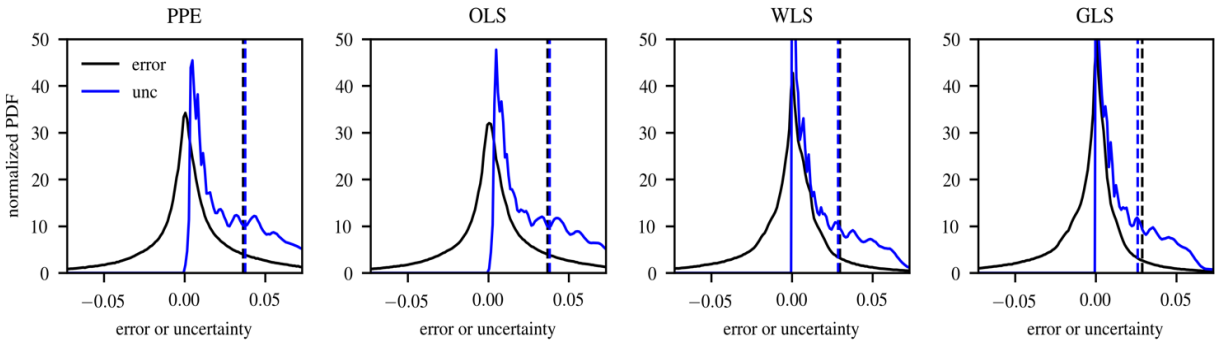

Figure 6.2 The histograms of the normalized errors and uncertainties of the pressure fields reconstructed using different methods from the synthetic flow fields with 10% uncorrelated velocity noise. The vertical lines represent the RMS values for error and uncertainty.

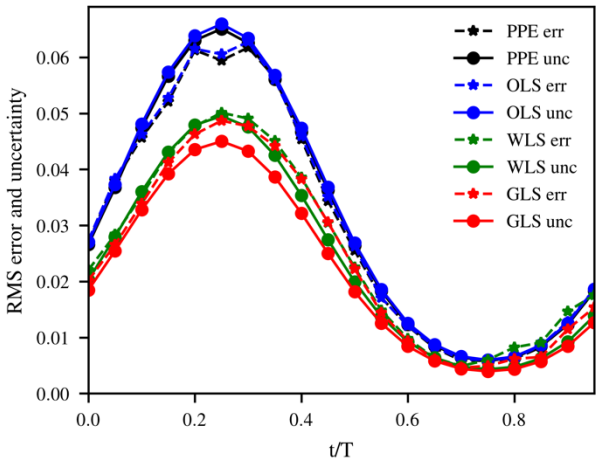

Figure 6.3 The temporal variations of the normalized errors and uncertainties of the pressure fields reconstructed using different methods from the synthetic flow fields with 10% uncorrelated velocity noise.

To study the effect of velocity noise level on the pressure errors and uncertainties, the RMS errors and uncertainties were determined from the cases with different α and presented in Figure 6.5. As α increased from 1 to 30%, the RMS pressure error increased from 0.3 to 14% for PPE and OLS and from 0.7 to 9% for WLS and GLS. Compared to PPE and OLS, the WLS and GLS methods yielded higher pressure errors for the cases with α <5%, while it was more accurate for the cases with more significant velocity noise. For PPE and OLS reconstructions, the RMS

uncertainty matched the RMS error with α <10% but was overestimated by about 10% for the cases with α >15%. At low noise levels ($\alpha \leq$5%), the WLS and GLS reconstructions' RMS uncertainty was underestimated by 40-60%, while the RMS uncertainty was within 10% of the RMS error for the remaining noise levels. At high noise levels (α >10%), the RMS uncertainty was overestimated by about 3% for WLS while underestimated by 5% for GLS. Similar errors and uncertainties were obtained from the PPE and OLS reconstructions, owning to the fact that the PPE and OLS share the same theoretical foundation as discussed in the work by Wang et al. (C. Y. Wang et al., 2017). Previous study has also shown similar performances of PPE and OLS on a synthetic 2D vortex ring flow (Zhang, Bhattacharya, et al., 2020).

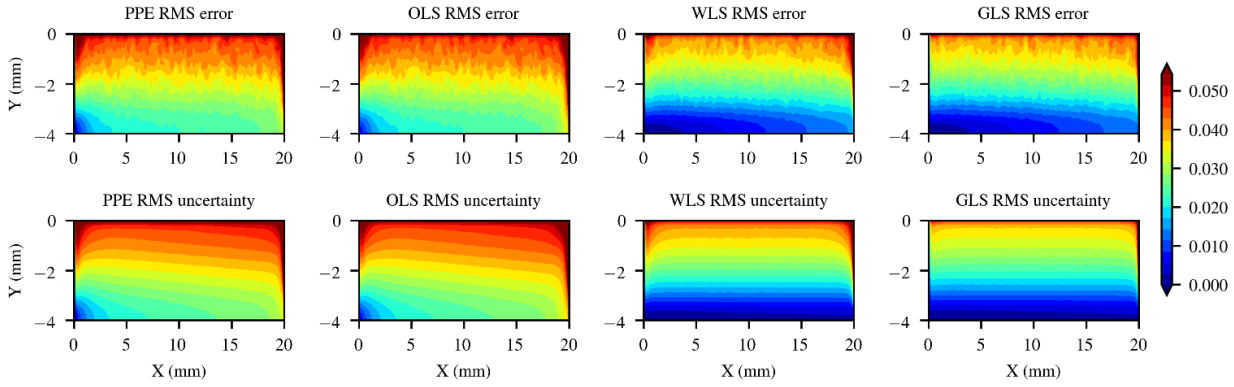

Figure 6.4 The spatial distributions of the normalized errors and uncertainties of the pressure fields reconstructed using different methods from the synthetic flow fields with 10% uncorrelated velocity noise.

The pressure error and uncertainty were obtained from the cases with spatially or temporally correlated noise to investigate the effect of the autocorrelation of velocity errors. Figure 6.6 (a) and (b) compares the pressure RMS errors and uncertainties for the cases with 10% noise (α =10%) and different levels of spatial and temporal autocorrelations, respectively. The correlation levels were represented by the correlation coefficient between neighboring spatial or temporal points ($\rho_{corr}(r = 1)$). As shown in Figure 6.6 (a), the RMS errors increased as the spatial correlation became stronger, e.g., the RMS error by PPE increased from 0.04 to 0.07 as the correlation coefficient increased from 0 to 0.8. The estimated uncertainties for PPE, OLS, and WLS were consistent with the corresponding pressure errors. For GLS reconstruction, the pressure uncertainty was underestimated by about 10% with uncorrelated noise and 20% with strongly correlated noise

($\rho_{corr}(r=1)=0.8$). As suggested in Figure 6.6 (b), the temporal autocorrelation between velocity errors had a negligible effect on the pressure error and uncertainty from this flow data. Figure 6.6 (c) presented the RMS error and uncertainty with respect to the level of component-wise correlation of velocity errors. Compared to the case with uncorrelated velocity error, a $\rho_{u,v}$ of 0.9 increased the pressure error by 15% for OLS and reduced the pressure error by 20% for GLS, while the pressure errors and uncertainties were not significantly affected by the component-wise correlation for PPE and WLS. The estimated pressure uncertainties replicated the trends of the pressure errors for PPE, WLS, and GLS reconstructions with the change of $\rho_{u,v}$.

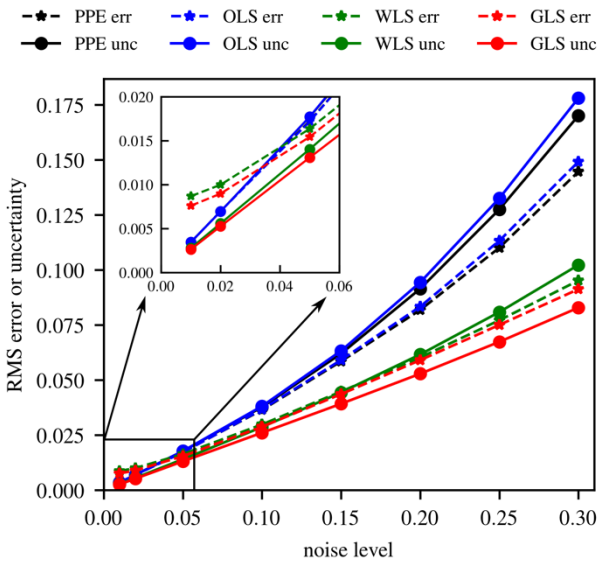

Figure 6.5 The normalized RMS errors and uncertainties of the pressure fields reconstructed using different methods from the synthetic flow fields with velocity noise levels from 1% to 30%.

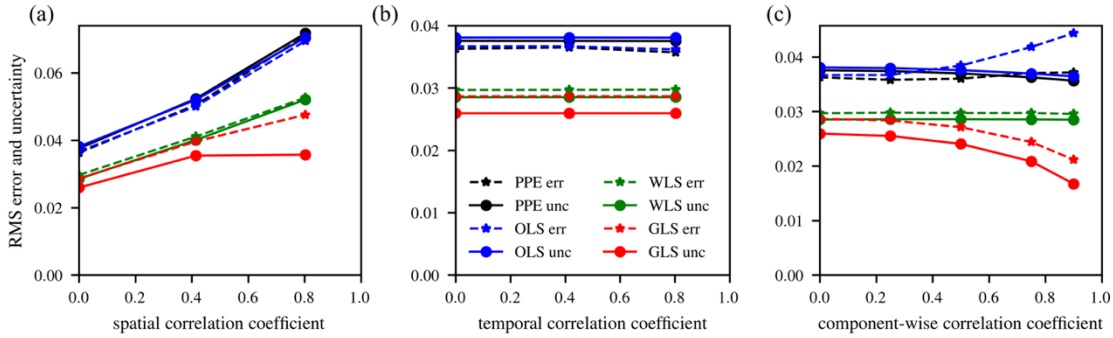

Figure 6.6 The normalized RMS errors and uncertainties of the pressure fields reconstructed using different methods from the synthetic flow fields with (a) spatially correlated velocity errors, (b) temporally correlated velocity errors, and (c) component-wise correlated velocity erros.

6.3.2 Planar PIV of the vortex ring flow

Figure 6.7 (a) presents the streamwise (U) velocity fields at the first timeframe for the "ground truth" from tomographic PIV and for the measurements using planar PIV with prana and DaVis. The velocity errors were quantified as the deviations from the "ground truth", and the velocity uncertainties were estimated using MC, IM, and CS methods. The histograms of the normalized velocity errors and uncertainties by the characteristic velocity (u_0) are presented in Figure 6.7 (b). Regarding the RMS values, the MC and IM uncertainties underestimated the velocity errors from prana by 28% and 60%, respectively, while the CS uncertainty was 47% lower than the velocity error from DaVis. Moreover, the velocity errors had broader distributions than the velocity uncertainties. The spatial distributions of the velocity errors and uncertainties are compared in Figure 6.7 (c) using the RMS at each spatial point normalized by the RMS of the whole field. Although the uncertainties predicted the locations of higher velocity errors, the uncertainties around the vortex cores were significantly underestimated, leading to more uniform spatial distributions than the velocity errors.

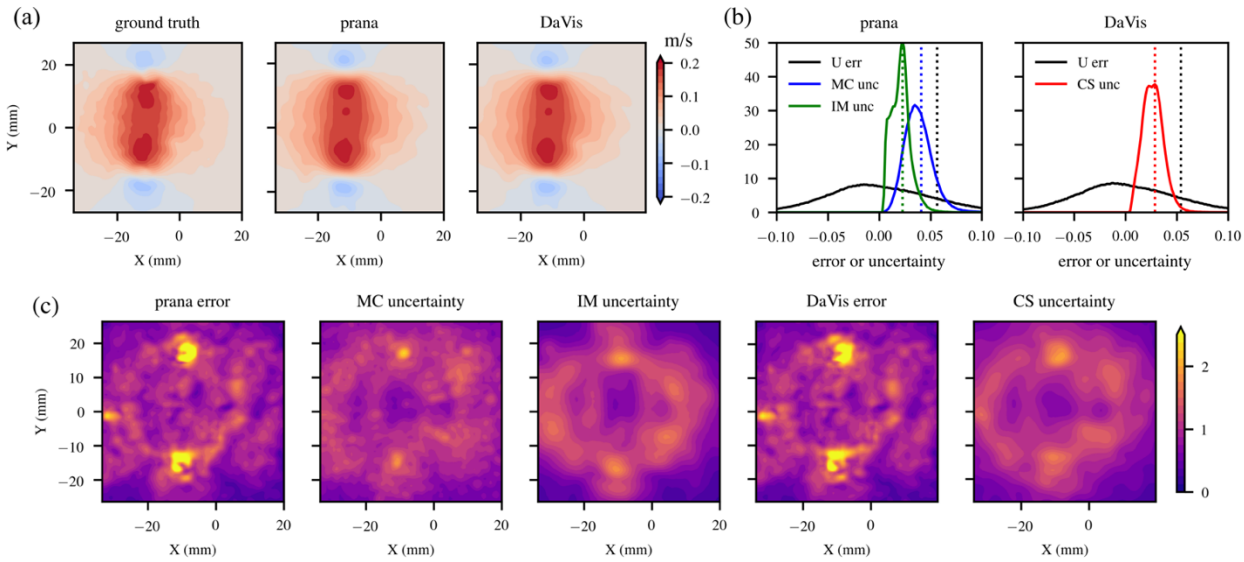

Figure 6.7 The streamwise velocity fields at the first timeframe from the "ground truth" and from the planar PIV measurement with prana and DaVis. (b) The histograms of the normalized velocity errors and uncertainties estimated with MC, IM, and CS. The RMS errors and uncertainties are indicated using vertical lines. (c) The spatial distributions of the normalized velocity errors and uncertainties.

The pressure errors from the reconstructions using PPE, OLS, WLS, and GLS were determined as the deviations from the "ground truth", and the pressure uncertainties were estimated using the proposed method based on the MC, IM, and CS velocity uncertainties. The histograms of the absolute pressure errors and uncertainties normalized by the characteristic pressure (p_0) are presented in Figure 6.8 (a) and (b) for the prana and DaVis datasets, respectively. Since the WLS and GLS reconstructions use both velocity and velocity uncertainty, different pressure results were obtained for prana velocity fields with different velocity uncertainties (MC and IM). As shown in Figure 6.8, the RMS uncertainties were underestimated compared to the RMS errors, and the distributions of pressure uncertainties were tighter than the pressure errors. The RMS errors and uncertainties were provided in Table 6.1 for the velocity and reconstructed pressure fields.

Table 6.1 The normalized RMS errors and uncertainties (%) of the velocity fields and the reconstructed pressure fields from the vortex ring flow measured with planar PIV

		velocity	PPE	OLS	WLS	GLS
prana	error	5.65	84.9	82.8	77.8	81.7
+MC	unc	4.09	66.8	64.9	59.2	21.4
prana	error	5.65	84.9	82.8	82.5	89.7
+IM	unc	2.29	40.0	39.1	36.9	17.3
DaVis	error	5.40	84.6	82.6	77.4	96.6
+CS	unc	2.88	50.1	48.5	42.6	40.8

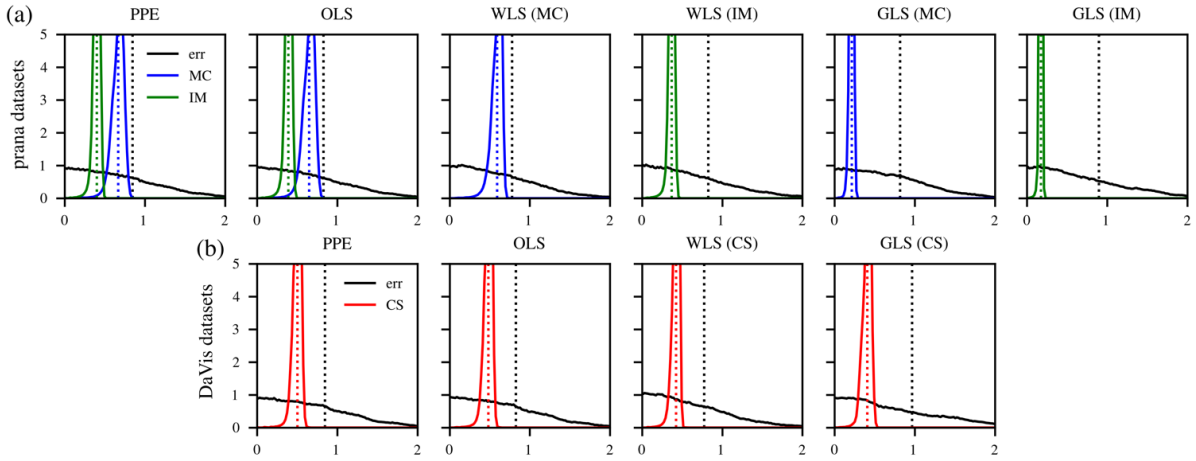

Figure 6.8 The histograms of the absolute pressure errors and the pressure uncertainties normalized by the characteristic pressure. The pressure uncertainties were estimated based on the velocity uncertainties obtained with MC and IM methods from the prana dataset (a) and with the CS method from the DaVis dataset (b).

Figure 6.10 shows the uncertainty coverage results for the velocity measurements and the pressure reconstructed with PPE, OLS, WLS, and GLS methods. The uncertainty coverage was calculated as the percentage of estimates for which the errors were contained within the standard uncertainty, and the target coverage is determined as the coverage of the standard deviation of the true errors and is shown as black squares in the figure. The velocity uncertainties were underestimated, yielding a coverage of 57% by MC, 33% by IM, and 44% by CS. Consequently, the pressure uncertainties obtained by propagating the velocity uncertainties were underestimated, yielding coverages of 34% to 55% for PPE, OLS, and WLS reconstructions, and only 17% to 35% for GLS reconstructions.

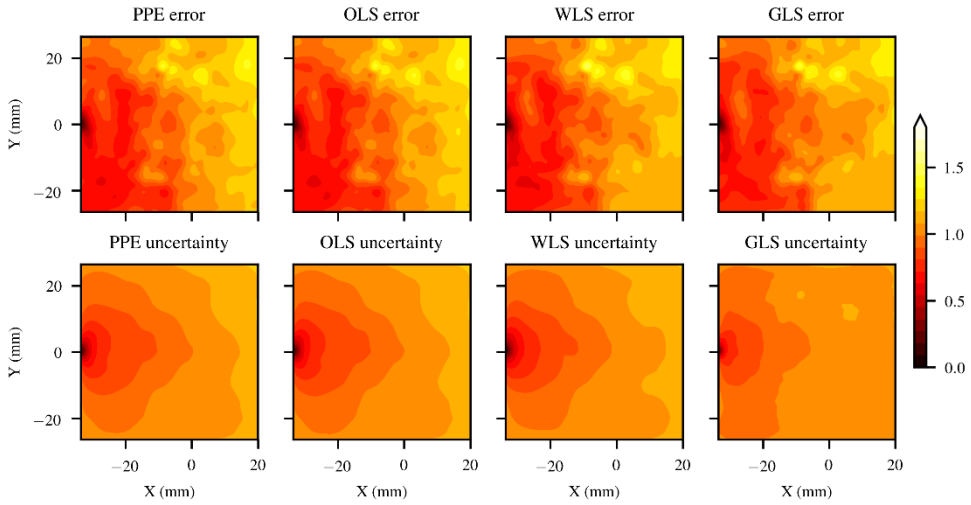

Figure 6.9 The spatial distributions of the normalized pressure errors and the normalized uncertainties estimated based on the MC velocity uncertainty for the reconstructions of the prana velocity fields using different pressure reconstruction methods.

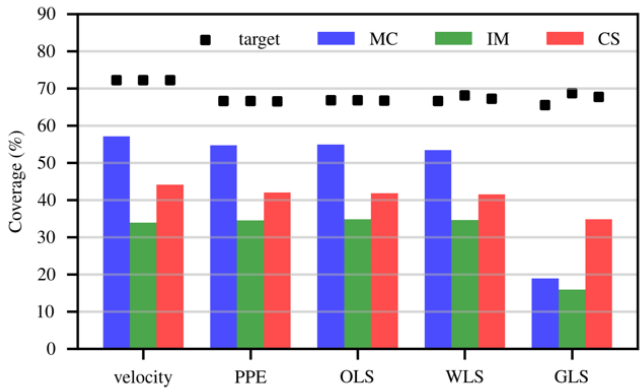

Figure 6.10 The uncertainty coverage for the velocity and reconstructed pressure with PPE, OLS, WLS, and GLS methods for the vortex ring flow. The three velocity uncertainty methods: moment of correlation (MC), image matching (IM), and correlation statistics (CS).

The spatial distributions of the pressure errors and uncertainties obtained from the prana velocity fields based on the MC uncertainty are presented in Figure 6.9 using the RMS values at each spatial point normalized by the RMS from the whole field. For all the reconstructions with different methods, the pressure errors and uncertainties increased from the reference point at the center of the left boundary to the right side of the domain. The pressure uncertainties were

underestimated around the vortex cores compared to the pressure errors, resulting in more uniform spatial distributions.

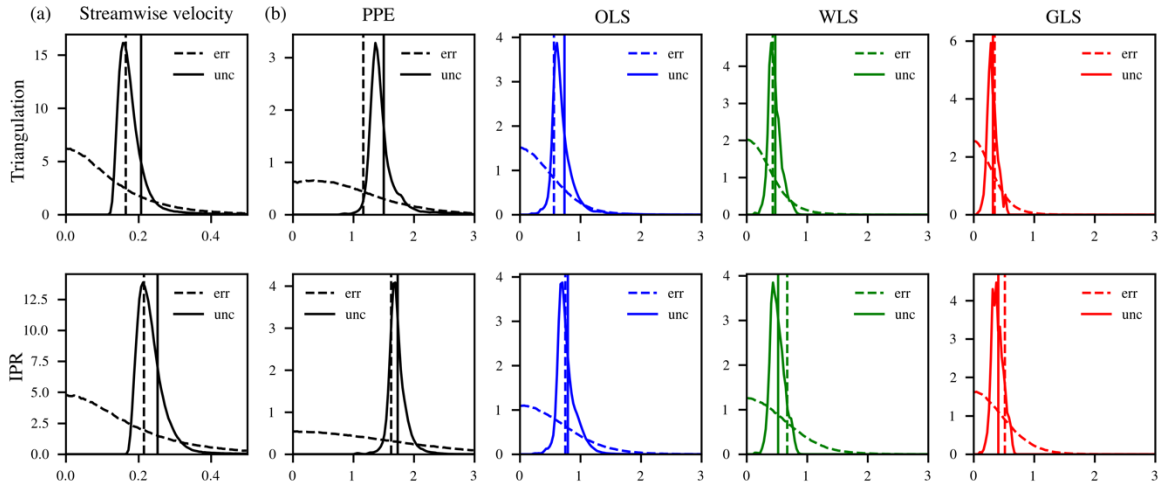

Figure 6.11 The histograms of the normalized absolute errors and uncertainties of (a) the streamwise velocity component and (b) the reconstructed pressure fields using different methods from the triangulation and IPR reconstructed velocity fields. The vertical lines indicate the RMS errors and RMS uncertainties.

6.3.3 Volumetric PTV of the laminar pipe flow

The error and uncertainty were determined for the velocity fields obtained using triangulation and IPR reconstructions and normalized by the characteristic velocity (u_0). The histograms of the normalized absolute error and the uncertainty for the streamwise component of the gridded velocity fields are presented in Figure 6.11(a). Regarding the RMS values presented in Table 6.2, the velocity uncertainty was 20% higher than the error for the triangulation reconstructed velocity fields, while the uncertainty was overestimated by 17% for the IPR reconstructed velocity fields. The spatial distributions of the normalized velocity errors and uncertainties are presented in Figure 6.12 (a) as a function of the streamwise location (X) along the centerline and as a function of the radial location (R) at X=2.5 mm. The normalized RMS errors ranged from 0.18 to 0.25 and from 0.23 to 0.32 for the triangulation and IPR reconstructions, respectively, while the range of normalized RMS uncertainties was 0.15 to 0.2 for the triangulation reconstructed velocity and was 0.17 to 0.22 for the IPR reconstructed velocity.

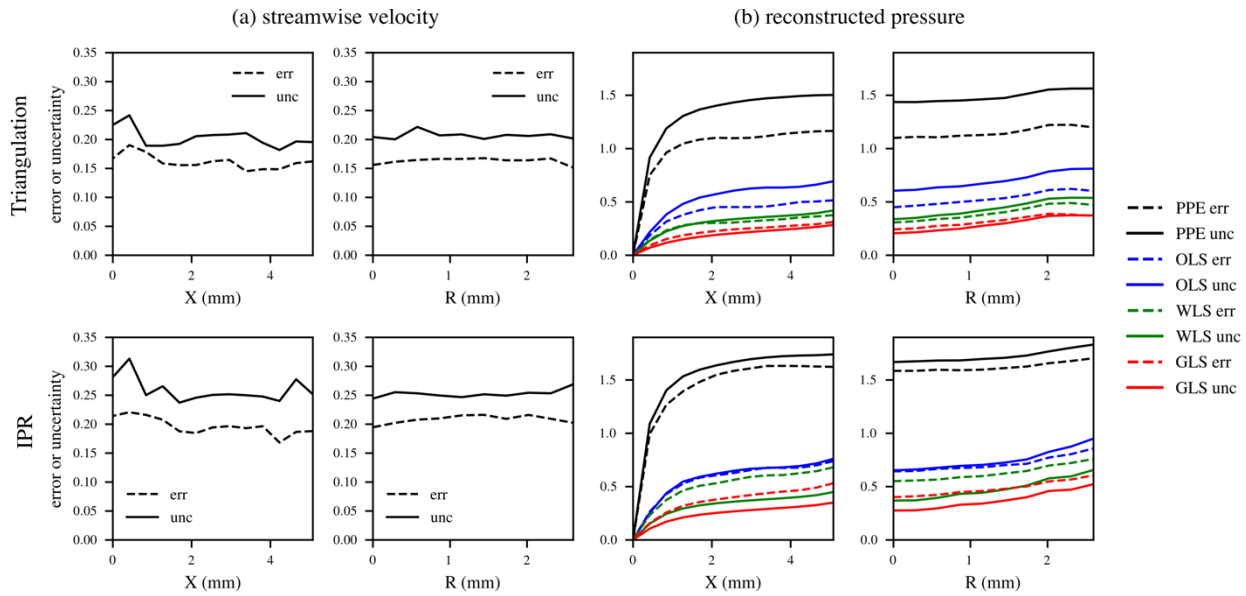

Figure 6.12 The spatial variations of the normalized RMS errors and uncertainties for the streamwise velocity (a) and the reconstructed pressure fields (b) from the PTV measurements with triangulation-based reconstruction and IPR reconstruction. The normalized RMS errors and uncertainties were shown as a function of the streamwise location (X) along the pipe centerline and as a function of the radial location (R) at X=2.5 mm.

The histograms of the absolute pressure errors and uncertainties normalized by the characteristic pressure (p_0) are shown in Figure 6.11 (b), and the RMS errors and uncertainties are given in Table 6.2. For the triangulation reconstructed datasets, the RMS pressure uncertainties were 25% higher than the corresponding RMS errors for the results by PPE and OLS, while the RMS uncertainty was overestimated by 10% for WLS and underestimated by 10% for GLS. For the pressure results from the IPR datasets, the RMS uncertainties were 5 to 10% higher than the RMS errors for PPE and OLS, while they were 20 to 25% lower than the RMS errors for WLS and GLS. The spatial variations of normalized RMS pressure errors and uncertainties are presented in Figure 6.12 (b) as a function of the streamwise location (X) along the centerline and as a function of the radial location (R) at X=2.5 mm. The pressure errors and the predicted uncertainties were lowest at X=0 mm along the centerline where the accurate Dirichlet pressure boundary condition was applied. Faiella et al. (Faiella et al., 2021) has shown and provided theoretical proof that the Dirichlet boundary condition can tame the error propagation in the velocity-based pressure reconstruction problem. The normalized RMS pressure errors and uncertainties increased by about 0.3 with the increase of the radial location R from 0 mm to 2.5 mm.

Table 6.2 The normalized RMS errors and uncertainties (%) of the gridded velocity fields and the reconstructed pressure fields of the laminar pipe flow measured with volumetric PTV

		velocity	PPE	OLS	WLS	GLS
Triangulation	error	16.5	116.6	56.8	43.0	34.7
	unc	20.8	150.2	73.8	47.5	32.0
IPR	error	21.5	162.8	75.4	66.8	51.9
	unc	25.2	173.4	79.4	52.1	40.9

The standard uncertainty coverage results of velocity and pressure are presented in Figure 6.13 and are compared to the targe coverage calculated as the coverage of the standard deviation of the true errors. The coverage was 84% for the velocity obtained using triangulation reconstruction and 81% for the velocity from IPR reconstruction. The uncertainty coverage results were 67% to 81% for the pressure reconstructed from triangulation reconstructed velocity fields, while the coverages were 58% to 72% for the pressure reconstructed from IPR reconstructed velocity fields.

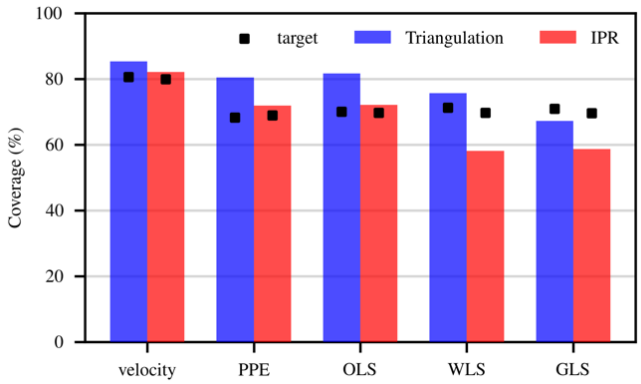

Figure 6.13 The uncertainty coverage for the velocity and pressure reconstructed with PPE, OLS, WLS, and GLS methods for the laminar pipe flow measured using PTV with triangulation and IPR reconstructions.

6.4 Discussion

This study introduced and applied a method to estimate the uncertainty in the pressure fields reconstructed from PIV/PTV measurements based on the velocity uncertainty. The standard velocity uncertainty was used to construct the covariance matrix of the velocity field, which was then propagated through the calculation and integration of the pressure-gradients to obtain the covariance matrix of the pressure field, therefore providing the local and instantaneous pressure

uncertainty. The uncertainty propagation was modeled as a linear transformation by neglecting the high-order error terms such as $\boldsymbol{\epsilon_u} \cdot \nabla \boldsymbol{\epsilon_u}$ in the calculation of pressure gradients, and the uncertainty propagation was performed using matrix operations as detailed in sections 6.2.1 and 6.2.2.

The proposed method can reproduce the effects of several characteristics of the velocity errors on the reconstructed pressure fields. First, the amount of measurement noise affects the accuracy of the calculated pressure-gradients and the reconstructed pressure fields, as shown in Figure 6.4, and the estimated pressure uncertainty was consistent with the pressure errors at varying velocity noise levels. In addition, the spatial autocorrelation of the measurement errors affects the accuracy of the reconstructed pressure fields. Higher correlation can lead to more low-frequency components in the velocity errors, which results in more amplified pressure error as shown in previous studies (R. De Kat & Van Oudheusden, 2012; Faiella et al., 2021). Figure 6.6 (a) shows that a stronger spatial correlation led to more significant pressure errors, captured by the proposed uncertainty estimation. It should be noted that the covariances need to be prescribed appropriately to capture the effect. However, the existing velocity uncertainty estimation methods do not provide covariances for PIV and PTV. In the present study, the velocity covariance was modeled as a function of the spatial distance and the window overlap as expressed in equation (6-29) for planar PIV measurement of the vortex ring flow. For the PTV measurement of the laminar pipe flow, the covariances of the gridded velocity data came from the IDW velocity interpolation from particle locations to the Cartesian grid points since the velocity at different grid points can be interpolated from the velocity in similar sets of particle positions, and the covariances were determined accordingly using equation (6-34). Moreover, the temporal autocorrelation of the measurement errors affect the accuracy of the calculated local acceleration $\frac{\partial \boldsymbol{u_m}}{\partial t}$ and thereby the reconstructed pressure fields, and the effect can be captured by specifying the temporal covariances in equation (6-6) for the uncertainty estimation. As suggested in Figure 6.6 (b), the change in the temporal autocorrelation coefficient had a negligible effect on the pressure errors and uncertainties for the synthetic flow fields, which was because of the error in $\frac{\partial \boldsymbol{u_m}}{\partial t}$ was negligible compared to the total error of all the terms in (6-2). As discussed in (van Oudheusden, 2013), the errors in the local acceleration $\frac{\partial \boldsymbol{u_m}}{\partial t}$ and the convective acceleration $\boldsymbol{u_m} \cdot \nabla \boldsymbol{u_m}$ with $\frac{1}{\Delta t}$ and $\frac{1}{h}$, respectively. Since $\Delta t = 0.05\ s$ and $h = \Delta x = \Delta y = 0.1\ mm$ for the synthetic flow data, the errors in $\frac{\partial \boldsymbol{u_m}}{\partial t}$ were roughly 0.2% of the errors in $\boldsymbol{u_m} \cdot \nabla \boldsymbol{u_m}$, therefore, the effect of the temporal

correlation on the pressure accuracy was unnoticeable for this flow data. For the experimental vortex ring flow and the laminar pipe flow in this study, the $\frac{\partial \boldsymbol{u_m}}{\partial t}$ was calculated from the velocity fields separated by 10 frames, and therefore the measurement errors were assumed to be uncorrelated. Also, the component-wise correlation between velocity errors can affect the pressure accuracy, as shown in Figure 6.6 (c). However, the effect was significant only when the correlation coefficient was greater than 0.5, which is improbable from actual measurements.

The proposed uncertainty estimation method also considers several other factors in pressure reconstruction. The effects of spatial and temporal resolutions on the reconstructed pressure's accuracy has been investigated by de Kat and van Oudheusden (R. De Kat & Van Oudheusden, 2012) using numerical simulations and analytical derivations. In the present study, the spatial and temporal resolutions were considered in the linear transformations constructed for the error propagation from velocity to pressure. Specifically, the temporal resolution was considered in the transformation matrix M_c in equation (6-4) for computing the pressure-gradients, while the spatial resolutions were embedded in the discrete linear operators such as ∇ and ∇^2 for computing spatial derivatives. The numerical schemes that affect the error propagation dynamics were also incorporated in the discrete linear operators. The accuracy of the pressure fields also depends on several factors in the pressure-gradient integration, including the boundary condition, the domain setup, and the integration method. Faiella et al. (Faiella et al., 2021) used the theory of vibrating elastic bodies to reveal the error dynamics of the velocity-based pressure reconstruction and analytically quantified the effects of these factors on the resulting pressure errors. These factors can control the form of the linear system for solving the pressure fields, as introduced in section 6.2.2. Using the pressure solver's transformation to construct the linear transformation for the uncertainty propagation, the effects of these factors can be reproduced in the estimated pressure uncertainty. As shown in Figure 6.2, the pressure fields reconstructed using different methods yielded different RMS errors, which were correctly predicted in the estimated uncertainty. Figure 6.3 showed that the area on the bottom left of the domain had lower pressure errors than the other regions due to the Dirichlet boundary point, which was also captured in the predicted uncertainty distributions.

The performance of the proposed uncertainty estimation method depends on the accuracy of the velocity uncertainty. For the experimental vortex ring flow, the velocity uncertainties obtained for the PIV measurements had different levels of underestimation as compared to the velocity

errors, as shown in Table 6.1. The relative underestimation was 28% by MC, 60% by IM, and 47% by CS in terms of the RMS values. The pressure uncertainty obtained based on the velocity uncertainty also underpredicted the pressure errors, e.g., the RMS uncertainty for the PPE pressure was underestimated by 22% with MC uncertainty, 54% with IM uncertainty, and 42% with CS uncertainty as compared to the RMS errors. For the experimental laminar pipe flow, the velocity uncertainty was 10-20% higher than the velocity errors, and the pressure uncertainty also overpredicted the pressure errors for the reconstructions with PPE and OLS methods as suggested by the RMS values in Table 6.2. However, the pressure uncertainties predicted for the GLS reconstructions were lower than the pressure errors for all the vortex ring flow and the laminar pipe flow, suggesting that the proposed method tends to underestimate the pressure uncertainty from GLS.

Moreover, the spatial distribution of the velocity uncertainty also affects the spatial distribution of the estimated pressure uncertainty. As shown in Figure 6.7 (c), the spatial distributions of the velocity uncertainties were more uniform than the velocity errors, with the uncertainty in the vortex cores being significantly underestimated. Consequently, the estimated pressure uncertainty shown in Figure 6.10 distributed more uniformly across the field than the pressure errors and did not capture the high-pressure errors in the vortex cores.

There are several limitations of the proposed pressure uncertainty estimation method. First, this method does not apply to the pressure-gradient calculation using a Lagrangian approach, which has different error propagation than the Eulerian approach considered in the present study. Since the Lagrangian approach is less sensitive to the velocity-error than the Eulerian approach (R. De Kat & Van Oudheusden, 2012), the pressure-gradient uncertainty from the Lagrangian approach is expected to be lower than the uncertainty estimated for the Eulerian approach. Moreover, the method only applies to the pressure-gradient integration using a linear solver, i.e., the pressure Poisson solver and the least-squares methods, since the error propagation from pressure-gradient to the integrated pressure field can be considered as a linear transformation. The error propagation characteristics for the omni-directional integration method (Liu & Katz, 2006) can be found in (Liu & Moreto, 2020). In addition, the proposed method does not account for the pressure uncertainty due to the truncation errors from numerical differentiation and integration, which can be an important source of error for flow data with low noise levels or low spatiotemporal resolutions. The numerical uncertainty estimation for the pressure-reconstruction will be

investigated in future work. Also, the uncertainty propagation through the pressure-gradient integration was carried with operations of large dense transformation matrices, which is computationally expensive and can be infeasible for large datasets, e.g., volumetric data with a large number of grid points along each dimension.

There are several limitations to this study. First, the covariances between velocity errors need to be specified to reproduce the effects of the autocorrelations of velocity errors on the pressure results. However, this information usually is unavailable from the existing velocity uncertainty estimation methods. Thus, the spatial correlation coefficients were modelled empirically for PIV measurement on the experimental vortex ring flow based on the analysis from (Sciacchitano & Wieneke, 2016), while the velocity errors at particle positions were assumed to be spatially uncorrelated for the PTV measurements of the laminar pipe flow. The model and assumption on the velocity-error autocorrelation can yield inaccurate covariances and affect the uncertainty estimation's performance. The pressure uncertainty can be underpredicted by as much as 30-50% if the covariances were assumed to be zero as indicated by the comparison between the cases with different levels of spatial correlation as shown in Figure 6.6 (a). However, the uncertainty estimation without the velocity error covariances can still capture the effects of other factors including the spatiotemporal resolutions, the boundary conditions, etc., on the pressure uncertainty. Also, the "ground truth" data for the vortex ring flow was from the tomographic PIV measurement, which also contains errors and may affect the error assessment.

In conclusion, a practical framework was introduced to estimate the uncertainty in the pressure fields reconstructed from velocity measurements with PIV/PTV by propagating the velocity uncertainty through the pressure reconstruction. The analyses with the synthetic flow fields shows that the proposed method can predict the local and instantaneous pressure uncertainty and reproduce the effects of several characteristics of the velocity errors on the reconstructed pressure fields, including the noise level, the autocorrelation, and the component-wise correlation between velocity errors. In addition, the method can capture the differences between the uncertainties of pressure fields reconstructed with different methods and boundary conditions. The method was applied to the PIV measurement of a vortex ring flow and the PTV measurement of a laminar pipe flow. From the analyses of the experimental results, it is found that the performance of the proposed uncertainty estimation method depends on the accuracy of the velocity uncertainty.

6.5 Authors' contributions

J.Z. developed and evaluated the method, performed the data analysis, and drafted the manuscript. S.B. performed the experimental measurement and pre-processed the data. P.P.V. designed and oversaw the study and all data analysis. All authors critically reviewed and edited the manuscript, and gave final approval for publication.

7. A MULTI-MODALITY APPROACH FOR ENHANCING 4D FLOW MRI VIA SPARSE REPRESENTATION

This chapter is reproduced with permission from: Zhang, J., Brindise, M.C., Rothenberger, S.M., Markl, M., Rayz, V.L., Vlachos, P.P., 2022. A multi-modality approach for enhancing 4D flow magnetic resonance imaging via sparse representation. J. R. Soc. Interface 19. https://doi.org/10.1098/rsif.2021.0751

7.1 Background and literature review

Cerebral aneurysms (CAs) present in about 3% of the population and are a significant health-care burden (Rinkel et al., 1998; Vlak et al., 2011). Risk stratification of unruptured cerebral aneurysms is critical for appropriate clinical management, as rupture yields high mortality while surgical intervention carries an inherent risk of complication (Asgari, Wanke, Schoch, & Stolke, 2003; International Study of Unruptured Intracranial Aneurysms Investigators, 1999; Komotar, Mocco, & Solomon, 2008; Rayz et al., 2015). In addition to multiple clinical (e.g., age, sex, comorbidities) and morphological factors (e.g., aneurysm location, size, shape) (International Study of Unruptured Intracranial Aneurysms Investigators, 1999; Komotar et al., 2008; Thompson et al., 2015), recent studies have shown that hemodynamic metrics such as wall shear stress (WSS) (Boussel et al., 2008; Jou et al., 2008; Meng et al., 2014) and vortex structures (Varble et al., 2017) are correlated with the growth and rupture of CAs.

4D flow magnetic resonance imaging (MRI) allows for the *in vivo* acquisition of time-resolved three-dimensional (3D) blood flow, enabling evaluation of hemodynamic quantities for CAs (Brindise et al., 2019; M Markl et al., 2016; Schnell et al., 2017; Zhang, Brindise, et al., 2020). However, the accuracy of flow-derived hemodynamic quantities is affected by the limited spatial and temporal resolution and noise inherent to 4D flow MRI. The WSS magnitude derived from *in-vivo* 4D flow MRI measurement in CAs was about 60% lower than the results from computational fluid dynamics (CFD) due to 4D flow MRI's low spatial resolution (Van Ooij et al., 2013). The spatio-temporal resolution of velocity data also influences the vortex identification and analysis in CAs (Sunderland et al., 2016) and the reconstruction of pressure fields (Zhang, Brindise, et al., 2020).

Computational fluid dynamics (CFD) have been used to evaluate hemodynamic quantities for patient-specific CAs with high resolution and precision (Boussel et al., 2008; Jou et al., 2008;

Meng et al., 2014; Sunderland et al., 2016; Varble et al., 2017). Recently, *in-vitro* volumetric flow measurements using particle imaging velocimetry (PIV) (Ford et al., 2008; Roloff et al., 2019) or particle tracking velocimetry (PTV) (Brindise et al., 2019) were performed to resolve the flow and determine hemodynamic factors in patient-specific CAs. However, the fidelity and reliability of *in silico* CFD simulations and *in vitro* flow measurements are limited by the uncertainty in vessel geometries and assumptions for boundary conditions. The fidelity of *in vitro* flow measurements is also influenced by the difficulty in model fabrication and pulsatile-flow matching. Despite using the same image data and inflow conditions, differences have been observed between hemodynamic quantities obtained from independent CFD simulations (Voß et al., 2019) or between the CFD simulations and PTV measurements (Brindise et al., 2019). Adjoint-based optimization approaches have been introduced to minimize the differences between the CFD and *in vivo* 4D flow MRI measurements (De Hoon, Van Pelt, Jalba, & Vilanova, 2014; Mohd Adib, Ii, Watanabe, & Wada, 2017; Töger et al., 2020a) to achieve higher fidelity. The patient-specific CFD solutions have also been used to enhance 4D flow MRI data with data fusion techniques (Bakhshinejad et al., 2017; Fathi et al., 2018; Perez-Raya et al., 2020).

Initially developed for image recognition and reconstruction (J. Wright, Member, Yang, Ganesh, & Sastry, 2009), the library-based sparse representation has been used for estimating complex flow structures from limited measurements (Brunton, Tu, Bright, & Kutz, 2014; Callaham, Maeda, & Brunton, 2019) with superior performance compared to least-squares regression. Previous studies have demonstrated that the sparse representation of a flow-library consisting of the proper orthogonal decomposition (POD) basis obtained from CFD snapshots could denoise and enhance the spatial resolution of 4D flow MRI (Fathi et al., 2018). The present study aims to apply a multi-modality approach incorporating both CFD and PTV to enhance the blood flow measurements with 4D flow MRI and evaluate the improvement to the hemodynamic analysis in cerebral aneurysms. The approach, named Multi-modality Sparse Representation (MSR), reconstructs the velocity field from 4D flow MRI by searching for a sparse representation in a library of high-resolution velocity fields obtained from CFD and *in vitro* PTV. The MSR method was tested using synthetic 4D flow MRI datasets of a basilar tip (BT) aneurysm and an internal carotid artery (ICA) aneurysm. The method was then applied to the *in vivo* 4D flow MRI data in two patients with cerebral aneurysms.

7.2 Materials and Methods

7.2.1 Flow reconstruction via library-based sparse representation

The MSR reconstruction assumes that the measurement process of 4D flow MRI can be modeled as:

$$\boldsymbol{u} = C\boldsymbol{U} + \boldsymbol{\epsilon}, \tag{7-1}$$

where $\boldsymbol{U} \in \mathbb{R}^N$ represents the underlying velocity field on a fine grid $\mathcal{G}_{fine}$ with N grid points, $\boldsymbol{u} \in \mathbb{R}^n$ contains the 4D flow MRI measured velocity values at n voxel-center locations, C is the measurement matrix with a shape of $n \times N$ which transforms $\boldsymbol{U}$ on $\mathcal{G}_{fine}$ to the coarse MRI grid $\mathcal{G}_{MRI}$, and $\boldsymbol{\epsilon} \in \mathbb{R}^n$ represents the measurement noise. The vectors $\boldsymbol{U}$ and $\boldsymbol{u}$ contain only one velocity component, and the measurement process modeled by (7-1) applies to each of the three velocity components acquired using 4D flow MRI. In the present study, each velocity-component field was reconstructed individually such that the optimization problem has a lower rank for enabling a sparse representation and a lower dimension to save computational cost. The smoothing effect of Cartesian 4D flow MRI due to finite k-space coverage was modeled by convolving the underlying velocity field with a truncated sinc-function kernel $\mathcal{K}$ (Rispoli et al., 2015) as:

$$\mathcal{K}(x,y,z) = \begin{cases} sinc\left(\frac{x}{\Delta x}\right) \times sinc\left(\frac{y}{\Delta y}\right) \times sinc\left(\frac{y}{\Delta y}\right), & \frac{x}{\Delta x}, \frac{y}{\Delta y}, \frac{z}{\Delta z} \in (-2,2) \\ 0, & otherwise \end{cases} \tag{7-2}$$

where Δx, Δy, and Δz correspond to the grid sizes of 4D flow MRI. Therefore, the coefficients in the measurement matrix C were assigned based on the kernel function values at the grid nodes related to each MRI voxel. The row number of the matrix C was used to index the MRI voxels, and the columns were linked to the grid points of $\mathcal{G}_{fine}$. The coefficient at the ith row and jth column of C was given as the kernel function value based on the distance between the ith voxel-center and the jth grid point normalized by the sum of the kernel function values from all grid points related to the ith voxel-center.

Using the high-resolution flow-data acquired from CFD simulations and in vitro PTV measurements, a flow-library $\{\boldsymbol{\Psi_k}\}$ with $\boldsymbol{\Psi_k} \in \mathbb{R}^N$ and $k = 1,2,\dots,m$ can be constructed. The library-components $\boldsymbol{\Psi_k}$ can be generated as a snapshot (Callaham et al., 2019) or the mode extracted from the high-resolution flow-data (Bakhshinejad et al., 2017; Brunton et al., 2014; Fathi et al., 2018; Kramer, Grover, Boufounos, Nabi, & Benosman, 2017) on the grid $\mathcal{G}_{fine}$. If the flow-library contains an extensive collection of representative examples of the probable flow structures in the same aneurysm geometries, $\boldsymbol{U}$ can be accurately expressed as a linear combination of the library components as:

$$\boldsymbol{U} \approx \Psi \boldsymbol{s}, \tag{7-3}$$

where $\boldsymbol{s} \in \mathbb{R}^m$ is the vector of library coefficients, and Ψ contains the library-components Ψ_k as its columns. To find the coefficient vector $\hat{\boldsymbol{s}}$ such that the MSR-reconstructed velocity field ($\widehat{\boldsymbol{U}}$) obtained as $\widehat{\boldsymbol{U}} = \Psi\hat{\boldsymbol{s}}$ accurately reproduces the underlying velocity field $\boldsymbol{U}$, the LASSO regression (Tibshirani, 2016) was used in the MSR flow-reconstruction:

$$\hat{\boldsymbol{s}} = \underset{s}{argmin}(\|\boldsymbol{u} - C\Psi\boldsymbol{s}\|_2 + \alpha\|\boldsymbol{s}\|_1), \tag{7-4}$$

where $\|\boldsymbol{u} - C\Psi\boldsymbol{s}\|_2$ represents the L2 norm of the fitting residuals, and $\alpha > 0$ is the parameter that controls the strength of the regularization term $\alpha\|\boldsymbol{s}\|_1$. The hyperparameter α was optimized iteratively using 5-fold cross-validation, and the optimization of (7-4) was carried using the Python scikit-learn subroutine "LassoCV" (Friedman, Hastie, & Tibshirani, 2010; Kim, Koh, Lustig, Boyd, & Gorinevsky, 2007). The penalization of $\|\boldsymbol{s}\|_1$ in (7-4) promotes a sparse representation, i.e., most of the coefficients in $\hat{\boldsymbol{s}}$ are zeros. However, minimizing $\|\boldsymbol{s}\|_1$ also tends to reduce the amplitude of the MSR-reconstructed field since $\widehat{U} = \Psi\hat{\boldsymbol{s}}$. Thus, the obtained flow field is rescaled to keep the same L1-norm between the measured velocity data $\boldsymbol{u}$ and the reproduced velocity measurement $\widehat{\boldsymbol{u}} = C\Psi\hat{\boldsymbol{s}}$ as

$$\widehat{\boldsymbol{U}} = \frac{\|\boldsymbol{u}\|_1}{\|\widehat{\boldsymbol{u}}\|_1}\Psi\hat{\boldsymbol{s}} = \frac{\|\boldsymbol{u}\|_1}{\|C\Psi\hat{\boldsymbol{s}}\|_1}\Psi\hat{\boldsymbol{s}}. \tag{7-5}$$

The procedure of the MSR reconstruction is shown schematically in Figure 7.1(a).

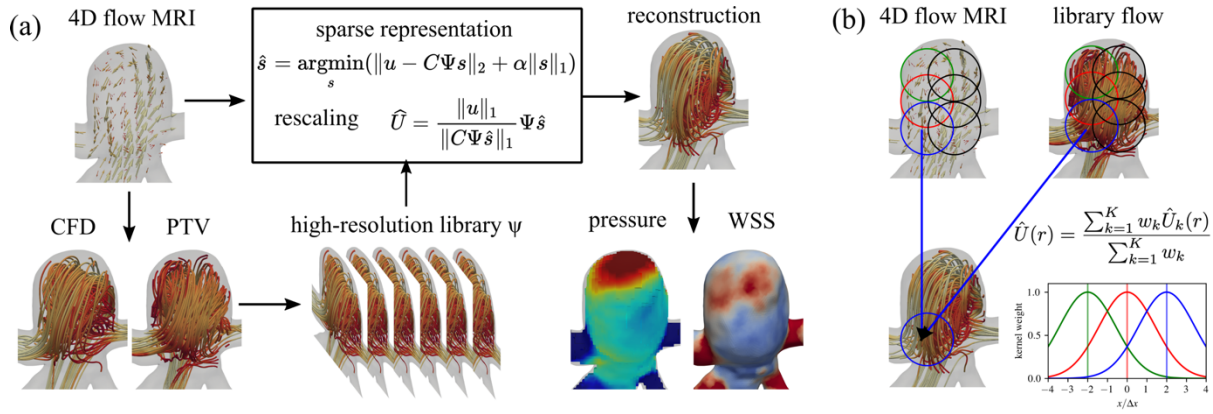

Figure 7.1 (a) Schematic of the multi-modality sparse representation flow reconstruction. (b) Schematic of the localized flow reconstruction. The MSR reconstruction was performed in each subdomain, and the global velocity field was subsequently constructed as the weighted superposition of the local reconstructions with a Gaussian kernel function.

For complex flow fields such as the aneurysmal flow, it may not be feasible to construct a flow-library containing representative examples of all the probable global flow fields. However, local flow regions may have a lower rank and enable sparse representation as demonstrated in previous studies (Callaham et al., 2019). As shown in Figure 7.1 (b), the aneurysmal flow fields were divided into subdomains whose centers were located on Cartesian grids with resolutions h_{sub} of 2 times of the MRI resolutions for the BT and ICA aneurysms. Each subdomain contains a region within $2h_{sub}$ from the center $\boldsymbol{r_{sub}}$ and overlaps with neighboring subdomains. The subdomains located near the wall only contain the regions within the blood flow. The MSR flow reconstruction was performed in each subdomain, and the global velocity field was subsequently constructed as the weighted superposition of the local reconstructions as:

$$\hat{U}(\boldsymbol{r}) = \frac{\sum_{k=1}^{K} w_k \hat{U}_k(\boldsymbol{r})}{\sum_{k=1}^{K} w_k}, \tag{7-6}$$

$$with\, w_k = exp\left(-\frac{|\boldsymbol{r}-\boldsymbol{r_{sub}}|^2}{h_{sub}^2}\right), \tag{7-7}$$

where $\hat{U}(\boldsymbol{r})$ represents the combined velocity value at spatial location $\boldsymbol{r}$, K is the total number of subdomains that contain $\boldsymbol{r}$, $\hat{U}_k(\boldsymbol{r})$ means the velocity value reconstructed in the kth subdomain

whose center locates at $\boldsymbol{r_{sub}}$, and w_k is the weight based on the spatial distance between $\boldsymbol{r}$ and $\boldsymbol{r_{sub}}$.

7.2.2 Multi-modality flow-data acquisition and flow library construction

In vivo flow data in a basilar tip (BT) aneurysm and an internal carotid artery (ICA) aneurysm were acquired using 4D flow MRI on a 3T scanner (Skyra, Siemens Healthcare, Erlangen, Germany). MRI acquisition of the BT aneurysm was performed at San Francisco VA Medical Center, and the ICA aneurysm was imaged at Northwestern Memorial Hospital (NMH). Gadolinium contrast was used for the BT aneurysm, whereas no contrast was used for the ICA aneurysm. The sac diameter was 7 mm and 10 mm for the BT aneurysm and ICA aneurysm, respectively. The *in vivo* flow-data were on Cartesian grids with the spatial resolution of $1.25 \times 1.25 \times 1.33\, mm^3$ for the BT aneurysm and $1.09 \times 1.09 \times 1.30\, mm^3$ for the ICA aneurysm, resulting in about 5 and 9 voxels across the diameter of the aneurysmal sac for the BT aneurysm and ICA aneurysm, respectively. The temporal resolution Δt was 40.5 ms (20 frames per cycle) and 44.8 ms (13 frames per cycle) for the BT and ICA aneurysms, respectively. The encoding velocity sensitivity (venc) was 100 cm/s for the BT aneurysm and 120 cm/s for the ICA aneurysm. Approval of all ethical and experimental procedures and protocols was granted by the institutional review boards at Purdue University, Northwestern Memorial Hospital, and San Francisco VA Medical Center.

In vitro flow measurements were done using PTV in 1:1 scaled silicone models of the two aneurysms with blood-mimicking fluids composed of water-glycerol-urea (Brindise et al., 2018). The flow phantom for each aneurysm was fabricated as follows: Based on the segmented vessel geometry, a positive-space model was 3D printed and embedded into a tear-resistant silicone block. The model was then cut from the block and replaced by a low melting point metal (Cerrobend 158 Bismuth alloy). The block was cut away and embedded in a block of optically clear polydimethylsiloxane silicone (PDMS-Slygard 184). The metal was then melted out after the PDMS was hardened. The time-dependent inflow waveform was driven by a computer-controlled gear pump and designed to match the waveform obtained from the *in vivo* 4D flow MRI data. The acquired particle images were processed using DaVis 10.0 (LaVision Inc.) with the Shake-the-Box (STB) method. The temporal resolution was 2.5 ms for the BT aneurysm and 1.5 ms for the ICA aneurysm. CFD simulations were performed using FLUENT 18.1 (ANSYS) for the two aneurysms.

An unstructured tetrahedral mesh generated using HyperMesh 14.0 (Altair Engineering, Troy, MI, USA) was employed with a nominal cell size of 0.15 mm. The flow-rate waveforms obtained from the *in vivo* 4D flow MRI were used as the boundary conditions for the CFD models. Newtonian fluid and rigid wall were assumed in the CFD models. The rigid wall was assumed because the previous investigation with cine MRI imaging showed no observable wall movement of intracranial vessels over the cardiac cycle (Boussel et al., 2008), and the aneurysm disease can reduce the elasticity of the arterial wall (Humphrey & Na, 2002). For each aneurysm, three cardiac cycles were simulated with a temporal resolution of 1.5 ms, and the results of the last cycle were used in the present study. More details on the *in vivo* imaging, *in vitro* measurement, and CFD models can be found in (Brindise et al., 2019).

The unstructured PTV and CFD data were linearly interpolated to Cartesian grids $\mathcal{G}_{fine}$ with isotropic resolutions of 0.3 and 0.4 mm for the BT and ICA aneurysms, respectively, with more than 20 grid points across the diameter of each aneurysmal sac. Instead of the basis from proper orthogonal decomposition (Bakhshinejad et al., 2017; Fathi et al., 2018), the velocity fields were directly used as the library-components. For each CA geometry and each velocity-component, the flow-library was constructed as a collection of 100 timeframes randomly selected from the high resolution PTV and CFD data on $\mathcal{G}_{fine}$. Different flow-libraries were constructed with different numbers of timeframes from CFD and PTV data. The flow-libraries with an equal number (50 each) of PTV and CFD components were referred to as the balanced flow-libraries. The flow-libraries with more PTV components than CFD were PTV-dominant, while the flow-libraries with more components from CFD than PTV were CFD-dominant.

7.2.3 Synthetic 4D flow MRI data generation

To evaluate MSR's performance, synthetic 4D flow MRI datasets were generated from the high-resolution PTV and CFD datasets. For each velocity component, the complex-valued signal was created as:

$$M_u = I exp\left(\frac{i\pi u_{fine}}{venc}\right), \qquad (7\text{-}8)$$

where M_u means the signal created for the u velocity component from the high-resolution data (u_{fine}), and I is the signal magnitude which was set as 1.0 inside the blood flow while 0.2 outside the blood flow. The signal of the 4D flow MRI data was generated by spatially and temporally smoothing M_u as:

$$M_{u,MRI} = M_u * \mathcal{T} * \mathcal{K}, \tag{7-9}$$

$$with\,\mathcal{T}(t) = \begin{cases} exp\left(-\frac{2t^2}{\Delta t^2}\right), & t \in (-\Delta t, \Delta t) \\ 0, & otherwise \end{cases}, \tag{7-10}$$

where $*$ denotes convolution, $\mathcal{K}$ is the spatial smoothing kernel function defined as (7-2), and $\mathcal{T}$ represents the temporal smoothing kernel function with Δt being the temporal resolution of the MRI data. Following a four-point reference method, one reference signal (M_0) was generated from a zero field. The phase data ψ for each velocity component were generated from the flow-sensitive and the reference signals, e.g.,

$$\psi_u = angle\left(M_{u,MRI} \times M_0^*\right), \tag{7-11}$$

where ψ_u is the phase for u velocity component, M_0^* is the complex conjugate of M_0, and $angle(\quad)$ means calculating the angle (between $-\pi$ to π) of a complex value. The velocity data was obtained from the phase data as:

$$u_{MRI} = \frac{venc}{\pi}\psi_u. \tag{7-12}$$

For each CA, two synthetic 4D flow MRI datasets with the same spatio-temporal resolutions as the *in vivo* measurements, named CFD-synMRI and PTV-synMRI, were created from the CFD data and the PTV data, respectively. To test the robustness of MSR, normally distributed noise was added to the complex-valued signal with the standard deviation defined as:

$$\sigma_I = \frac{I}{SNR_I} = \frac{I}{VNR}\frac{\pi}{\sqrt{2}}\frac{\bar{V}}{venc}, \tag{7-13}$$

where SNR_I is the signal to noise ratio, $\bar{V}$ is the mean velocity magnitude, and VNR is the velocity to noise ratio (Lee et al., 1995). The reciprocal of the VNR is defined as the noise level of the synthetic dataset, and four noise levels (5, 10, 15, and 20%) were considered in the present study. To test the performance of MSR on different MRI grid resolutions, additional synthetic MRI datasets were created with grid sizes varying from 2 to 5 times of the grid sizes of the CFD and PTV data on $\mathcal{G}_{fine}$.

7.2.4 Methods for velocity and hemodynamic analysis

The CFD and PTV velocity fields at the corresponding timeframes of the synthetic 4D flow MRI data were considered as the ground truth for CFD-synMRI and PTV-synMRI, respectively. To assess the accuracy of the synthetic MRI and the MSR-reconstructed velocity fields, velocity error was determined as the difference from the ground truth, and the velocity error level for each dataset was quantified as the root-mean-square (RMS) of the velocity error magnitudes normalized by the RMS of the velocity magnitudes from the ground truth. It should be noted that the velocity fields from the ground truth timeframes were excluded from the flow-library for the reconstruction of CFD-synMRI and PTV-synMRI data such that the "ground truth" was not embedded in the flow-library.

To study the effects of the MSR reconstruction on the flow-derived hemodynamic quantities, pressure and WSS were computed from the MRI and the MSR-reconstructed velocity fields. The pressure reconstruction was carried using the measurement-error based weighted least-squares method (Zhang, Brindise, et al., 2020). A pressure of 0 Pa was assigned at the inflow locations of the aneurysmal sac as the reference pressure for both CAs. The WSS was calculated from the near-wall velocity using thin-plate spline radial basis functions (Brindise et al., 2019), and the time-averaged WSS (TAWSS) were subsequently obtained by averaging the WSS magnitudes across the full cardiac cycle. The pressure and WSS evaluated from the high-resolution ground-truth velocity fields were employed as the ground truth for the error analysis of the pressure and WSS from the synthetic MRI cases.

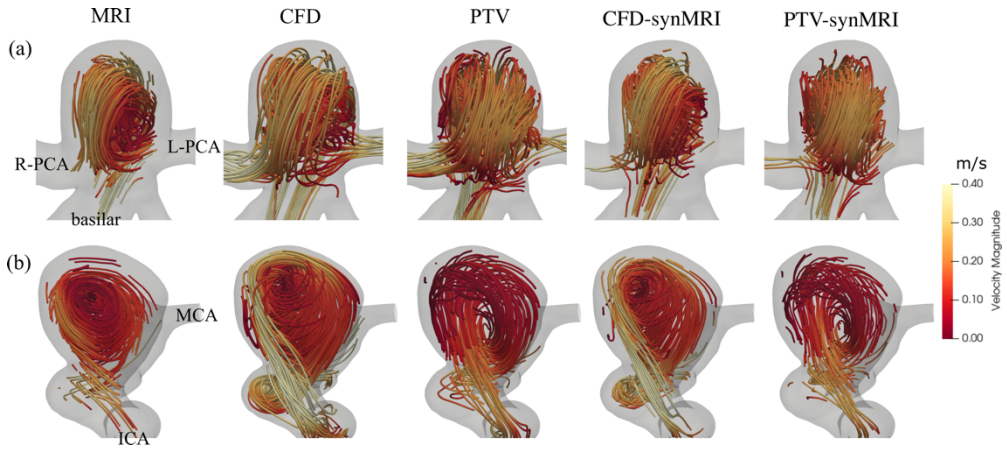

Figure 7.2 Velocity fields at peak systole represented using 3D pathlines from *in vivo* 4D flow MRI, CFD simulations, *in vitro* PTV measurements, and synthetic MRI datasets for the basilar tip aneurysm (a) and internal carotid artery aneurysm (b). The synthetic MRI data has the same spatial resolutions as the in vivo 4D MRI data and with 10% noise. R-PCA and L-PCA indicate the left and right posterior cerebral arteries, respectively. MCA stands for the middle cerebral artery. The angle of view is the anterior view.

7.3 Results

7.3.1 Multi-modality velocity fields

The velocity fields at peak systole for all three modalities and the synthetic MRI data are presented in Figure 7.2 for both aneurysms. For the BT aneurysm, the basilar artery's flow swirled in the aneurysmal sac and exited mainly through the posterior cerebral arteries (PCAs). For the ICA aneurysm, the flow entered from the ICA, swirled in the aneurysmal sac, and exited through the distal ICA and middle cerebral artery (MCA). In the BT aneurysmal sac, the maximum descending velocity was 0.4 m/s from MRI and CFD, while it was 0.3 m/s from PTV. In the ICA aneurysm, a stronger inflow towards the aneurysmal sac was observed from CFD compared to the other two modalities, with the maximum velocity around the “neck” of the aneurysmal sac being 0.55 m/s from CFD, 0.35 m/s from MRI, and 0.3 m/s from PTV. Compared to the corresponding

CFD/PTV data, the flow structures observed from the synthetic MRI were similar but were under-resolved in the near-wall regions and smaller vessels.

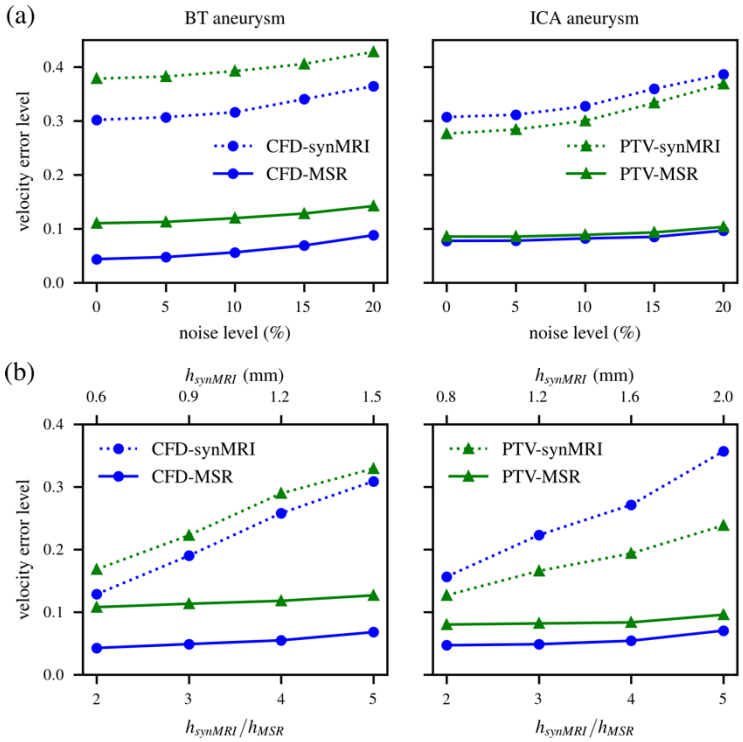

Figure 7.3 (a) The velocity error levels of the synthetic MRI data (synMRI) with the *in vivo* MRI resolutions and the MSR-reconstructed flow data (MSR) using balanced flow-library as functions of the noise level of the synthetic MRI data. (b) The velocity error levels of the synthetic MRI data and the MSR-reconstructed flow data using balanced flow-library as functions of the spatial resolution of the synthetic MRI data (h_{synMRI}). The grid size of the MSR-reconstructed fields (h_{MSR}) is 0.3 mm for the BT aneurysm and 0.4 mm for the ICA aneurysm. The synthetic MRI datasets contain 10% noise.

7.3.2 Reconstruction of synthetic 4D flow MRI

The velocity error level for each synthetic MRI dataset is presented in Figure 7.3(a) as a function of the noise levels. Even without noise, the error level of synthetic MRI velocity data was more than 0.27 due to the smoothing effect. As the noise level increased from 0 to 20%, the velocity error level increased by 0.06 to 0.1. The error levels of the MSR-reconstructed velocity fields were lower than 0.15 for all the cases as shown in Figure 7.3 (a), leading to an error reduction of more than 70% for each case. The increase of the MSR-reconstructed velocity's error level due to the increase of noise level was less than 0.04. The velocity error levels as functions of the spatial resolution of the synthetic MRI data are presented in Figure 7.3 (b). As the MRI resolution increased from 2 to 5 times of the MSR-reconstructed resolution h_{MSR}, the velocity error level of synthetic MRI increased by more than 0.1 due to greater spatial smoothing effect, while the error level of the MSR-reconstructed velocity fields increased by only 0.03 and did not exceed 0.13.

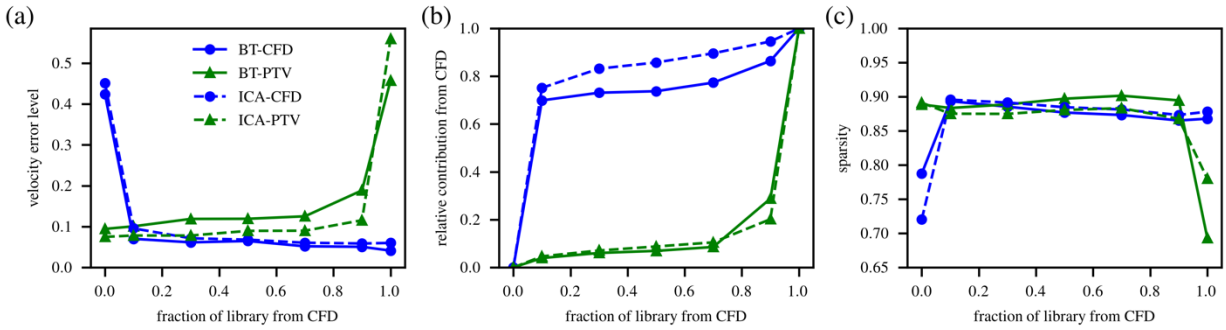

Figure 7.4 Using the flow libraries with different number of components from CFD and PTV data, the MSR-reconstructed velocity error level (a), relative reconstruction contribution from CFD components (b), and the sparsity of the obtained coefficients (c) for the MSR reconstructions of the synthetic MRI datasets as functions of the flow-library composition represented using the fraction of library components from CFD data. The synthetic MRI data was generated with the *in vivo* MRI resolutions and 10% noise.

To investigate the effect of the flow-library on the MSR's performance, flow-libraries consisting of different numbers of components from CFD and PTV data were used for the reconstruction of the synthetic MRI data. The MSR-reconstructed velocity error level as a function of the library-composition is shown in Figure 7.4(a) for the synthetic datasets with the *in vivo* MRI resolution and 10% noise. The library-composition was represented by the fraction of library-components from the CFD data, with the rest of the PTV data components, and the total number of components was 100 for all the flow-libraries. For the reconstruction of CFD-synMRI datasets,

the velocity error levels were greater than 0.4 if the flow-library did not contain any components from CFD data. In contrast, the velocity error levels were lower than 0.1 if there were at least 10 library components from CFD. Similarly, the reconstructions of PTV-synMRI datasets resulted in velocity error levels greater than 0.45 with libraries containing only CFD components, while the velocity error level was less than 0.18 with at least 10 PTV components. For the MSR-reconstructed flow fields, the relative contribution from the CFD library-components was determined as the L1-norm of the coefficients in $\hat{s}$ corresponding to the CFD library-components normalized by the total L1-norm of $\hat{s}$, with the rest of the contribution from PTV library-components. Figure 7.4 (b) presents the relative contribution from the CFD library-components for the reconstructions of synthetic MRI datasets as a function of the library-composition. With the flow-libraries containing a mix of CFD and PTV components, the reconstructions of CFD-synMRI datasets yielded relative contributions from CFD of more than 0.7, while the reconstructions of PTV-synMRI datasets relied less than 0.3 on the CFD components. Fig. 4(c) shows the sparsity of the MSR reconstruction defined as the number of zero-valued coefficients divided by the total number of coefficients in $\hat{s}$ as a function of the library-composition. The reconstructions of PTV-synMRI datasets with flow-libraries containing only CFD components yielded sparsity less than 0.8, and the reconstructions of CFD-synMRI datasets with flow-libraries containing only PTV components had a sparsity less than 0.78. The reconstructions from other cases showed relative sparsity of above 0.85.

To assess the accuracy of the flow-derived hemodynamic quantities, Bland-Altman analysis was performed to compare the pressure and WSS evaluated from the synthetic MRI and from the MSR-reconstructed data with the ground truth as shown in Figure 7.5. In addition, the statistical distributions of these hemodynamic parameters were compared in Fig. 5 using probability density functions (PDFs) with the mean values indicated using vertical lines. Compared to the synthetic MRI data created from the CFD and PTV data, the hemodynamic quantities derived from the MSR-reconstructed fields were more consistent with the ground truth as suggested by the lower bias and STDs of the differences in the Bland-Altman plots. As suggested in Figure 7.5, The WSS derived from synthetic MRI data also showed greater underestimation with greater mean WSS values, while the WSS from the MSR-reconstructed data did not have this correlation. Moreover, the PDFs of the WSS and pressure from MSR-reconstructed fields closely resembled those of the ground

truth. The mean of the WSS from the synthetic MRI data was underestimated by 40-60% compared to the ground truth.

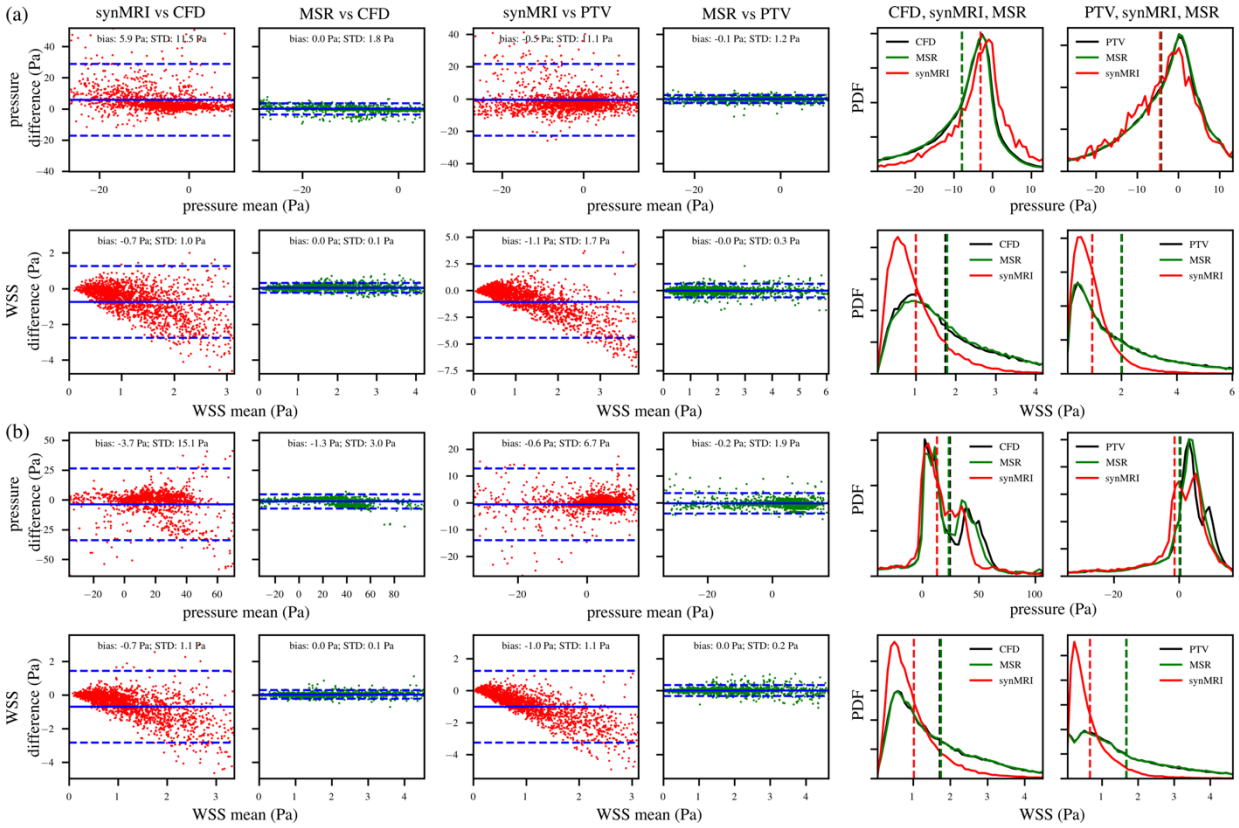

Figure 7.5 Bland-Altman analysis and the statistical distributions of pressure and WSS obtained from synthetic 4D flow MRI data with the *in vivo* MRI resolutions and 10% noise and the MSR-reconstructed data in the BT aneurysm (a) and ICA aneurysm (b). For the Bland-Altman plots, the mean differences from the ground truth are indicated by the solid blue lines while the 95% confidence intervals are given as the dashed blue lines. For the statistical distributions, the mean values are indicated by the vertical lines.

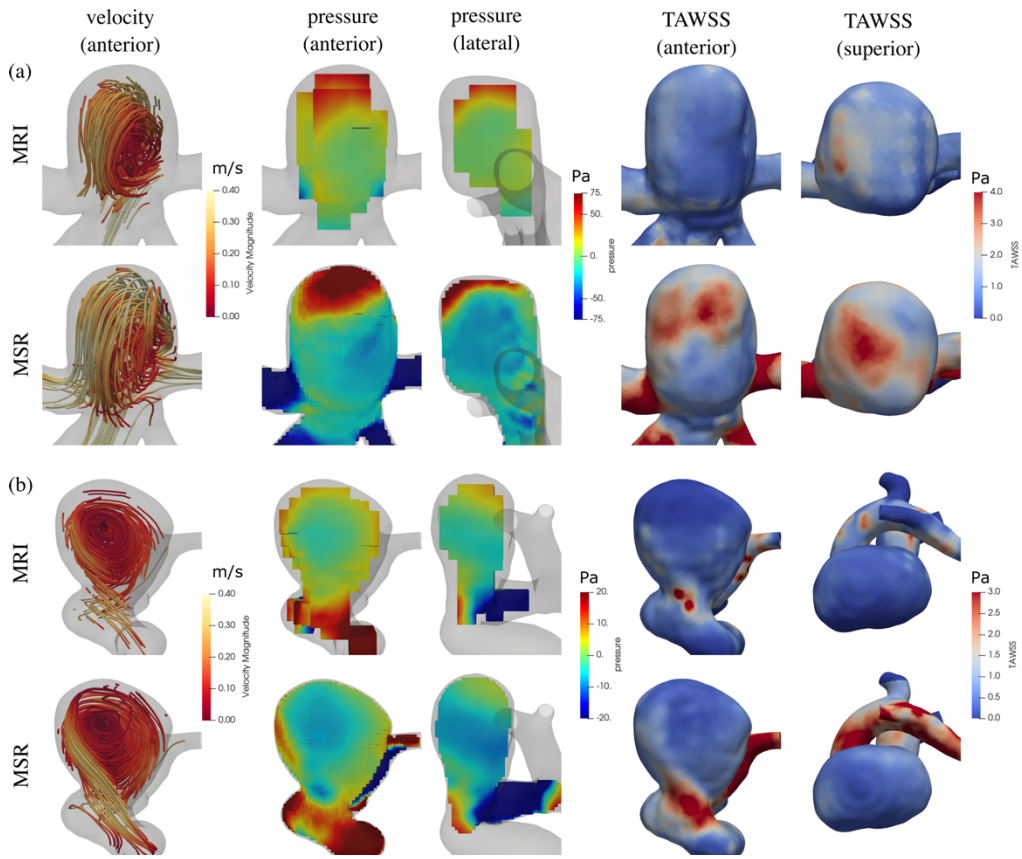

Figure 7.6 The comparison on the flow structure, pressure distribution, and TAWSS between the *in vivo* 4D flow MRI data and the MSR-reconstructed data for the basilar tip aneurysm (a) and the internal carotid artery aneurysm (b). The flow structure is presented using pathlines on the anterior view. The pressure distribution is shown on the anterior view, and the pressure on the middle slice of the aneurysmal sac is shown on the lateral view. The TAWSS is shown on the anterior view and superior view.

7.3.3 Reconstruction of in vivo 4D flow MRI

The MSR flow-reconstruction was applied to the *in vivo* 4D flow MRI data acquired for the same two CAs using the balanced flow-libraries with 50 CFD components and 50 PTV components. The flow fields at peak systole, pressure fields at peak systole, and TAWSS obtained from the *in vivo* MRI and from the MSR-reconstructed flow fields are presented in Figure 7.6(a) and (b) for the BT and ICA aneurysms, respectively. For both aneurysms, the MSR-reconstructed flow structures in the aneurysmal sacs were qualitatively similar with the *in vivo* MRI data, while the flow in the near-wall region and small vessels were better resolved by the MSR reconstruction. Compared to the *in vivo* MRI, the MSR-reconstructed flow-data yielded more distinct low-pressure

region around the center of the aneurysmal sac as clearly shown on the lateral view. For the BT aneurysm, the minimum relative pressure observed around the core of the aneurysmal sac was 0 Pa and -25 Pa from the *in vivo* MRI and MSR-reconstructed flow data, respectively. For the ICA aneurysm, the relative pressure was -5 Pa and -10 Pa around the center of the aneurysmal sac for the *in vivo* MRI and MSR-reconstructed flow data, respectively. The TAWSS obtained from the MSR-reconstructed fields were higher than the TAWSS from *in vivo* MRI. The TAWSS of the BT aneurysm calculated from the MSR-reconstructed data also had different spatial distributions compared to the TAWSS from the MRI data as suggested by the anterior and superior views. For example, regions with TAWSS as high as 4 Pa were observed from the anterior and superior views of the MSR-reconstructed data for the BT aneurysm, which were absent from the *in vivo* MRI data. For the ICA aneurysm, the high TAWSS region (greater than 3 Pa) around the neck of the aneurysmal sac was smaller from the *in vivo* MRI data compared to the MSR-reconstructed data.

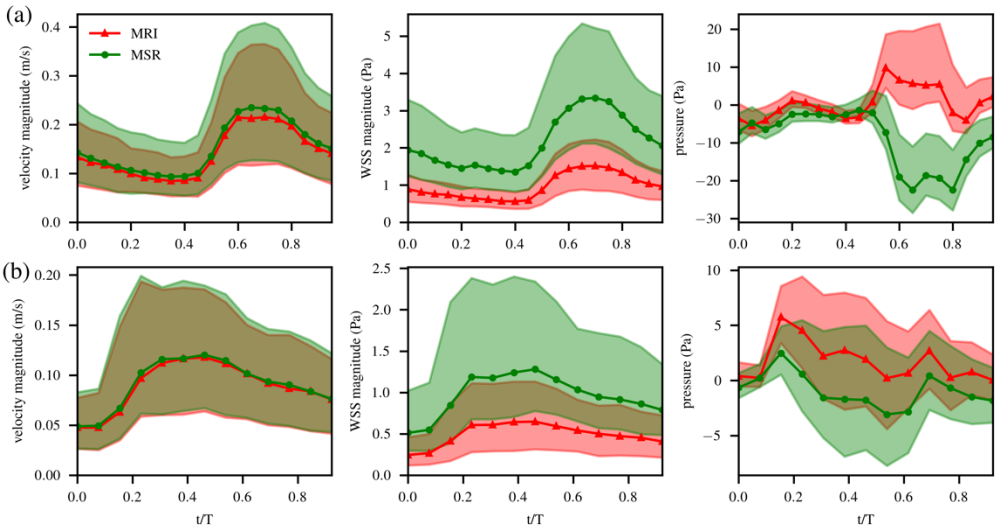

Figure 7.7 The statistical distributions of velocity magnitudes, WSS, and pressure at all time points in the cardiac cycle from the *in vivo* 4D flow MRI data and the MSR-reconstructed data for the basilar tip aneurysm (a) and the internal carotid artery aneurysm (b). The median of the statistical distributions were represented using solid lines, while the shaded regions corresponded to the range between the 1st and 3rd quartiles.

The time-dependent median and the interquartile range of velocity magnitudes, WSS, and pressure obtained from the MRI and MSR-reconstructed data are presented in Figure 7.7 at all timepoints within the cardiac cycle. As suggested by the median values, the velocity and WSS magnitudes of the MSR-reconstructed fields were greater at around peak systole (at $t/T \approx 0.7$ for

the BT aneurysm and $t/T \approx 0.4$ for the ICA aneurysm), while preserved similar waveforms with MRI. The MSR reconstruction increased the mean velocity magnitudes by 13% and 6% compared to the MRI data of the BT and ICA aneurysms, respectively, while the mean WSS were increased by 60% and 51% for the BT and ICA aneurysms, respectively. As a reference, the mean WSS from CFD was 39% and 61% higher than the MRI data of the BT and ICA aneurysms, respectively, while the mean WSS from PTV was 47% and 60% higher than the MRI data of the BT and ICA aneurysms, respectively. As shown in Figure 7.7, the MSR-reconstruction altered the pressure waveforms and reduced the median pressure at peak systole by 30 Pa and 5 Pa for the BT and ICA aneurysms, respectively. The reduction on the median pressure was due to the improvement on the spatial resolution by the MSR reconstruction, which allowed the pressure estimation to better resolve the low-pressure region around the center of the aneurysmal sac corresponding to the core of the vortical flow structure as shown in Figure 7.6. The contributions of the CFD and PTV library-components were also obtained for the reconstructions of the in vivo 4D flow MRI data. The 2D histograms in Figure 7.8 show the distributions of the relative contributions of the CFD library-components in all subdomains as a function of time. The relative contribution from CFD library-components varied from 20-70% for the BT aneurysm, while it was 40-80% for the ICA aneurysm. The sparsity of the reconstruction was 0.88 for the BT aneurysm and 0.8 for the ICA aneurysm.

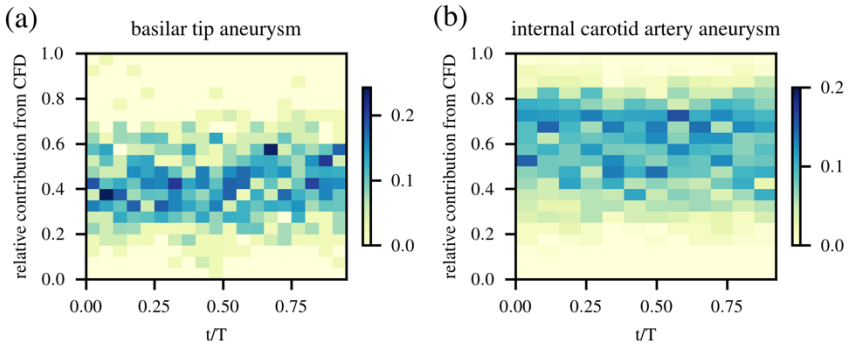

Figure 7.8 The distributions of the relative contributions of the CFD library-components in all subdomains as a function of time for the reconstructions of the in vivo 4D flow MRI data in the basilar tip aneurysm (a) and the internal carotid artery aneurysm (b).

7.4 Discussion

This study evaluated and applied a multi-modality approach to enhance the flow measurement and hemodynamic evaluation in cerebral aneurysms with 4D flow MRI. From the low-resolution MRI data, the MSR method reconstructed the velocity fields as sparse representation of the high-resolution velocity fields from PTV measurements and CFD simulations. The MSR enhanced the 4D flow MRI data in two aspects. First, the spatial resolution was substantially improved as the MSR-reconstructed velocity fields were on the same grid as the high-resolution data from CFD and PTV. The MSR reconstruction can provide up to a five-fold increase in the spatial resolution of the flow fields as suggested in Figure 7.3(b). Second, the MSR reconstruction improved the accuracy of the velocity data. Multiple factors affected the 4D flow MRI data's accuracy, including the spatio-temporal smoothing effect and the measurement noise. The MSR reconstruction overcame the spatial smoothing with the design of the measurement matrix, which performs the discrete convolution with the spatial smoothing kernel. Thus, the MSR reconstruction could retrace the measurement process to recover the underlaying velocity field prior to the spatial smoothing. The robustness of MSR was ensured by searching for a sparse representation with the penalization on $\|s\|_1$ in (7-4) to avoid overfitting the measurement noise. As a result, the MSR led to more than 70% error reduction compared to the 4D flow MRI data, as suggested in Figure 7.3(a).

The enhanced 4D flow MRI data from the MSR-reconstruction improved the hemodynamic analysis of the cerebral aneurysms. The synthetic MRI data showed a significant (40-60%) underestimation on the mean WSS as shown in Figure 7.5, which was consistent with the findings of previous studies (Roloff et al., 2019; van Ooij et al., 2015). The MSR reconstruction of the synthetic 4D flow MRI provided WSS more consistent with the ground truth, as suggested by the Bland-Altman analysis in Figure 7.5, owing to its ability to increase the spatial resolution and correct the spatial smoothing. With the improved spatial resolution by the reconstruction, visualization of the near-wall flow structures was enabled, and the pressure in the near-wall regions and smaller vessels could be obtained, as shown in Figure 7.6. The increase in velocity magnitude and WSS by MSR shown in Figure 7.7 suggests the accuracy of these quantities was improved, since 4D flow MRI underestimates the velocity magnitude by 10-20% (Roloff et al., 2019) and the WSS by 40-50% (Van Ooij et al., 2013) in cerebral aneurysms. Additionally, the WSS values from the MSR-reconstructed fields were more similar to those from the CFD and PTV results since they

were 39-61% higher than the 4D flow MRI results. Moreover, the low-pressure regions predicted at the vortex-cores around the center of the aneurysmal sac from the MSR-reconstructed data in Figure 7.7 were consistent with the previously published pressure distribution in cerebral aneurysm (Amili et al., 2018), while these low-pressure regions were absent from the pressure fields obtained from *in vivo* 4D flow data. Consequently, the more accurate hemodynamic quantities obtained from the MSR reconstruction would potentially allow for a more reliable risk evaluation of cerebral aneurysms with *in vivo* 4D flow MRI.

The MSR reconstruction's performance was affected by the flow-library composition as suggested by the error analysis with synthetic MRI data in Figure 7.4(a). The reconstruction of the CFD-synMRI data failed when using a flow-library containing only PTV components, while the reconstruction of PTV-synMRI data failed with the flow-library containing only CFD components. As presented in Figure 7.2, the flow fields from PTV and CFD had noticeable differences, suggesting that the velocity fields from one modality were not representative of the other modality's flow field. Thus, the assumption that the flow-library contains a sufficiently extensive collection of representative flow fields was violated, and the underlying flow field could not be reconstructed as a sparse representation of the library-components, leading to low-fidelity reconstruction and the less sparse coefficients as shown in Figure 7.4(c). For the MSR clinical application to *in vivo* 4D flow MRI data, a sufficiently extensive flow-library may be constructed using the flow fields obtained from multiple patient-specific CFD simulations with varying flow-boundary conditions within the uncertainty of the *in vivo* measurement. If there is also significant uncertainty in the aneurysm geometry, the results from several segmentations of the imaged geometries should also be collected to extend the flow-library. Since the aneurysmal flow can be complex due to the pulsatile inflow conditions and the tortuous vessel geometries, obtaining a proper sparse representation is challenging. Thus, we adopted the localized reconstruction strategy from (Callaham et al., 2019), such that the MSR only needs to find the sparse representation in each subdomain. This localized approach moderates the requirement on the extensiveness of the flow-library as finding the sparse representation in a smaller region with fewer measurements and lower rank is easier than the global reconstruction (Fathi et al., 2018). Since the radius of the subdomain was defined as 4 times of the spatial resolution of the 4D flow data, a subdomain located at the center of the aneurysmal sac could almost cover the bulk flow in the sac. However, the subdomain is still smaller than the whole region of interest (ROI) and therefore eliminates the

effect of the flow-data acquired in further upstream or downstream regions on the reconstruction within the subdomain. For example, the flow-reconstruction at the tip of the BT aneurysmal sac does not depend on the flow data in the R-PCA or L-PCA, which helps finding the sparse representation and avoids overfitting, therefore improving the robustness of the reconstruction. In the present study, the sparsity of the MSR-reconstructions of the *in vivo* aneurysmal 4D flow data was above 0.8, and different coefficients were obtained in different subdomains as suggested by the broad distributions of the relative contributions in Figure 7.8.

There are several limitations of MSR for reconstructing the aneurysmal flow measurement by 4D flow MRI. First, constructing an extensive flow-library requires several patient-specific CFD simulations or *in vitro* PTV measurements, which can be time-consuming and expensive to conduct. Patient-specific computational modeling of the cerebral aneurysmal flow typically takes several hours to complete, while the *in vitro* PTV measurements require special expertise and can be challenging due to the difficulties in the phantom fabrication, flow-loop building, particle imaging, and image processing procedures. Also, the flow-library prepared for one 4D flow MRI acquisition may be inappropriate for the data acquired at a different time point in a longitudinal study because of the possible morphological changes of CAs in time. Thus, the flow-library needs to be constructed for each 4D flow MRI acquisition, which is a limitation of MSR for clinical applications. Efficient flow-library generation approaches need to be developed in future studies. Alternatively, the recently introduced deep learning network based methods (Fathi et al., 2020; Ferdian et al., 2020) may be applied without the need for constructing flow-library for each reconstruction. Moreover, the linear matrix C may not be able to represent the measurement process of 4D flow MRI which is nonlinear in practice.

There are some additional limitations in this study. First, the construction of the measurement matrix C only considers the spatial smoothing effect of the 4D flow MRI measurement approximated as the convolution with a smoothing kernel. However, 4D flow MRI also causes temporal smoothing of the velocity field. Moreover, the kernel functions employed in this study may not accurately reproduce the smoothing effects of *in vivo* 4D flow MRI measurements which can also be affected by the encoding settings, the use of parallel imaging and compressive sensing techniques, etc. Also, the flow-library constructed for the *in vivo* 4D flow MRI data in this study contained only two datasets (one from CFD and one from PTV) for each CA, which might not be sufficiently extensive. More CFD simulations and *in vitro* PTV

measurements can be performed with different flow boundary conditions and used to extend the flow-library in future investigations. In addition, the CFD simulations did not consider the wall motion or fluid-tissue iterations, and the present study did not consider the blood density variance or the variability in RR intervals. The Newtonian fluid assumption may introduce additional errors in the CFD simulations, especially in regions with low shear rates.

7.5 Authors' contributions

J.Z. performed the flow reconstruction, data analysis, and drafted the manuscript; M.C.B. conducted the particle tracking velocimetry experiments and pre-processed the in vitro data; S.M.R. performed the flow simulations and manufactured the in vitro models; M.M obtained and pre-processed the in vivo data; and V.L.R. and P.P.V. designed and oversaw the study and all data analysis. All authors contributed to data analysis, critically reviewed and edited the manuscript and gave final approval for publication.

7.6 Data accessibility

Data and source codes used in this study are available in the Purdue University Research Repository (Title: A multi-modality approach for enhancing 4D flow MRI via sparse representation. URL: https://purr.purdue.edu/publications/3872/1).

7.7 Ethical statements

Approval of all ethical and experimental procedures and protocols was granted by the institutional review boards at Purdue University, Northwestern Memorial Hospital, and San Francisco VA Medical Center.

8. EVALUATION OF LEFT VENTRICULAR FLOW PROPAGATION VELOCITY FROM MULTI-DIMENSIONAL CARDIAC IMAGING

8.1 Background and literature review

The propagation velocity of the inflow jet during the left ventricular (LV) early diastole is dependent on the LV relaxation and has been used to assess the diastolic function (Hernandez-Suarez, Palm, Lopez-Menendez, Mesa Pabon, & Lopez-Candales, 2017; Nagueh, 2020; Nagueh et al., 2016). The normal LV relaxation creates a pressure drop from mitral orifice towards apex (De Boeck et al., 2005; Steine, Stugaard, & Smiseth, 1999) and enhances the vortex ring at the mitral valve tips (Charonko, Kumar, Stewart, Little, & Vlachos, 2013), aiding the early diastolic filling. The Vp of normal filling can exceed the speed of the blood cell (De Boeck et al., 2005; Sessoms, Lisauskas, & Kovács, 2002) and resembles the motion of an entire column of blood with short delay between the occurrence of peak velocity at mitral tip and apical region (Steine et al., 1999). With left ventricular diastolic dysfunction (LVDD), the LV relaxation is impaired, reducing the pressure force towards the apex and subsequently slowing the flow propagation (De Boeck et al., 2005; Steine et al., 1999).

The conventional propagation velocity (Vp) is determined from the spatiotemporal velocity map provided by Color M-mode (CMM) echocardiography as the slope of the iso-velocity contour corresponding to the front of the inflow wave (Brun et al., 1992; Garcia et al., 2000; Garcia, Thomas, & Klein, 1998; Kelley C. Stewart et al., 2011; M. Stugaard, Brodahl, Torp, & Ihlen, 1994; Marie Stugaard, Smiseth, Risöe, & Ihlen, 1993; Takatsuji et al., 1996; Yotti et al., 2005). Vp can also be quantified based on the time difference between the occurrences of peak velocity in the apical region and at the mitral tip (Steine et al., 1999; M. Stugaard et al., 1994; Marie Stugaard et al., 1993). These methods assume a constant Vp during early diastole, while the inflow wave front shows a curvilinear feature (Sessoms et al., 2002; Kelley C. Stewart et al., 2011), suggesting that the Vp is spatially and temporally varying, and therefore multiple Vp values can be extracted from a single image based on different iso-velocity contours (De Boeck et al., 2005; Thomas, 2011). As a consequence, large differences were found between the Vp obtained using different methods due to a lack of consensus on the definition of Vp (Sessoms et al., 2002). Recent developments consider the spatiotemporal variation of Vp and improved the classification ability (Chakraborty, Meyers, Iwano, Hall, & Vlachos, 2021; Kelley C. Stewart et al., 2011). However, the existing Vp

measurement methods are only applicable to CMM echocardiography which provides one-dimensional measurement, and the accuracy of the velocity and Vp is affected by the angle between M-mode cursor and flow (Nagueh et al., 2016).

The objective of the present study is to introduce a new method for determining flow propagation velocity from cardiac flow data and to resolve the spatiotemporal variations of Vp. This enables investigation of the correlation between Vp and the complex flow structures observed in the LV. The method was validated using synthetic flow data of a self-induced vortex ring. The method was demonstrated using *in vivo* data acquired using two-dimensional phase-contrast magnetic resonance imaging (pc-MRI) and 4D flow MRI.

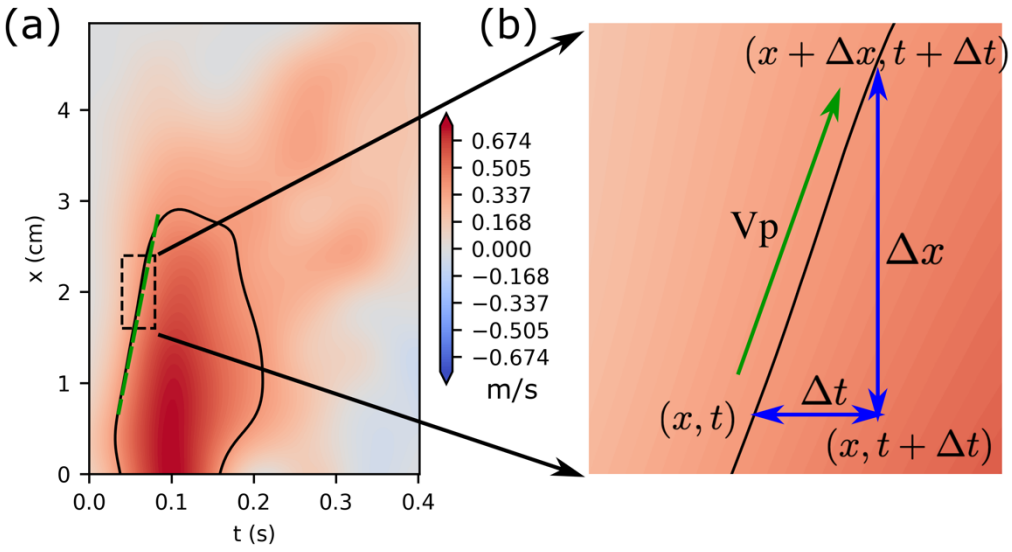

Figure 8.1 (a) The schematic demonstrates the common approach to measure Vp from the spatiotemporal velocity map. The black contour represents the velocity at 50% of the peak diastolic transmitral velocity. The Vp is estimated as the slope of green dashed line which is the linear approximation of the E-wave front based on the iso-velocity contour. (b) The schematic demonstrates the relationship between the Vp and the velocity values at different spatiotemporal points within the region of the velocity map indicated using the black dashed box shown in (a).

8.2 Methods

8.2.1 Theory

Figure 8.1 (a) illustrates the conventional approach to measure Vp from the spatiotemporal velocity map as the slope of a linear approximation of the iso-velocity contour (Garcia et al., 2000; Sessoms et al., 2002). This approach estimates the flow propagation by tracking the spatiotemporal occurrence of the contour-level velocity, e.g., from (x, t) to $(x + \Delta x, t + \Delta t)$ with $Vp = \Delta x/\Delta t$ as demonstrated in Figure 8.1 (b). Alternatively, the propagation can be inferred from the following relationship between the velocity values and gradients at different spatiotemporal points as:

$$u(x, t + \Delta t) = u(x + \Delta x, t + \Delta t) - \frac{\partial u}{\partial x}\Delta x = u(x, t) + \frac{\partial u}{\partial t}\Delta t, \quad (8\text{-}1)$$

where $\frac{\partial u}{\partial t}$ and $\frac{\partial u}{\partial x}$ are the temporal (t) and spatial (x) velocity gradients, respectively. Since both (x, t) and $(x + \Delta t, t + \Delta t)$ are on the iso-velocity contour line, $u(x, t) = u(x + \Delta t, t + \Delta t)$, and the following formulation can be derived from equation (8-1) as:

$$\frac{\partial u}{\partial t} + Vp\frac{\partial u}{\partial x} = 0. \quad (8\text{-}2)$$

Equation (8-2) is the first order wave equation governing the propagation of a waveform denoted by $u(x, t)$. With multi-dimensional and multi-component velocity data $\vec{u}(\vec{x}, t)$, Equation (8-2) can be modified as:

$$\frac{\partial \vec{u}}{\partial t} + \overrightarrow{Vp} \cdot \nabla \vec{u} = 0, \quad (8\text{-}3)$$

where ∇ represents the spatial gradient operator, and $\overrightarrow{Vp}$ is the vector consisting of the propagation velocity along all spatial dimensions. Equations (8-2) and (8-3) suggest that Vp can be estimated from the velocity gradients. We use V_{prop} to denote the propagation velocity estimated based on the first order wave equation herein, which is a scalar if estimated from one-dimensional data and a vector if estimated from multi-dimensional data.

8.2.2 V_{prop} estimation with weighted least-squares

The V_{prop} was estimated from the velocity gradients numerically calculated from the velocity fields using second order central (SOC) difference scheme. For each timeframe, the V_{prop} at each spatial point was determined by the weighted least-squares (WLS) fitting of the wave propagation equation (8-3) as:

$$V_{prop} = argmin\left(\sum_i^n w_i^2 \left|\frac{\partial \vec{u}}{\partial t} + V_{prop} \cdot \nabla \vec{u}\right|_i^2\right), \quad (8\text{-}4)$$

where n is the total number of data points within the field, and w_i is the weight for the i-th data point which was generated based on its spatial distance $|\Delta \vec{x}|$ from the point of interest as:

$$w_i = \begin{cases} exp\left(-\frac{|\Delta \vec{x}|^2}{L_0}\right) & if\ |\Delta \vec{x}| < L_0 \\ 0 & else \end{cases}, \quad (8\text{-}5)$$

where $L_0 = 0.5\ cm$ is the length scale, yielding a kernel width of 1 cm which corresponds approximately to the radius of the mitral valve. The weight decreases with the increase of the distance $|\Delta \vec{x}|$, and only the data within L_0 is employed for the fitting. The proposed WLS optimization will yield V_{prop} that is dependent on the local flow structure and ensures the robustness of the fitting.

To quantify the relative strength of the propagation, the V_{prop} component along the direction from mitral orifice towards the apex is extracted and spatially integrated in the LV. The integral at each timeframe is normalized by the average of all the timeframes during diastole and is named as the propagation intensity (I_{prop}).

8.2.3 Synthetic vortex ring flow

Synthetic flow fields of a self-induced Lamb-Oseen vortex ring were created to assess the accuracy of the proposed V_{prop} calculation method. The radius of the circular vortex ring (r_0) is $2\ cm$, and the angular velocity relative to the ring's circular axis can be expressed as:

$$u_\theta = u_{max}\left(1+\frac{1}{2\alpha}\right)\frac{r_{max}}{r}\left(1-e^{-\alpha\frac{r^2}{r_{max}^2}}\right), \quad (8\text{-}7)$$

where $u_{max} = 0.5\ m/s$ is the maximum angular velocity, $r_{max} = \sqrt{\alpha} \times r_c$ is the distance from the vortex core where the maximum angular velocity is reached, $r_c = 0.5\ cm$ is the vortex core radius, and the constant $\alpha = 1.25643$ (Devenport & Rife, 1996). The self-induction velocity (u_0) of the vortex ring is along the z-axis and can be determined from:

$$u_0 = u_{max}\left(1+\frac{1}{2\alpha}\right)\frac{r_{max}}{2r_0}\left(1-e^{-\alpha\frac{r_0^2}{r_{max}^2}}\right), \quad (8\text{-}8)$$

which is considered as the "ground truth" propagation velocity of the vortex ring flow. Three-dimensional (3D) velocity fields were created on a Cartesian grid with a spatial resolution of 2 mm in a domain spanning from $-2r_0$ to $2r_0$ along each spatial dimension. A total of 41 timeframes were uniformly sampled during the time when the vortex ring propagated from $z = -r_0$ to $z = r_0$, yielding a sampling rate at 98 Hz. In addition to the 3D data, two-dimensional (2D) and one-dimensional (1D) datasets were extracted at the center z-x plane and along the z-axis, respectively. To test the robustness of the proposed method against measurement noise, normally distributed random noise was added to the velocity data with the standard deviation varying from 0% to 20% of the maximum velocity magnitude along the z-axis.

8.2.4 Cardiac Magnetic Resonance (CMR) Image acquisition

Two-dimensional pc-MRI measurements were acquired from three patients, one with normal filling and two with LVDD, in accordance with the pre-established Institutional Review Board guidelines. The scans were performed at the Wake Forest University Baptist Medical Center in Winston-Salem, NC on an Avanto 1.5T scanner from Siemens Medical Solutions. Velocity encoding (VENC) was 100–130 cm/s, with a repetition time (TR) of 20 ms and an echo time (TE) of 3.3 ms. Flip angle was 20°, and the spatial resolution was 1.25 mm/pixel in-plane with a 5-mm slice thickness. Retrospective ECG gating was used for the acquisition with 40 or 45 reconstructed phases depending on patient heart rate. The pc-MRI images were segmented based on a separate

high signal-to-noise ratio imaging scan acquired over the same field of view, and the time-dependent LV boundaries were created for the pc-MRI fields. These data have been used in previous studies (Brindise, Meyers, & Vlachos, 2020; K. C. Stewart, Charonko, Niebel, Little, & Vlachos, 2012).

4D flow MRI data were acquired for three subjects with normal LV diastole at the Children's National Hospital in an Institutional Review Board-approved retrospective study (Loke et al., 2021). A Siemens 1.5-T scanner was used for acquiring the CMR data, with the field of view (FOV) of 280-480 × 140-230 mm and a matrix of 160×77. The TE was 2.19 ms, and the TR was 37.9-59.4 ms. The flip angle was 15°, and the VENC was 2-2.5 m/s. The slice size was 1.8 mm or 2.75 mm, and the pixel size was 1.75 or 2.735 mm, depending on the patient size. The number of reconstructed phases was 20-30 of a cardiac cycle. The time-dependent LV boundaries for the 4D flow data were created based on the long-axis and short-axis cine images acquired for the same subjects.

8.2.5 Velocity data preprocessing

The following preprocessing procedure was performed on the velocity fields of the synthetic data and the *in vivo* cardiac flow prior to the V_{prop} estimation. The spurious velocity measurements were detected using the universal outlier detection (UOD) method (Westerweel & Scarano, 2005) based on the local variation of velocity in the neighborhood containing 3 pixels along each spatial dimension, and the outlier measurements were replaced with the median of the neighborhood. To ensure the smoothness of the velocity field, the velocity profile along each dimension was reconstructed as an ensemble of radial basis functions (RBFs):

$$u(x) = \sum_{j=1}^{N} s_j T_j(r_j), \quad (8\text{-}9)$$

$$with\, T(r) = r^4 ln\ r, \quad (8\text{-}10)$$

where N is the total number of RBFs, s_j is the amplitude of the j-th RBF T_j, and $r_j = |x - x_j|$ is the distance to the j-th RBF centered at x_j. The 4-th order thin-plate spline is employed for the RBF as expressed in equation (10). The RBFs were distributed uniformly along each dimension with 5 mm separation. The RBF amplitudes were determined as:

$$s_j = argmin\left(\left|\sum_{j=1}^{N} s_j T_j(r_j) - u\right|^2\right), \quad (8\text{-}11)$$

which minimizes the least-squares residual between the original velocity profile with the RBF representation to ensure the fidelity of the reconstruction.

8.2.6 Postprocessing methods

Instantaneous pressure fields were estimated from the LV velocity fields using the measurement-error based WLS method (Zhang, Brindise, et al., 2020). The pressure gradients (p_{grad}) were calculated using the Navier-Stokes momentum equation, which were then spatially integrated to obtain the pressure field (p_{WLS}) as:

$$p_{WLS} = argmin\left(\left|W(\nabla p - p_{grad})\right|^2\right), \quad (8\text{-}12)$$

where W is the weight matrix generated based on the velocity error predicted from the spurious divergence of the velocity field. A 0 Pa reference pressure was assigned at the mitral orifice such that the estimated pressure is relative to the mitral orifice. The pressure difference between the mitral orifice and the apical region is defined as the intraventricular pressure difference (IVPD). A positive IVPD means that the pressure at the mitral orifice is higher than the pressure in the apical region.

The vortical structures were identified from the LV velocity fields based on the local swirling strength denoted as λ_{ci} which is quantified as the imaginary part of the complex eigenvalues of the velocity gradient tensor (J. Zhou, Adrian, Balachandar, & Kendall, 1999). Vortices were identified as the connected regions where the absolute value of λ_{ci} is above 4% of the maximum value measured in the LV over the diastole.

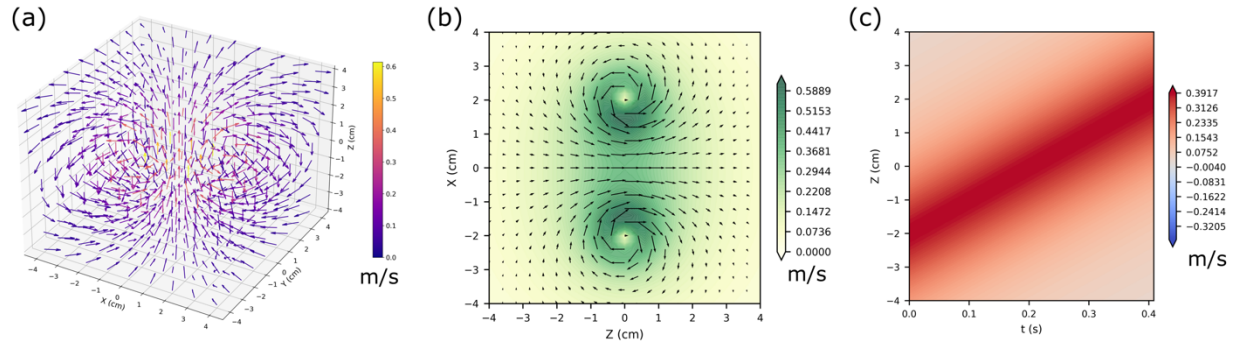

Figure 8.2 (a) The three-dimensional velocity field of the vortex ring flow from the middle timeframe. The color of the arrows corresponds to the local velocity magnitude. (b) The two-dimensional velocity field of the vortex ring flow on the center x-z plane from the middle timeframe. The background color suggests the local velocity magnitude. (c) The spatiotemporal velocity map sampled along the z-axis.

8.3 Results

8.3.1 Error analysis with synthetic vortex ring flow

Figure 8.2 (a) and (b) show the velocity field in the 3D volume and on the center x-z plane, respectively, from the middle timeframe when the vortex ring center is located at $z = 0\ mm$. Figure 8.2 (c) presents the spatiotemporal velocity map of the 1D data sampled along the z-axis. The errors in the estimated V_{prop} were assessed as the differences from the vortex ring's self-induction velocity u_0. For each dataset, the quartiles of the absolute V_{prop} errors were determined in a moving region defined as $|z - z_o| < r_0$, where z_o is the z-location of the vortex ring center which propagates from $-r_0$ to r_0 during the sampled time. The quartiles are normalized by u_0 and shown in Figure 8.3 as a function of the velocity noise level. The normalized median absolute error in the V_{prop} estimated from the 1D data increases from 0.007 to 0.82 as the velocity noise level

increases from 0% to 20%, while the normalized median absolute Vp error increases from 0.008 to 0.37 and from 0.004 to 0.29 for the estimations from 2D and 3D datasets, respectively.

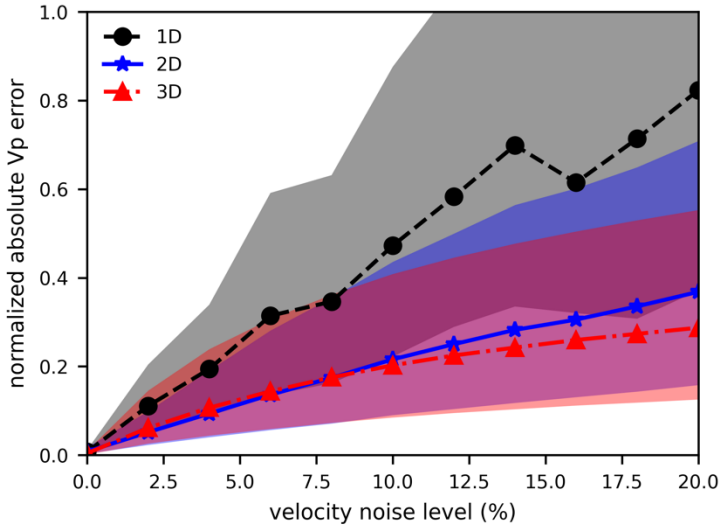

Figure 8.3 The normalized absolute error in the V_{prop} calculated using the proposed method from the 1D, 2D, and 3D data of the vortex ring flow as a function of the velocity noise level. The lines suggest the median absolute error, and the shaded region indicates the interquartile range of the error distribution.

8.3.2 Results from two-dimensional pc-MRI

Figure 8.4 (a) shows the waveforms of the mitral inflow, the IVPD, and the propagation intensity (I_{prop}) during LV diastole for the normal filling patient. At the beginning of the normal LV filling, the IVPD and I_{prop} increases as the inflow velocity increases. The peak I_{prop} coincides with the peak IVPD at around 0.05 s after the start of the LV diastole. The IVPD quickly drops to negative when the peak inflow velocity is reached, suggesting that the pressure in the apical region becomes higher than the mitral orifice pressure. The secondary peaks of the I_{prop} and IVPD can be observed during the atrial filling around 0.4 s. For LVDD patients shown in Figure 8.5 (a), the peaks of the mitral inflow velocity and IVPD during early diastole are lower than the normal filling. The peaks of Ip and IVPD are higher during the atrial filling at around 0.3 s than the peaks during

early diastole for the HCM patient, while the DCM patient shows no prominent peaks of IVPD or I_{prop} during the entire diastole.

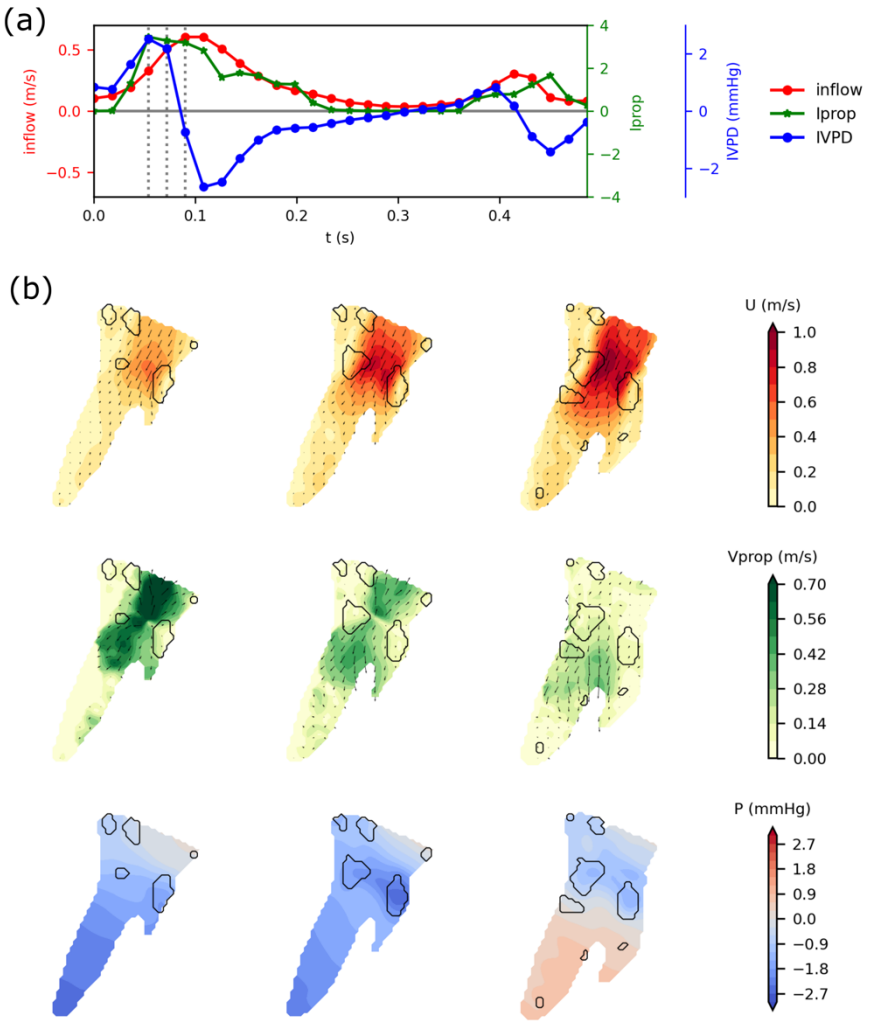

Figure 8.4 (a) The waveforms of the mitral inflow velocity, the intraventricular pressure difference (IVPD), and the propagation intensity (I_{prop}) during the LV diastole of the normal filling patient imaged with two-dimensional pc-MRI. (b) The fields of the blood flow velocity, the Vp, and the relative pressure from the timeframes indicated using the dotted lines in the waveform plots in (a).

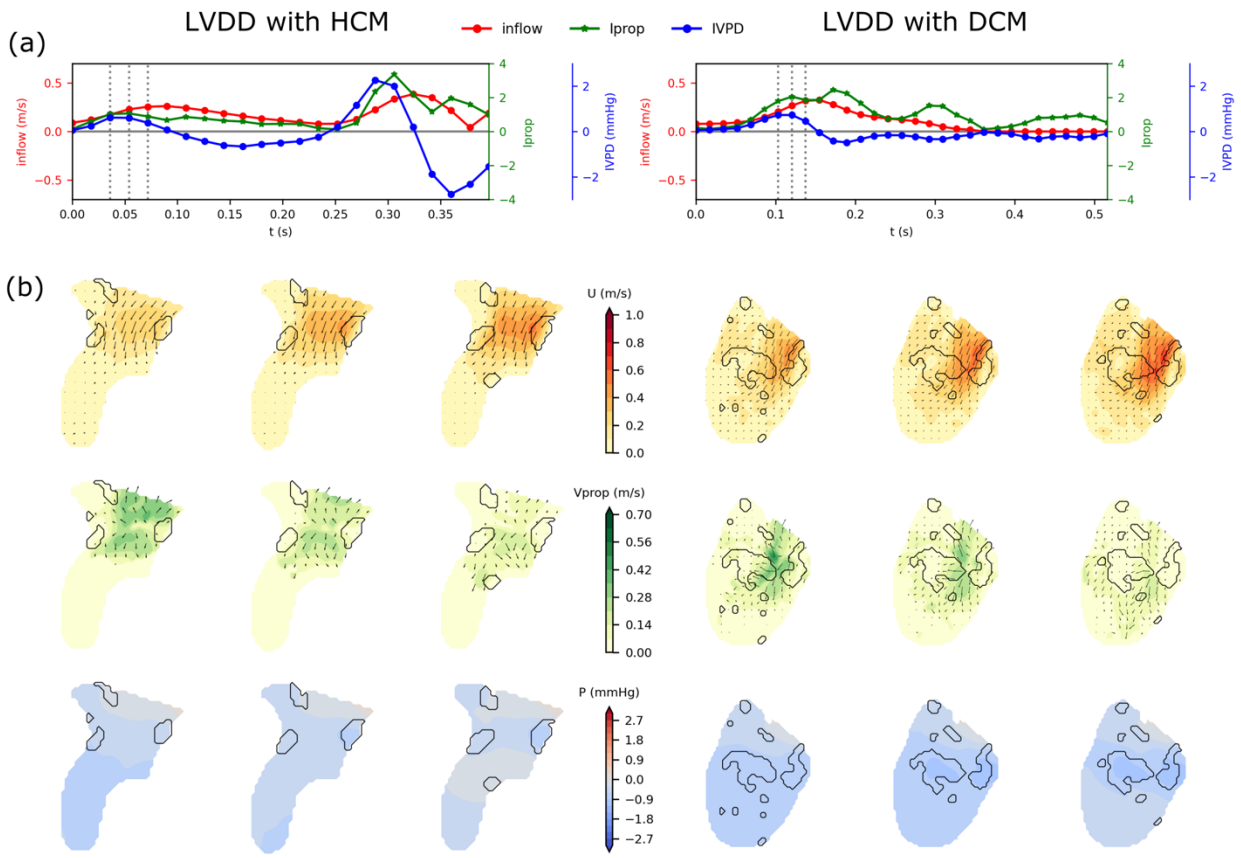

Figure 8.5 (a) The waveforms of the mitral inflow velocity, the intraventricular pressure difference (IVPD), and the propagation intensity (I_{prop}) during the LV diastole of the LVDD patients imaged with two-dimensional pc-MRI. The left column shows the HCM patient, and the right column corresponds the DCM patient. (b) The fields of the blood flow velocity, the Vp, and the relative pressure from the timeframes indicated using the dotted lines in the waveform plots in (a).

The fields of flow velocity, V_{prop}, and relative pressure in the LV at three consecutive timeframes during early diastole are presented in Figure 8.4 (b) and Figure 8.5 (b) for the normal filling and LVDD patients, respectively. The plotted timeframes are indicated using the vertical dotted lines in the corresponding waveform plots. The black contours in the fields identify the borders of the vortex structures. For the normal filling, a vortex ring is formed near the mitral valve tips around the inflow jet, and strong flow propagation towards apex can be observed downstream of the vortex ring. The pressure decreases from the mitral orifice to the apex at the first timeframe, while the pressure in the apical region rises and becomes higher than the pressure around the mitral orifice at the third timeframe. From the LVDD patients, both the inflow jet and the flow propagation are weaker than the normal filling. The flow propagation of the LVDD patients also

shows a shorter penetration than the normal filling, as the filling V_{prop} is only found near the vortex ring from the LVDD patients, while the filling V_{prop} is still significant further downstream of the vortex ring into the apical region of the normal LV. The Vp downstream of the vortex ring is more aligned towards the apex in the normal LV, while the V_{prop}'s direction quickly diverges after passing the vortex ring in the LVDD patients. The pressure has a more uniform distribution in the LV of the LVDD patients than in the normal LV.

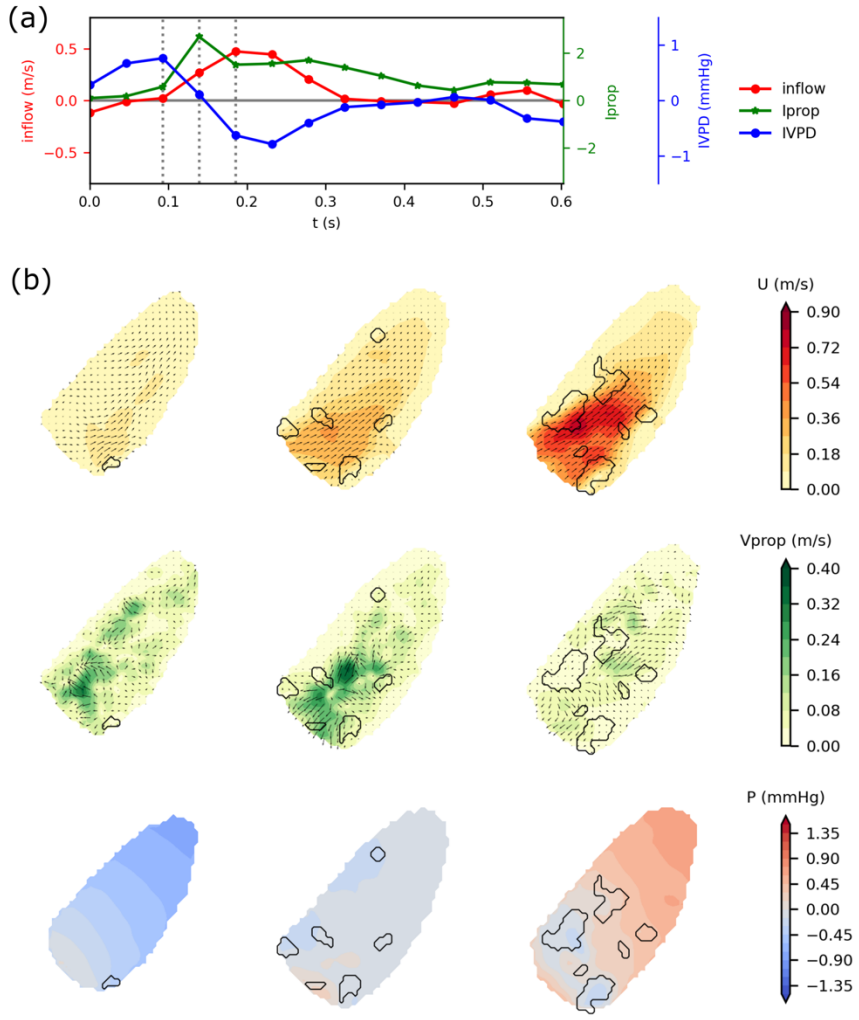

Figure 8.6 (a) The waveforms of the mitral inflow velocity, the intraventricular pressure difference (IVPD), and the propagation intensity (I_{prop}) during the LV diastole determined from the 4D flow MRI data of a normal filling subject. (b) The fields of the blood flow velocity, the V_{prop}, and the relative pressure on the four-chamber view from the timeframes indicated using the dotted lines in the waveform plots in (a).

8.3.3 Results from 4D flow MRI

The waveforms of the mitral inflow, the IVPD, and I_{prop} determined from the 4D flow data of a normal subject are presented in Figure 8.6 (a). Positive IVPD is found at the beginning of the diastole as the mitral inflow increases and drops to negative when the peak inflow is reached. The peak of I_{prop} during early diastole is found between the peak IVPD and peak mitral inflow. Three timeframes during early diastole with increasing mitral inflow are selected as indicated by the vertical dotted lines. Figure 8.6 (b) shows the in-plane velocity, V_{prop}, and relative pressure fields during the selected timeframes on the four-chamber view. Like the results from the normal filling patient shown in Figure 8.4, a vortex ring forms with the mitral inflow, and the relative pressure in the apical region rises as the inflow jet reaches the apex. As shown in the middle frame in Figure 8.5 (b), the region with significant filling V_{prop} towards apex is located downstream of the vortex ring. The waveforms and the fields of the other two subjects are provided in Appendix B.

8.4 Discussion

This study introduces a method to measure the LV filling propagation velocity from multi-dimensional cardiac flow imaging. The proposed method estimates the V_{prop} at each spatiotemporal point by fitting the first order wave equation to the velocity gradients in the neighborhood. The method's performance was evaluated with synthetic vortex ring flow data, and the error analysis results suggested that more accurate V_{prop} can be obtained from multi-dimensional data (2D and 3D) than from 1D data. Compared to the result from 1D data with 20% noise, the median absolute V_{prop} error was 55% and 65% lower from the 2D data and 3D data with the same noise level, respectively. Determining V_{prop} from multi-dimensional data also avoids the limitation of the one-dimensional CMM that the measurement accuracy is affected by the angle between the M-mode cursor and the flow. The V_{prop} estimated from multi-dimensional data is also directional as shown in the V_{prop} fields from Figure 8.4, Figure 8.5, and Figure 8.6.

The proposed method provides the spatial distribution and the temporal evolution of V_{prop}, which helps in understanding the mechanism of the LV filling propagation and its relationship with the pressure gradient and the vortical structures. For the normal filling shown in Figure 8.4, the peak flow propagation in terms of I_{prop} occurs around the time when the maximum IVPD is reached with relatively low mitral inflow. At the later timeframes with the peak mitral inflow, the

inflow jet reaches the apical region and increases the apical pressure. The pressure gradient no longer aids LV filling, and the V_{prop} becomes lower than the previous timeframes despite the stronger convection caused by the blood flow towards apex. This suggests that the pressure gradient created by the LV relaxation has a stronger effect on the flow propagation during early diastole than the local convection, which is consistent with the previous findings based on CMM echocardiography (De Boeck et al., 2005; Sessoms et al., 2002). For the LVDD patients, the timing of the peak I_{prop} also coincides with the peak IVPD during the early diastole as shown in Fig. 4, although the mitral inflow, IVPD, and V_{prop} are significantly lower than the values from the normal filling patient. Additionally, the V_{prop} is correlated with the vortex ring formed near the mitral valve tips during the early diastole. As shown in Figure 8.4, Figure 8.5, and Figure 8.6, the flow propagation towards apex is mainly found at the front of the inflow jet downstream of the vortex ring. For the normal filling, the vortex ring creates a virtual channel, allowing the inflow jet to propagate into the LV without spreading (Charonko et al., 2013). For the LVDD patients, the vortex ring at the mitral valve tips is smaller in size and closer to the base of the ventricle, leading to the shorter penetration of the flow propagation which quickly diverges after passing the vortex ring as shown in Figure 8.5.

There are some limitations of the proposed method. First, the V_{prop} is estimated from the velocity gradients whose accuracy is sensitive to the noise in the velocity data. We performed UOD followed by the RBF reconstruction to enhance the smoothness and the fidelity of the velocity data and therefore to ensure the reliability of the velocity gradient evaluation. Moreover, the V_{prop} measurement requires time-resolved velocity data. The maximum resolvable V_{prop} from the proposed method can be approximated as $0.5L_p/\Delta t$, where L_p is the flow propagation distance, and Δt is the time difference between acquired phases. The factor 0.5 is due to the SOC scheme which estimates the temporal derivative from two timeframes separated by $2\Delta t$. With a typical L_p of 4 cm, the minimum sampling rate required to resolve a common normal filling V_{prop} at 1 m/s is 50 Hz ($\Delta t = 25\ ms$), which can be difficult to achieve for some imaging modality such as 4D flow MRI. In the present study, the maximum normal filling V_{prop} obtained from the 4D flow MRI is around 0.4 m/s, which is lower than the maximum V_{prop} determined from the two-dimensional pc-MRI data at about 0.8 m/s. This may be caused by the difference in the temporal resolutions as the 4D flow data was acquired with a Δt of 28-46 ms, while the two-dimensional pc-MRI has a Δt of 18 ms.

Overall, this study introduces a novel flow propagation velocity measurement method for multi-dimensional cardiac flow imaging. The method estimates the V_{prop} by fitting the first order wave equation to the velocity gradients and can resolve the spatiotemporal variation of V_{prop}. The error analysis with synthetic vortex ring flow suggests that measuring V_{prop} from multi-dimensional data is more robust than from 1D data. The method was applied to the multi-dimensional CMR data and demonstrated the V_{prop}'s distribution in the LV and the evolution during the diastole. The results also reveal that the flow propagation during the early diastole is mainly driven by the pressure gradient, and the vortex ring formation near the mitral valve tips can aid the flow propagation.

9. CONCLUSIONS AND FUTURE WORK

9.1 Conclusions

The present works introduce and apply the flow-physics constrained data enhancement and augmentation methods for 4D flow MRI to help the risk stratification of unruptured cerebral aneurysms. A divergence-free constrained phase unwrapping method is introduced in Chapter 2, which improves the dynamic range of the 4D flow measurement. The method also denoises the phase field and thus enhances the velocity-to-noise ratio of the resulting velocity data. Additionally, the evaluation of hemodynamic parameters is improved by the pressure reconstruction and WSS estimation methods introduced in Chapter 3 and 4. The proposed pressure reconstruction method with WLS reduces the pressure error by 50% to 200% as compared to the method by solving the pressure Poisson equation (PPE), and the proposed WSS estimation method reduces the underestimation of mean WSS by 39% to 50% for the aneurysmal flow. Moreover, a multi-modality approach is introduced and applied to enhance the blood flow measurements and the hemodynamic analysis with 4D flow MRI in cerebral aneurysms as presented in Chapter 7. Using a library of high-resolution velocity fields from patient-specific CFD simulations and in vitro PTV measurements, the flow field of 4D flow MRI data is reconstructed as the sparse representation of the library. The reconstruction increased the velocity and WSS by 6-13% and 39-61%, respectively, suggesting the accuracy of these quantities was improved since the raw MRI data underestimated the velocity and WSS by 10-20% and 40-50%, respectively. We also proposed a method to measure the LV flow propagation velocity (V_{prop}) from cardiac flow imaging including 4D flow MRI as presented in Chapter 8. The method estimates V_{prop} based on the first order wave equation and exhibits the capability of resolving the spatiotemporal variation of V_{prop}, and the mechanisms of V_{prop} during early LV diastole was revealed. The proposed V_{prop} measurement method provides a more comprehensive investigation and potentially improves the evaluation of LV diastolic function.

The present works also demonstrate the flow-physics data enhancement and augmentation approach on the flow data acquired using other techniques. An instantaneous pressure reconstruction method for PIV/PTV is introduced in Chapter 5, which uses the uncertainty information from PIV/PTV and reconstructs the pressure fields with generalized least-squares

(GLS). The method improves the pressure reconstruction from 2D or 3D velocity fields including laminar and turbulent flow conditions with as much as 96% error reduction in the reconstructed pressure field. Additionally, a practical framework to estimate the reconstructed pressure's uncertainty is introduced in Chapter 6 by propagating the velocity uncertainty from PIV/PTV through the pressure reconstruction. The framework is shown to be able to predict the local and instantaneous pressure uncertainty and reproduce the effects of velocity error characteristics, boundary conditions, and the pressure integration method on the reconstructed pressure fields. Moreover, we have developed data enhancement and augmentation methods to improve the density field measurement with background oriented schlieren (BOS) (Rajendran, Zhang, Bane, & Vlachos, 2020) and the measurement of concentration-dependent diffusion coefficient (Ahmadzadegan, Zhang, Ardekani, & Vlachos, 2022).

9.2 Limitations and future work

There are several limitations of the present study. First, the vessel wall was assumed to be rigid, and the wall motion or fluid-tissue iterations were not considered. Although the rigid wall assumption is reasonable for modeling the flow in cerebral arteries as cine MR images showed no appreciable movements of these vessels over the cardiac cycle in a previous investigation (Boussel et al., 2008), it may not be appropriate for the aortic wall. Moreover, the Newtonian flow was assumed, which may not be ideal in low WSS regions. The present studies did not consider the blood density variance or the variability in RR intervals, which may lead to additional errors in the calculations of hemodynamic parameters. Additionally, the proposed methods require the blood flow region (ROI) to be segmented prior to the processing, which can be difficult for acquisitions with tissue movement. The uncertainty in the wall location may affect the accuracy of the WSS estimation. Another limitation of the present works is the lack of ground truth for the *in vivo* 4D flow data, which prevents the error analysis of the velocity measurement and the derived hemodynamic parameters from the *in vivo* datasets. We overcame this limitation by investigating the consistency between the results across different modalities and by analyzing the correlation between the results with the flow structures to assess the proposed methods' performance on *in vivo* 4D flow data.

Several future works are proposed for the present study. First, the flow-physics constrained data enhancement and augmentation methods will be applied to a suitable cohort containing a

sufficiently large number of patients with longitudinal recordings in order to evaluate and establish the statistical correlation of the hemodynamic factors with the growth and rupture of cerebral aneurysms. Furthermore, biomarkers will be derived from the flow propagation velocity measured using the proposed method in Chapter 8 to improve the diagnosis of the LV diastolic dysfunction. We also propose to expand the application of the data enhancement and augmentation methods to other parts of the cardiovascular system including the carotid artery and pulmonary artery and investigate the correlation between hemodynamic metrics with cardiovascular diseases. Moreover, further developments on the flow-physics constrained data enhancement and augmentation methods will be conducted, including an efficient flow-library generation approach for the multi-modality flow reconstruction with sparse representation. We will also explore using machine learning methods such as artificial neural network to incorporate flow-physics constraints for enhancing 4D flow data.

APPENDIX A. WSS ERROR ANALYSIS WITH SYNTHETIC 4D FLOW MRI DATA

Synthetic 4D flow MRI data generation methodology

Synthetic 4D flow MRI datasets were created based on the velocity fields from CFD simulations and analytical Womersley flow. The flow sensitive MRI signal corresponding to the u velocity component was generated as:

$$M_u = I_{mag} exp\left(\frac{i\pi u}{venc}\right), \quad (A\text{-}1)$$

where M_u is the complex-valued MRI signal for u velocity, I_{mag} represents the signal magnitude, and venc is the velocity encoding sensitivity parameter. The value of I_{mag} was set as 1.0 in the flow ($r < R$) and 0.2 elsewhere, yielding a saturation raito of 0.2. The synthetic 4D flow data were generated on a Cartesian grid with a voxel size of $\Delta x \times \Delta y \times \Delta z$. To mimic the spatial smoothing effect of 4D flow MRI, the MRI signal at each grid point was generated by convolving M_u with a sinc-function kernel $\mathcal{K}$ as:

$$M_{w,MRI} = M_w * \mathcal{K}, \quad (A\text{-}2)$$

with $\mathcal{K}(x, y, z) = sinc\left(\frac{x}{\Delta x}\right) sinc\left(\frac{y}{\Delta y}\right) sinc\left(\frac{z}{\Delta z}\right)$,

where $*$ denotes the convolution operation. The sinc-function kernel has been employed to simulate the spatial blurring of Cartesian 4D flow MRI due to limited k-space coverage in previous studies (Rispoli et al., 2015; Zhang et al., 2022, 2021). The MRI signals for the other velocity components ($M_{v,MRI}$ and $M_{w,MRI}$) were created similar to (A-1). According to a four-point acquisition method, the reference MRI signal ($M_{0,MRI}$) was created from a zero-velocity field such that the phase difference between the flow-sensitive signal and $M_{0,MRI}$ matched the corresponding velocity component. To consider the measurement noise, normally distributed noise (ϵ_{MRI}) was added to the complex-valued MRI signal (den Dekker & Sijbers, 2014). This complex noise is defined as:

$$\epsilon_{MRI} = \epsilon_{RE} + i\epsilon_{IM}, \quad (A\text{-}3)$$

with $\epsilon_{Re}, \epsilon_{Im} \in \mathcal{N}(0, \sigma^2)$,

where ϵ_{RE} and ϵ_{IM} indicate the noise added to the real and imaginary parts, respectively. The standard deviation σ was set based on the predefined velocity-to-noise ratio (VNR) (Lee et al., 1995) as:

$$\sigma = \frac{I_{mag}}{VNR}\frac{\pi}{\sqrt{2}}\frac{\bar{V}}{venc} \quad (A\text{-}4)$$

where $\bar{V}$ is the mean velocity in the flow field. The 4D flow velocity data was then obtained from the MRI signal, *e.g.*, for the u component as:

$$u_{MRI} = \frac{venc}{\pi}\psi_u = \frac{venc}{\pi}angle\left(M_{u,MRI}M^*_{0,MRI}\right), \quad (A\text{-}5)$$

where ψ_u is the phase difference, $M^*_{0,MRI}$ is the complex conjugate of $M_{0,MRI}$, and $angle(\cdot)$ evaluates the angle of the complex number.

Synthetic 4D flow data of analytical Womersley flow

Womersley flow is representative of pulsatile flow in a circular pipe driven by an oscillatory pressure gradient and has been used to represent arterial flow in the cardiovascular system (Womersley, 1955). The streamwise velocity component (w along z-direction) can be analytically expressed as:

$$w(r,t) = Real\left\{\sum_{n=0}\frac{iP_{n'}}{\rho n\omega}\left[1 - \frac{J_0\left(\alpha n^{1/2}i^{3/2}\frac{r}{R}\right)}{J_0\left(\alpha n^{1/2}i^{3/2}\right)}\right]e^{in\omega t}\right\}, \quad (A\text{-}6)$$

where r is the radial coordinate, R is the pipe radius, ω is the angular frequency of the first harmonic of the oscillatory pressure gradient $\frac{dp}{dz}$, $\alpha = R\left(\frac{\omega\rho}{\mu}\right)^{1/2}$ represents the Womersley number, $P_n{}'$ is the pressure gradient magnitude for the harmonic at frequency $n\omega$, $J_0(\cdot)$ is the zeroth-order

Bessel function of the first kind, i is the imaginary number, and $Real\{\cdot\}$ takes the real component of a complex number. The velocity components along other spatial dimensions are zero. The WSS can be determined analytically as

$$\tau_w(t) = Real\left\{\sum_{n=0} {P_n}' \frac{R}{\Lambda_n} \frac{J_1(\Lambda_n)}{J_0(\Lambda_n)} e^{in\omega t}\right\}, \quad \textit{(A-7)}$$

with $\Lambda_n = \alpha n^{1/2} i^{3/2}$,

where $J_1(\cdot)$ is the first-order Bessel function of the first kind. The oscillatory pressure gradient was specified as:

$$\frac{dp}{dz}(t) = P_0\, sin(2\pi t), \quad \textit{(A-8)}$$

with $\omega = 2\pi$ rad/s corresponding to a heart rate of 60 bpm. The velocity profile and WSS of the Womersley flow depend on the Womersley number, α. We considered the following α values to cover the typical range in the cardiovascular system: 1, 2, 4, 8, 12, 16, which lead to the following pipe diameters: 1.5, 3.1, 6.2, 12.4, 18.6, and 24.8 mm, with $\rho = 1100\ kg/m^3$, $\mu = 0.004\ Pa \cdot s$, and $\omega = 2\pi$.

Synthetic 4D flow data were created from the analytical solution of the Womersley flow using the approach described in section S1. The venc was 1.5 times the maximum velocity in the flow field to avoid velocity aliasing. The synthetic 4D flow data were generated on a Cartesian grid in a 4R long pipe section. The isotropic voxel sizes were 1/2, 1/3, 1/4, 1/5, 1/7, 1/9, 1/11, and 1/14 of the pipe diameter (D), and the temporal resolution (Δt) was 50 ms, yielding 20 frames per cycle. For each Womersley number and spatial resolution, one dataset without noise and one dataset with a VNR of 10 (10% noise) were created. For each dataset, 100 wall points were selected for the WSS evaluation and analysis.

APPENDIX B. FLOW PROPAGATION VELOCITY ESTIMATED FROM 4D FLOW DATA

The figures in this appendix present the results evaluated from the 4D flow data of two normal filling subjects. (a) The waveforms of the mitral inflow velocity, the intraventricular pressure difference (IVPD), and the propagation intensity (I_{prop}) during the LV diastole determined from the 4D flow MRI data of a normal filling subject. (b) The fields of the blood flow velocity, the V_{prop}, and the relative pressure on the four-chamber view from the timeframes indicated using the dotted lines in the waveform plots in (a).

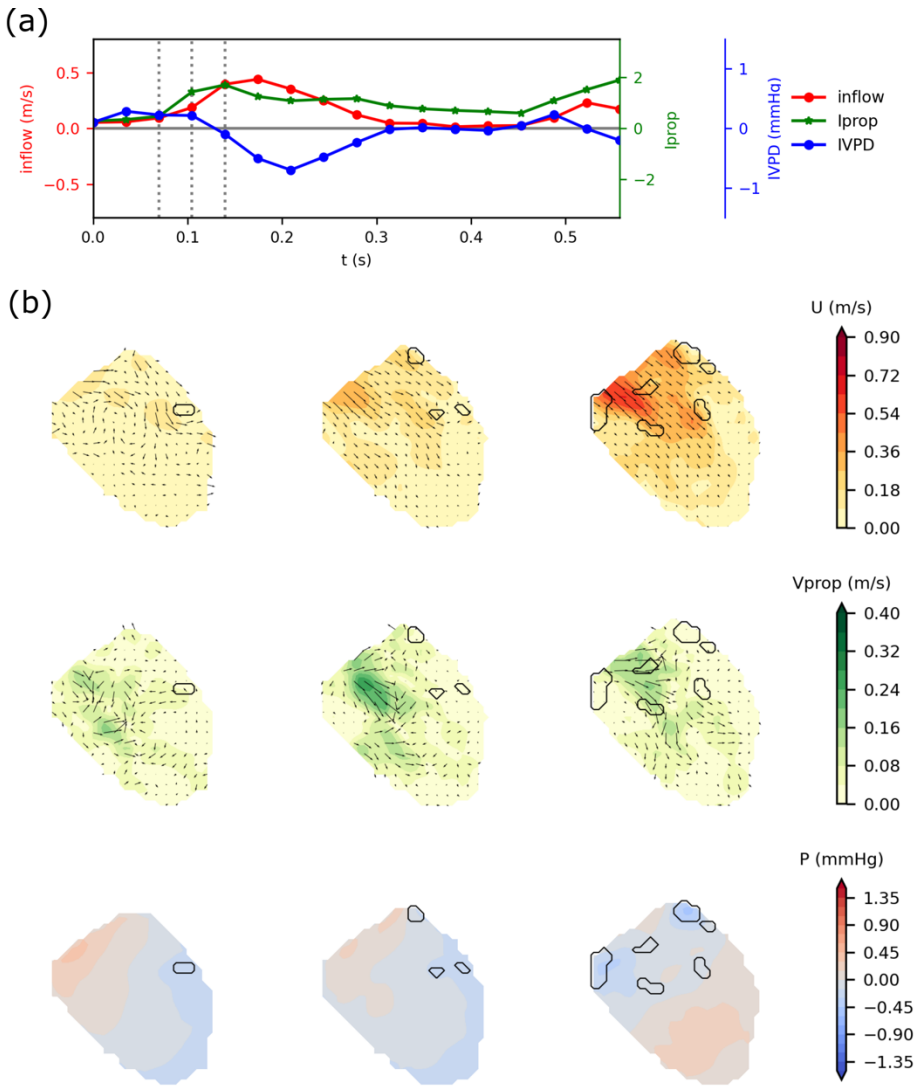

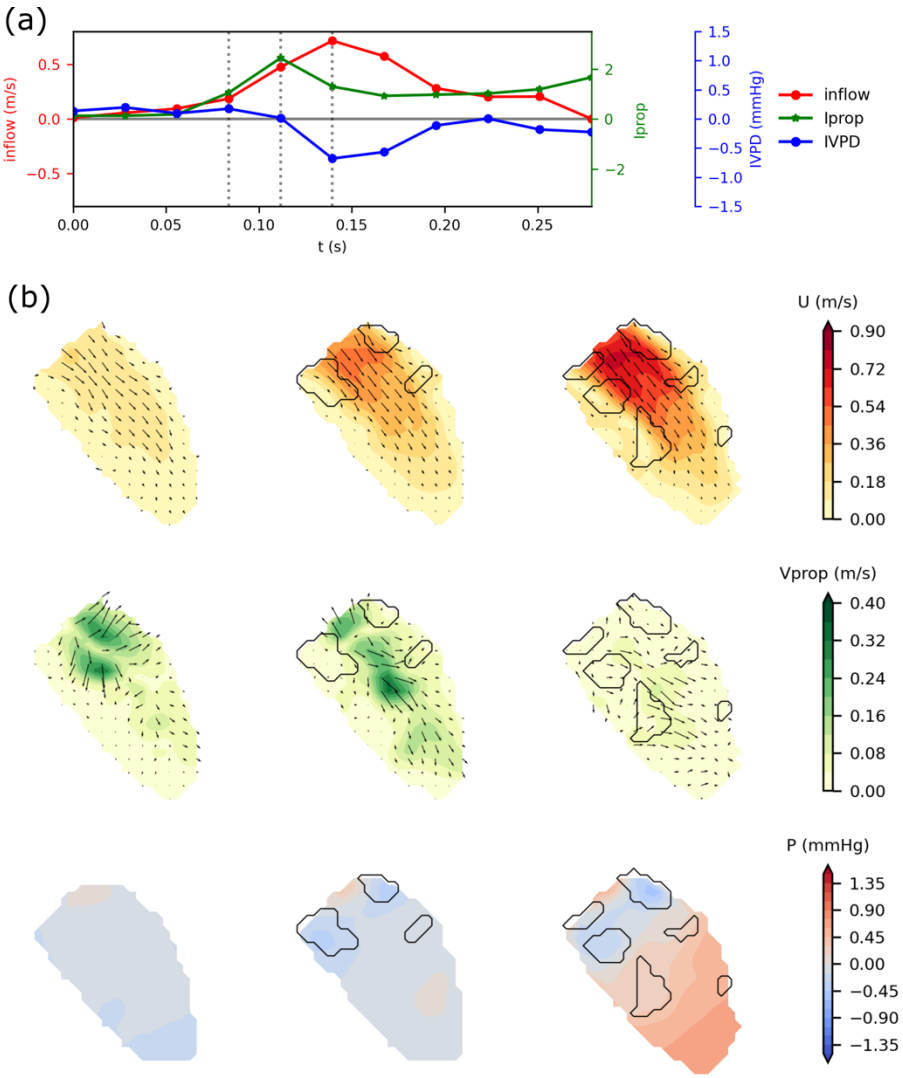
(a)
inflow (m/s)
lprop
lVPD (mmHg)
t (s)
inflow
lprop
lVPD
(b)
U (m/s)
Vprop (m/s)
P (mmHg)

REFERENCES

Ahmadzadegan, A., Zhang, J., Ardekani, A., & Vlachos, P. P. (2022). Spatiotemporal Measurement of Concentration-Dependent Diffusion Coefficient. *Authorea*, (March 31). https://doi.org/10.22541/au.164873358.86144442/v1

Ajiboye, N., Chalouhi, N., Starke, R. M., Zanaty, M., & Bell, R. (2015). Unruptured Cerebral Aneurysms: Evaluation and Management. *Scientific World Journal*, *2015*. https://doi.org/10.1155/2015/954954

Amili, O., Schiavazzi, D., Moen, S., Jagadeesan, B., Pierre- Francois Van de Moortele, & Coletti, F. (2018). Hemodynamics in a giant intracranial aneurysm characterized by in vitro 4D flow MRI. *PLoS ONE*, *13*(1), e0188323. https://doi.org/https://doi.org/10.1371/journal.pone.0188323

Aristova, M., Vali, A., Ansari, S. A., Shaibani, A., Alden, T. D., Hurley, M. C., … Schnell, S. (2019). Standardized Evaluation of Cerebral Arteriovenous Malformations Using Flow Distribution Network Graphs and Dual-venc 4D Flow MRI. *Journal of Magnetic Resonance Imaging*, *50*(6), 1718–1730. https://doi.org/10.1002/jmri.26784

Asgari, S., Wanke, I., Schoch, B., & Stolke, D. (2003). Recurrent hemorrhage after initially complete occlusion of intracranial aneurysms. *Neurosurgical Review*, *26*(4), 269–274. https://doi.org/10.1007/s10143-003-0285-6

Azijli, I., & Dwight, R. P. (2015). Solenoidal filtering of volumetric velocity measurements using Gaussian process regression. *Experiments in Fluids*, *56*(198). https://doi.org/10.1007/s00348-015-2067-7

Azijli, I., Sciacchitano, A., Ragni, D., Palha, A., & Dwight, R. P. (2016a). A posteriori uncertainty quantification of PIV-based pressure data. *Experiments in Fluids*, *57*(5), 1–15. https://doi.org/10.1007/s00348-016-2159-z

Azijli, I., Sciacchitano, A., Ragni, D., Palha, A., & Dwight, R. P. (2016b). A posteriori uncertainty quantification of PIV-based pressure data. *Experiments in Fluids*, *57*(5), 72. https://doi.org/10.1007/s00348-016-2159-z

Baek, H., Jayaraman, M. V., & Karniadakis, G. E. (2009). Wall Shear Stress and Pressure Distribution on Aneurysms and Infundibulae in the Posterior Communicating Artery Bifurcation. *Annals of Biomedical Engineering*, *37*(12), 2469–2487. https://doi.org/10.1007/s10439-009-9794-y

Bakhshinejad, A., Baghaie, A., Vali, A., Saloner, D., Rayz, V. L., & D'Souza, R. M. (2017). Merging computational fluid dynamics and 4D Flow MRI using proper orthogonal decomposition and ridge regression. *Journal of Biomechanics*, *58*, 162–173. https://doi.org/10.1016/j.jbiomech.2017.05.004

Barker, A. J., Lanning, C., & Shandas, R. (2010). Quantification of hemodynamic wall shear stress in patients with bicuspid aortic valve using phase-contrast MRI. *Annals of Biomedical Engineering*, *38*(3), 788–800. https://doi.org/10.1007/s10439-009-9854-3

Barker, A. J., Markl, M., Bürk, J., Lorenz, R., Bock, J., Bauer, S., … Von Knobelsdorff-Brenkenhoff, F. (2012). Bicuspid aortic valve is associated with altered wall shear stress in the ascending aorta. *Circulation: Cardiovascular Imaging*, *5*(4), 457–466. https://doi.org/10.1161/CIRCIMAGING.112.973370

Berg, P., Stucht, D., Janiga, G., Beuing, O., Speck, O., & Thévenin, D. (2014). Cerebral blood flow in a healthy circle of willis and two intracranial aneurysms: Computational fluid dynamics versus four-dimensional phase-contrast magnetic resonance imaging. *Journal of Biomechanical Engineering*, *136*(4), 1–9. https://doi.org/10.1115/1.4026108

Berhane, H., Scott, M., Elbaz, M., Jarvis, K., Mccarthy, P., Carr, J., … Markl, M. (2020). Fully automated 3D aortic segmentation of 4D flow MRI for hemodynamic analysis using deep learning. *Magnetic Resonance in Medicine*, *00*, 1–15. https://doi.org/10.1002/mrm.28257

Bhalerao, A., Westin, C.-F., & Kikinis, R. (1997). Unwrapping Phase in 3D MR Phase Contrast Angiograms (pp. 193–202).

Bhattacharya, S., Charonko, J. J., & Vlachos, P. P. (2017). Stereo-particle image velocimetry uncertainty quantification. *Measurement Science and Technology*, *28*(1), 015301. https://doi.org/10.1088/1361-6501/28/1/015301

Bhattacharya, S., Charonko, J. J., & Vlachos, P. P. (2018). Particle image velocimetry (PIV) uncertainty quantification using moment of correlation (MC) plane. *Measurement Science and Technology*, *29*, 115301. https://doi.org/https://doi.org/10.1088/1361-6501/aadfb4

Bhattacharya, S., & Vlachos, P. P. (2019). Volumetric Particle Tracking Velocimetry (PTV) Uncertainty Quantification. *ArXiv Preprint ArXiv:1911.12495*.

Bhattacharya, S., & Vlachos, P. P. (2020). Volumetric particle tracking velocimetry (PTV) uncertainty quantification. *Experiments in Fluids*, *61*(9), 197. https://doi.org/10.1007/s00348-020-03021-6

Biasetti, J., Hussain, F., & Gasser, T. C. (2011). Blood flow and coherent vortices in the normal and aneurysmatic aortas: a fluid dynamical approach to intra-luminal thrombus formation. *Journal of The Royal Society Interface*, *8*(63), 1449–1461. https://doi.org/10.1098/rsif.2011.0041

Bieging, E. T., Frydrychowicz, A., Wentland, A., Landgraf, B. R., Johnson, K. M., Wieben, O., & François, C. J. (2011). In vivo three-dimensional mr wall shear stress estimation in ascending aortic dilatation. *Journal of Magnetic Resonance Imaging*, *33*(3), 589–597. https://doi.org/10.1002/jmri.22485

Binter, C., Knobloch, V., Manka, R., Sigfridsson, A., & Kozerke, S. (2013). Bayesian multipoint velocity encoding for concurrent flow and turbulence mapping. *Magnetic Resonance in Medicine*, *69*(5), 1337–1345. https://doi.org/10.1002/mrm.24370

Björck, A. (1996). *Numerical Methods Least Squares Squares*. Society for Industrial and Applied Mathematics, Philadelphia.

Bock, J., Kreher, B. W., Hennig, J., & Markl, M. (2007). Optimized pre-processing of time-resolved 2D and 3D phase contrast MRI data. In *Proc. Intl. Soc. Mag. Reson. Med* (Vol. 15, p. 3138).

Bock, Jelena, Frydrychowicz, A., Lorenz, R., Hirtler, D., Barker, A. J., Johnson, K. M., … Markl, M. (2011). In vivo noninvasive 4D pressure difference mapping in the human aorta: Phantom comparison and application in healthy volunteers and patients. *Magnetic Resonance in Medicine*, *66*(4), 1079–1088. https://doi.org/10.1002/mrm.22907

Boussel, L., Rayz, V., Martin, A., Acevedo-bolton, G., Lawton, M. T., Higashida, R., … Saloner, D. (2009). Phase-Contrast MRI measurements in intra-cranial aneurysms in-vivo of flow patterns, velocity fields and wall shear stress: A comparison with CFD. *Magn Reson Med.*, *61*(2), 409–417. https://doi.org/10.1002/mrm.21861.Phase-Contrast

Boussel, L., Rayz, V., McCulloch, C., Martin, A., Acevedo-Bolton, G., Lawton, M., … Saloner, D. (2008). Aneurysm growth occurs at region of low wall shear stress: Patient-specific correlation of hemodynamics and growth in a longitudinal study. *Stroke*, *39*(11), 2997–3002. https://doi.org/10.1161/STROKEAHA.108.521617

Brindise, M. C., Busse, M. M., & Vlachos, P. P. (2018). Density- and viscosity-matched Newtonian and non-Newtonian blood-analog solutions with PDMS refractive index. *Experiments in Fluids*, *59*(11), 1–8. https://doi.org/10.1007/s00348-018-2629-6

Brindise, M. C., Meyers, B. A., & Vlachos, P. P. (2020). Universality of vortex ring decay in the left ventricle. *Journal of Biomechanics*, *103*, 109695. https://doi.org/10.1016/j.jbiomech.2020.109695

Brindise, M. C., Rothenberger, S., Dickerhoff, B., Schnell, S., Markl, M., Saloner, D., … Vlachos, P. P. (2019). Multi-modality cerebral aneurysm haemodynamic analysis: in vivo 4D flow MRI, in vitro volumetric particle velocimetry and in silico computational fluid dynamics. *Journal of The Royal Society Interface*, *16*(158), 20190465. https://doi.org/10.1098/rsif.2019.0465

Brun, P., Tribouilloy, C., Duval, A. M., Iserin, L., Meguira, A., Pelle, G., & Dubois-Rande, J. L. (1992). Left ventricular flow propagation during early filling is related to wall relaxation: A color M-mode Doppler analysis. *Journal of the American College of Cardiology*, *20*(2), 420–432. https://doi.org/10.1016/0735-1097(92)90112-Z

Brunton, S. L., Tu, J. H., Bright, I., & Kutz, J. N. (2014). Compressive sensing and low-rank libraries for classification of bifurcation regimes in nonlinear dynamical systems. *SIAM Journal on Applied Dynamical Systems*, *13*(4), 1716–1732. https://doi.org/10.1137/130949282

Buonocore, M. H. (1994). Algorithms for improving calculated streamlines in 3-D phase contrast angiography. *Magnetic Resonance in Medicine*, *31*(1), 22–30. https://doi.org/10.1002/mrm.1910310104

Busch, J., Giese, D., Wissmann, L., & Kozerke, S. (2013). Reconstruction of divergence-free velocity fields from cine 3D phase-contrast flow measurements. *Magnetic Resonance in Medicine*, *69*(1), 200–210. https://doi.org/10.1002/mrm.24221

Callaham, J. L., Maeda, K., & Brunton, S. L. (2019). Robust flow reconstruction from limited measurements via sparse representation. *Physical Review Fluids*, *4*(10), 103907. https://doi.org/10.1103/PhysRevFluids.4.103907

Carrillo, H., Osses, A., Uribe, S., & Bertoglio, C. (2019). Optimal Dual-VENC Unwrapping in Phase-Contrast MRI. *IEEE Transactions on Medical Imaging*, *38*(5), 1263–1270.

Castro, M. A., Putman, C. M., Sheridan, M. J., & Cebral, J. R. (2009). Hemodynamic patterns of anterior communicating artery aneurysms: A possible association with rupture. *American Journal of Neuroradiology*, *30*(2), 297–302. https://doi.org/10.3174/ajnr.A1323

Cecchi, E., Giglioli, C., Valente, S., Lazzeri, C., Gensini, G. F., Abbate, R., & Mannini, L. (2011). Role of hemodynamic shear stress in cardiovascular disease. *Atherosclerosis*, *214*(2), 249–256. https://doi.org/10.1016/j.atherosclerosis.2010.09.008

Chakraborty, S., Meyers, B. A., Iwano, H., Hall, M. E., & Vlachos, P. P. (2021). A Wavelet Approach to the Estimation of Left Ventricular Early Filling Wave Propagation Velocity from Color M-Mode Echocardiograms. *Ultrasound in Medicine and Biology*, *47*(5), 1397–1407. https://doi.org/10.1016/j.ultrasmedbio.2021.01.009

Charonko, J. J., King, C. V, Smith, B. L., & Vlachos, P. P. (2010). Assessment of pressure field calculations from particle image velocimetry measurements. *Measurement Science and Technology*, *21*(10), 105401. https://doi.org/10.1088/0957-0233/21/10/105401

Charonko, J. J., Kumar, R., Stewart, K., Little, W. C., & Vlachos, P. P. (2013). Vortices formed on the mitral valve tips aid normal left ventricular filling. *Annals of Biomedical Engineering*, *41*(5), 1049–1061. https://doi.org/10.1007/s10439-013-0755-0

Charonko, J. J., & Vlachos, P. P. (2013). Estimation of uncertainty bounds for individual particle image velocimetry measurements from cross-correlation peak ratio. *Measurement Science and Technology*, *24*(6), 065301. https://doi.org/10.1088/0957-0233/24/6/065301

Chiu, J. J., & Chien, S. (2011). Effects of disturbed flow on vascular endothelium: Pathophysiological basis and clinical perspectives. *Physiological Reviews*, *91*(1), 327–387. https://doi.org/10.1152/physrev.00047.2009

Cibis, M., Potters, W. V., Gijsen, F. J., Marquering, H., Van Ooij, P., Van Bavel, E., … Nederveen, A. J. (2016). The effect of spatial and temporal resolution of cine phase contrast MRI on wall shear stress and oscillatory shear index assessment. *PLoS ONE*, *11*(9), 1–15. https://doi.org/10.1371/journal.pone.0163316

Conturo, T. E., & Smith, G. D. (1990). Signal-to-Noise in Phase Angle Reconstruction : Dynamic Range Extension Using Phase Reference Offsets. *Magnetic Resonance in Medicine*, *15*, 420–437.

Cunningham, K. S., & Gotlieb, A. I. (2005). The role of shear stress in the pathogenesis of atherosclerosis. *Laboratory Investigation*, *85*(1), 9–23. https://doi.org/10.1038/labinvest.3700215

Cusack, R., & Papadakis, N. (2002). New Robust 3-D Phase Unwrapping Algorithms: Application to Magnetic Field Mapping and Undistorting Echoplanar Images. *NeuroImage*, *16*(3), 754–764. https://doi.org/10.1006/nimg.2002.1092

Dabiri, J. O., Bose, S., Gemmell, B. J., Colin, S. P., & Costello, J. H. (2014). An algorithm to estimate unsteady and quasi-steady pressure fields from velocity field measurements. *Journal of Experimental Biology*, *217*(Pt 3), 331–336. https://doi.org/10.1242/jeb.092767

De Boeck, B. W. L., Oh, J. K., Vandervoort, P. M., Vierendeels, J. A., Van Der Aa, R. P. L. M., & Cramer, M. J. M. (2005). Colour M-mode velocity propagation: A glance at intra-ventricular pressure gradients and early diastolic ventricular performance. *European Journal of Heart Failure*, *7*(1), 19–28. https://doi.org/10.1016/j.ejheart.2004.03.010

De Hoon, N., Van Pelt, R., Jalba, A., & Vilanova, A. (2014). 4D MRI flow coupled to physics-based fluid simulation for blood-flow visualization. *Computer Graphics Forum*, *33*(3), 121–130. https://doi.org/10.1111/cgf.12368

de Kat, R., & Van Oudheusden, B. W. (2012). Instantaneous planar pressure determination from PIV in turbulent flow. *Experiments in Fluids*, *52*(5), 1089–1106. https://doi.org/10.1007/s00348-011-1237-5

De Kat, R., & Van Oudheusden, B. W. (2012). Instantaneous planar pressure determination from PIV in turbulent flow. *Experiments in Fluids*, *52*(5), 1089–1106. https://doi.org/10.1007/s00348-011-1237-5

de Kat, Roeland, van Oudheusden, B. W., & Scarano, F. (2009). Instantaneous Pressure Field Determination Around a Square-Section Cylinder Using Time-Resolved Stereo-PIV. In *39th AIAA Fluid Dynamics Conference* (pp. 1–10). https://doi.org/10.2514/6.2009-4043

den Dekker, A. J., & Sijbers, J. (2014). Data distributions in magnetic resonance images: A review. *Physica Medica*, *30*(7), 725–741. https://doi.org/10.1016/j.ejmp.2014.05.002

Devenport, B. W. J., & Rife, M. C. (1996). The structure and development of a wing-tip vortex.

Dietrich, O., Raya, G., Reeder, S. B., Reiser, M. F., & Schoenberg, S. O. (2007). Measurement of Signal-to-Noise Ratios in MR Images : Influence of Multichannel Coils , Parallel Imaging , and Reconstruction Filters. *Journal of Magnetic Resonance Imaging*, *26*, 375–385. https://doi.org/10.1002/jmri.20969

Difrancesco, M. W., Rasmussen, J. M., Yuan, W., Pratt, R., Dunn, S., Dardzinski, B. J., & Holland, S. K. (2008). Comparison of SNR and CNR for in vivo mouse brain imaging at 3 and 7 T using well matched scanner configurations. *Medical Physics*, *35*(9), 3972–3978. https://doi.org/10.1118/1.2968092

Donati, F., Figueroa, C. A., Smith, N. P., Lamata, P., & Nordsletten, D. A. (2015). Non-invasive pressure difference estimation from PC-MRI using the work-energy equation. *Medical Image Analysis*, *26*(1), 159–172. https://doi.org/10.1016/j.media.2015.08.012

Donati, F., Nordsletten, D. A., Smith, N. P., & Lamata, P. (2014). Pressure mapping from flow imaging: Enhancing computation of the viscous term through velocity reconstruction in near-wall regions. In *2014 36th Annual International Conference of the IEEE Engineering in Medicine and Biology Society* (pp. 5097–5100). IEEE. https://doi.org/10.1109/EMBC.2014.6944771

Dyverfeldt, P., Bissell, M., Barker, A. J., Bolger, A. F., Carlhäll, C., Ebbers, T., … Markl, M. (2015). 4D flow cardiovascular magnetic resonance consensus statement. *Journal of Cardiovascular Magnetic Resonance*, *17*(72), 1–19. https://doi.org/10.1186/s12968-015-0174-5

Ebbers, T., & Farnebäck, G. (2009). Improving computation of cardiovascular relative pressure fields from velocity MRI. *Journal of Magnetic Resonance Imaging*, *30*(1), 54–61. https://doi.org/10.1002/jmri.21775

Eckstein, A., & Vlachos, P. P. (2009). Assessment of advanced windowing techniques for digital particle image velocimetry (DPIV). *Measurement Science and Technology*, *20*(7). https://doi.org/10.1088/0957-0233/20/7/075402

Faiella, M., Grant Jeon Macmillan, C., Whitehead, J. P., & Pan, Z. (2021). Error propagation dynamics of velocimetry-based pressure field calculations (2): on the error profile. *Measurement Science and Technology*, *32*(8), 084005. https://doi.org/10.1088/1361-6501/abf30d

Fathi, M. F., Bakhshinejad, A., Baghaie, A., Saloner, D., Sacho, R. H., Rayz, V. L., & D'Souza, R. M. (2018). Denoising and spatial resolution enhancement of 4D flow MRI using proper orthogonal decomposition and lasso regularization. *Computerized Medical Imaging and Graphics*, *70*, 165–172. https://doi.org/10.1016/j.compmedimag.2018.07.003

Fathi, M. F., Perez-Raya, I., Baghaie, A., Berg, P., Janiga, G., Arzani, A., & D'Souza, R. M. (2020). Super-resolution and denoising of 4D-Flow MRI using physics-Informed deep neural nets. *Computer Methods and Programs in Biomedicine*, *197*, 105729. https://doi.org/10.1016/j.cmpb.2020.105729

Ferdian, E., Suinesiaputra, A., Dubowitz, D. J., Zhao, D., Wang, A., Cowan, B., & Young, A. A. (2020). 4DFlowNet: Super-Resolution 4D Flow MRI Using Deep Learning and Computational Fluid Dynamics. *Frontiers in Physics*, *8*(May), 1–14. https://doi.org/10.3389/fphy.2020.00138

Ford, M. D., Nikolov, H. N., Milner, J. S., Lownie, S. P., DeMont, E. M., Kalata, W., … Steinman, D. A. (2008). PIV-measured versus CFD-predicted flow dynamics in anatomically realistic cerebral aneurysm models. *Journal of Biomechanical Engineering*, *130*(2), 1–9. https://doi.org/10.1115/1.2900724

Friedman, J., Hastie, T., & Tibshirani, R. (2010). Regularization Paths for Generalized Linear Models via Coordinate Descent. *Journal of Statistical Software*, *33*(1), 1–22. https://doi.org/10.1016/j.expneurol.2008.01.011

Frigge, M., Hoaglin, D. C., Iglewicz, B., Frigge, M., Hoaglin, D. C., & Iglewicz, B. (1989). Some Implementations of the Boxplot. *The American Statistician*, *43*(1), 50–54.

Friman, O., Hennemuth, A., Harloff, A., Bock, J., Markl, M., & Peitgen, H. O. (2011). Probabilistic 4D blood flow tracking and uncertainty estimation. *Medical Image Analysis*, *15*(5), 720–728. https://doi.org/10.1016/j.media.2011.06.002

Frydrychowicz, A., Stalder, A. F., Russe, M. F., Bock, J., Bauer, S., Harloff, A., … Markl, M. (2009). Three-dimensional analysis of segmental wall shear stress in the aorta by flow-sensitive four-dimensional-MRI. *Journal of Magnetic Resonance Imaging*, *30*(1), 77–84. https://doi.org/10.1002/jmri.21790

Fujisawa, N., Tanahashi, S., & Srinivas, K. (2005). Evaluation of pressure field and fluid forces on a circular cylinder with and without rotational oscillation using velocity data from PIV measurement. *Measurement Science and Technology*, *16*(4), 989–996. https://doi.org/10.1088/0957-0233/16/4/011

Gambaruto, A. M., & João, A. J. (2012). Flow structures in cerebral aneurysms. *Computers and Fluids*, *65*, 56–65. https://doi.org/10.1016/j.compfluid.2012.02.020

Garcia, M. J., Smedira, N. G., Greenberg, N. L., Main, M., Firstenberg, M. S., Odabashian, J., & Thomas, J. D. (2000). Color M-mode Doppler flow propagation velocity is a preload insensitive index of left ventricular relaxation: Animal and human validation. *Journal of the American College of Cardiology*, *35*(1), 201–208. https://doi.org/10.1016/S0735-1097(99)00503-3

Garcia, M. J., Thomas, J. D., & Klein, A. L. (1998). New doppler echocardiographic applications for the study of diastolic function. *Journal of the American College of Cardiology*, *32*(4), 865–875. https://doi.org/10.1016/S0735-1097(98)00345-3

Gesemann, S., Huhn, F., Schanz, D., & Schröder, A. (2016). From Noisy Particle Tracks to Velocity , Acceleration and Pressure Fields using B-splines and Penalties. In *18th International Symposium on the Application of Laser and Imaging Techniques to Fluid Mechanics*.

Ghaemi, S., Ragni, D., & Scarano, F. (2012). PIV-based pressure fluctuations in the turbulent boundary layer. *Experiments in Fluids*, *53*(6), 1823–1840. https://doi.org/10.1007/s00348-012-1391-4

Ghiglia, D. C., & Romero, L. A. (1994). Robust two-dimensional weighted and unweighted phase unwrapping that uses fast transforms and iterative methods. *Journal of the Optical Society of America A*, *11*(1), 107. https://doi.org/10.1364/JOSAA.11.000107

Groen, H. C., Gijsen, F. J. H., Van Der Lugt, A., Ferguson, M. S., Hatsukami, T. S., Van Der Steen, A. F. W., … Wentzel, J. J. (2007). Plaque rupture in the carotid artery is localized at the high shear stress region: A case report. *Stroke*, *38*(8), 2379–2381. https://doi.org/10.1161/STROKEAHA.107.484766

Guzzardi, D. G., Barker, A. J., Van Ooij, P., Malaisrie, S. C., Puthumana, J. J., Belke, D. D., … Fedak, P. W. M. (2015). Valve-Related Hemodynamics Mediate Human Bicuspid Aortopathy: Insights From Wall Shear Stress Mapping. *Journal of the American College of Cardiology*, *66*(8), 892–900. https://doi.org/10.1016/j.jacc.2015.06.1310

Ha, H., Kim, G. B., Kweon, J., Kim, Y., Kim, N., Yang, D. H., & Lee, S. J. (2016). Multi-VENC Acquisition of Four-Dimensional Phase- Contrast MRI to Improve Precision of Velocity Field Measurement. *Magnetic Resonance in Medicine*, *75*, 1909–1919. https://doi.org/10.1002/mrm.25715

Ha, H., Lantz, J., Ziegler, M., Casas, B., Karlsson, M., Dyverfeldt, P., & Ebbers, T. (2017). Estimating the irreversible pressure drop across a stenosis by quantifying turbulence production using 4D Flow MRI. *Scientific Reports*, *7*(November 2016), 1–14. https://doi.org/10.1038/srep46618

Hernandez-Suarez, D. F., Palm, D., Lopez-Menendez, F., Mesa Pabon, M., & Lopez-Candales, A. (2017). Left Ventricular Velocity of Propagation: A Useful Non-Invasive Measurement When Assessing Hemodynamic Alterations in Pulmonary Arterial Hypertension. *Cardiology Research*, *8*(2), 44–51. https://doi.org/10.14740/cr541w

Hofinan, M. B. M., Visser, F. C., Rossum, A. C. Van, Vink, G. Q. M., Sprenger, M., & Westerhof, N. (1995). In Vivo Validation of Magnetic Resonance Blood Volume Flow Measurements with Limited Spatial Resolution in Small Vessels. *Magnetic Resonance in Medicine*, *33*(6), 778–784.

Hope, T. A., Hope, M. D., Purcell, D. D., von Morze, C., Vigneron, D. B., Alley, M. T., & Dillon, W. P. (2010). Evaluation of intracranial stenoses and aneurysms with accelerated 4D flow. *Magnetic Resonance Imaging*, *28*(1), 41–46. https://doi.org/10.1016/j.mri.2009.05.042

Huhn, F., Schanz, D., Gesemann, S., & Schröder, A. (2016). FFT integration of instantaneous 3D pressure gradient fields measured by Lagrangian particle tracking in turbulent flows. *Experiments in Fluids*, *57*, 151. https://doi.org/10.1007/s00348-016-2236-3

Humphrey, J. D., & Na, S. (2002). Elastodynamics and Arterial Wall Stress. *Annals of Biomedical Engineering*, *30*(4), 509–523. https://doi.org/10.1114/1.1467676

Hunt, J. C. R., Wray, A. A., & Moin, P. (1998). Eddies, streams, and convergence zones in turbulent flows. In *Studying turbulence using numerical simulation databases, 2. In: Proceedings of the 1988 summer program;* (pp. 193–208).

International Study of Unruptured Intracranial Aneurysms Investigators. (1999). Unruptured intracranial aneurysms - risk of rupture and risks of surgical intervention. *N Engl J Med*, *340*(9), 744.

Isoda, H., Ohkura, Y., Kosugi, T., Hirano, M., Takeda, H., Hiramatsu, H., … Sakahara, H. (2010). In vivo hemodynamic analysis of intracranial aneurysms obtained by magnetic resonance fluid dynamics (MRFD) based on time-resolved three-dimensional phase-contrast MRI. *Neuroradiology*, *52*(10), 921–928. https://doi.org/10.1007/s00234-009-0635-3

Jeon, Y. J., Gomit, G., Earl, T., Chatellier, L., & David, L. (2018). Sequential least-square reconstruction of instantaneous pressure field around a body from TR-PIV. *Experiments in Fluids*, *59*(2), 27. https://doi.org/10.1007/s00348-018-2489-0

Jochimsen, T. H., Schäfer, A., Bammer, R., & Moseley, M. E. (2006). Efficient simulation of magnetic resonance imaging with Bloch-Torrey equations using intra-voxel magnetization gradients. *Journal of Magnetic Resonance*, *180*(1), 29–38. https://doi.org/10.1016/j.jmr.2006.01.001

Jou, L.-D., Lee, D. H., Morsi, H., & Mawad, M. E. (2008). Wall Shear Stress on Ruptured and Unruptured Intracranial Aneurysms at the Internal Carotid Artery. *American Journal of Neuroradiology*, *29*(9), 1761–1767. https://doi.org/10.3174/ajnr.A1180

Kähler, C. J., Astarita, T., Vlachos, P. P., Sakakibara, J., Hain, R., Discetti, S., … Cierpka, C. (2016). Main results of the 4th International PIV Challenge. *Experiments in Fluids*, *57*(6), 97. https://doi.org/10.1007/s00348-016-2173-1

Kallmes, D. F. (2012). Point: CFD - Computational fluid dynamics or confounding factor dissemination. *American Journal of Neuroradiology*, *33*(3), 395–396. https://doi.org/10.3174/ajnr.A2993

Karri, S., Charonko, J., & Vlachos, P. P. (2009). Robust wall gradient estimation using radial basis functions and proper orthogonal decomposition (POD) for particle image velocimetry (PIV) measured fields. *Measurement Science and Technology*, *20*(045401). https://doi.org/10.1088/0957-0233/20/4/045401

Kecskemeti, S., Johnson, K., Wu, Y., Mistretta, C., Turski, P., & Wieben, O. (2012). High Resolution 3D Cine Phase Contrast MRI of Small Intracranial Aneurysms using a Stack of Stars k-Space Trajectory. *J Magn Reson Imaging*, *35*(3), 518–527. https://doi.org/10.1002/jmri.23501.High

Kim, S., Koh, K., Lustig, M., Boyd, S., & Gorinevsky, D. (2007). An Interior-Point Method for Large-Scale l1 -Regularized Least Squares. *IEEE Journal of Selected Topics in Signal Processing*, *1*(4), 606–617.

Komotar, R. J., Mocco, J., & Solomon, R. A. (2008). Guidelines for the surgical treatment of unruptured intracranial aneurysms: the first annual J. Lawrence Pool memorial research symposium-controversies in the management of cerebral aneurysms. *Neurosurgery*, *62*(1), 183–194. https://doi.org/10.1227/01.NEU.0000296982.54288.12

Kramer, B., Grover, P., Boufounos, P., Nabi, S., & Benosman, M. (2017). Sparse sensing and DMD-based identification of flow regimes and bifurcations in complex flows. *SIAM Journal on Applied Dynamical Systems*, *16*(2), 1164–1196. https://doi.org/10.1137/15M104565X

Krittian, S. B. S., Lamata, P., Michler, C., Nordsletten, D. A., Bock, J., Bradley, C. P., … Smith, N. P. (2012). A finite-element approach to the direct computation of relative cardiovascular pressure from time-resolved MR velocity data. *Medical Image Analysis*, *16*(5), 1029–1037. https://doi.org/10.1016/j.media.2012.04.003

Lall, R. R., Eddleman, C. S., Bendok, B. R., & Batjer, H. H. (2009). Unruptured intracranial aneurysms and the assessment of rupture risk based on anatomical and morphological factors: Sifting through the sands of data. *Neurosurgical Focus*, *26*(5), 1–7. https://doi.org/10.3171/2009.2.FOCUS0921

Lamata, P., Pitcher, A., Krittian, S., Nordsletten, D., Bissell, M. M., Cassar, T., … Smith, N. P. (2014). Aortic Relative Pressure Components Derived from Four-Dimensional Flow Cardiovascular Magnetic Resonance. *Magnetic Resonance in Medicine*, *72*, 1162–1169. https://doi.org/10.1002/mrm.25015

Laskari, A., de Kat, R., & Ganapathisubramani, B. (2016). Full-field pressure from snapshot and time-resolved volumetric PIV. *Experiments in Fluids*, *57*(3), 1–14. https://doi.org/10.1007/s00348-016-2129-5

Latta, P., Gruwel, M. L. H., Jellúš, V., & Tomanek, B. (2010). Bloch simulations with intra-voxel spin dephasing. *Journal of Magnetic Resonance*, *203*(1), 44–51. https://doi.org/10.1016/j.jmr.2009.11.019

Lee, A. T., Bruce Pike, G., & Pelc, N. J. (1995). Three-Point Phase-Contrast Velocity Measurements with Increased Velocity-to-Noise Ratio. *Magnetic Resonance in Medicine*, *33*(1), 122–126. https://doi.org/10.1002/mrm.1910330119

Leuprecht, A., Kozerke, S., Boesiger, P., & Perktold, K. (2003). Blood flow in the human ascending aorta: A combined MRI and CFD study. *Journal of Engineering Mathematics*, *47*(3–4), 387–404. https://doi.org/10.1023/B:ENGI.0000007969.18105.b7

Li, X. S. (2005). An Overview of SuperLU : Algorithms , Implementation , and User Interface. *ACM Transactions on Mathematical Software*, *31*(3), 302–325.

Liu, X., & Katz, J. (2006). Instantaneous pressure and material acceleration measurements using a four-exposure PIV system. *Experiments in Fluids*, *41*(2), 227–240. https://doi.org/10.1007/s00348-006-0152-7

Liu, X., & Moreto, J. R. (2020). Error propagation from the PIV-based pressure gradient to the integrated pressure by the omnidirectional integration method. *Measurement Science and Technology*, *31*(5). https://doi.org/10.1088/1361-6501/ab6c28

Loecher, M., Johnson, K., Landgraf, B., & Wieben, O. (2011). 4D Gradient Based Phase Unwrapping for PC-MR Flow Data. In *Proc. Intl. Soc. Mag. Reson. Med* (Vol. 19, p. 3284).

Loecher, Michael, & Ennis, D. B. (2018). Velocity reconstruction with nonconvex optimization for low-velocity-encoding phase-contrast MRI. *Magnetic Resonance in Medicine*, *80*(1), 42–52. https://doi.org/10.1002/mrm.26997

Loecher, Michael, Kecskemeti, S., Turski, P., & Wieben, O. (2012). Comparison of divergence-free algorithms for 3D MRI with three-directional velocity encoding. *Journal of Cardiovascular Magnetic Resonance*, *14*(S1), W64. https://doi.org/10.1186/1532-429x-14-s1-w64

Loecher, Michael, Schrauben, E., Johnson, K. M., & Wieben, O. (2016). Phase unwrapping in 4D MR flow with a 4D single-step laplacian algorithm. *Journal of Magnetic Resonance Imaging*, *43*(4), 833–842. https://doi.org/10.1002/jmri.25045

Loke, Y. H., Capuano, F., Cleveland, V., Mandell, J. G., Balaras, E., & Olivieri, L. J. (2021). Moving beyond size: vorticity and energy loss are correlated with right ventricular dysfunction and exercise intolerance in repaired Tetralogy of Fallot. *Journal of Cardiovascular Magnetic Resonance*, *23*(1), 1–15. https://doi.org/10.1186/s12968-021-00789-2

Londono-hoyos, F. J., Swillens, A., Cauwenberge, J. Van, Meyers, B., Koppula, M. R., Vlachos, P., … Segers, P. (2018). Assessment of methodologies to calculate intraventricular pressure differences in computational models and patients. *Med Biol Eng Comput*, *56*, 469–481. https://doi.org/10.1007/s11517-017-1704-0

Maas, H. G., Gruen, A., & Papantoniou, D. (1993). Particle tracking velocimetry in three-dimensional flows - Part 1. Photogrammetric determination of particle coordinates. *Experiments in Fluids*, *15*(2), 133–146. https://doi.org/10.1007/BF00190953

Malek, A. M., Alper, S. L., & Izumo, S. (1999). Hemodynamic Shear Stress and Its Role in Atherosclerosis Adel. *JAMA: The Journal of the American Medical Association*, *282*(21), 2035–2042.

Markl, M, Schnell, S., Wu, C., Bollache, E., Jarvis, K., Barker, A. J., … Rigsby, C. K. (2016). Advanced flow MRI: emerging techniques and applications. *Clinical Radiology*, *71*(8), 779–795. https://doi.org/10.1016/j.crad.2016.01.011

Markl, Michael, Brendecke, S. M., Simon, J., Barker, A. J., Weiller, C., & Harloff, A. (2013). Co-registration of the distribution of wall shear stress and 140 complex plaques of the aorta. *Magnetic Resonance Imaging*, *31*(7), 1156–1162. https://doi.org/10.1016/j.mri.2013.05.001

Markl, Michael, Frydrychowicz, A., Kozerke, S., Hope, M., & Wieben, O. (2012). 4D Flow MRI. *J Magn Reson Imaging*, *36*(5), 1015–1036. https://doi.org/10.1002/jmri.23632

Markl, Michael, Wallis, W., & Harloff, A. (2011). Reproducibility of Flow and Wall Shear Stress Analysis Using Flow-Sensitive Four-Dimensional MRI. *Journal of Magnetic Resonance Imaging*, *33*, 988–994. https://doi.org/10.1002/jmri.22519

McClure, J., & Yarusevych, S. (2017a). Instantaneous PIV/PTV-based pressure gradient estimation: a framework for error analysis and correction. *Experiments in Fluids*, *58*(8), 1–18. https://doi.org/10.1007/s00348-017-2369-z

McClure, J., & Yarusevych, S. (2017b). Optimization of planar PIV-based pressure estimates in laminar and turbulent wakes. *Experiments in Fluids*, *58*(5), 1–18. https://doi.org/10.1007/s00348-017-2337-7

Meckel, S., Stalder, A. F., Santini, F., Radü, E. W., Rüfenacht, D. A., Markl, M., & Wetzel, S. G. (2008). In vivo visualization and analysis of 3-D hemodynamics in cerebral aneurysms with flow-sensitized 4-D MR imaging at 3 T. *Neuroradiology*, *50*(6), 473–484. https://doi.org/10.1007/s00234-008-0367-9

Meng, H., Tutino, V. M., Xiang, J., & Siddiqui, A. (2014). High WSS or Low WSS? Complex interactions of hemodynamics with intracranial aneurysm initiation, growth, and rupture: Toward a unifying hypothesis. *American Journal of Neuroradiology*, *35*(7), 1254–1262. https://doi.org/10.3174/ajnr.A3558

Miguel Ángel, G. B., Zisserman, A. P., & Brady, M. (2002). Estimation of the partial volume effect in MRI. *Medical Image Analysis*, *6*, 389–405.

Mohd Adib, M. A. H., Ii, S., Watanabe, Y., & Wada, S. (2017). Minimizing the blood velocity differences between phase-contrast magnetic resonance imaging and computational fluid dynamics simulation in cerebral arteries and aneurysms. *Medical and Biological Engineering and Computing*, *55*(9), 1605–1619. https://doi.org/10.1007/s11517-017-1617-y

Moody, L. F. (1944). Friction Factor for Pipe Flow. *Transactions of the ASME*, *66*(8), 671–684.

Naggara, O. N., Lecler, A., Oppenheim, C., Meder, J. F., & Raymond, J. (2012). Endovascular treatment of intracranial unruptured aneurysms: A systematic review of the literature on safety with emphasis on subgroup analyses. *Radiology*, *263*(3), 828–835. https://doi.org/10.1148/radiol.12112114

Nagueh, S. F. (2020). Left Ventricular Diastolic Function: Understanding Pathophysiology, Diagnosis, and Prognosis With Echocardiography. *JACC: Cardiovascular Imaging*, *13*(1), 228–244. https://doi.org/10.1016/j.jcmg.2018.10.038

Nagueh, S. F., Appleton, C. P., Gillebert, T. C., Marino, P. N., Oh, J. K., Smiseth, O. A., … Evangelisa, A. (2009). Recommendations for the evaluation of left ventricular diastolic function by echocardiography. *European Journal of Echocardiography*, *10*(2), 165–193. https://doi.org/10.1093/ejechocard/jep007

Nagueh, S. F., Smiseth, O. A., Appleton, C. P., Byrd, B. F., Dokainish, H., Edvardsen, T., … Waggoner, A. D. (2016). Recommendations for the Evaluation of Left Ventricular Diastolic Function by Echocardiography: An Update from the American Society of Echocardiography and the European Association of Cardiovascular Imaging. *European Heart Journal – Cardiovascular Imaging*, *17*(12), 1321–1360. https://doi.org/10.1093/ehjci/jew082

Nayak, K. S., Nielsen, J., Bernstein, M. A., Markl, M., Gatehouse, P. D., Botnar, R. M., … Oshinski, J. N. (2015). Cardiovascular magnetic resonance phase contrast imaging. *Journal of Cardiovascular Magnetic Resonance*, *17*(71), 1–26. https://doi.org/10.1186/s12968-015-0172-7

Neeteson, N. J., Bhattacharya, S., Rival, D. E., Michaelis, D., Schanz, D., & Schröder, A. (2016). Pressure-field extraction from Lagrangian flow measurements: first experiences with 4D-PTV data. *Experiments in Fluids*, *57*(6), 1–18. https://doi.org/10.1007/s00348-016-2170-4

Neeteson, Nathan J., & Rival, D. E. (2015). Pressure-field extraction on unstructured flow data using a Voronoi tessellation-based networking algorithm: a proof-of-principle study. *Experiments in Fluids*, *56*(44), 44. https://doi.org/10.1007/s00348-015-1911-0

Nett, E. J., Johnson, K. M., Frydrychowicz, A., Munoz, A., Rio, D., Schrauben, E., … Wieben, O. (2012). Four-Dimensional Phase Contrast MRI With Accelerated Dual Velocity Encoding. *JOURNAL OF MAGNETIC RESONANCE IMAGING*, *35*, 1462–1471. https://doi.org/10.1002/jmri.23588

Øie, L. R., Solheim, O., Majewska, P., Nordseth, T., Müller, T. B., Carlsen, S. M., … Gulati, S. (2020). Incidence and case fatality of aneurysmal subarachnoid hemorrhage admitted to hospital between 2008 and 2014 in Norway. *Acta Neurochirurgica*, *162*(9), 2251–2259. https://doi.org/10.1007/s00701-020-04463-x

Oliveira, R. K. F. De, Ferreira, E. V. M., Ramos, R. P., Messina, C. M. S., Kapins, C. E. B., Silva, C. M. C., & Ota-arakaki, J. S. (2014). Usefulness of pulmonary capillary wedge pressure as a correlate of left ventricular fi lling pressures in pulmonary arterial hypertension. *Journal of Heart and Lung Transplantation*, *33*(2), 157–162. https://doi.org/10.1016/j.healun.2013.10.008

Ong, F., Uecker, M., Tariq, U., Hsiao, A., Alley, M. T., Vasanawala, S. S., & Lustig, M. (2015). Robust 4D Flow Denoising Using Divergence-Free Wavelet Transform. *Magnetic Resonance in Medicine*, *73*, 828–842. https://doi.org/10.1002/mrm.25176

Paige, C. C., & Saunders, M. A. (1982a). Algorithm 583: LSQR: Sparse Linear Equations and Least Squares Problems. *ACM Transactions on Mathematical Software (TOMS)*, *8*(2), 195–209. https://doi.org/10.1145/355993.356000

Paige, C. C., & Saunders, M. A. (1982b). LSQR: An Algorithm for Sparse Linear Equations and Sparse Least Squares. *ACM Transactions on Mathematical Software (TOMS)*, *8*(1), 43–71. https://doi.org/10.1145/355984.355989

Pan, Z., Whitehead, J., Thomson, S., & Truscott, T. (2016). Error propagation dynamics of PIV-based pressure field calculations: How well does the pressure Poisson solver perform inherently? *Measurement Science and Technology*, *27*(084012), 084012. https://doi.org/10.1088/0957-0233/27/8/084012

Perez-Raya, I., Fathi, M. F., Baghaie, A., Sacho, R. H., Koch, K. M., & D'Souza, R. M. (2020). Towards multi-modal data fusion for super-resolution and denoising of 4D-Flow MRI. *International Journal for Numerical Methods in Biomedical Engineering*, *36*(9), 1–20. https://doi.org/10.1002/cnm.3381

Perinajová, R., Juffermans, J. F., Mercado, J. L., Aben, J. P., Ledoux, L., Westenberg, J. J. M., … Kenjereš, S. (2021). Assessment of turbulent blood flow and wall shear stress in aortic coarctation using image-based simulations. *BioMedical Engineering Online*, *20*(1), 1–20. https://doi.org/10.1186/s12938-021-00921-4

Perinajová, R., Juffermans, J. F., Westenberg, J. J. M., van der Palen, R. L. F., van den Boogaard, P. J., Lamb, H. J., & Kenjereš, S. (2021). Geometrically induced wall shear stress variability in CFD-MRI coupled simulations of blood flow in the thoracic aortas. *Computers in Biology and Medicine*, *133*(April). https://doi.org/10.1016/j.compbiomed.2021.104385

Potters, W. V., Van Ooij, P., Marquering, H., VanBavel, E., & Nederveen, A. J. (2015). Volumetric arterial wall shear stress calculation based on cine phase contrast MRI. *Journal of Magnetic Resonance Imaging*, *41*(2), 505–516. https://doi.org/10.1002/jmri.24560

Potters, W. V, Ooij, P. Van, & Nederveen, A. (2012). Vectorial wall shear stress calculations in vessel structures using 4D PC-MRI. *Journal of Cardiovascular Magnetic Resonance*, *14(Suppl 1*(W5). https://doi.org/10.1186/1532-429X-14-S1-W5

Pritt, M. D., & Shipman, J. S. (1994). Least-Squares Two-Dimensional Phase Unwrapping Using FFT's. *IEEE Transactions on Geoscience and Remote Sensing*, *32*(3), 706–708. https://doi.org/10.1109/36.297989

Raaymakers, T. W. M., Rinkel, G. J. E., Limburg, M., & Algra, A. (1998). Mortality and morbidity of surgery for unruptured intracranial aneurysms: A meta-analysis. *Stroke*, *29*(8), 1531–1538. https://doi.org/10.1161/01.STR.29.8.1531

Rajendran, L., Zhang, J., Bane, S., & Vlachos, P. (2020). Uncertainty-based weighted least squares density integration for background-oriented schlieren. *Experiments in Fluids*, *61*(11), 239. https://doi.org/10.1007/s00348-020-03071-w

Rayz, V. L., Abla, A., Boussel, L., Leach, J. R., Acevedo-Bolton, G., Saloner, D., & Lawton, M. T. (2015). Computational Modeling of Flow-Altering Surgeries in Basilar Aneurysms. *Annals of Biomedical Engineering*, *43*(5), 1210–1222. https://doi.org/10.1007/s10439-014-1170-x

Rich, A., Potter, L. C., Jin, N., Ash, J., Simonetti, O. P., & Ahmad, R. (2016). A Bayesian model for highly accelerated phase-contrast MRI. *Magnetic Resonance in Medicine*, *76*(2), 689–701. https://doi.org/10.1002/mrm.25904

Rich, A., Potter, L. C., Jin, N., Liu, Y., Simonetti, O. P., & Ahmad, R. (2019). A Bayesian approach for 4D flow imaging of aortic valve in a single breath-hold. *Magnetic Resonance in Medicine*, *81*(2), 811–824. https://doi.org/10.1002/mrm.27386

Rinaudo, A., & Pasta, S. (2014). Regional variation of wall shear stress in ascending thoracic aortic aneurysms. *Proceedings of the Institution of Mechanical Engineers, Part H: Journal of Engineering in Medicine*, *228*(6), 627–638. https://doi.org/10.1177/0954411914540877

Rinkel, G. J. E., Djibuti, M., Algra, A., & Van Gijn, J. (1998). Prevalence and risk of rupture of intracranial aneurysms: A systematic review. *Stroke*, *29*(1), 251–256. https://doi.org/10.1161/01.STR.29.1.251

Rispoli, V. C., Nielsen, J. F., Nayak, K. S., & Carvalho, J. L. A. (2015). Computational fluid dynamics simulations of blood flow regularized by 3D phase contrast MRI. *BioMedical Engineering Online*, *14*(1), 1–24. https://doi.org/10.1186/s12938-015-0104-7

Rivero Rodríguez, D., Scherle Matamoros, C., Cúe, L. F., Miranda Hernández, J. L., Pernas Sánchez, Y., & Pérez Nellar, J. (2015). Predictor's of mortality in patients with aneurysmal subarachnoid haemorrhage and reebleding. *Neurology Research International*, *2015*. https://doi.org/10.1155/2015/545407

Roloff, C., Stucht, D., Beuing, O., & Berg, P. (2019). Comparison of intracranial aneurysm flow quantification techniques: Standard PIV vs stereoscopic PIV vs tomographic PIV vs phase-contrast MRI vs CFD. *Journal of NeuroInterventional Surgery*, *11*(3), 275–282. https://doi.org/10.1136/neurintsurg-2018-013921

Rothenberger, S. M., Zhang, J., Brindise, M. C., Schnell, S., Markl, M., Vlachos, P. P., & Rayz, V. L. (2022). Modeling Bias Error in 4D flow MRI Velocity Measurements. *IEEE Transactions on Medical Imaging*, *xx*(X), 1–1. https://doi.org/10.1109/TMI.2022.3149421

Salfity, M F, Huntley, J. M., Graves, M. J., Marklund, O., & Cusack, R. (2006). Extending the dynamic range of phase contrast magnetic resonance velocity imaging using advanced higher-dimensional phase unwrapping algorithms. *Journal of the Royal Society Interface*, *3*, 415–427. https://doi.org/10.1098/rsif.2005.0096

Salfity, María F, Ruiz, P. D., Huntley, J. M., Graves, M. J., Cusack, R., & Beauregard, D. A. (2006). Branch cut surface placement for unwrapping of undersampled three-dimensional phase data : application to magnetic resonance imaging arterial flow mapping. *Applied Optics*, *45*(12), 2711–2722.

Santelli, C., Loecher, M., Busch, J., Wieben, O., Schaeffter, T., & Kozerke, S. (2016). Accelerating 4D Flow MRI by Exploiting Vector Field Divergence Regularization. *Magnetic Resonance in Medicine*, *75*, 115–125. https://doi.org/10.1002/mrm.25563

Sato, K., & Yoshimoto, Y. (2011). Risk profile of intracranial aneurysms: Rupture rate is not constant after formation. *Stroke*, *42*(12), 3376–3381. https://doi.org/10.1161/STROKEAHA.111.625871

Scarano, F. (2002). Iterative image deformation methods in PIV. *Measurement Science and Technology*, *13*(13), 1–19.

Schanz, D., Gesemann, S., & Schröder, A. (2016). Shake-The-Box: Lagrangian particle tracking at high particle image densities. *Experiments in Fluids*, *57*, 70. https://doi.org/10.1007/s00348-016-2157-1

Schiavazzi, D. E., Nemes, A., Schmitter, S., & Coletti, F. (2017). The effect of velocity filtering in pressure estimation. *Experiments in Fluids*, *58*, 50. https://doi.org/10.1007/s00348-017-2314-1

Schneiders, J. F. G., Dwight, R. P., & Scarano, F. (2014). Time-supersampling of 3D-PIV measurements with vortex-in-cell simulation. *Experiments in Fluids*, *55*(1692), 1692. https://doi.org/10.1007/s00348-014-1692-x

Schneiders, J. F. G., Pröbsting, S., Dwight, R. P., van Oudheusden, B. W., & Scarano, F. (2016). Pressure estimation from single-snapshot tomographic PIV in a turbulent boundary layer. *Experiments in Fluids*, *57*(53), 53. https://doi.org/10.1007/s00348-016-2133-9

Schneiders, J. F. G., & Scarano, F. (2016). Dense velocity reconstruction from tomographic PTV with material derivatives. *Experiments in Fluids*, *57*, 139. https://doi.org/10.1007/s00348-016-2225-6

Schneiders, J. F. G., & Sciacchitano, A. (2017). Track benchmarking method for uncertainty quantification of particle tracking velocimetry interpolations. *Measurement Science and Technology*, *28*, 065302. https://doi.org/10.1088/1361-6501/aa6a03

Schnell, S., Ansari, S. A., Vakil, P., Wasielewski, M., Carr, M. L., Hurley, M. C., … Markl, M. (2014). 3D Hemodynamics in Intracranial Aneurysms: Influence of Size and Morphology. *J Magn Reson Imaging*, *39*(1), 1–7. https://doi.org/10.1161/CIRCULATIONAHA.110.956839

Schnell, S., Ansari, S. A., Wu, C., Garcia, J., Murphy, I. G., Rahman, O. A., … Markl, M. (2017). Accelerated dual-venc 4D flow MRI for neurovascular applications. *Journal of Magnetic Resonance Imaging*, *46*(1), 102–114. https://doi.org/10.1002/jmri.25595

Sciacchitano, A. (2019). Uncertainty quantification in particle image velocimetry. *Measurement Science and Technology*, *30*(9). https://doi.org/10.1088/1361-6501/ab1db8

Sciacchitano, A., Neal, D. R., Smith, B. L., Warner, S. O., Vlachos, P. P., Wieneke, B., & Scarano, F. (2015). Collaborative framework for PIV uncertainty quantification: comparative assessment of methods. *Measurement Science and Technology*, *26*(7), 074004. https://doi.org/10.1088/0957-0233/26/7/074004

Sciacchitano, A., & Wieneke, B. (2016). PIV uncertainty propagation. *Measurement Science and Technology*, *27*(084006), 084006. https://doi.org/10.1088/0957-0233/27/8/084006

Sciacchitano, A., Wieneke, B., & Scarano, F. (2013). PIV uncertainty quantification by image matching. *Measurement Science and Technology*, *24*(4). https://doi.org/10.1088/0957-0233/24/4/045302

Sessoms, M. W., Lisauskas, J., & Kovács, S. J. (2002). The left ventricular color M-mode Doppler flow propagation velocity Vp: In vivo comparison of alternative methods including physiologic implications. *Journal of the American Society of Echocardiography*, *15*(4), 339–348. https://doi.org/10.1067/mje.2002.117899

Sforza, D. M., Kono, K., Tateshima, S., Viñuela, F., Putman, C., & Cebral, J. R. (2016). Hemodynamics in growing and stable cerebral aneurysms. *Journal of NeuroInterventional Surgery*, *8*(4), 407–412. https://doi.org/10.1136/neurintsurg-2014-011339

Shojima, M., Oshima, M., Takagi, K., Torii, R., Nagata, K., Shirouzu, I., … Kirino, T. (2005). Role of the Bloodstream Impacting Force and the Local Pressure Elevation in the Rupture of Cerebral Aneurysms. *Stroke*, *36*(9), 1933–1938. https://doi.org/10.1161/01.STR.0000177877.88925.06

Soloff, S. M., Adrian, R. J., & Liu, Z. C. (1997). Distortion compensation for generalized stereoscopic particle image velocimetry. *Measurement Science and Technology*, *8*(12), 1441–1454. https://doi.org/10.1088/0957-0233/8/12/008

Song, S. M., Napel, S., Pelc, N. J., & Glover, G. H. (1995). Phase Unwrapping of MR Phase Images Using Poisson Equation. *IEEE Transactions on Image Processing*, *4*(5), 667–676.

Stalder, A. F., Russe, M. F., Frydrychowicz, A., Bock, J., Hennig, J., & Markl, M. (2008a). Quantitative 2D and 3D Phase Contrast MRI : Optimized Analysis of Blood Flow and Vessel Wall Parameters. *Magnetic Resonance in Medicine*, *60*, 1218–1231. https://doi.org/10.1002/mrm.21778

Stalder, A. F., Russe, M. F., Frydrychowicz, A., Bock, J., Hennig, J., & Markl, M. (2008b). Quantitative 2D and 3D phase contrast MRI: Optimized analysis of blood flow and vessel wall parameters. *Magnetic Resonance in Medicine*, *60*(5), 1218–1231. https://doi.org/10.1002/mrm.21778

Stankovic, Z., Allen, B. D., Garcia, J., Jarvis, K. B., & Markl, M. (2014). 4D flow imaging with MRI. *Cardiovascular Diagnosis and Therapy*, *4*(2), 173–192. https://doi.org/10.3978/j.issn.2223-3652.2014.01.02

Steine, K., Stugaard, M., & Smiseth, O. A. (1999). Mechanisms of Retarded Apical Filling in Acute Ischemic Left Ventricular Failure. *Circulation*, *99*(15), 2048–2054. https://doi.org/10.1161/01.CIR.99.15.2048

Stewart, K. C., Charonko, J. C., Niebel, C. L., Little, W. C., & Vlachos, P. P. (2012). Left ventricular vortex formation is unaffected by diastolic impairment. *AJP: Heart and Circulatory Physiology*, *303*(10), H1255–H1262. https://doi.org/10.1152/ajpheart.00093.2012

Stewart, Kelley C., Kumar, R., Charonko, J. J., Ohara, T., Vlachos, P. P., & Little, W. C. (2011). Evaluation of LV diastolic function from color M-mode echocardiography. *JACC: Cardiovascular Imaging*, *4*(1), 37–46. https://doi.org/10.1016/j.jcmg.2010.09.020

Sträter, A., Huber, A., Rudolph, J., Berndt, M., Rasper, M., Rummeny, E. J., … Radiology, I. (2018). 4D-Flow MRI: Technique and Applications. *Fortschr Röntgenstr*, *190*(11), 1025–1035.

Stugaard, M., Brodahl, U., Torp, H., & Ihlen, H. (1994). Abnormalities of left ventricular filling in patients with coronary artery disease: Assessment by colour m-mode doppler technique. *European Heart Journal*, *15*(3), 318–327. https://doi.org/10.1093/oxfordjournals.eurheartj.a060497

Stugaard, Marie, Smiseth, O. A., Risöe, C., & Ihlen, H. (1993). Intraventricular early diastolic filling during acute myocardial ischemia: Assessment by multigated color M-mode doppler echocardiography. *Circulation*, *88*(6), 2705–2713. https://doi.org/10.1161/01.CIR.88.6.2705

Sunderland, K., Haferman, C., Chintalapani, G., & Jiang, J. (2016). Vortex analysis of intra-aneurismal flow in cerebral aneurysms. *Computational and Mathematical Methods in Medicine*, *2016*. https://doi.org/10.1155/2016/7406215

Szajer, J., & Ho-Shon, K. (2018). A comparison of 4D flow MRI-derived wall shear stress with computational fluid dynamics methods for intracranial aneurysms and carotid bifurcations — A review. *Magnetic Resonance Imaging*, *48*(November 2017), 62–69. https://doi.org/10.1016/j.mri.2017.12.005

Takatsuji, H., Mikami, T., Urasawa, K., Teranishi, J. I., Onozuka, H., Takagi, C., … Kitabatake, A. (1996). A new approach for evaluation of left ventricular diastolic function: Spatial and temporal analysis of left ventricular filling flow propagation by color M-mode Doppler echocardiography. *Journal of the American College of Cardiology*, *27*(2), 365–371. https://doi.org/10.1016/0735-1097(96)81240-X

Thomas, J. D. (2011). Flow propagation analysis: Computer or eyeball? *JACC: Cardiovascular Imaging*, *4*(1), 47–49. https://doi.org/10.1016/j.jcmg.2010.11.009

Thompson, B. G., Brown, R. D., Amin-Hanjani, S., Broderick, J. P., Cockroft, K. M., Connolly, E. S., … Torner, J. (2015). *Guidelines for the Management of Patients With Unruptured Intracranial Aneurysms: A Guideline for Healthcare Professionals From the American Heart Association/American Stroke Association*. *Stroke; a journal of cerebral circulation* (Vol. 46). https://doi.org/10.1161/STR.0000000000000070

Tibshirani, R. (2016). Regression Shrinkage and Selection via the Lasso. *Journal of the Royal Statistical Society. Seires B (Methological)*, *58*(1), 267–288.

Timmins, B. H., Wilson, B. W., Smith, B. L., & Vlachos, P. P. (2012). A method for automatic estimation of instantaneous local uncertainty in particle image velocimetry measurements. *Experiments in Fluids*, *53*(4), 1133–1147. https://doi.org/10.1007/s00348-012-1341-1

Töger, J., Zahr, M. J., Aristokleous, N., Markenroth Bloch, K., Carlsson, M., & Persson, P.-O. (2020a). Blood flow imaging by optimal matching of computational fluid dynamics to 4D-flow data. *Magnetic Resonance in Medicine*, (February), 1–15. https://doi.org/10.1002/mrm.28269

Töger, J., Zahr, M. J., Aristokleous, N., Markenroth Bloch, K., Carlsson, M., & Persson, P. O. (2020b). Blood flow imaging by optimal matching of computational fluid dynamics to 4D-flow data. *Magnetic Resonance in Medicine*, 1–9. https://doi.org/10.1002/mrm.28269

Tronchin, T., David, L., & Farcy, A. (2015). Loads and pressure evaluation of the flow around a flapping wing from instantaneous 3D velocity measurements. *Experiments in Fluids*, *56*(7), 7. https://doi.org/10.1007/s00348-014-1870-x

Van Gent, P. L., Schrijer, F. F. J., & Van Oudheusden, B. W. (2018a). Assessment of the pseudo-tracking approach for the calculation of material acceleration and pressure fields from time-resolved PIV: Part I. Error propagation. *Measurement Science and Technology*, *29*(4), 045204. https://doi.org/10.1088/1361-6501/aaa0a5

Van Gent, P. L., Schrijer, F. F. J., & Van Oudheusden, B. W. (2018b). Assessment of the pseudo-tracking approach for the calculation of material acceleration and pressure fields from time-resolved PIV: Part II. Spatio-temporal filtering. *Measurement Science and Technology*, *29*(4), 045206. https://doi.org/10.1088/1361-6501/aaab84

van Gent, P., Michaelis, D., van Oudheusden, B. W., Weiss, P.-E., de Kat, R., Laskari, A., … Schrijer, F. (2017). Comparative assessment of pressure field reconstructions from particle image velocimetry measurements and Lagrangian particle tracking. *Experiments in Fluids*, *58*(33), 33. https://doi.org/10.1007/s00348-017-2324-z

van Ooij, P., Potters, W. V., Collins, J., Carr, M., Carr, J., Malaisrie, S. C., … Barker, A. J. (2015). Characterization of Abnormal Wall Shear Stress Using 4D Flow MRI in Human Bicuspid Aortopathy. *Annals of Biomedical Engineering*, *43*(6), 1385–1397. https://doi.org/10.1007/s10439-014-1092-7

Van Ooij, P., Potters, W. V., Guédon, A., Schneiders, J. J., Marquering, H. A., Majoie, C. B., … Nederveen, A. J. (2013). Wall shear stress estimated with phase contrast MRI in an in vitro and in vivo intracranial aneurysm. *Journal of Magnetic Resonance Imaging*, *38*(4), 876–884. https://doi.org/10.1002/jmri.24051

van Oudheusden, B. W. (2013). PIV-based pressure measurement. *Measurement Science and Technology*, *24*(3), 032001. https://doi.org/10.1088/0957-0233/24/3/032001

Varble, N., Trylesinski, G., Xiang, J., Snyder, K., & Meng, H. (2017). Identification of vortex structures in a cohort of 204 intracranial aneurysms. *Journal of the Royal Society Interface*, *14*(130). https://doi.org/10.1098/rsif.2017.0021

Violato, D., Moore, P., & Scarano, F. (2011). Lagrangian and Eulerian pressure field evaluation of rod-airfoil flow from time-resolved tomographic PIV. *Experiments in Fluids*, *50*(4), 1057–1070. https://doi.org/10.1007/s00348-010-1011-0

Vlachos, P. P., Niebel, C. L., Chakraborty, S., Pu, M., & Little, W. C. (2014). Calculating Intraventricular Pressure Difference Using a Multi-Beat Spatiotemporal Reconstruction of Color M-Mode Echocardiography. *Annals of Biomedical Engineering*, *42*(12), 2466–2479. https://doi.org/10.1007/s10439-014-1122-5

Vlak, M. H. M., Algra, A., Brandenburg, R., & Rinkel, G. J. E. (2011). Prevalence of unruptured intracranial aneurysms, with emphasis on sex, age, comorbidity, country, and time period: A systematic review and meta-analysis. *The Lancet Neurology*, *10*(7), 626–636. https://doi.org/10.1016/S1474-4422(11)70109-0

Voß, S., Beuing, O., Janiga, G., & Berg, P. (2019). Multiple Aneurysms AnaTomy CHallenge 2018 (MATCH)— Phase Ib : Effect of morphology on hemodynamics. *PLOS ONE*, *14*(5).

Wang, C. Y., Gao, Q., Wei, R. J., Li, T., & Wang, J. J. (2017). Spectral decomposition-based fast pressure integration algorithm. *Experiments in Fluids*, *58*(84), 84. https://doi.org/10.1007/s00348-017-2368-0

Wang, Z., Gao, Q., Wang, C., Wei, R., & Wang, J. (2016). An irrotation correction on pressure gradient and orthogonal-path integration for PIV-based pressure reconstruction. *Experiments in Fluids*, *57*, 104. https://doi.org/10.1007/s00348-016-2189-6

Wermer, M. J. H., Van Der Schaaf, I. C., Algra, A., & Rinkel, G. J. E. (2007). Risk of rupture of unruptured intracranial aneurysms in relation to patient and aneurysm characteristics: An updated meta-analysis. *Stroke*, *38*(4), 1404–1410. https://doi.org/10.1161/01.STR.0000260955.51401.cd

Westerweel, J., & Scarano, F. (2005). Universal outlier detection for PIV data. *Experiments in Fluids*, *39*(6), 1096–1100. https://doi.org/10.1007/s00348-005-0016-6

Wetzel, S., Meckel, S., Frydrychowicz, A., Bonati, L., Radue, E. W., Scheffler, K., … Markl, M. (2007). In vivo assessment and visualization of intracranial arterial hemodynamics with flow-sensitized 4D MR imaging at 3T. *American Journal of Neuroradiology*, *28*(3), 433–438.

Wieneke, B. (2008). Volume self-calibration for 3D particle image velocimetry. *Experiments in Fluids*, *45*(4), 549–556. https://doi.org/10.1007/s00348-008-0521-5

Wieneke, B. (2017). PIV anisotropic denoising using uncertainty quantification. *Experiments in Fluids*, *58*(94), 94. https://doi.org/10.1007/s00348-017-2376-0

Wieneke, Bernhard. (2013). Iterative reconstruction of volumetric particle distribution. *Measurement Science and Technology*, *24*, 024008. https://doi.org/10.1088/0957-0233/24/2/024008

Wieneke, Bernhard. (2015). PIV uncertainty quantification from correlation statistics. *Measurement Science and Technology*, *26*(7). https://doi.org/10.1088/0957-0233/26/7/074002

Wolf, R. L., Ehman, R. L., Riederer, S. J., & Rossman, P. J. (1993). Analysis of systematic and random error in MR volumetric flow measurements. *Magnetic Resonance in Medicine*, *30*(1), 82–91. https://doi.org/10.1002/mrm.1910300113

Womersley, J. R. (1955). Method for the calculation of velocity, rate of flow and viscous drag in arteries when the pressure gradient is known. *The Journal of Physiology*, *127*(3), 553–563. https://doi.org/10.1113/jphysiol.1955.sp005276

Wood, E. H., Leusen, I. R., Warner, H. R., & Wright, J. L. (1954). Measurement of Pressures in Man by Cardiac Catheters. *Circulation Research*, *11*.

Wright, G. B., & Fornberg, B. (2006). Scattered node compact finite difference-type formulas generated from radial basis functions. *Journal of Computational Physics*, *212*(1), 99–123. https://doi.org/10.1016/j.jcp.2005.05.030

Wright, J., Member, S., Yang, A. Y., Ganesh, A., & Sastry, S. S. (2009). Robust Face Recognition via Sparse Representation. *IEEE TRANSACTIONS ON PATTERN ANALYSIS AND MACHINE INTELLIGENCE*, *31*(2), 210–227.

Xiang, J., Tutino, V. M., Snyder, K. V., & Meng, H. (2014). CFD: Computational fluid dynamics or confounding factor dissemination? the role of hemodynamics in intracranial aneurysm rupture risk assessment. *American Journal of Neuroradiology*, *35*(10), 1849–1857. https://doi.org/10.3174/ajnr.A3710

Xiang, Q. (1995). Temporal phase unwrapping for CINE velocity imaging. *Journal of Magnetic Resonance Imaging*, *5*(5), 529–534.

Xue, Z., Charonko, J. J., & Vlachos, P. P. (2014). Particle image velocimetry correlation signal-to-noise ratio metrics and measurement uncertainty quantification. *Measurement Science and Technology*, *25*(11), 115301. https://doi.org/10.1088/0957-0233/25/11/115301

Xue, Z., Charonko, J. J., & Vlachos, P. P. (2015). Particle image pattern mutual information and uncertainty estimation for particle image velocimetry. *Measurement Science and Technology*, *26*(074001), 074001. https://doi.org/10.1088/0957-0233/26/7/074001

Yotti, R., Bermejo, J., Antoranz, J. C., Desco, M. M., Cortina, C., Rojo-Álvarez, J. L., … García-Fernández, M. A. (2005). A noninvasive method for assessing impaired diastolic suction in patients with dilated cardiomyopathy. *Circulation*, *112*(19), 2921–2929. https://doi.org/10.1161/CIRCULATIONAHA.105.561340

You, S. H., Kong, D. S., Kim, J. S., Jeon, P., Kim, K. H., Roh, H. K., … Hong, S. C. (2010). Characteristic features of unruptured intracranial aneurysms: Predictive risk factors for aneurysm rupture. *Journal of Neurology, Neurosurgery and Psychiatry*, *81*(5), 479–484. https://doi.org/10.1136/jnnp.2008.169573

Yu, J., Agarwal, H., Stuber, M., & Schär, M. (2012). Practical Signal-to-Noise Ratio Quantification for Sensitivity Encoding: Application to Coronary MRA. *J Magn Reson Imaging*, *33*(6), 1330–1340. https://doi.org/10.1002/jmri.22571.Practical

Zhang, J., Bhattacharya, S., & Vlachos, P. P. (2020). Using uncertainty to improve pressure field reconstruction from PIV/PTV flow measurements. *Experiments in Fluids*, *61*(6), 131. https://doi.org/10.1007/s00348-020-02974-y

Zhang, J., Brindise, M. C., Rothenberger, S. M., Markl, M., Rayz, V. L., & Vlachos, P. P. (2022). A multi-modality approach for enhancing 4D flow magnetic resonance imaging via sparse representation. *Journal of The Royal Society Interface*, *19*(186). https://doi.org/10.1098/rsif.2021.0751

Zhang, J., Brindise, M. C., Rothenberger, S., Schnell, S., Markl, M., Rayz, V. L., & Vlachos, P. P. (2019). 4D Flow MRI Pressure Estimation Using Velocity Measurement-Error based Weighted Least-Squares. *IEEE Transactions on Medical Imaging*. https://doi.org/10.1109/TMI.2019.2954697

Zhang, J., Brindise, M. C., Rothenberger, S., Schnell, S., Markl, M., Saloner, D., … Vlachos, P. P. (2020). 4D Flow MRI Pressure Estimation Using Velocity Measurement-Error-Based Weighted Least-Squares. *IEEE Transactions on Medical Imaging*, *39*(5), 1668–1680. https://doi.org/10.1109/TMI.2019.2954697

Zhang, J., Rothenberger, S. M., Brindise, M. C., Scott, M. B., Berhane, H., Baraboo, J. J., … Vlachos, P. P. (2021). Divergence-Free Constrained Phase Unwrapping and Denoising for 4D Flow MRI Using Weighted Least-Squares. *IEEE Transactions on Medical Imaging*, *40*(12), 3389–3399. https://doi.org/10.1109/TMI.2021.3086331

Zhou, G., Zhu, Y., Yin, Y., Su, M., & Li, M. (2017). Association of wall shear stress with intracranial aneurysm rupture: Systematic review and meta-analysis. *Scientific Reports*, *7*(1), 1–8. https://doi.org/10.1038/s41598-017-05886-w

Zhou, J., Adrian, R. J., Balachandar, S., & Kendall, T. M. (1999). Mechanisms for generating coherent packets of hairpin vortices in channel flow. *Journal of Fluid Mechanics*, *387*, 353–396. https://doi.org/10.1017/S002211209900467X

Zhou, X., Papadopoulou, V., Leow, C. H., Vincent, P., & Tang, M. X. (2019). 3-D Flow Reconstruction Using Divergence-Free Interpolation of Multiple 2-D Contrast-Enhanced Ultrasound Particle Imaging Velocimetry Measurements. *Ultrasound in Medicine and Biology*, *45*(3), 795–810. https://doi.org/10.1016/j.ultrasmedbio.2018.10.031

PUBLICATIONS

Zhang, J., Bhattacharya, S., & Vlachos, P. P. (2022). Uncertainty of PIV/PTV based Eulerian pressure estimation using velocity uncertainty. *Measurement Science and Technology*, *33*(6), 065303. https://doi.org/10.1088/1361-6501/ac56bf

Zhang, J., Brindise, M. C., Rothenberger, S. M., Markl, M., Rayz, V. L., & Vlachos, P. P. (2022). A multi-modality approach for enhancing 4D flow magnetic resonance imaging via sparse representation. *Journal of The Royal Society Interface*, *19*(186). https://doi.org/10.1098/rsif.2021.0751

Ahmadzadegan, A., **Zhang, J.**, Ardekani, A., & Vlachos, P. P. (2022). Spatiotemporal Measurement of Concentration-Dependent Diffusion Coefficient. *Authorea*, *March 31*. https://doi.org/10.22541/au.164873358.86144442/v1

Rothenberger, S. M., **Zhang, J.**, Brindise, M. C., Schnell, S., Markl, M., Vlachos, P. P., & Rayz, V. L. (2022). Modeling Bias Error in 4D flow MRI Velocity Measurements. *IEEE Transactions on Medical Imaging*, *xx*(X), 1–1. https://doi.org/10.1109/TMI.2022.3149421

Zhang, J., Rothenberger, S. M., Brindise, M. C., Scott, M. B., Berhane, H., Baraboo, J. J., Markl, M., Rayz, V. L., & Vlachos, P. P. (2021). Divergence-Free Constrained Phase Unwrapping and Denoising for 4D Flow MRI Using Weighted Least-Squares. *IEEE Transactions on Medical Imaging*, *40*(12), 3389–3399. https://doi.org/10.1109/TMI.2021.3086331

Rajendran, L.*, **Zhang, J.***, Bane, S., & Vlachos, P. (2020). Uncertainty-based weighted least squares density integration for background-oriented schlieren. *Experiments in Fluids*, *61*(11), 239. https://doi.org/10.1007/s00348-020-03071-w

Zhang, J., Bhattacharya, S., & Vlachos, P. P. (2020). Using uncertainty to improve pressure field reconstruction from PIV/PTV flow measurements. *Experiments in Fluids*, *61*(6), 131. https://doi.org/10.1007/s00348-020-02974-y

Rajendran, L. K., **Zhang, J.**, Bhattacharya, S., Bane, S. P. M., & Vlachos, P. P. (2020). Uncertainty quantification in density estimation from background-oriented Schlieren measurements. *Measurement Science and Technology*, *31*(5), 054002. https://doi.org/10.1088/1361-6501/ab60c8

Singh, B., Rajendran, L. K., **Zhang, J.**, Vlachos, P. P., & Bane, S. P. M. (2020). Vortex rings drive entrainment and cooling in flow induced by a spark discharge. *Physical Review Fluids*, *5*(11), 114501. https://doi.org/10.1103/PhysRevFluids.5.114501

Zhang, J., Brindise, M. C., Rothenberger, S., Schnell, S., Markl, M., Saloner, D., Rayz, V. L., & Vlachos, P. P. (2020). 4D Flow MRI Pressure Estimation Using Velocity Measurement-Error-Based Weighted Least-Squares. *IEEE Transactions on Medical Imaging*, *39*(5), 1668–1680. https://doi.org/10.1109/TMI.2019.2954697

***** indicates shared co-authorship between primary authors